Scientific Tools for Fuel Characterization for Clean and Efficient Biomass Combustion

SciToBiCom Final Report

Glarborg, Peter; Jensen, Peter Arendt; Dam-Johansen, Kim; Illerup, Jytte Boll; Karlström, Oskar; Brink, Anders; Zevenhoven, Maria; Huoa, Mikko; Scharler, Robert; Brunner, Thomas

Total number of authors:
13

Publication date:
2013

Scientific Tools for Fuel Characterization for Clean and Efficient Biomass Combustion - SciToBiCom

4th Version, May, 2013

Peter Glarborg, DTU
Peter Arendt Jensen, DTU
Kim Dam-Johansen, DTU
Jytte Boll Illerup, DTU
Oskar Karlström, Åbo Akademi University
Anders Brink, Åbo Akademi University
Maria Zevenhoven, Åbo Akademi University
Mikko Hupa, Åbo Akademi University
Robert Scharler, BE2020+/Graz University of Technology
Thomas Brunner, BE2020+/Graz University of Technology
Ingwald Obernberger, BE2020+/Graz University of Technology
Terese Løvås, NTNU

Ed. Flemming Jappe Frandsen, DTU.

Table of Content:

1. Introduction

The utilisation of conventional wood derived fuels, new agricultural biomass fuels and pre-treated fuels is of increasing interest in all EU countries due to the growing relevance of energy utilisation from biomass. Moreover, fuel flexibility is of growing importance for all biomass furnace and boiler manufacturers which again makes an improved characterisation of fuels and fuel mixtures highly relevant.

In this respect, it has been essential to gain knowledge about the combustion and volatiles release behaviour of the different fuels and fuel mixtures. This is of special relevance for "new" and "difficult-to-use" fuels (e.g. short rotation crops, energy grasses, residues from agricultural industries), which usually show considerably higher ash contents and lower first ash melting points in comparison to conventional wood fuels (wood pellets, wood chips, bark) leading to increased problems concerning slagging, ash deposit formation and fine particulate emissions. Moreover, these fuels usually also show elevated N S and Cl contents leading to increasing NO_x, SO_x and HCl emissions.

Modern simulation tools are needed to efficiently analyse the underlying processes during biomass combustion. For biomass combustion plants, CFD modelling has proved to be a highly efficient tool for process analyses as a basis to optimise plant design concerning flue gas burnout, CO emissions, plant efficiencies and availabilities. However, practical experiences showed that a number of processes are still not sufficiently described like solid fuel combustion itself, NO_x formation as well as ash, aerosol and deposit formation.

An important problem related to the utilization of some biomass fuels is their contents of metal species, especially components containing alkali metals that are partly volatilized and molten during combustion and then condensed when the gas temperature falls below a certain level, either homogeneously into a fume, or heterogeneously on condensation nuclei or walls, eventually forming deposits on heat transfer surfaces, and, depending on the cleaning devices employed, escaping into the surroundings with known deleterious health effects. The latter is particularly important in small combustors where the gas cleaning equipment is more primitive compared to larger plants.

The fuels also may contain other precursors to pollutants, such as nitrogen as part of the organic structure that may be oxidized into nitrogen oxides with a well-known inconvenience to the environment. An improved knowledge of the transformations of nitrogen compounds released from the fuel and carried to the exhaust gas form a basis for reduction procedures to convert the N-compounds into free nitrogen instead of nitrogen oxides. Furthermore, many biomasses are obtained with high content of moisture and they may be directly used in a boiler without drying. This influences the progress of combustion and has to be taken into account to predict the behavior of a fuel during conversion, particularly in case of grate firing. The inclusion of the information regarding the primary release from the fuel particles into a description of the conversion process in a furnace has also been very important. In some cases it may be advantageous to prepare the biomass feedstock upstream the combustion process – both in combustors using one fuel and in processes with co-combustion of two or more fuels. For the design of such processes the physical and chemical characteristics of the fuels are of utmost importance.

Through years the Nordic countries and Austria have been very active in promoting biomass utilization for heat and power production. In this project we have succeeded in conducting a research plan including main actors in the field of biomass combustion from Denmark, Norway, Finland and Austria. The project has aimed at the development of advanced fuel analysis and characterisation methods concerning the combustion of different biomass fuels in various plant technologies of different size ranges, see Table 1-1. The goal has been to provide the basis for an improved understanding of the combustion behaviour and to collect the data in an advanced fuel database as an important contribution to topic 2 of the present ERANET call. Moreover, advanced CFD-based simulation routines considering different phenomena like single particle conversion, solid biomass combustion on the grate, release of ash forming elements, gas phase combustion and NO_x formation has been developed as efficient, future process analysis and plant design tools which represents an important contribution to topic 1 of the present ERANET call.

Table 1-1: Research areas and WPs in SciToBiCom.

	Generic models for NOx formation	**Generic models - ash and small particulates**	**Combustors – Technology dependent models**	**Fuels**
Topic 1 Modeling of the combustion process	**WP1** **Generic models for NOx formation** **DTU,** NTNU Model for gas phase and heterogeneous nitrogen chemistry	**WP2** **Generic models - Ash formation/ deposition and formation of small particles** **AAU**, BE2020+/ TUG, DTU Volatiles release model for ash forming species Thermodynamic equilibrium calculations based on wet-chemical fuel analyses Aerosol formation model for use in CFD	**WP3** **Combustors – Technology dependent models** **BE2020+/TUG,** AAU Implementation of generic models developed in other WPs Models for grate furnaces Models for fluidized bed combustion plants	Standard wood pellets Wood chips Bark Straw Miscanthus Arundo Donax Residues from bioethanol production Waste wood Fuel blends
Topic 2 Advanced characterization of biomass fuels	**WP4** **Advanced characterization – NOx related issues** **NTNU**, AAU Release characteristics for NOx precursors Fuels specific parameters for particle models (C, N, H, O, S)	**WP5** **Advanced characterization – Ash related issues** **BE2020+/TUG,** AAU, NTNU Fuel characterization based on fuel indexes Fuel characterization based on selective leaching, SEM and other techniques TGA/DSC analyses of ashes Lab-scale combustion tests in a fixed-bed reactor Determination of release curves for alkalis and heavy metals Establishment of an advanced fuel database	**WP6** **Advanced characterization – Fuel pretreatment** **DTU**, AAU Charaterization of fuel properties important for pretreatment (heat transfer, Cl-release, grindability) Pulverized combustion	

2. WP1: Generic Models for NOx Formation
Coordinated by Prof. Peter Glarborg, DTU

A detailed model for the gas-phase nitrogen chemistry has been developed and validated. It emphasizes mainly the oxidation chemistry of amines (NH_3, $C_2H_5NH_2$, CH_3NHCH_3). Based on the detailed chemical kinetic model, a simplified scheme for oxidation of N-volatiles from biomass has been completed. For high-temperature applications, only 26 species are required to yield a good prediction of NO_x. Biomass char-N oxidation has been characterized in laboratory experiments. Results were obtained for straw and bark, with reference experiments for a bituminous coal. A simplified model for char-N oxidation, involving only two steps (char-N+O_2 → NO, char+NO → O_2) has been developed and parameterized based on the experimental results.

Formation of nitrogen oxides (NO_x) is a significant concern in combustion of biomass. Extensive research over the last decades at DTU, NTNU and Aabo in nitrogen chemistry has provided a good understanding of formation mechanisms, but details of the NO formation mechanisms, in particular those involving heterogeneous reactions, are still uncertain and current, simplified schemes for use in CFD are inadequate.

Development of simplified, but reliable, sub-models for NO_x is critical in order to facilitate CFD-calculations of emissions in biomass combustion units and evaluation of primary measures for NO_x reduction. There are two challenges: 1) development of a simple scheme to describe gas-phase NO formation from volatile oxidation, and 2) development of a predictive model for NO formation during biomass-char oxidation.

WP1 of the SciToBiCom project, had the following original objectives:

- Establishment of a detailed chemical kinetic model for gas-phase nitrogen chemistry, based on previous work and literature results, emphasizing conversion of biomass volatile-N
- Development and test of a simplified scheme for NO_x formation, based on the models for volatile and char nitrogen conversion
- Experimental characterization of NO formation from biomass char oxidation

- Development of biomass char-N oxidation model, based on novel experiments and literature results

In the following sections, the results of each subtask are described. Most of the results have been published as articles and the present report provides only an abbreviated presentation.

2.1 Task 1.1: Establishment of a Detailed Chemical Kinetic Model

The objective of this task was the establishment of a detailed chemical kinetic model for gas-phase nitrogen chemistry, emphasizing conversion of biomass volatile-N. Since biomass volatile nitrogen is mostly released as amines, the work in Task 1.1 has focused primarily on developing and validating the ammonia [1] and C_2-amine [2] subsets of the nitrogen chemistry. However, also hydrocarbon / nitrogen interactions have been analyzed, through modeling of nitrohydrocarbon flames [3,4].

Theoretical work

Here, key reactions in the amine chemistry, for which inadequate experimental data are available, are analyzed by high-level ab initio calculations in order to provide reliable rate constants for modeling. For citations of literature work, see [1,2].

Lifetime of NNH

The lifetime of NNH has been the subject of a number of theoretical studies (see [1]). Predictions for the ground state lifetime (τ_0) range from 3×10^{-11} to 4×10^{-8} s. Meanwhile, the excited vibrational states have lifetimes that are generally about three orders of magnitude shorter. Because of the vast difference in the lifetimes between the ground and excited vibrational states, we anticipate that a rigorous theoretical analysis would show a fairly broad regime of temperature and pressure where the steady-state population distribution during dissociation has significant population only in the ground state, resulting in a thermal dissociation rate coefficient that can be approximated accurately as the tunneling rate coefficient in this state. Of course, at temperatures and pressures where the excited states can be populated effectively from the ground state by collisions

the rate coefficient will change, resulting in a dependence on temperature and pressure. However, the calculated lifetimes for the excited states suggest that pressures of the order of 100 -1000 atmospheres would be required for this effect to be significant. Any excited NNH formed directly from the NH_2+NO reaction would show up on the phenomenological time scale as contributing to the reaction NH_2+NO→N_2+H+OH reaction in the regime of interest. At least at lower temperatures experiments indicate that this latter reaction is not significant. A problem with our argument is that, because of the very short lifetimes involved, NNH dissociation may not yield to a rate-coefficient (phenomenological) description at all. Nevertheless, the lifetime used in a model should not be longer than the ground-state lifetime (it represents an upper limit) and under the present conditions, should be roughly of that magnitude. We cannot make any more precise statements about the thermal dissociation of NNH(or even verify our picture of it) without performing a fairly sophisticated theoretical analysis. This exercise must be left for another time.

The most recent study, by Bozkaya et al. (see [1]), yields the longest predicted τ_o of 3.6 x 10^{-8} s. The underlying electronic structure calculations in this study are the most extensive to date and yield a classical barrier height of 10.6±0.2 kcal/mol. However, the lifetime is obtained from simple one-dimensional asymmetric Eckart tunneling calculations, which are not expected to be particularly accurate in this case. Indeed, errors exceeding an order of magnitude would not be unusual.

Earlier full dimensional quantum dynamics calculations by Koizumi, Schatz, and Walch (see [1]) (KSW) predicted a ground state lifetime of 3 x 10^{-9} s. Related calculations by Li and Guo (see [1]) employing the same KSW potential, but with different dynamical methods, yielded an essentially identical ground state lifetime. Unfortunately, the classical barrier height of 11.4 kcal/mol for the KSW potential is significantly greater than the value determined by Bozkaya et al. Notably, the sample calculations of Koizumi et al. for a second surface with a classical barrier height of 10.5 kcal/mol yield a predicted τ_o that is within a factor of 5 of their main prediction.

More recently, Caridade et al. (see [1]) have used full-dimensional quantum dynamics calculations to predict a ground state lifetime of 4 x 10^{-10} s for a new more accurate potential energy surface. However, their predictions for the KSW potential differ by a factor of two from the earlier calculations of Koizumi et al. and of Li and Guo. Furthermore, their calculations for the KSW potential have a

stated uncertainty of 9 times the predicted value. Although not reported, their uncertainties for their reference potential are presumably of similar magnitude.

Taken together, the Koizumi et al. and Caridade et al. calculations suggest that the best estimate for τ_0 is approximately 8 x 10^{-10} s, which correlates with a decrease in the KSW value by a factor of 4 due to the overestimated barrier height. It also correlates with a factor of two increase in the Caridade et al. estimate in response to apparent errors in their dynamics methods. Importantly, this estimate is for tunneling from the ground rotational state. Guo and Thompson (see [1]) have performed an interesting semiclassical study of the effect of rotation on the lifetime. Their calculations suggest that the lifetime increases by a factor of 2.4 for a rotational energy of 5 kcal/mol. Including such a rotational correction implies a best estimate for the lifetime of thermal rotational states of NNH at 1000-1500 K of 1 or 2 x 10^{-9} s. Unfortunately, the uncertainty in this prediction is still significant. Ideally, the lifetimes for explicit rotational states of NNH would be calculated for a highly accurate potential energy surface, such as the one recently presented by Motas and Varandas (see [1]). We have adopted a value of $\tau_0 = 10^{-9}$ s in the modeling discussed below.

NNH + O_2

There do not appear to be any prior experimental or ab initio theoretical studies of the NNH + O_2 reaction, although Dean and Bozzelli (see [1]) applied qualitative QRRK concepts to estimate the rates and branching for this reaction. The radical character of the NNH and O_2 species suggests that the NNH + O_2 reaction might involve the formation of an OONNH complex, as Dean and Bozzelli presume. However, this complex is endothermic relative to reactants, and so no complex formation is predicted here. Instead, the reaction of NNH with O_2 involves a barrierless abstraction to form the highly exothermic products N_2 + HO_2 (-57 kcal/mol).

The abstraction minimum-energy paths (MEPs) are obtained from constrained optimizations with multi-reference second-order perturbation theory CASPT2 employing the aug-cc-pVDZ basis set. The active orbitals in the 11-electron, 9-orbital (11e,9o) CAS part of this calculation correlate with the radical orbital of NNH (1e,1o), the NH σ,σ^* orbitals (2e,2o), and the π spaces of NNH (2e,2o) and O_2 (6e,4o). The cis,cis abstraction pathway, which involves the partial formation of a five-membered OOHNN ring, is clearly the dominant pathway. The cis,trans and trans,cis pathways are also essentially barrierless, with the latter involving the

partial formation of a four-membered OOHN ring. The trans,trans path was also explored, but it was found to relax to the cis,cis path at OH separations of 2.4 Å and smaller.

The VRC-TST calculations include one-dimensional corrections for limitations in the basis set, for larger active spaces, and for the effects of geometry relaxation, each of which is obtained from consideration of the cis,cis MEP. The basis set corrections are obtained from the average of CBS estimates based on the extrapolation of cc-pVnZ or aug-cc-pVnZ calculations, where n=T and Q for both cases. The active-space correction is given by the difference between CASPT2(11e,90)/aug-cc-pVDZ and CASPT2(7e,50)/aug-cc-pVDZ results. The geometry relaxation correction is obtained from the difference of the full and partially optimized MEPs. The reaction-coordinate and dividing-surface optimizations consider both a fixed center-of-mass separation and a fixed OH separation, each for a range of distances.

The present direct CASPT2-based VRC-TST predictions for the NNH + $O_2 \rightarrow N_2$ + HO_2 rate coefficient are illustrated in [1]. The predictions include a dynamical correction factor of 0.85 as evaluated for related radical-radical reactions. These predictions are estimated to have an overall uncertainty of a factor of 1.5. The modified Arrhenius expression $5.55 \times 10^{13}\ T^{-0.385}\ \exp(13.4/RT)$ $cm^3\ mol^{-1}\ s^{-1}$ provides a satisfactory reproduction of these results over the 200 – 2400 K temperature range.

Notably, Dean and Bozzelli (see [1]) predict a rate coefficient of ~10^{11} $cm^3\ mole^{-1}\ s^{-1}$, which is two orders of magnitude smaller than the present predictions. They also predict 20% branching to OH + N_2O. Our own limited B3LYP density-functional-theory search for a pathway leading to these products suggests that the latter branching is negligible.

Under conditions with a large concentration of O_2, the reaction of NNH with O_2 could conceivably provide an alternative route to the formation of NO through an HNO + NO channel. However, limited B3LYP calculations suggest a very high barrier of about 58 kcal/mol for this channel, which effectively negates any possible contribution from it.

NNH + O

The reaction of NNH with O has been the subject of a recent high-level theoretical study (see [1]). Here, we build on this work, making improvements to a number of key aspects. Most importantly, we employ VRC-TST and trajectory simulations on potential energy surfaces based on multireference electronic-structure theory to obtain more accurate estimates of the entrance channel and NH + NO transition-state fluxes. We also make a number of corrections to the energies and pathways in the underlying potential energy surface for subsequent isomerizations and dissociations. These corrections are incorporated in our master equation for the overall kinetics.

The potential energy surface for the interaction of NNH with O is remarkably attractive (see [1]). There are barrierless reaction paths for addition to the terminal N from both the cis and trans side, for addition to the central N atom from the trans side, and for abstraction of the H atom. An analytic representation of this interaction potential was obtained here via a fit to a set of Davidson-corrected multi reference singles and doubles configuration interaction calculations (CAS+1+2+QC). The (7e,6o) active space for these calculations consists of the (4e,3o) *p* space of O, the radical orbital of NNH, and the (2e,2o) π space of NNH. These calculations employed an aug-cc-pVDZ basis set and the CAS part of the calculation averaged over the three states correlating with the nearly degenerate states of O(^{3}P). Analytic potentials were obtained for both the ground and first excited states, both of which are attractive. The third state is repulsive at short separation and so does not contribute to the kinetics.

We have evaluated the total rate coefficient and branching fractions for the four different channels with both trajectory simulations and VRC-TST calculations. The branching ratio estimates require approximate dividing surfaces for delineating the different channels. This separation is somewhat imprecise due to the attractiveness at all orientations. Nevertheless, the predictions are reasonably insensitive to modest variations in the divisions between the channels. The predicted overall rate coefficient from the trajectory calculations is ~0.89 times that from the VRC-TST estimates. The branching fractions predicted by the two methods are also quite similar. The contributions to the rate coefficients from the first excited state are typically about 85% of those from the ground state.

For computational reasons, the final master-equation analysis for the channel-specific bimolecular rate coefficients employs adjusted VRC-TST predictions for

the individual fluxes. These adjustments involve a reduction in the rate coefficients for the cis and trans additions; the corrections involve multiplicative factors of 0.8 and 0.7, respectively. These reductions yield a total rate coefficient and branching ratios that reasonably reproduce the more limited trajectory values.

The potential energy surface for the subsequent isomerizations and dissociations in the reaction of NNH with O was studied here with electronic-structure methods that are closely related to those employed by Haworth et al. (see [1]). The rovibrational properties and zero-point energies were analyzed with the B3LYP/6-311++G(d,p) density functional method. The primary energies come from RQCISD(T)/CBS calculations with the CBS extrapolation given by the average of extrapolations based on either cc-pVnZ or aug-cc-pVnZ basis sets, with n=Q,5. The two extrapolations typically agreed to within a few tenths of a kcal/mol, and the extrapolation generally predicted a difference from n=5 results of 0.6 kcal/mol or less. Core-valence correlation corrections (0.4 kcal/mol or less) were evaluated from CBS extrapolations of aug-cc-pCVnZ calculations, with n=T,Q. Relativistic corrections (0.3 kcal/mol or less) were obtained from CAS calculations with the aug-pCVTZ basis set.

Related results for the stationary-point energies from Haworth et al. are also reported in [1]. The predicted energies are remarkably different for a number of species. In many instances the two calculations differ by more than their stated maximum uncertainty of 1.0 kcal/mol. An attempt to reproduce their results indicates some error in their CCSD(T)/aug-cc-pV5Z energies, which gets magnified in their basis set extrapolation. For comparison we report our own RCCSD(T)/CBS results including corrections, which should be closely comparable to their results. Another more minor discrepancy involves the relativistic corrections, with theirs being larger by about a factor of two.

A final distinction between the two calculations arises from our preference for the RQCISD(T) method. From our experience, the RQCISD(T) method provides energy estimates that are similar to the UCCSD(T) method, both of which are more accurate than the RCCSD(T) method. Reference [1] includes the results from each of these methods. There are clearly some significant differences between them for this system. The differences between the RCCSD(T) and UCCSD(T) results are greatest for the cases with large T1 diagnostics, which is taken to be an indicator of multireference effects. The differences between the

RQCISD(T) and UCCSD(T) results are harder to understand and provide some indication of the level of uncertainty in the PES.

Fortunately, the two transition states with large T1 diagnostics have little bearing on the rate-coefficient predictions. The torsional transition state for isomerization from trans-ONNH to cis-ONNH is low enough in energy that isomerization is expected to be rapid even with a moderate change in its energy. Furthermore, there is a low-energy bending transition state that also serves to rapidly equilibrate the cis-trans isomers. The transition state for decomposition to N_2 + OH from ONHN has little effect on the predicted branching to N_2 + OH from NNH + O because the direct abstraction provides the dominant pathway to these products. Thus, we have chosen not to perform any multireference evaluations for these two transition states with high T1 diagnostics.

The collisionless-limit rate coefficients were evaluated from master-equation calculations employing transition-state-theory estimates for each of the channels illustrated in the schematic PES (see [1]). The partition functions for the transition states with well defined saddle points were obtained from rigid-rotor, harmonic-oscillator estimates, including hindered-rotor corrections as appropriate. Those for the barrierless entrance channels were obtained from the combination of VRC-TST and trajectory calculations, as described above. The barrierless NH + NO channel was also treated with VRC-TST as described below. The calculations indicate essentially no pressure dependence for realistic ranges of pressure. Indeed, the total association rate coefficient is within 20% of the collisionless-limit rate coefficient for temperatures up to 2000 K.

The present predictions for the overall and channel-specific rate coefficients are illustrated in [1]. The predictions are similar to those of Haworth et al., although the two sets of predictions differ by as much as a factor of three. The primary products are predicted to be N_2 + OH, with significant branching to N_2O + H. The endothermicity of the NO + NH channel makes this a relatively minor channel even at 2000 K. The calculated rate coefficients are reproduced well by the modified Arrhenius expressions: $k_{N2+OH} = 1.20\text{x}10^{13}\ T^{0.145}\ \exp(217/RT)$, $k_{NNO+H} = 1.87\text{x}10^{14}\ T^{-0.274}\ \exp(21.7/RT)$, and $k_{NH+NO} = 5.18\text{x}10^{11}\ T^{0.388}\ \exp(409/RT)$ $cm^3\ mol^{-1}\ s^{-1}$ over the 300 – 2500 K temperature range. The predicted rate coefficients for each of these channels are estimated to have an uncertainty of a factor of 2.

NH + NO

The NNH + O potential energy surface also allows us to examine the kinetics of the NH + NO and H + N_2O reactions. The entrance channel for the NH + NO reaction is barrierless, and so again we apply direct VRC-TST to this channel. In this case, the orientation-dependent interaction energies were obtained from CASPT2(7e,6o)/aug-cc-pVDZ calculations. A one-dimensional correction for geometry relaxation was obtained with the same method, while a correction for limitations in the basis set was obtained from an average of cc-pVnZ- and aug-cc-pVnZ-based CBS extrapolations with n=T,Q. The active space in these CAS calculations consisted of the two radical orbitals in ^{3}NH and the (5e,4o) π-space of NO. The CAS wavefunction is for an average of the two states correlating with the doubly degenerate ground state of NO.

The contributions from both the ground state, correlating with the 2A' state in Cs symmetry, and the first excited state, correlating with the 2A" state, were included in the VRC-TST analysis. The first excited state was found to make a negligible contribution for temperatures up to 3000 K. Similarly, a quartet pathway was explored and found to be insignificant.

The VRC-TST analysis included an approximate separation into cis and trans addition products. Pivot points were placed at a grid of locations along the internuclear axis for both NH and NO.

The present ab initio TST based predictions for the NH + NO rate coefficients are plotted in [1]. Again little pressure dependence is expected, and so we consider only the collisionless-limit rate coefficients. This reaction has been studied extensively in the laboratory. For simplicity, we restrict our comparison to the recent review of Baulch et al. (see [1]), which suggests that the literature rate coefficients have an uncertainty of a factor of 2. Overall, the present predictions are in good agreement with this review, with a maximum discrepancy between the two total rate constants of less than a factor of 1.5. However, our *ab initio* based predictions suggest a shallower decay with temperature in the 1000-2000 K region and no rise at higher temperatures. The absence of a rise at higher temperature correlates with a lower predicted rate coefficient for the NNH + O channel. Baulch et al. use a larger high-temperature rate coefficient for this channel to explain the experimentally observed rise in the total rate constant. The present predictions for the channel-specific rate coefficients are reproduced well by the modified Arrhenius expressions $k_{NNO+H} = 1.75x10^{14}\ T^{-0.351}\ \exp(244/RT)$,

k_{N2+OH} = 2.69 x10^{12} $T^{-0.0721}$ exp(513/RT), and k_{NNH+O} = 1.94x10^{10} $T^{0.624}$ exp(-10870/RT), cm^3 mol^{-1} s^{-1} over the 500 to 3000 K temperature range. We estimate the uncertainty in our prediction of the total rate coefficient to be a factor of 1.3.

$H + N_2O$

The last reaction we want to use to test our potential for the ONNH system is that between nitrous oxide and hydrogen atoms. This reaction has been studied a number of times in the laboratory, but the 1987 paper of Marshall et al. (see [1]) appears to be the most accurate and comprehensive investigation to date. These authors measured the total rate coefficient between 390 K and 1310 K. There appears to be little or no disagreement in the literature about the products – the consensus is that the reaction produces N_2 + OH exclusively under conditions of interest. The master-equation analysis employed an exponential-down energy transfer model with $\langle\Delta E_{down}\rangle$ = 100 $(T/300)^{0.85}$ cm^{-1}. This expression is typical of what we have found for small molecules interacting with weak colliders. In [1] we compare our theoretical predictions of the rate coefficient with the results of Marshall et al. The agreement is remarkably good. The most interesting result of our analysis is that the "low-temperature curvature" in the Arrhenius plot is not due to tunneling, as suggested by Marshall et al. Instead, it is due to stabilization in the cis- and trans-HNNO wells at low temperatures. The bimolecular channels (N_2 + OH, NH + NO, and NNH + O) have rate coefficients that are essentially independent of pressure at least up to p=1 atm. The most important of the three channels is, in fact, N_2 + OH, as indicated in the figure. The other channels only begin to come into play at high temperature where the N_2 + OH curve begins to deviate from k_{tot}.

The collisionless-limit channel-specific rate coefficients are reproduced well by the modified Arrhenius expressions k_{N2+OH} = 6.44x10^{7} $T^{1.84}$ exp(-13490/RT), k_{NO+NH} = 7.34x10^{20} $T^{-1.55}$ exp(-36940/RT), and k_{NNH+O} = 2.25x10^{19} $T^{-1.10}$ exp(-48180/RT), cm^3 mol^{-1} s^{-1} over the 500 to 2500 K temperature range. The uncertainty in these predictions is about a factor of 2 near 1000 K.

$NH_2 + O_2$

Although the reaction of NH_2 with O_2 has been the subject of a few experimental studies, little is known about it other than that it is slow (see [1]). Nevertheless, this reaction has been reported to be of significance to the Thermal $DeNO_x$ process at high concentrations of O_2 (see [1]). Building on earlier work of Melius

and Binkley [90] and Sumathi and Peyerimhoff [91], we have evaluated the stationary-point energies in the $NH_2 + O_2$ reaction at the QCISD(T)/CBS{T,Q}//B3LYP/6-311++G(d,p) level. There are two product channels:

$NH_2 + O_2 \rightarrow H_2NO + O$ (R12)
$NH_2 + O_2 \rightarrow HNO + OH$ (R13)

The $H_2NO + O$ channel arises from a simple bond fission of the initial H_2NOO adduct, while the HNO + OH channel arises from isomerization via a tight 4-center transition state, leading to HNOOH, followed by decomposition of this complex to HNO + OH. The much lower entropy for the 4-center transition state coupled with its lower energy implies that the HNO + OH channel should be dominant at low temperature, while the $H_2NO + O$ channel should be dominant at high temperature. Due to the low stability of the H_2NOO complex no pressure dependence is expected at combustion temperatures.

We have used TST to make predictions for the temperature dependence of the rate coefficient for each of the channels. For HNO + OH we have employed rigid-rotor, harmonic-oscillator assumptions within tunneling corrected conventional TST. However, there is a large T1 diagnostic of 0.065 for the 4-center TS leading to HNOOH. Thus, we have also performed multireference CASPT2/CBS and CAS+1+2+QC/CBS calculations with both (3e,3o) and (7e,7o) actives spaces. The geometries and vibrational frequencies for these multireference calculations were obtained at the CASPT2(3e,3o)/cc-pVTZ level. The orbitals in this (3e,3o) active space correlate in H_2NOO with the radical orbital and the σ,σ^* orbitals of the active NH bond (or equivalently in HNOOH with the radical orbital and the σ,σ^* orbitals of OH). The (7e,7o) active space also includes the NO and OO σ,σ^* orbitals. The 4-center transition state is predicted to be 29.3, 34.8, 30.4, or 33.3 kcal/mol above the H_2NOO minimum for the CASPT2(3e,3o), CAS+1+2+QC(3e,3o), CASPT2(7e,7o), and CAS+1+2+QC(7e,7o) calculations, respectively. The (7e,7o) CASPT2 and CAS+1+2+QC barriers are 1.5 kcal/mol below and above the QCISD(T) results, respectively, suggesting the uncertainty in this barrier is ~ 2 kcal/mol.

For the $H_2NO + O$ channel we have implemented direct CAS+1+2+QC VRC-TST. The $H_2NO + O$ reaction has many similarities to the NNH + O reaction. In particular, there are two strongly attractive doublet surfaces and one repulsive surface. In this case, the contribution from the first excited state is about ½ that from the ground state. There are also multiple reaction sites with barrierless attacks at the

H's, the N, and the O. Here, we are only interested in the addition to form H_2NOO due to our focus on the $NH_2 + O_2$ reaction. With this in mind an approximate separation from the other channels is implemented. The orientation-dependent interaction energies for the VRC-TST calculations are evaluated at the CAS+1+2+QC(5e,4o)/aug-cc-pVDZ level. The CAS part is averaged over the three states correlating with the degenerate states of the O atom. Calculations at the CAS+1+2+QC(7e,5o) level were used to obtain one-dimensional geometry relaxation, active-space (both with the aug-cc-pVDZ basis), and basis-set corrections (with basis-set extrapolation of aug-cc-pVTZ and aug-cc-pVQZ calculations). A range of pivot points displaced above and below the O atom in H_2NO were considered in addition to center-of-mass pivot points.

One additional complication arises for the $H_2NO + O$ channel. In particular, H_2NO is slightly distorted from planarity, which implies that the umbrella mode should be highly anharmonic with a double well potential. At the B3LYP/6-311++G(d,p) level this mode has a frequency of only 89 cm^{-1}. In contrast, at the QCISD(T)/CBS{T,Q} level this mode has a frequency of 349 cm^{-1}. We have evaluated the angular potential for this mode at the QCISD(T)/cc-pVQZ level and used that to obtain an anharmonic correction for the partition function. Although the potential is highly anharmonic, the effect on the partition function of the double minimum and the restriction on angular ranges largely cancel. As a result, at least from room temperature to 2000 K, the anharmonic partition function differs by less than 20% from the corresponding harmonic one.

The present *ab initio* TST based predictions for the rate coefficients are illustrated in [1]. These predictions are reproduced well by the modified Arrhenius expressions $k_{H2NO+O} = 2.62x10^{11}\ T^{0.487}\ exp(-29050/RT)$ and $k_{HNO+OH} = 2.88x10^{-2}\ T^{3.76}\ exp(-18180/RT)\ cm^3\ mol^{-1}\ s^{-1}$ over the 500 to 2500 K temperature range. Near 1000 K we estimate the uncertainty in our predictions to be factors of 2 and 4 for the $H_2NO + O$ and HNO + OH channels, respectively. For temperatures of 600 K and higher, the $H_2NO + O$ channel is dominant. The earlier qualitative QRRK calculations of Dean and Bozzelli (see [1]) yielded remarkably good estimates for the rate coefficient for this channel, as illustrated in *Fig. 10*. In contrast, their predictions for the HNO + OH channel are too small by one to two orders of magnitude.

In the absence of direct measurements for the $NH_2 + O_2$ rate coefficient, we have evaluated our calculated rate constant by comparing model predictions to global experimental data for NH_3 oxidation. Shock tube ignition delay experiments for

NH_3 are quite sensitive to the rate constant for $NH_2 + O_2$. In [1], model predictions with the calculated rate constant and the chemical kinetic model discussed below are compared to data from Fujii et al. (see [1]). Sensitivity analysis for these conditions confirms that calculations of the NH_3 concentration as a function of time are primarily sensitive to the rate constant for $NH_2 + O_2$. The good agreement obtained supports the accuracy of the rate constant.

C_2-amines

The structures and vibrational frequencies (scaled by a factor of 0.99) of target molecules and reference species were computed via density functional theory at the B3LYP/6-311G(d,p) level of theory. Coupled-cluster energies at these geometries, approximately extrapolated to the complete basis set limit in a series of additive steps, were obtained by application of the CBS-QB3 methodology of Petersson and co-workers (see [2]). These steps were carried out using the Gaussian 09 program. With the inclusion of vibrational zero-point energy, the enthalpy changes between reactants and products at 0 K were derived for a series of working reactions outlined below. Heat capacities, entropies and enthalpy corrections, C_P, S and H_T-H_0, were calculated for each species as a function of temperature T with the usual assumption of a rigid-rotor harmonic oscillator model, but also incorporating the algorithm of Ayala and Schlegel (see [2]) as implemented in Gaussian 09 to account for the contributions of any free or hindered internal rotors. These data were employed to derive $\Delta_r H_{298}$ for the working reactions, where all but one of the enthalpies of formation are known. In each reaction, $\Delta_f H_{298}$ was then derived for the one unknown species, denoted with an asterisk. Initial reference species are H atoms and ethylamine. For the latter we adopted the precise value of $\Delta_f H_{298}$ = -11.97 ± 0.36 kcal mol^{-1} recommended by Bodi et al. (see [2]). For acetonitrile we used $\Delta_f H_{298}$ = 17.70 ± 0.09 kcal mol^{-1} from An and Mansson (see [2]). As new species were determined, they were used to derive enthalpies of further species by successive H-atom eliminations, e.g (see [2]):

$$CH_3CH_2NH_2 \rightarrow H + CH_2CH_2NH_2^*$$

The transition states for several reactions were characterized with the same computational approach, i.e., density functional theory for the geometry and frequencies followed by CBS-QB3 theory for the energy, in order to derive the kinetics. Unimolecular rate theory was applied as implemented in the MultiWell program suite, to derive rate constants at 0.04 bar of Ar bath gas as a function of

temperature.

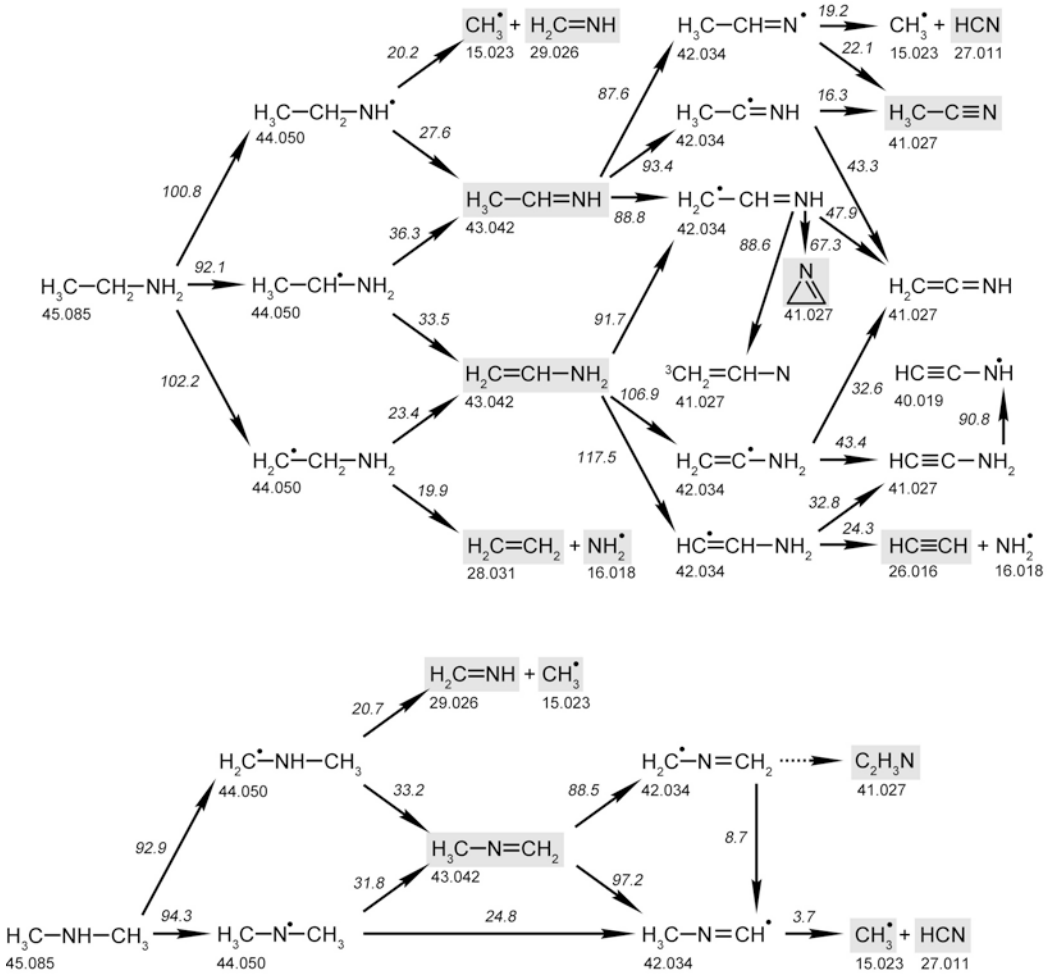

Figure 2-1: Proposed destruction pathways for ethylamine (*top*) and dimethylamine fuel (*bottom*). The exact masses are indicated below the respective species, and selected bond dissociation energies derived via quantum chemistry are denoted in italic near the arrow for the respective reaction steps. Species highlighted in grey were detected in the experiment.

The effects of hindered rotors and quantum mechanical tunneling through an Eckart potential were included. To estimate energy transfer between Ar and reactant molecules, the exponential down model with an assumed parameter of 350 cm^{-1} was employed, and Lennard-Jones parameters of σ = 3.62 Å and ε/k_B = 372 K, suggested for ethylamine (see [2]), were used for all the intermediates.

The various C-H and N-H bond dissociation enthalpies we derived computationally

are included in italic numbers in the proposed fuel decomposition schemes shown in Fig. 1.1., and the new thermochemistry is summarized in [2]. One check on the methodology employed here is that the derived $\Delta_f H_{298}$ for $(CH_3)_2NH$ of -4.6 kcal mol^{-1} is in excellent accord with the literature value of -4.5 ± 0.4 kcal mol^{-1} (see [2]). Some especially low bond dissociation enthalpies for loss of H-atoms may be seen in Figure 2-1, where the reactant is a radical and the product has a new π-bond. Examples of this kind of process include reactions 4 and 5, where the products CH_3CHNH and CH_2CHNH_2 are the imine and enamine analogs of keto/enol isomers. Acetaldehyde is about 10 kcal mol^{-1} more stable than ethenol (see [2]) but the gap is smaller here, with the imine more stable than the enamine by only about 3 kcal mol^{-1}. Presumably this reflects stabilization of the enamine by π-donation from the NH_2 group (see [2]). Interconversion of these species by a 1,3 hydrogen shift is symmetry-forbidden by the Woodward-Hoffman rules and accordingly has a high barrier (see [2]), computed here to be 80 kcal mol^{-1} relative to CH_3CHNH. An alternative pathway for interconversion could be H-atom addition at one site followed by H-atom loss from another. Radical intermediates from where H-atom loss forms CH_3CN yield the lowest bond dissociation enthalpies found here, of ca. 20 kcal mol^{-1}, so that CH_3CHN and CH_3CNH are of low stability at elevated temperatures. In the latter case, C-N fission in the species CH_3NCH to make CH_3 + HCN is also especially facile, driven by the stability of HCN, with ΔH ~ 1 kcal mol^{-1} and a barrier of 20 kcal mol^{-1}. Among the dissociation products of DMA, we note that extra stability is expected for CH_2NCH_2 because it is a resonantly stabilized radical isoelectronic with allyl. The CH_2CHNH and CHCNH radicals might also exhibit stability because they are analogous to allyl and propargyl, respectively. Two mechanisms for ring-opening of 2H-azirine are considered here. One is that proposed by Doughty et al. (see [2]) which proceeds via unimolecular dissociation to singlet vinyl nitrene. The second is bimolecular addition of an H-atom at either end of the double bond to form cyclic radicals with more than enough internal energy to overcome the barriers to dissociation to CH_2NCH_2 and CH_2CHNH. The rate-limiting step for this mechanism is H- addition, which was characterized via conventional transition state theory.

Chemical kinetic model

Here, the detailed chemical kinetic model for amine oxidation is established, based partly in earlier work by the authors, partly on literature data, and partly on the theoretical work described above. For citations of literature work, see [1,2].

NH_3 oxidation

The model for ammonia oxidation is based on the reaction mechanism of Miller and Glarborg (see [1]) for NH_3 oxidation and the Thermal $DeNO_x$ process. A number of changes to the mechanism were made, based on the present work (discussed above) as well as recent work of the authors.

The most important changes to the mechanism of Miller and Glarborg, based on the work outlined in the previous section, relate to the following reactions (reaction numbering consistent with [1]),

$NNH = N_2 + H$ (R33)
$NNH + O$ = products (R35-37)
$NH_2 + O_2$ = products (R12,13)

With the shorter lifetime for NNH of 10^{-9} s, the value of k_{33} has been increased by more than an order of magnitude. The overall rate constant for NNH + O is in the same range as used previously in modeling, but the channel to NH + NO is now considered to be minor, with k_{37} being substantially smaller than most previous estimates. Miller and Glarborg derived the $NH_2 + O_2$ rate constant based on an assumption of a very fast rate for the reverse step, $H_2NO + O$ (R12b). The present value of k_{12} is about an order of magnitude smaller, being more in line with the value from Dean and Bozzelli (see [1]) used recently in modeling studies of NH_3 oxidation (see [1]). The novel rate coefficients for NH + NO = products (R26,27) and $N_2O + H = N_2 + OH$ (R60) are more in line with values used previously in modeling, even though they imply an increasing significance of the NH + NO = N_2O + H reaction (R26) in forming and consuming N_2O.

In addition to the reactions of NNH discussed above, key steps include reactions of NH_2 and NH with NO and NO_2. The NH_2 + NO reaction involves two product channels,

$NH_2 + NO = N_2 + H_2O$ (R14)
$NH_2 + NO = NNH + OH$ (R15)

In particular the branching fraction for this reaction, defined as $\alpha = k_{15} / (k_{14} + k_{15})$, is important for model predictions of Thermal $DeNO_x$. In the present work, α was chosen to be consistent with the theoretical value of Miller and Klippenstein [16]. Their value for the branching fraction is slightly smaller than the recommendation of Miller and Glarborg in the 1100-1400 K range, but it is in excellent agreement with a wide range of experimental determinations (see [1]). The overall rate

constant for NH_2 + NO, $k_{NH2+NO,tot}$, has been measured over a wide temperature range, and data agree roughly within a factor of two. We retain $k_{NH2+NO,tot}$ from previous modeling work (see [1]). A recent determination by Song et al. (see [1]) indicates an overall rate constant that is about 25% smaller in the Thermal $DeNO_x$ temperature window than our present value, but this difference has only a minor impact on model predictions.

Similar to the NH_2 + NO reaction, NH_2 + NO_2 has two product channels:

$NH_2 + NO_2 = N_2O + H_2O$ (R17)
$NH_2 + NO_2 = H_2NO + NO$ (R18)

For this reaction we select the overall rate constant from the work of Song et al., together with a branching fraction $\beta = k_{17} / (k_{17} + k_{18})$ of 20% (see [1]). While the value of β is maintained from previous modeling work (see [1]), it is worth noting that the overall rate constant of Song et al. is about a factor of two larger.

The NH + NO reaction system was discussed above. The NH + NO_2 reaction has only been characterized at low temperature. We have adopted the overall rate constant from the measurement of Harrison et al. (see [1]) and the branching fraction between the two product channels, HNO + NO and N_2O + OH, from Quandt and Hershberger (see [1]).

In addition to these changes, a few other rate constants were updated. Notably, rate coefficients for a number of reactions in the amine subset, including NH_2 + OH, were drawn from the recent theoretical work of Klippenstein et al. (see [1]).

C_2-amine oxidation

The starting mechanism for the oxidation of $CH_3CH_2NH_2$ and CH_3NHCH_3 was drawn from the recent study of NH_3-doped CH_4/O_2/Ar flames (see [2]). This mechanism relied on work on the oxidation of C_1/C_2-hydrocarbons, NH_3, and HCN, as well as interactions of these components. The starting mechanism contained a subset for methylamine oxidation, drawn mostly from the review of Dean and Bozzelli (see [2]). This subset was updated with recent data on the reaction of CH_3NH_2 with OH (see [2]). In the present work, the starting mechanism was extended to describe oxidation of $CH_3CH_2NH_2$ and CH_3NHCH_3. Very little has been reported in the literature about the thermochemistry or elementary reactions of ethylamine and dimethylamine. With a few exceptions, the thermochemistry was

established in the present work, as discussed above. Due to the scarcity of reliable rate constants in the literature for reactions of C_2-hydrocarbon amines, these subsets had to be established from analogy with reaction sets for other species, i.e., C_1/C_2- hydrocarbons, methylamine, ethanol, and propane, or via quantum chemistry. Unfortunately, the detailed mechanisms for CH_3NH_2, C_2H_5OH, and C_3H_8 contain a significant number of reactions for which no experimental data have been reported and only rough estimates or QRRK estimates are available. The uncertainty in the data for the reactions used for analogy is embedded in the present mechanism for the C_2-hydrocarbon amines.

Thermal dissociation of ethylamine has at least four potential product channels (reaction numbering consistent with [2]:

$CH_3CH_2NH_2(+M)=C_2H_4+NH_3(+M)$ (R1)
$CH_3CH_2NH_2(+M)=C_2H_5+NH_2(+M)$ (R2b)
$CH_3CH_2NH_2(+M)=CH_3CHNH_2+H$ (+M) (R3b)
$CH_3CH_2NH_2(+M)=CH_2CH_2NH_2+H$ (+M) (R4b)

The rate constant k_1 for (R1) was calculated via RRKM theory in the present work as described above. The value for k_2 was assumed to be similar to that for the $CH_3 + NH_2$ recombination reaction, in reasonable agreement with the room temperature measurement of k_2 at 400 Pa by Demissy and Lesclaux (see [2]). k_3 and k_4 were estimated by analogy with the reactions $C_2H_5 + H$ (+M) and i-$C_3H_7 + H$ (+M). For the reactions of $CH_3CH_2NH_2$ with the radical pool, overall rate constants for O and OH are available. For both these steps we have assumed hydrogen abstraction from the α-position to form CH_3CHNH_2 to be dominating, similar to what has been reported for ethanol. The channels to $CH_2CH_2NH_2$ and CH_3CH_2NH are presumably minor; the rate constants for these steps, as well as those for reaction of $CH_3CH_2NH_2$ with other radicals, were estimated by analogy to reactions of ethanol and methylamine. Available data for reactions with O and OH indicate that hydrogen abstraction from ethylamine is faster than from methyl amine and ethanol, respectively, but slower than for dimethylamine.

The hydrogen abstraction reactions from $CH_3CH_2NH_2$ yield the three isomeric radicals $CH_2CH_2NH_2$, CH_3CHNH_2, and CH_3CH_2NH. Dissociation of these radicals by breaking either the C-C or C-N bond feeds into the C_1/C_2-hydrocarbon pool and small amines. Information on dissociation of $CH_2CH_2NH_2$ to form C_2H_4 and NH_2 (R22b) can be obtained from studies of the reverse step. At low temperatures the reaction between NH_2 and C_2H_4 forms an adduct, while at higher temperatures H-

abstraction becomes dominating, There is significant scatter in the reported low-temperature data (see [2]); we have adopted the rate constant determined by Khe and Lesclaux (see [2]). It should be noted that (R22) is likely to be in the fall-off region at the temperature and pressure range of the present study, and the chosen rate constant may not extrapolate well to these conditions. Dissociation of CH_3CHNH_2 is expected to yield either CH_2CHNH_2 + H (R30b) or CH_3CHNH + H (R31), while dissociation of CH_3CH_2NH in addition to CH_3CHNH + H (R43) may yield CH_3 and CH_2NH (R42). In the absence of experimental data, the rate constant for (R42) was estimated by analogy to the dissociation of CH_3CH_2O at low pressure. Other steps of the three isomeric radicals are mostly comparatively fast radical-radical reactions, most of which involve hydrogen abstraction. Abstraction of H from $CH_2CH_2NH_2$ and CH_3CHNH_2 leads to CH_2CHNH_2, while CH_3CH_2NH yields CH_3CHNH. However, by analogy with reactions of iso-electronic species such as the propyl isomers and CH_3CHOH, we expect a number of the C_2H_6N + radical reactions to involve breaking of the C-C or C-N bond, most pronounced for CH_3CHNH_2.

Both CH_2CHNH_2 and CH_3CHNH are stable molecules. CH_2CHNH_2 is mainly consumed by reaction with the radical pool. For CH_2CHNH_2, H-abstraction from the C-atoms was assumed to be similar to that for C_2H_4, while breaking of the N-H bond was estimated by analogy with that for CH_3NH_2. Rate constants for CH_3CHNH reactions were estimated by analogy with reactions of CH_3HCO and CH_2NH. For CH_3CHNH, thermal dissociation to form HCNH + CH_3 (R65b) may become important at higher temperatures. Isomerization between CH_2CHNH_2 and CH_3CHNH (R66) is at most a minor pathway due to a high activation energy, as discussed above.

Hydrogen abstraction from CH_2CHNH_2 and CH_3CHNH yields a range of C_2H_4N radicals, i.e. $CHCHNH_2$, CH_2CNH_2, CH_2CHNH, CH_3CNH, and CH_3CHN. The $CHCHNH_2$ radical dissociates fairly easily to form C_2H_2 + NH_2 (R82b); the reverse step (addition) has been characterized by Moskaleva and Lin (see [2]). The reactivity of CH_2CNH_2 could be expected to be similar to that of C_2H_3, yielding $CHCNH_2$ as well as oxygenated intermediates. CH_2CHNH is a resonantly stabilized radical, similar to CH_2CHO, and rate constants have been estimated by analogy with this species. CH_3CNH and CH_3CHN are expected to decompose easily into the cyanide pool, forming either HCN/HNC + CH_3 or CH_3CN + H. Of the remaining C_2-amines, only the reactions of CH_3CN are comparatively well established. Reactions of $CHCNH_2$ and the derived radical $CHCNH_2$ are uncertain, but these species are of minor importance in the present flames.

Special attention was paid to the chemistry of the cyclic species 2H-azirine (c-C_2H_3N), involving a three-membered ring. The key reactions for this species were characterized from ab initio theory, as discussed above. The ring species could be formed by cyclization of CH_2CHNH and subsequent H-atom loss (R154b). A favorable path for 2H-azirine decomposition is via a nitrene intermediate, CH_2CHN, which in turn can isomerize to acetonitrile. Another possibility is the ring-opening isomerization to acetonitrile (R152), as proposed by Tian et al. (see [2]), and as discussed above.

The nitrene CH_2CHN is analogue to a carbene, e.g., methylene, and similarly to methylene, the ground state triplet and excited state singlet are sufficiently close in energy that both need to be taken into account. It can be formed by hydrogen abstraction from CH_3CHN (R116-117, R120-121). The nitrene reactions, including intersystem crossing between the two states, are estimated from analogy with CH_2 (R143-151). The bimolecular reactions of singlet CH_2CHN are presumably fast. Still, they may not be able to compete with unimolecular isomerization to CH_3CN (R148), which has a low barrier of about 8 kcal mol^{-1}.

The subset for CH_3NHCH_3 (Appendix B) is simpler than that for $CH_3CH_2NH_2$ in that it involves fewer species and reactions. Dimethylamine is mainly consumed by reaction with the radical pool. The overall reactions with O (R192, R193) and OH (R194, R195) have been characterized experimentally (see [2]); the branching fractions to CH_3NHCH_2 and CH_3NCH_3 were estimated (CH_3NHCH_3 + O) or drawn from theoretical work (CH_3NHCH_3 + OH). Other reactions of CH_3NHCH_3 with the radical pool were assumed to be similar to those of CH_3NH_2; judging from the diethylamine + O/OH reactions, the dimethylamine steps would be expected to be somewhat faster than the corresponding methylamine steps. The fuel-derived radicals CH_3NHCH_2 and CH_3NCH_3 may dissociate to form either CH_3NCH_2 + H (R201, R209) or CH_3 + CH_2NH (R200); the rate coefficients for these steps were calculated in the present work as discussed above. Radical abstraction reactions of CH_3NHCH_2 and CH_3NCH_3 to form CH_3NCH_2 are not well known, but can be assumed to be fairly fast.

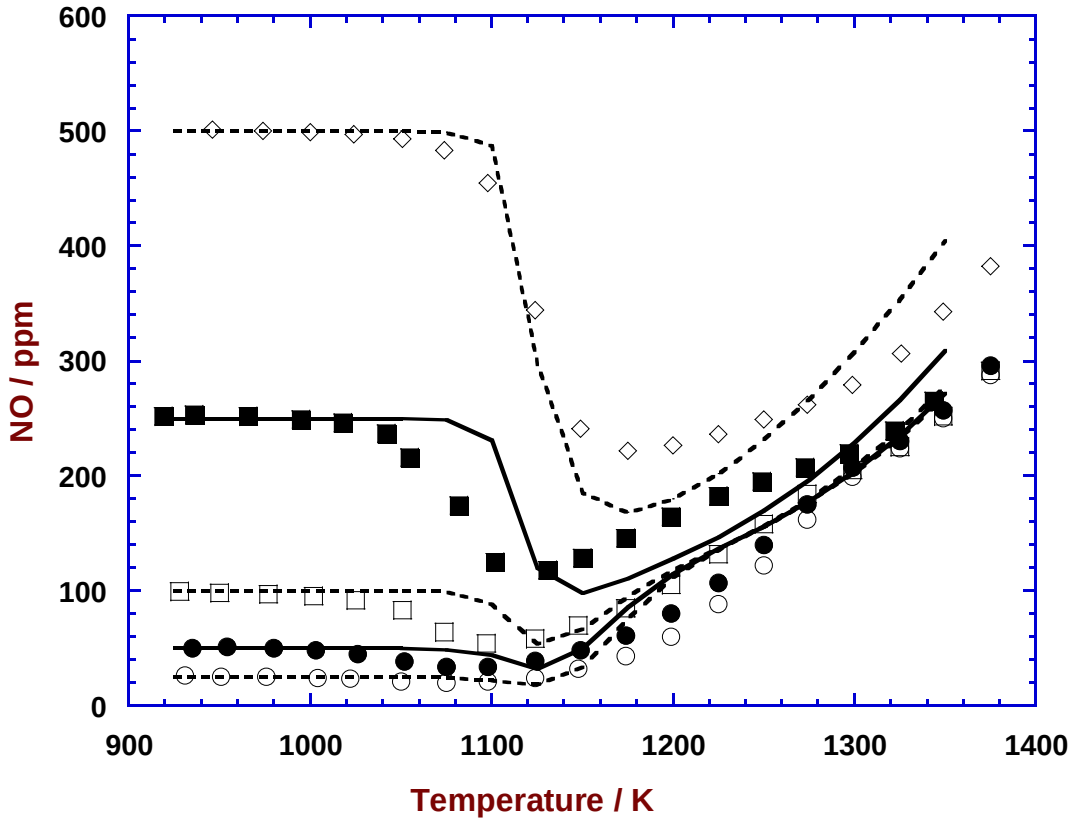

Figure 2-2: Comparison of predictions of the present model with the experimental results of Vilas and Glarborg (unpublished) for NO as function of temperature and inlet NO concentration in oxidation of NH_3. Inlet mole fractions: NH_3 = 1000±100 ppm, O_2 = 40±1.2%, NO varying (25, 50, 100, 250, 500 ppm), H_2O = trace, balance N_2. Residence time (s) = 48.7/T[K].

The stable species CH_3NCH_2 reacts mainly with radicals to form either CH_2NCH_2 or CH_3NCH. Little is known about these steps, but they are presumably similar to reactions of C_1-hydrocarbon amines. Isomerization of CH_2NCH_2 to CH_3NCH (R226) was calculated in the present work, but constitutes only a minor pathway. Also cyclization followed by H-atom elimination to form 2H-azirine (R153b) is at most a minor pathway. Reactions of CH_2NCH_2 and CH_3NCH feed into the cyanide pool; CH_2NCH_2 is expected to react with O/H radicals to yield H_2CN, while CH_3NCH dissociates rapidly to form HCN (R230).

NH_3 oxidation

The ammonia oxidation subset was validated against a wide range of experimental data [1]. Figure 2-2 shows results for the transition from NH_3 oxidation to Thermal $DeNO_x$. In these experiments, the NH_3 and O_2 inlet levels were maintained at 1000 ppm and 40%, respectively, while the initial NO mole fraction was increased gradually from 25 ppm to 500 ppm. Several interesting features of this system are evident. Under conditions where the inlet NH_3 concentration is significantly greater than that of NO, i.e. for inlet levels of NO up to 250 ppm, the onset temperature for reaction is independent of the NO level. Even at the smallest NO concentration of 25 ppm, a minimum in NO is observed just above the initiation temperature, and inspection of the data shows that the fractional conversion of NO at the minimum is quite similar over the range of NO levels from 25 to 250 ppm. At higher temperatures (> 1200 K), the exit NO concentration asymptotically approaches a common value, independent of the inlet level between 25 and 250 ppm. The model predictions capture all these trends well.

C_2-amine oxidation

For validation, laminar premixed flames of the two smallest isomeric amines, dimethylamine and ethylamine, were investigated under one-dimensional low-pressure (40 mbar) conditions with the aim to elucidate pathways that may contribute to fuel-nitrogen conversion in the combustion of biomass. For this, identical flames of both fuels diluted with 25% Ar were studied for three different stoichiometries (Φ=0.8, 1.0, and 1.3) using *in situ* molecular-beam mass spectrometry (MBMS). Quantitative mole fractions of reactants, products and numerous stable and reactive intermediates were determined by electron ionization (EI) MBMS with high mass resolution to separate overlapping features from species with different heavy elements by exact mass. Species assignment was assisted by using single-photon vacuum-ultraviolet (VUV) photoionization (PI) MBMS. The results indicate formation of a number of nitrogenated intermediates, including toxic species such as HCN, in appreciable concentrations. Such intermediate species mole fractions may depend not only on stoichiometry, but also on fuel structure.

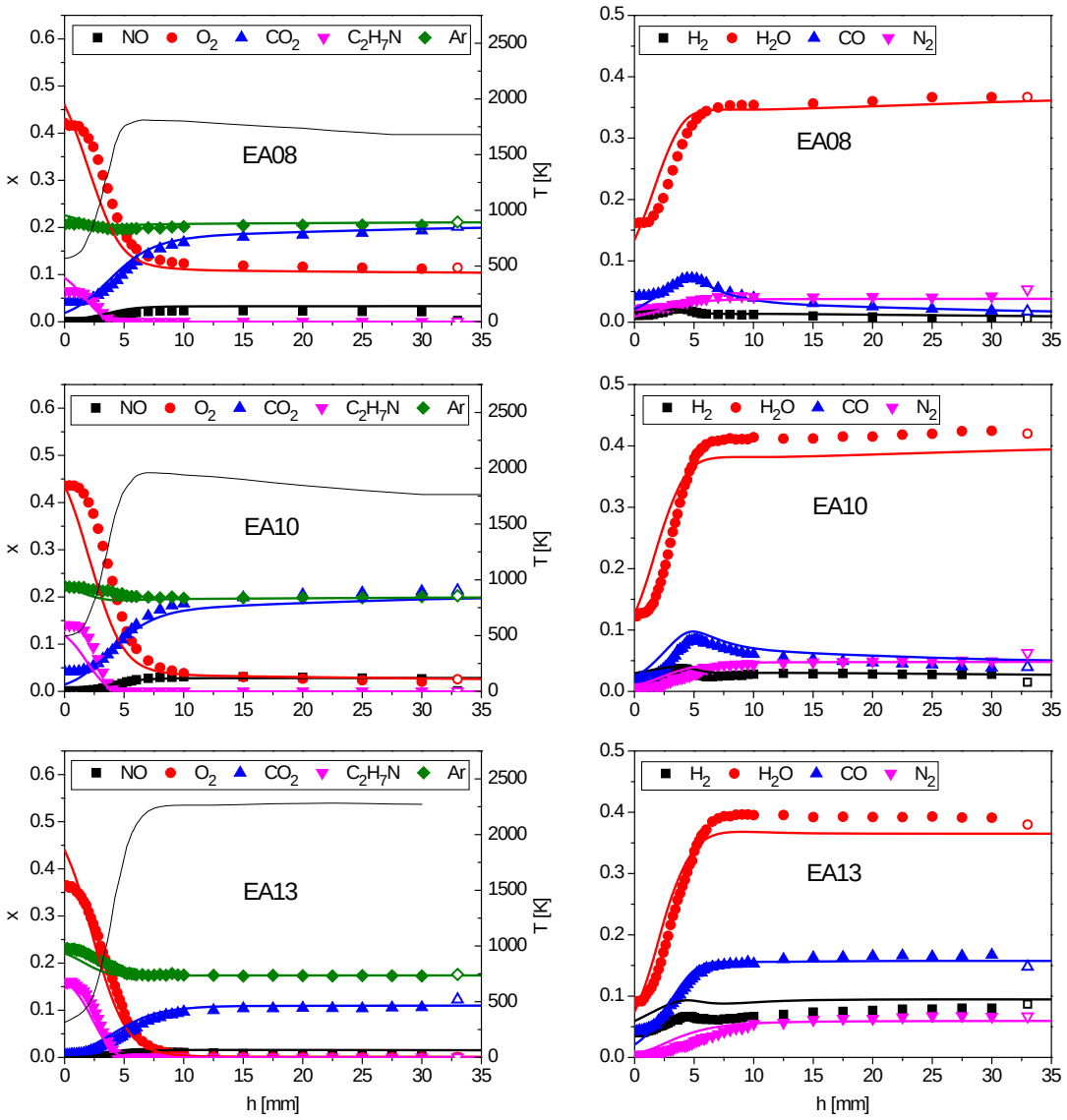

Figure 2-3: Major species and temperature profiles in the three investigated ethylamine (EA) flames; EA08 is Φ=0.8, EA10 is Φ=1.0, EA13 is Φ=1.3. Symbols are experimental values, and corresponding lines represent simulations. Equilibrium values are marked as open symbols at 33 mm.

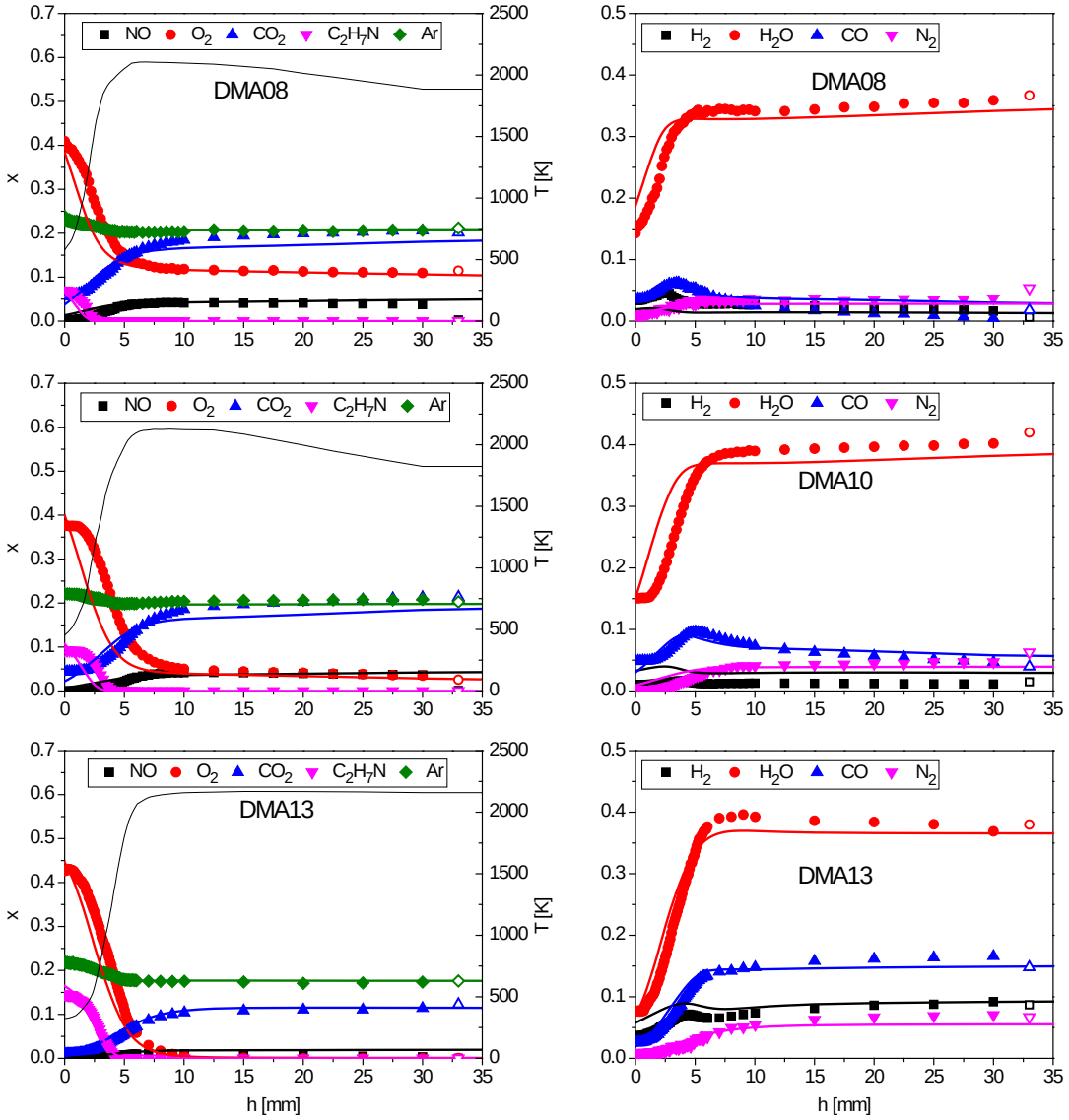

Figure 2-4: Major species and temperature profiles in the three investigated dimethylamine (DMA) flames; DMA08 is Φ=0.8, DMA10 is Φ=1.0, DMA13 is Φ=1.3. Symbols are experimental values, and corresponding lines represent simulations. Equilibrium values are marked as open symbols at 33 mm.

The overall flame structure for the two fuels is given in Figs. 2-3 and 2-4, which show the major species profiles, the temperature profiles, and the equilibrium mole fractions of all flames investigated in this work. The flame pairs of EA and DMA show only minor differences in the species spectrum observed at the same stoichiometry, and the exhaust mole fractions match the equilibrium values quite well. Peak temperatures are near 2000 K for all six flames, with some variation for the different equivalence ratios. This variation is largest for the EA flame where

peak temperatures are almost 500 K higher in the fuel-rich than in the lean flame, while differences are less pronounced for the DMA flames. The absolute temperature uncertainty is typically below 100 K. Temperature may influence the NO_x formation considerably [1], but less so for the fuel-NO mechanism (as in this work) than for thermal NO.

All NO profiles in Figure 2-3 and 2-4 show a slight decay towards the burnt gas but remain at levels of 1-4%, likely to be found in combustion exhaust when burning these amines. This is of similar magnitude as for the Φ=1.3 morpholine flame, with an NO mole fraction in the burnt gases of about 0.02, well-predicted by the respective model, with the consideration, however, of a twofold higher N/C ratio in the amine fuels here. For the ammonia-blended methane flames with an NH_3/CH_4 ratio of 0.5 (see [2]), the NO mole fraction is also near 2% and persists well into the burnt gas. The differences in NO are negligible for the fuel-rich EA and DMA flames, where intermediate-type profiles are observed, and where some reburning reactions might consume NO, regarding the higher amounts of small hydrocarbon species under fuel-rich conditions. In the stoichiometric flames, the secondary amine DMA gives apparently rise to about 25% higher NO levels, a tendency which is more pronounced for the two lean flames where the NO peak mole fractions differ by about a factor of two. This may be owed in part to a temperature effect. In general the fuel-lean and stoichiometric flames show an NO mole fraction significantly higher than the equilibrium values. The simulations with the flame model are found in very good agreement for both N_2 and NO, with a ratio of NO/N_2 of ~0.7 for EA and ~1 for DMA.

However, while many trends seen in the experiments can be successfully reproduced by the simulations, additional efforts may be needed to reliably describe the fuel-nitrogen chemistry in the combustion of biomass-related model fuels with amine functions.

Premixed nitromethane and nitroethane flames

Further model validation, focusing on hydrocarbon/NO_x interactions, was conducted based on experimental work on three premixed nitromethane / oxygen / argon flames at low pressure (4.655 kPa) with equivalence ratios (φ) of 1.0, 1.5 and 2.0 [3]. Flame species were identified with tunable synchrotron vacuum ultraviolet photoionization. The mole fraction profiles of more than 30 species including intermediates and radicals were obtained by near-threshold burner scan with selected photon energies. With a Pt–6%Rh/Pt–30%Rh

thermocouple, the flame temperature profiles were measured. A detailed kinetic mechanism with 88 species and 701 reactions was proposed and validated against experimental results of all three flames. The computed predictions showed satisfactory agreement with the experimental results. Based on a rate-of-production analysis, reaction pathway diagrams were obtained to describe the hydrocarbon oxidation process and nitrogenous species chemistry in the nitromethane flame with $\varphi = 1.5$ [3].

Further work was conducted on three premixed nitroethane/oxygen/argon flames at low pressure (4.655 kPa) with the equivalence ratios (Φ) of 1.0, 1.5 and 2.0 [4]. Over 30 flame species were identified with tunable synchrotron vacuum ultraviolet photoionization mass spectrometry, with their mole fractions quantified as the function of the height above burner. The flame temperature profiles were measured with a Pt-6%Rh/Pt-30%Rh thermocouple. A detailed kinetic mechanism with 115 species and 730 reactions was proposed and validated against experimental results. The computed predictions have shown satisfactory agreement with the experimental results. Basing on the rate-of-production analysis, the reaction pathways that feature the combustion of nitroethane were revealed, including the primary decomposition of C-N bond fission, the oxidation of C2 and C1 hydrocarbons and the formation of nitrogenous species. The presence of NO_2 and NO has been proved to be important for these processes [4].

2.2 Task 1.2: Development and Test of a Simplified Scheme for NO_x Formation

While the details of high-temperature, gas-phase nitrogen chemistry are now fairly well established (see above), it remains a major challenge to establish simple and reliable models for nitrogen chemistry for use in CFD calculations. Available submodels in commercial CFD codes such as Fluent typically date back to the 70's (i.e., the DeSoete model for NO_x formation from nitrogen volatile species - HCN and NH3) and they are either inaccurate or directly misleading, depending on the reaction conditions. However, the nitrogen chemistry is quite complex, due to its close interaction with the fuel oxidation process, and efforts during the past 10-15 years in this area have shown that it is difficult to obtain sufficient accuracy without compromising the simplicity required in CFD-applications. In the present proposal, a number of alternative approaches to

develop a simplified, yet sufficiently accurate, description of NO_x formation from biomass N-volatiles will be investigated and validated against reference calculations with a detailed reaction mechanism.

A number of investigations have been carried out to characterize the chemical kinetics of the combustion process of solid fuels such as coal and biomass (see [5]). However, due to the complex composition of biomass which has C, H, O, N, S, Cl and other minor and trace elements in the chemical composition, combustion of such a fuel needs special attention with respect to emissions. The chemical mechanism should contain a wide range of species and therefore, a large number of reactions to be able to perform a precise modeling analysis of the biomass combustion reactors. On the other hand, to perform a complete CFD analysis, all the phenomena, including fluid flow, heat transfer and chemical kinetics should be modeled at the same time. Hence, implementing a complex and detailed mechanism into a CFD simulation is not always feasible due to expected long computational time and restricted hardware resources. Consequently, simplifying the computations by reducing the description of the chemical kinetics without loss of accuracy is an important task.

There are several ways to simplify the chemical model. A common procedure is to identify the major reaction paths by performing an element flux analysis, referred to as a reaction flow analysis. This type of analysis will enable the removal of the minor paths which are deemed not important for the reliable prediction of the significant combustion parameters, such as temperature and major emissions. However, this method is usually combined with a sensitivity analysis to ensure that important species involved in only minor reaction flows are indeed kept in the model. A further reduction is possible based on mathematical transformation of the chemical system based on a time scale analysis. The underlying assumption is that many chemical reactions occur for time scales much shorter than the physical processes governing the system. The identification of reactions that are unimportant for both the fast and slow parts of the mechanisms enables that these can be treated in less detail by the numerical solver without considerable loss of accuracy, hence saving computational time. However, these methods require either a tabulation of the fast subspace or a separate treatment of the short lived species in the solver. This methodology is not included in the present work, however, this will be a topic for further investigations.

In the present work a detailed mechanism for biomass volatile oxidation has been the subject for a reaction flow and sensitivity analysis in order to generate a

strongly reduced skeletal model. The selected detailed mechanism in this study contains 81 species and 703 elementary reactions (1403 forward and backward reactions). This mechanism includes C, H, O, and N in the structure while S, Cl, and the other trace elements are not included in the reaction flows. The mechanism has been used for predicting emissions from varying types of biomass sources (see [5]). It has furthermore been modified and extended over a period of time, and the latest version has been optimized only recently (see Task 1.1). It is developed for the use in general solid fuel combustion systems, and the radical scheme is applicable for fuels ranging from bituminous coal to biomass. It should be noted that the present study only considers gas phase reactions as the chemical model in question does not include multi-phase reactions (solid to gas). The full treatment of conversion from solid state to gas phase species will require extensive modeling including heat and mass transfer between the states, which is outside the scope of this work. Furthermore, a major section of the biomass furnace contains only gas phase species in a turbulent flow field. Hence, reduced chemical models for this section of the furnace are of great importance. Furthermore, to the knowledge of the authors, reduced mechanism for oxidation of biomass volatiles is almost non-existent.

Biomass Combustion Kinetics

Equation 1 shows the global reaction formula for the combustion of biomass, shown as CH_mO_n where the average values of different biomass types can be assumed as m≈1.4 and n≈0.65 (see [5]). The values *m* and *n* are defined based on the wt% daf (dry and ash free basis) ultimate analysis of biomass.

$$\begin{aligned} & CH_mO_n + \lambda(1+m/4-n/2)(O_2+3.76N_2) \\ & \rightarrow \text{intermediate}\,(CO, H_2, CO_2, CH_4,\ char, ...) \\ & \rightarrow CO_2 + m/2H_2O + (\lambda-1)O_2 + \lambda 3.76N_2 \end{aligned} \qquad (1)$$

However, such a description only reveals the ratio of fuel to oxidant for complete conversion of fuel to final products, and does not identify the numerous reaction paths which lead to these products. To have a clear view of the primary gas composition from a biomass reactor, describing and properly combining the different features of this complex process is necessary. The process includes biomass structure (cellulose, hemicellulose, and lignin) analysis, devolatilization process and char gasification. However, in the current work, only the gas phase processes are considered and the primary (pyrolysis) gas is taken as the initial fuel

mixture with the composition as shown in [5]. The values used are averages for fiberboard (composed of spruce and pine) and pine wood pellets based on experimental data from the literature. Addition of a small amount of nitrogen containing species (NH_3 and HCN) to the gas composition is to be able to predict NOx emissions from fuel nitrogen. In general, the total NOx emission from biomass can be divided into fuel-NOx, and thermal-NOx and prompt-NOx. Fuel-N content is responsible for the majority of NOx emission from any biomass combustion plant, and the two main NOx precursors are NH_3 and HCN which are the main products of fuel-N conversion after the thermal degradation (see [5]).

The chemical mechanism that has been used in this study, is as mentioned above an extended detailed chemical kinetics mechanism developed by combustion groups at DTU and NTNU (see [5]). The mechanism contains 81 species and 703 elementary reversible reactions (total forward and backward reactions: 1401) including a significant sub-set for treating nitrogen reactions. Some researchers have used GRI-Mech for biomass combustion. However, it is designed originally for methane combustion and is validated and optimized for high temperature combustion only. This is a limiting factor for biomass combustion furnaces, as will be discussed further below.

An ideal 0-D reactor model, in this case a perfectly stirred reactor (PSR), has been used for the modeling using DARS© reduction software (see [5]). In the 0-D ignition reactor model, no information is provided for the position of the particles and assumed that an inlet and outlet duct connected to a 0-D vessel. A steady flow of gas as the reactants with a certain composition and temperature flows through the inlets. The gas undergoes chemical reactions, and, after a certain time, exits the chamber through the outlets. In this way, the 0-dimentional reactor can be regarded as a vessel in which there is extremely strong mixing, giving rise to steady-state solutions of the balance equations. This makes the PSR model relevant for CFD applications where each grid cell in the domain is treated as a homogenous reactor. The residence time in the PSR will then represent the computational time step of the CFD simulation. It is therefore important that the defined conditions for the reduction analysis is wide enough to cover typical physical parameters such as temperature, residence time and fuel gas composition found in biomass combustion furnaces.

It is not uncommon to use a plug flow reactor (PFR) in combination with a PSR to model the entire furnace (see [5]). In a PFR reactor, reactants flow through the reactor as a series of infinitely thin coherent plugs, each with a uniform composition. The composition is just changed in the axial direction. However, like

a PSR, it is assumed that fluid is perfectly mixed in the radial direction but not in the axial direction. Here the real reactor conditions can be modeled defining the length, flow speed, and residence time. A PFR model will be discussed furthermore in the results section.

It is important to note that the PSR model selected for the reduction analysis is based on a 0-dimentional system. Although the resulting reduced mechanism is valid for the wide range of conditions considered in the present work and is independent of flow structures in the system, the resulting reduced model is only reliable for ignition scenarios. Therefore, simulations of flame structures should be carried out with great care and tracking of the errors of employing reduced mechanism for different flame properties is necessary where diffusion plays an important role.

For the present combustion scenario, the validity is checked for a wide range of residence times, i.e., 1-1000 ms, since the NOx formation and reduction happens at longer time scales than for ignition only. The temperature varies in a wide range, from low temperature chemistry to one case considering only high temperature chemistry. This will be discussed in more detail below. Furthermore, the pyrolysis fuel gas contains also hydrocarbons as indicated by experimental data (see [5]). These species are often omitted in reduced models as this considerably simplifies the NOx chemistry. However, in the present study it is a goal to make as few restricting assumptions as possible regarding the application range.

Reduction Procedure

DARS© is a chemical reaction system analysis tool especially designed for combustion and catalytic processes (see [5]). Among different analyses types, DARS© has the possibility to carry out chemical mechanism reduction by four methods: reaction flow analysis, sensitivity analysis, necessity analysis, and life time analysis. Flow analysis considers the mass flow of a specific atom from one species to another one during combustion, while in the sensitivity analysis, the influence of reactions and species on variables like temperature is regarded as the key for discarding a reaction. In this manner species that may only be involved in minor flows and hence may be regarded as redundant species by a reaction flow analysis, are still retained in the mechanism if they exhibit strong sensitivity with respect to the final result. The life time analysis considers how fast the reactants and products are consumed or produced in a chemical reaction. This is a measure for the life time of species and can be used to identify so-called steady

state species for removal. However, this approach is not within the scope of this study.

In the necessity analysis, a number of species such as NOx, CO, and SOx are defined as the target species, i.e., species of high importance as combustion products, beside other necessary targets such as temperature. The analysis aims at finding which species and reactions are necessary for the correct prediction of formation of the defined gases at the defined temperature condition. A list of necessary species can also be predefined by the user (species such as main reactants and products). This method is especially beneficial when the modeling aim is to study emissions from combustion processes (see [5]). The necessity of species *i* is given by an index I_i, derived from the following equation:

$$I_i = \max\left(I_j p_{i,j}^a, I_j c_{i,j}^a, I_i;\ j = \{1, N_s\}, a = \{1, N_a\}\right) \tag{2}$$

where the initial necessity value is calculated by:

$$I_{i,0} = \max\left(\frac{S_{j,i}^s}{\max\left(S_{j,k}^s\right)_{k=\{1,N_s\}}}, B_i\right) \tag{3}$$

N_a and N_s are number of atoms and species respectively, $S_{j,i}^s$ is the species sensitivity of species *i*, and B_i is 1 if species *i* is a user-defined necessary species and is 0 if not. Species sensitivity, S^s, is defined as how much a chosen target variable *Y* is changed when the concentration of species *i* is changed by a small amount, typically one percent, according to the following equation.

$$S_{Y,j}^s = \frac{1}{c_i}\frac{dY}{d\alpha_i} \tag{4}$$

where *Y* is the sensitivity analysis target (e.g., mass fraction of any target species or the temperature) and $\alpha_i = 1 + \varepsilon_i$, where α_i can be considered an error term for the concentration of species *i*. $p_{i,j}^a$ and $c_{i,j}^a$ are the reaction flow parameters and give the flow rate of element *a* by production of species *i* from species *j* and consumption from species *i* to species *j*, as defined below:

$$p_{i,j}^a = \frac{\int_{t=0}^{t_1}\left(\sum_{R=1}^{N_R} r_R(t)\, n_i^a \nu'_{jR}\nu''_{iR}\frac{1}{\Delta n_R^a}\right)dt}{\int_{t=0}^{t_1}\left(\sum_{R=1}^{N_R} r_R \nu'_{jR}\right)dt} \tag{5}$$

$$c_{i,j}^{a} = \frac{\int_{t=0}^{t_1} \left(\sum_{R=1}^{N_R} r_R(t) n_i^a v'_{jR} v''_{iR} \frac{1}{\Delta n_R^a} \right) dt}{\int_{t=0}^{t_1} \left(\sum_{R=1}^{N_R} r_R v''_{jR} \right) dt} \qquad (6)$$

where t is time, t_1 is final time, $r_R(t)$ is the reaction rate of reaction R, n_i^a is the number of a-type element in species i, v'_{jR} and v''_{iR} are the stoichiometric coefficients of species j in the left and right hand side of reaction R respectively, and Δn_R^a stands for the total flow of element a in the reaction R.

The modeling is done at the reactor temperature of 700-1400 °C, residence time 1, 0.1, 0.01, 0.001 s, and the equivalence ratio of φ=0.3-1.2 (excess air ratio of 0.8-3.3). For all the simulations isothermal condition is applied to a single PSR. The total fuel-N content is considered to be 1000 ppm which is typically valid for high nitrogen containing fuels, and here the selected gas composition for the model input is selected to have almost 2 wt% nitrogen in the original fuel. The HCN/NH_3 ratio is 0.65 based on a study on different types of biomass (whey protein, soya beans, yellow peas, shea, and bark) which showed that HCN/NH3 ratio is not significantly correlated with fuel O/N ratio, although it is slightly a function of temperature. H_2, N_2, H_2O, C_2H_2, C_2H_4, C_2H_6, NH_3, HCN, CO, CO_2, CH_4, O_2 are assumed as the necessary species and the necessity analysis targets are set to NO, NO_2, O_2, H_2O, and temperature. The necessity target species are selected in a way to carefully capture the NOx concentration in the flue gas by the reduced mechanism. NOx is a generic term for a mix of NO and NO_2, and since the final results are compared at the same flue gas condition (dry flue gas and 11% O_2 in the flow) to remove the effect of various degrees of dilution, therefore, O_2 and H_2O are also considered as they may have a small effect on the final results, so that true comparison of the NOx level can be made for all cases. Reaction flow analysis is also used to check the flow of species at different conditions.

Model validation

The detailed mechanism was first applied to a two stage combustion configuration in order to resemble a realistic biomass furnace with air staging, where two plug flow reactors (PFR) are used to see the effect of variables on NOx reduction by the mentioned technology and validate the results. The PFR configuration was chosen since this reactor resembles better the axial flow in a typical biomass reactor.

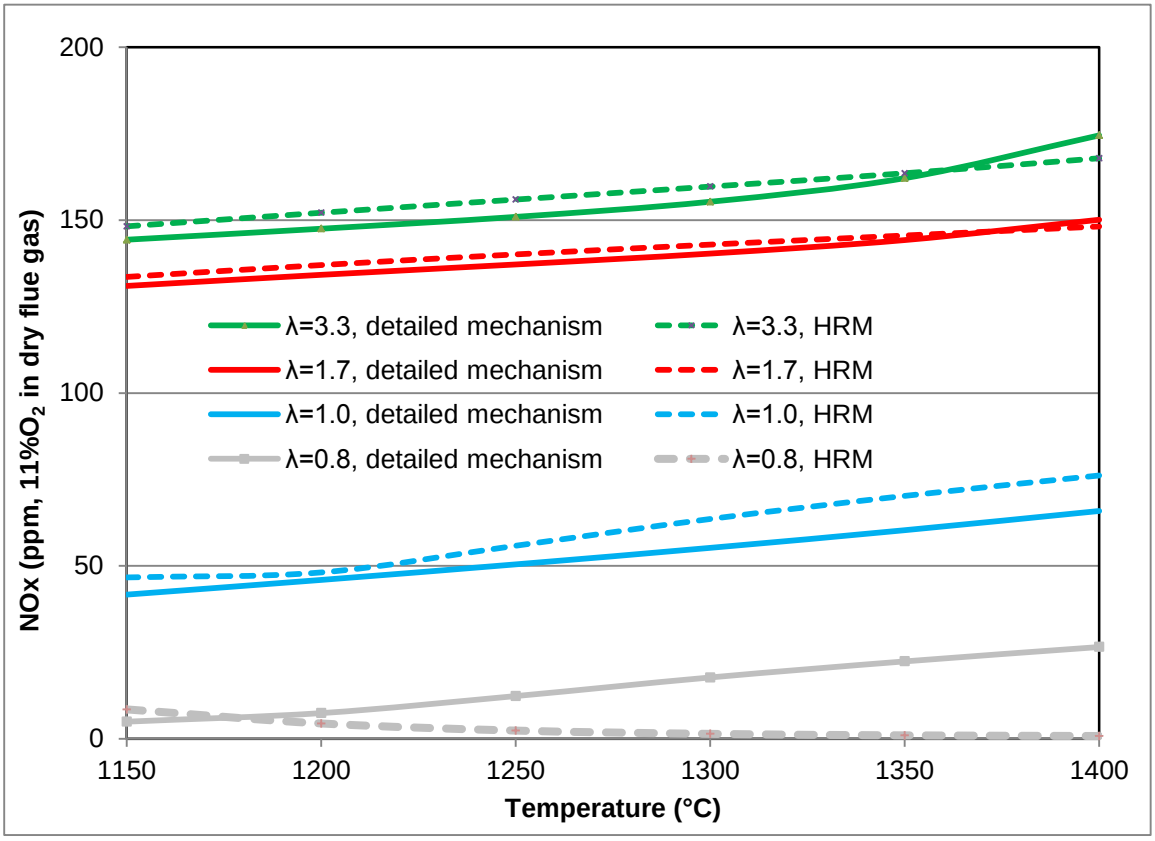

Figure 2-5: NOx emission level in ppm (corrected to 11% O_2 in the dry flue gas) as a function of temperature, residence time=1 s: validation of highly reduced mechanism (HRM) containing only 26 species for the high temperature range.

After performing the DARS reduction analysis, a number of mechanisms with increasing level of reduction are generated. The reduced mechanisms in this study contain much fewer reactions and chemical species; hence a significant computational speed-up is observed which will be discussed below. However, until a maximum level of reduction is reached, the models should predict emissions of NOx, and CO in a manner which is acceptably close to those of the complete mechanism under a set of defined conditions, typically with less than 10% deviation. It is found that most of the species with necessity level of less than 0.15 could be set as the redundant species. It was found that low temperature chemistry is difficult to capture with strongly reduced mechanisms. Hence, three reduced mechanisms are proposed. One which is valid mainly for the low temperature range, however less strongly reduced (containing 52 species corresponding to approximately 35% reduction), one which is valid for the medium temperature range up to 1100°C (containing 35 species corresponding to

approximately 65% reduction), and one which is valid only for the high temperature range up to 1400°C (containing 26 species corresponding to approximately 70% reduction). However, even in the largest of these reduced mechanisms the number of differential equations is reduced by almost 70%. Since the lengths of the equations are also shortened with the number of reactions which have been removed, principally the CPU time can be reduced as much as by n^2, where n is the number of species reduced.

Using necessity analysis for the highest temperature range, i.e., 1150-1400 °C, a highly reduced mechanism is derived to be applied and used for this temperature range. The mechanism contains 26 species and 91 reactions, and results in considerable amount of calculation time and CPU saving. A comparison of the predicted NOx levels from this very compact mechanism and the detailed mechanism is shown in Figure 2-5 as a function of temperature for selected excess air ratios. The reduced scheme is seen to provide a satisfactory description of the nitrogen chemistry under these conditions, but it should be noted that it does not extrapolate well to lower temperatures.

In summary of Task 1.2, a number of reduced mechanisms have been developed for biomass volatile oxidation. The chemical kinetics mechanism for biomass combustion is very sensitive to the combustion conditions and should be treated carefully in order to get the correct results, and particularly the given temperature range has to be considered carefully when choosing the level of reduction. Furthermore, variations in temperature, excess air ratio, and residence time showed large effects on the NOx level.

The reduced mechanisms suggested in this study, as a result of necessity analysis, have 52 species and 430 reactions, 35 species and 198 reactions, and 26 species and 91 reactions (compared with 81 species and 703 reactions in the detailed mechanism) applicable for low, medium and high temperature range, respectively. However, even the intermediately reduced mechanism minimized the size of detailed mechanism by almost 70% corresponding to the same amount of reduction in the time needed for such modeling or simulation works. The reduced mechanisms predict concentrations of NOx very close to those of the complete mechanism in the range of reaction conditions of interest. In general it is found that for temperatures above 800 °C and excess air ratios of above 1.5 the reduced models give acceptable NOx results corresponding to errors less than 10%, although the very low residence time conditions have more narrow satisfactory range.

A close to linear relationship is found between the reduction degree and the computational savings, which is reasonable taking into account the highly optimized solver used in this work and the already short calculation times associated with the PSR. Higher computational savings should be expected for less optimized solvers and for CFD applications.

2.3 Task 1.3: Experimental Characterization of NO Formation from Biomass Char Oxidation

The purpose of this task is to obtain novel experimental data to characterize NO formation from biomass char oxidation (Task 1.3) and, based on these results, to develop a simplified quantitative model for the process (Task 1.4). We investigated the char properties in the horizontal tube reactor and studied the NO formation from biomass char oxidation in fixed bed reactor [6]. Two typical Denmark biomass, bark and straw, were used. As a reference, SAKLEI bituminous coal was studied and the results were included in this report. Details of the work are presented in [6].

Experimental

Bark, straw and SAKLEI bituminous coal were used in the experiment and the properties are showed in [6]. The bark and straw were grinded and sieved to 0.063–0.09 mm. The coal was sieved to 0.035-0.045 mm. To achieve char yield and char properties, pyrolysis experiments were performed before the char combustion experiments [6]. The pyrolysis time was 10 minutes; then the samples were weighted to get the char yield and subsequently analyzed for C, H, N and S.

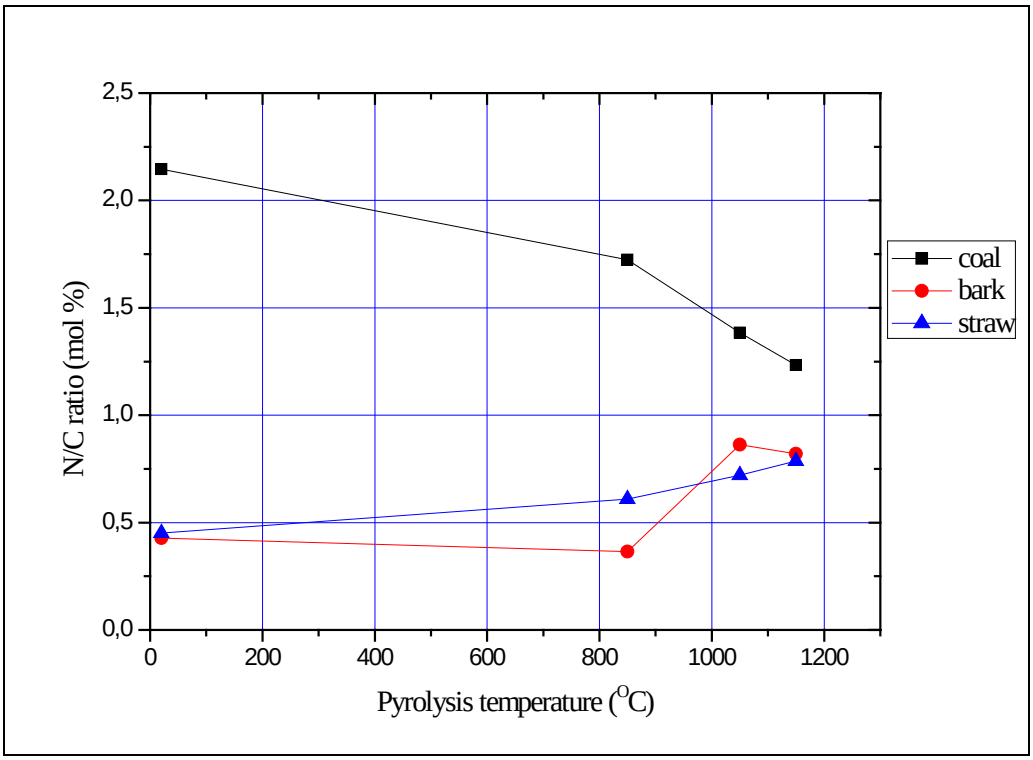

Figure 2-6: N/C ratio in chars as a function of pyrolysis temperature.

A laboratory-scale fixed bed reactor made of quartz was used for the char combustion experiments. The reactor was equipped with a solid feeder device, which allowed sample admission into the reactor under inert conditions without disassembling the reactor. The reaction temperature was measured by a thermocouple 0.5 cm below the porous plate where the reaction took place. The uncertainty of the thermocouple measurement was ±1.5°C. The gases flowing out of the reactor were conveyed to the analysis equipment, passing through two filters. The double filtering had the purpose of preventing the condensed pyrolysis products (tar) from reaching the analysers. Using a three-way valve, the outlet stream of the reactor could be directed to ventilation or to the analysis system. The reactor was placed inside an electrically heated oven, with three independent zones for controlling the temperature. A schematic of the reactor and listing of the conditions of the char combustion experiment are summarized in [6].

The experimental methodology is described in [6]. The sample (bark, straw, or coal) was mixed with 2 g sand (0.18-0.25 mm) and then introduced in the reactor with in a nitrogen atmosphere. After pyrolysis in the nitrogen atmosphere for 3 minutes, oxygen was introduced to achieve an O_2/N_2 mixture gas with oxygen

concentration of 10%. The O_2/N_2 mixture flowed through the sample bed and porous plate whereby char in the bed combusted. The composition of the flue gas was analyzed for NO, CO, CO_2, SO_2 and O_2. An ultraviolet analyzer was used for NO and SO_2, and an infrared analyzer were used for CO, CO_2, and O_2. In several conditions, GC was used to measure N_2O. In the preliminary experiment, chemiluminescence analyzer was used for NO and NO_2 but no NO_2 was detected. Therefore, NO_2 was not analyzed in the subsequent experiment.

2.4 Task 1.4: Development of a Biomass Char-N Oxidation Model

Figure 2-7a-d, shows the net conversion ratio from char-N to NO in the char combustion experiment. The net conversion ratio depended on the amount of char burned, the combustion temperature, and the char type. For all the 4 chars, the net nitrogen conversion ratio decreased as the amount of char increased. Because the increasing char mass lead to an increasing reduction ratio of the produced NO when the passed through the char-sand bed. Compared to the net conversion ratio at large char masses (more than 2 mg), the net conversion ratio decreased with the increasing of temperature. This attributed to the increasing NO reduction rate with increasing temperature.

At single-particle conditions (i.e. the limit of zero char mass) of bituminous char, the conversion ratio lied between 70-100 %. The net conversion ratio of single particle was lowest at 850 ^{o}C and the values were more close to 100 % at 1050 ^{o}C and 1150 ^{o}C. This nitrogen gap may be attributed to N_2O. In several conditions, showed in Table 2-1, N_2O was collected to gas bag and analyzed by GC. For coal char at 850 ^{o}C, slight N_2O was produced with the conversion ratio of 1.52 - 3.56 % while the conversion ratio of NO was 51.9 - 54.1 %. Then the NO was dominant production of nitrogen oxides in the gas and the N_2O didn't attribute to the nitrogen gap obviously as supposed earlier. Two conditions of biomass char combustion were selected to analyze N_2O, but no N_2O was detected in the gas.

The lignite char was lower nitrogen content and much higher reaction rate than the bituminous coal char. As showed in the Figure 9 and Equation 6 – 9, the rate constant of lignite char was about a factor of 2-4 at 1050 ^{o}C - 1150 ^{o}C and a factor of 15 at 850 ^{o}C than that of bituminous coal char. So the experiment of single-particle conditions was not performed because of weak NO signal in gas.

The net nitrogen conversion ratio at single-particle of biomass char, given by the Equation 1, was lower than that of bituminous coal char:

$$\overline{\eta_{NO}} = \frac{\int C_{NO} dt}{m_{char,0} \times N_{char}} \qquad (1)$$

Where $\overline{\eta_{NO}}$ is the net conversion ratio from char-N to NO, $m_{char,o}$ is the initial char mass and calculated from the CO and CO_2 gas profile, C_{NO} is the NO concentration in the flue gas and measured by gas analyzer, and N_{char} is the nitrogen content in char.

Model representation of NO formation in the char combustion experiment

Two models, named slow char-N to NO model and rapid char-NO model respectively, were used to interpret the experiment process. The two models represent two extreme possible of char-NO reaction in the experiment.

- Rapid char-N to NO model, which assumed char-N to NO at a reaction front the char-sand bed, allowed the maximum possible of the char-NO reaction.
- Slow char-N to NO model, which assumed char-N to NO evenly conversion through the char-sand bed, allowed the minimum possible of the char-NO reaction.

The reactor was modeled as a plug flow reactor. The char-N was assumed to liberate from each particle as either NO or N_2. The NO reduction on char was assumed as first order with respect to both NO concentration and char concentration. Then the NO reduction by char is given by the Equation 2:

$$r_{NO} = -k_{NO} \times \frac{m_{char,0}(1 - X_C)}{V_f} \times C_{NO} \qquad (2)$$

Where k_{NO} is the NO reduction rate constant (in $m^3/kg^{-1}s^{-1}$), $m_{char,o}$ is the initial char mass, V_f is the free volume in the char-sand bed, C_{NO} is the NO concentration in the gas, and X_C is the carbon conversion ratio of char.

If char conversion takes place at a rapid char-N to NO model, net NO conversion ratio is given by

$$\overline{\eta_{NO}} = \eta_0 \times \frac{1 - \exp(-k_{NO} \times m_{char,0} / V_g)}{k_{NO} \times m_{char,0} / V_g} \qquad (3)$$

Where η_0 is the net conversion ratio from char-N to NO at single particle condition, V_g is the volumetric gas flow rate.

In the case of slow char-N to NO model, net NO conversion ratio in the combustion experiment in the fixed bed reactor is given by

$$\overline{\eta_{NO}} = \frac{\int C_{NO} dt}{\int C_{NO} dt + \frac{1}{2} k_{NO} \times (m_{char,0} / V_g) \times \int C_{NO} (1 - X_C) dt} \qquad (4)$$

In both of the models, the k_{NO} was selected to fit the experiment data and the model results showed in Figure . The experimental results could be explained by the model expressions further. As the dimensionless variable of $k_{NO} \times m_{char,o}/V_g$ increases, the NO conversion ratio decreases for both of the models. For all the fuels at all the 3 combustion temperatures, increasing the $m_{char,o}$ leaded to increasing the $k_{NO} \times m_{char,o}/V_g$ and reached a lower net conversion ratio. Increasing temperature could affect both k_{NO} and V_g. The k_{NO}, NO reduction rate constant, increased rapidly as the temperature increased or predicted by Arrhenius Equation. The increasing of V_g was supposed as ideal gas in both of the two models. Then the increasing of k_{NO} was dominant and the increasing temperature leaded to a lower conversion ratio. The k_{NO} was affected by temperature and char type. Comparison with all the fuels at the same combustion temperature at large char contents, the conversion ratio was only affected by k_{NO}. The lignite showed lowest conversion ratio because of higher reaction rate than other chars.

Table 2-2: Conversion ratio from char-N to N_2O or NO at 850 °C

	mass (mg C)	Char-N to N_2O (%)	Char-N to NO (%)
Coal char	1.70	1.52	54.1
Coal char	3.84	3.56	51.9
Bark char	3.36	0	62.1
Straw char	4.65	0	55.4

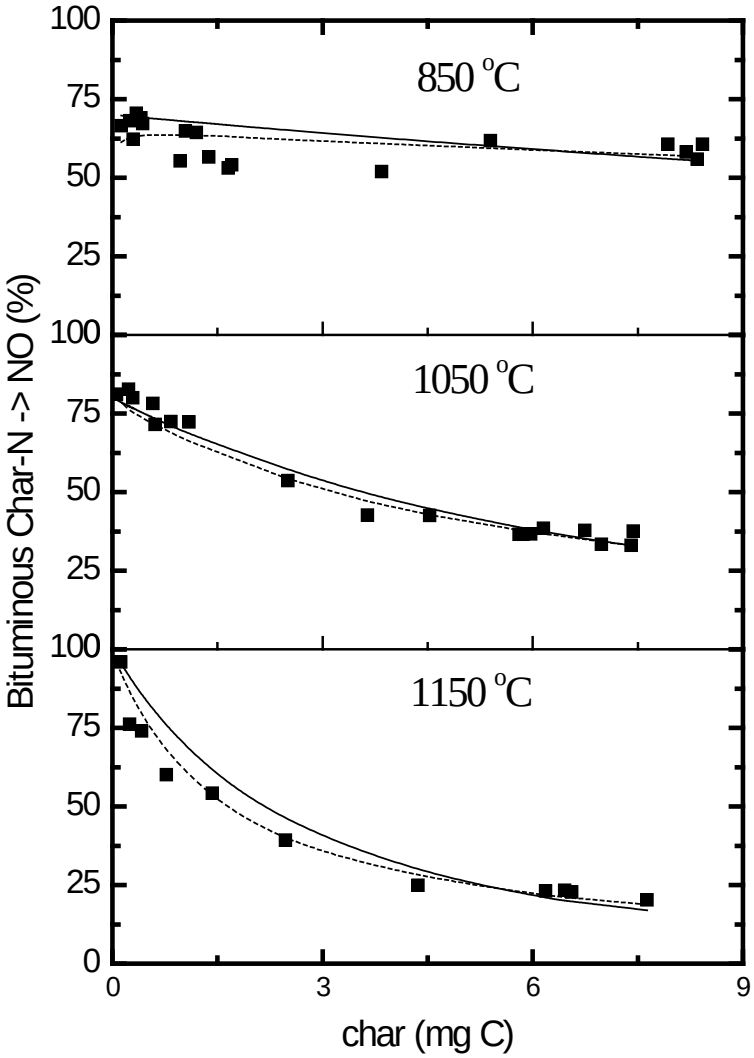

(a) Bituminous coal char

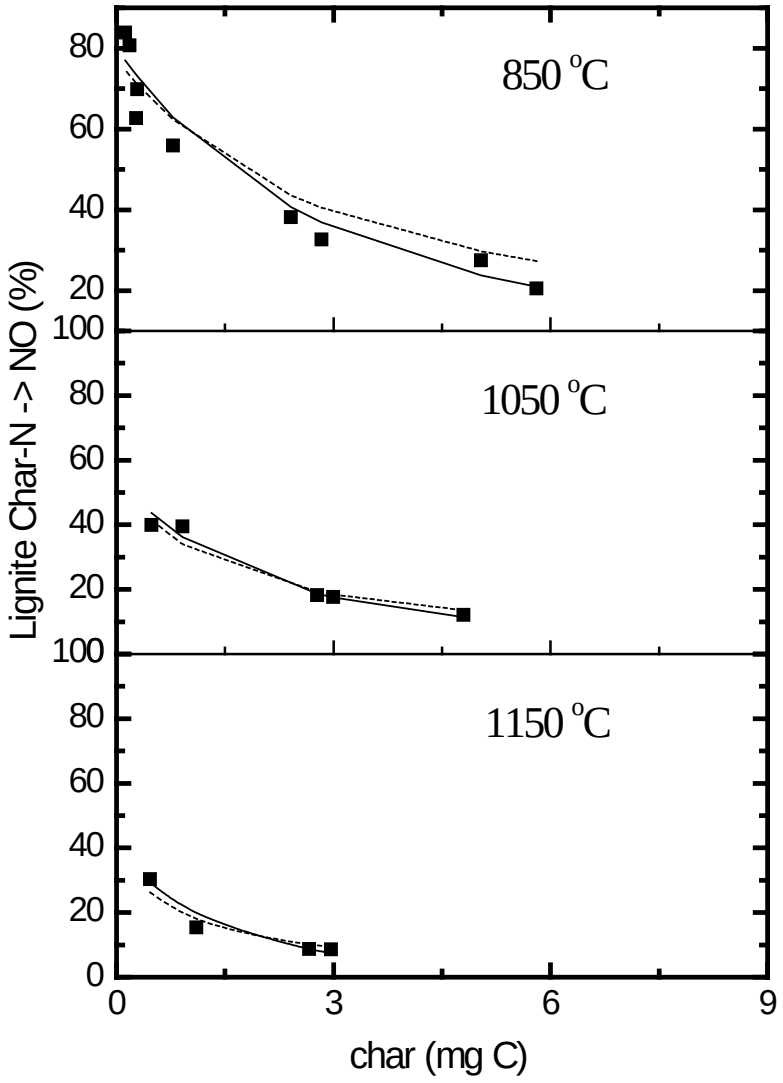

(b) Lignite char

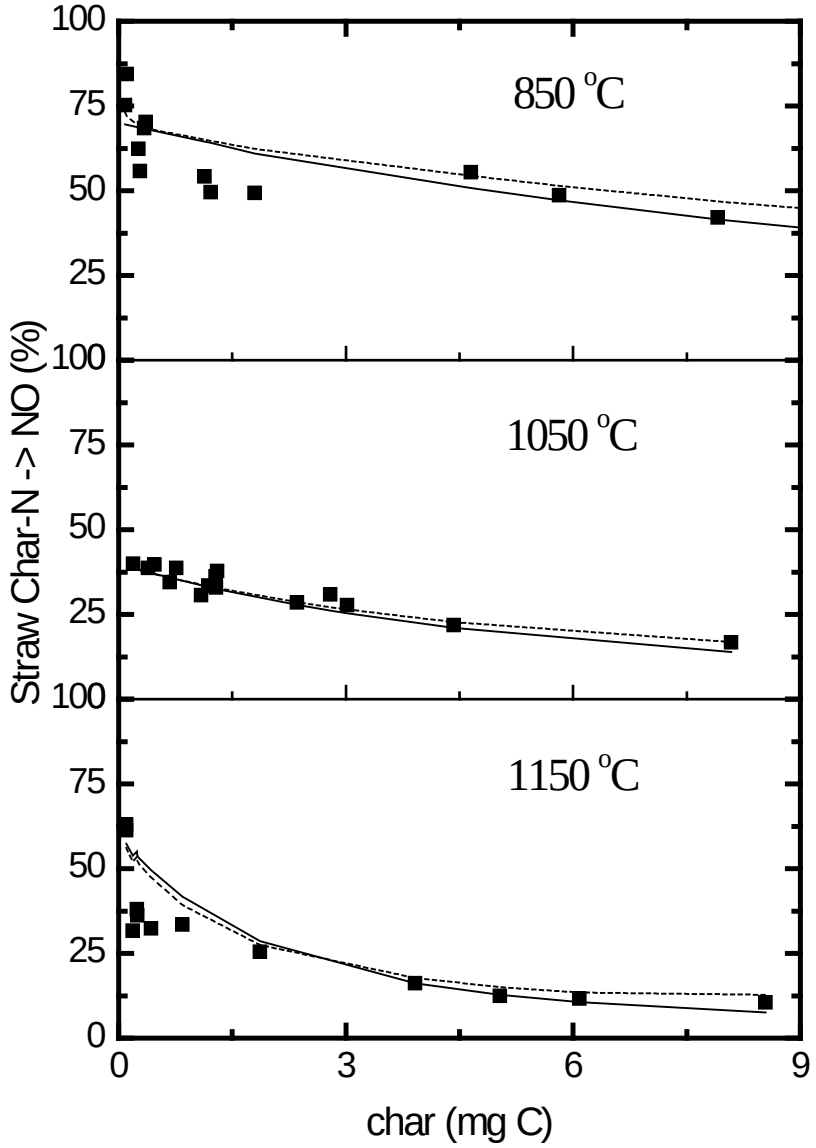

(c) Straw char

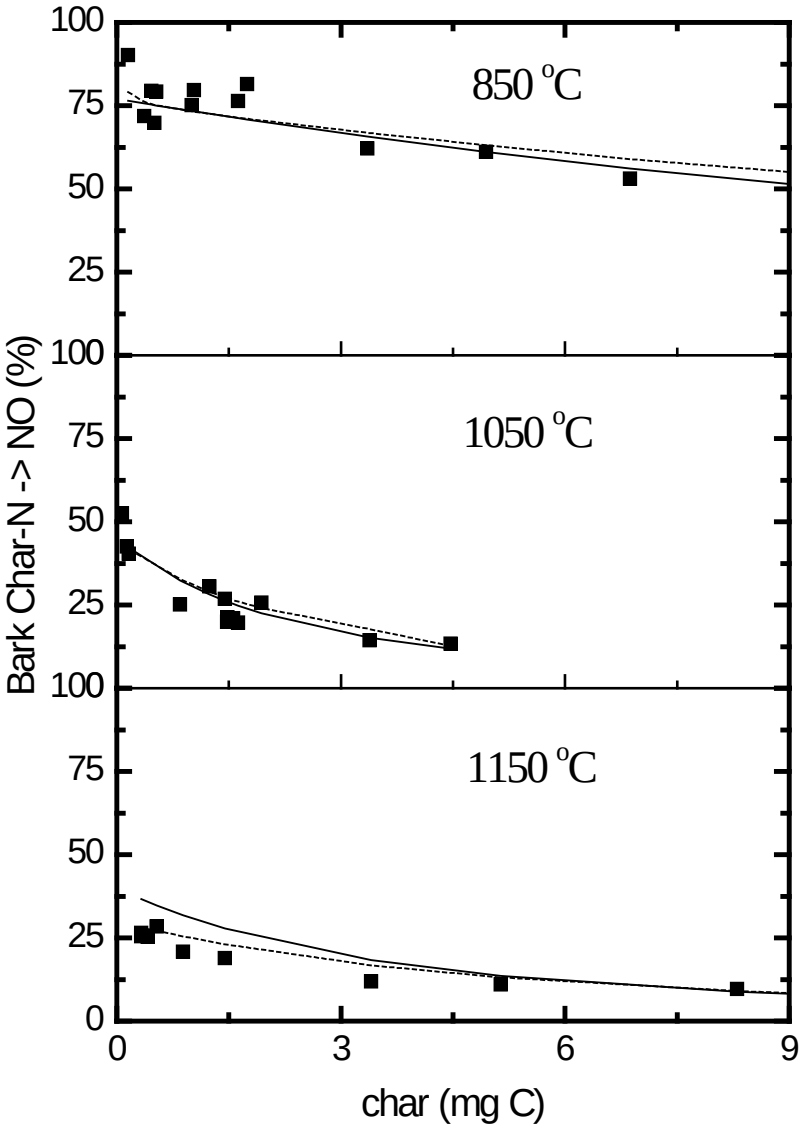

(d) Bark char

Figure 2-7: Net conversion ratio from char-N to NO as a function of burned char mass. Experimental data are shown as points and the lines are two model fits (combustion temperatures: 850 °C, 1050 °C, 1150 °C; steady-state O_2 concentration: 10 vol. %; gas flow: 1.5 NL/min; solid line (—) for rapid char-N to NO model; dash line (---) for slow char-N to NO model)

NO reduction in O_2-free experiment

The reaction rate constants in the O_2-free experiment were showed in Figure 2-8. To compare the NO reduction rate constant in char oxidation experiment, both

NO concentration and char concentration were also believed as first order reaction of the NO reduction on char.
The rate constant was seen to vary significantly with time. The variation of rate constant may the results of both thermal deactivation and char consumption. The NO reduction on char reaction, consuming carbon at the same time, is described by the following overall reaction:

$NO+C \rightarrow 1/2\ N_2 + CO, CO_2$ (5)

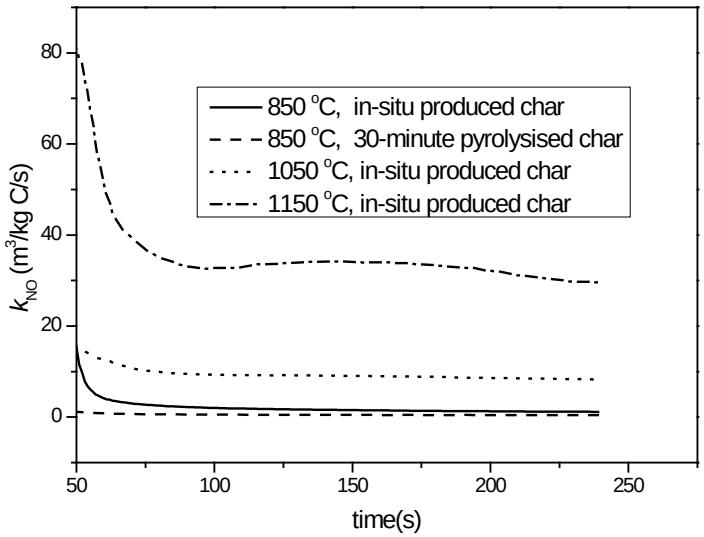

Figure 2-8: Variation of reaction rate constant for NO reduction with time in the O_2-free experiment (reaction temperature: 850 °C, 1050 °C, 1150 °C; gas flow: 1.2 NL/min; NO concentration, 640 ppmv NO/ N_2 in the inlet gas)

CO and CO_2 are identified as the major oxygenated products [23-25]. The CO and CO_2 gas profiles showed in Figure . It could be calculated that only 5.4 % and 23% of the char were consumed after 240 s at 850 °C and 1150 °C. Comparing the decreasing rate of reaction constant rate, the consumption of char was a much stable and slow rate. So the thermal deactivation was believed as the dominant reason at the initial reaction for the variation of rate constant. The ratio of CO in carbon oxides varied with reaction temperature. CO attributed about 60 % at 850 °C and 91% at 1150 °C in carbon oxides in the production gas.

Comparison of NO reduction rate constant by different experiments

In the present work, the NO reduction rate constants were calculated from char combustion experiment and O_2-free conditions respectively. The results are showed in Figure . In the char combustion experiment, two models, representing two extreme NO reduction conditions in the experiment, were used to calculate the maximum and minimum value of the reaction rate constant.

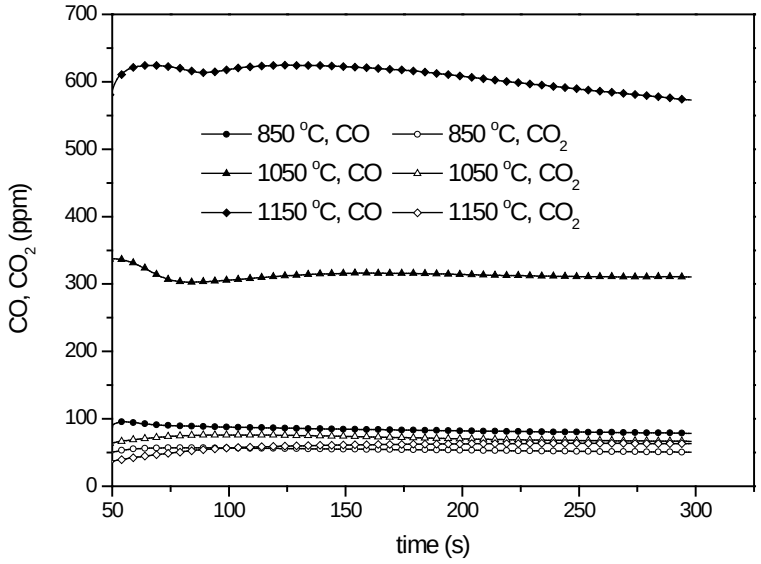

Figure 2-9: CO and CO_2 gas profile with time in the O_2-free experiment (reaction temperature: 850 °C, 1050 °C, 1150 °C; gas flow: 1.2 NL/min; NO concentration, 640 ppmv NO/ N_2 in the reactor inlet gas)

The maximum limit was greater by a factor of 1.5 - 3 than the minimum limit. As showed in Figure, the reaction rate constant by O_2-free experiment was lower about an order of magnitude than the maximum data in char combustion experiment. Thermal deactivation, increasing surface area during char combustion, higher char particle temperature, and enhancing reactivation by combustion gas are four possible reasons and discussed following:

I. Thermal deactivation: Pyrolysis conditions are known to affect the composition and structure of the char and then affect its activity. In the char oxidation experiment, the fuel was in-situ pyrolysis at N_2 for 3 minutes to prepare the char. Then O_2 was introduced to burn the char immediately. The burnout times of char samples were 4-10 s (calculated from the CO and CO_2 gas profile) depending on temperature, char mass and char type. So

the total time in high temperature was about 184-190 s. Concerning the O_2-free experiments, the char was also pyrolysis at N_2 for 3 minutes. However, the reaction continued 240 s. Therefore, the total time in high temperature was 420 s which was obviously higher than the time in char oxidation experiment. The rate constant for NO reduction on char in O_2-free experiment is showed in Figure 3. The results showed that it was important to consider thermal deactivation during experiment. Within 4 minutes, thermal deactivation of the char causes drop in the rate constant by about a factor 2-5. The thermal deactivation were proved by Jensen et al.[9] and Garijo et al.[8]for coal char and Garijo et al.[19] for biomass char.

II. Increasing surface area during char oxidation: A much higher surface area accompanied the combustion. Diego Alvarez et al.[26]selected 3 pulverized coals and studied the surface areas during combustion in drop tube furnace. The BET surface areas of coal char was 2-20 m^2/g. However, the BET surface areas significantly increased to 180-500 m^2/g with the burnouts of 50 – 70 %. Calo et al. [27] studied the role of surface area in the NO reduction on char and the results showed that the NO reactivity was relevant with surface area.

III. Increasing effect by the produced gas: CO, SO_2, and O_2 were generated in char combustion experiment and then increasing the NO reduction. The effect of CO on NO reduction on char is showed in Figure . It is obviously that CO enhancing the NO reduction on coal char. The CO concentrations in O_2-free and char combustion experiment are showed in Figure 4 and Figure 8 respectively. Comparison the bituminous coal char at 850 ^oC, the CO was about 90 ppm in the O_2-free experiment but the maximum of CO was about 7350 ppm in the char combustion experiment with 10 % oxygen in inlet gas. Therefore, the enhancing effect by CO in the char combustion experiment was more important than that in O_2-free experiment. It is worthy to mention that the increasing effect by CO was also proved by biomass char in recent years[12, 14, 15]. Dong et al. [15] results showed SO_2 could enhance the reactivation[15]. Suzuki et al.[28] and Illan-Gomez et al.[29] and Dong et al.[15] suggested that O_2 promoted the formation of highly active sites which react with NO.

IV. Higher char particle temperature: The gas temperature was measured by a thermocouple 0.5 cm below the porous plate where the reaction took place. The increases of gas temperature in all char mass were less than 15 ^oC. But, the char particle temperature was possible somewhat higher than gas temperature and difficult to measure directly. To predict the possible increase of char temperature, effect of O_2 concentration on net char-N to

NO conversion from char was studied and the results show in Figure. In this experiment, the lower O_2 concentration was used to decrease the char combustion rate and then let the char temperature close to gas temperature. The gas profile is showed in Figure . The burnout time was longer a factor of 5-10 in 1% O_2 than that in 10% O_2, which means the char combustion rate decreased obviously. However, no significant differences were observed in the 1 - 10 % O_2. Therefore, the char temperature was possible to increase a few degrees, but it was almost no effect on the NO reduction rate constant in the char combustion experiment.

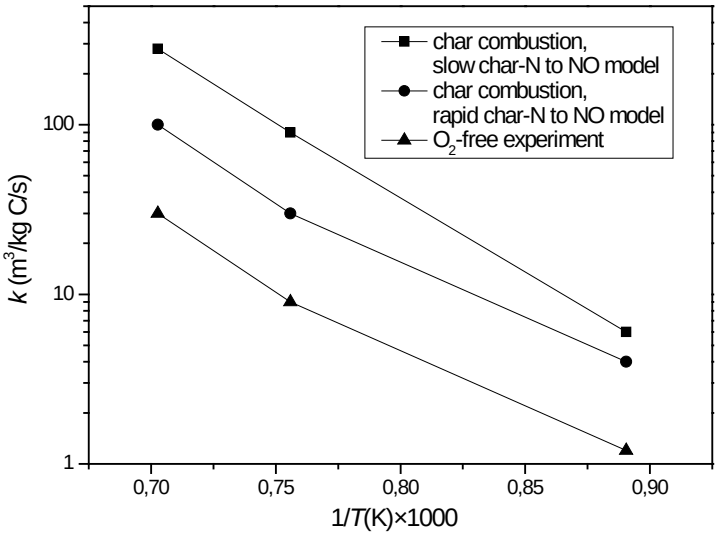

Figure 2-10: Arrhenius plot showing a comparison of reaction rate constant for NO reduction on bituminous coal char determined by different experiments.

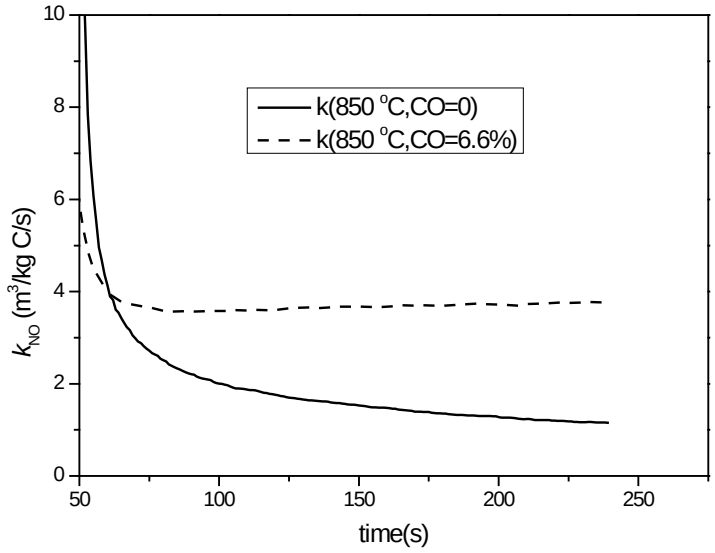

Figure 2-11: Effect of CO on NO reduction on bituminous coal char at 850 °C

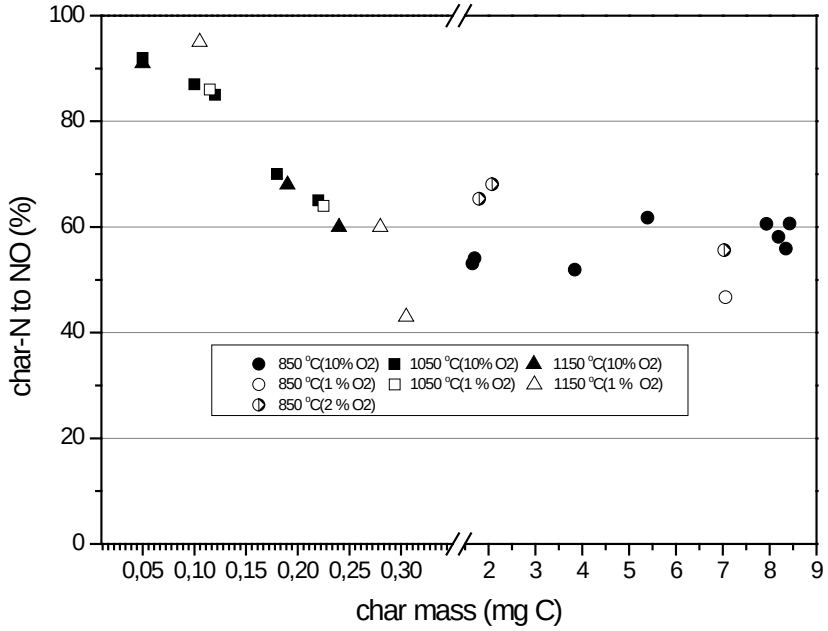

Figure 2-12: Effect of O_2 concentration on net conversion ratio from char-N to NO from bituminous coal char (The data at low mass char at 1050 °C and 1150 °C were performed by Jensen et. al[9] using the same reactor)

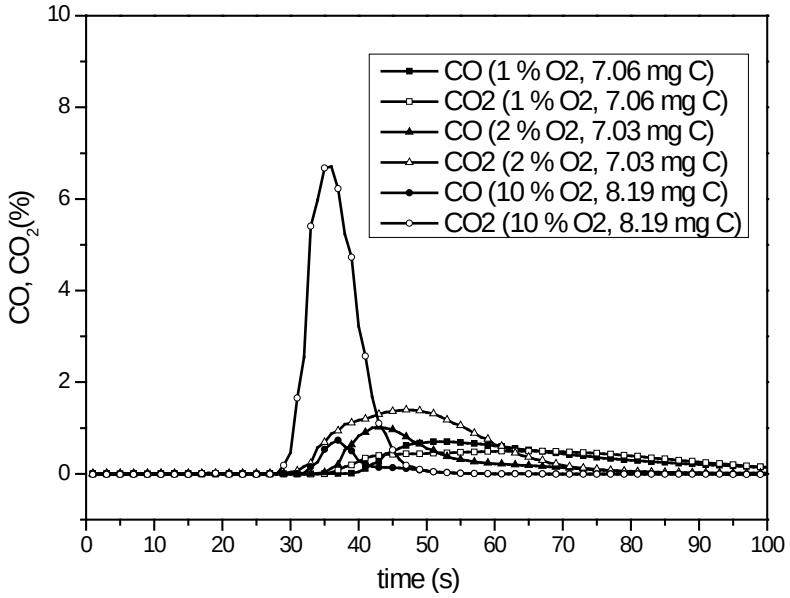

Figure 2-13: Effect of O_2 concentration on CO and CO_2 concentration (combustion temperatures: 850 °C; gas flow: 1.5 NL/min; fuel: bituminous coal)

As mentioned and discussed above, three reaction rate constants of NO reduction on char were achieved, which were slow char-N to NO model in the char combustion experiment, rapid char-N to NO model in the char combustion experiment, and O_2-free experiment respectively. The rate constants from O_2-free experiment were lower about a factor of 10 than that from the slow char-N to NO

model (the minimum possible of the char-NO reaction and the maximum of the reaction rate constant) in the char combustion experiment. The NO reduction rate in the first few seconds after pyrolysis is relevant for NO in pulverized fuel combustion. Furthermore, the char surface area and reaction atmosphere in the char oxidation experiments are more relevant to the pulverized fuel combustion. So the reaction conditions of char combustion experiment were closer to pulverized fuel combustion than that of O_2-free experiment. The rapid char-N to NO model in the char combustion experiment, which assumed that the char-NO was infinite rapid to form the all NO the front of the bed and then reduced along the char-sand bed, is easier to simplify the reduction expression and get some knowledge. However, it showed an obviously higher possible to reduce the NO and leaded to the minimum rate constant. Therefore, the rate constants from the slow char-N to NO model were close to real NO reduction on char in the pulverized combustion. The rates for NO reduction from this model were concluded as following:

$r_{NO}=-2.80\times10^{5}\times\exp(-9.68\times10^{3}/T)\times C_{char\text{-}C}\times C_{NO}$ for bark char (6)

$r_{NO}=-1.20\times10^{10}\times\exp(-2.49\times10^{4}/T)\times C_{char\text{-}C}\times C_{NO}$ for straw char (7)

$r_{NO}=-9.04\times10^{8}\times\exp(-2.13\times10^{4}/T)\times C_{char\text{-}C}\times C_{NO}$ for bituminous char (8)

$r_{NO}=-1.37\times10^{7}\times\exp(-1.39\times10^{4}/T)\times C_{char\text{-}C}\times C_{NO}$ for lignite char (9)

The reaction rate will be in mol/m^3/s if units of kg C/m^3 are used for char-C and mol/m^3 are used for NO. Lignite char was highest activation within the 4 chars. Both straw and bark char were showed higher activation than bituminous char at 850 °C, about 4 times higher than bituminous char, due to a higher content of catalytic activity substances and a less ordered structure of the organic matrix. Jensen et al.[30, 31] studied the release of potassium in straw during pyrolysis. Potassium is not released below 700 °C, above that temperature it increased and about 25% potassium released at 1050 °C. So the reaction rates of bituminous char were close to that of biomass char at higher temperature (especially at 1150 °C) because the catalytic substances vaporized to gas phase.

References:

1. Klippenstein, S.J., L.B. Harding, P. Glarborg, and J.A. Miller, "The Role of NNH in NO Formation and Control", Combust. Flame 158 (2011) 774-789.
2. Lucassen, A., K. Zhang, J. Warkentin, K. Moshammer, P. Glarborg, P. Marshall, K. Kohse-Höinghaus, "Fuel-nitrogen conversion in the combustion

of small amines using dimethylamine and ethylamine as biomass-related model fuels", Combust. Flame 159 (2012) 2254-2279
3. Zhang, K., Y. Li, T. Yuan, J. Cai, P. Glarborg, and F. Qi; "An experimental and kinetic modeling study of premixed nitromethane flames at low pressure", Proc. Combust. Inst. 33 (2011) 407-414.
4. Zhang, K., L. Zhang, M. Xie, L.i Ye, F. Zhang, P. Glarborg, F. Qi; "An experimental and kinetic modeling study of premixed nitroethane flames at low pressure", Proc. Combust. Inst., in press (2012).
5. Houshfar, E. Ø. Skreiberg, P. Glarborg, T. Løvås, "A reduced chemical kinetics mechanism for NO_x emission prediction in biomass combustion", Int. J. Chem. Kinet. 44 (2012) 219-231.
6. Zhao, K., P. Glarborg, A.D. Jensen; ERANET Report Task 1.3: NO Formation from Biomass Char Oxidation, DTU Chemical Engineering, December 2012.

3. WP2: Generic Models for Ash Formation/Deposition and Formation of Small Particles

Coordinated by Dr. Maria Zevenhoven, AAU

Combustion of biomass under unfavorable conditions can produce significant amounts of harmful pollutants. One of the most important pollutants from biomass combustion is fine particulate emissions (< 2.5 µm). During combustion of biomass, the particle emissions from the furnace consist mainly of fly ash and also if the combustion is incomplete of soot particles. The smallest particles (< 0.5 µm) are very hard to collect in ordinary cleaning devices. However, for large scale plants, advanced gas cleaning equipment (e.g. electrostatic precipitators, baghouse filters) that reduces the emissions of fine particles is an acceptable option and therefore a relatively high amount of particles in the flue gas leaving the boiler may be tolerated. However, for small and medium-scale equipments such as pellet burners and smaller district heating plants advanced gas cleaning devices are not an option due to their relatively high costs.

Fine fly ash particles, < 1 µm are produced from vaporization of easily volatilized elements (K, Na, S, Cl, Zn and in some case also P) from the fuel/ash particles in the bed or from the entrained char/ash particles. Fine particles (< 1 µm) from incomplete combustion (e.g. soot particles are produced in the oxygen lean early flame and these particles are thereafter oxidized rapidly in the hot oxygen rich post flame zone. If the soot particles survive the oxidation process they can probably act as condensation nuclei for alkali sulfates and Zn. After the flame, the fine mode mass concentration and particle diameter grow by gas-to-particle conversion of metals. Simultaneously, the fine mode number concentration decreases and the particle diameter increases due to coagulation between the particles.

Until now main ash forming matter has been studied together with Zn. Knowledge of speciation of ash forming matter in biomass fuels and new fuels may help to improve existing prediction models concerning aerosol and deposit formation.

Here, the focus will be on the alkali chemistry and easily volatile heavy metals (e.g. Zn and Pb) as mentioned in the EU directive on incineration of waste. The

knowledge of the formation mechanisms and how fuel and process parameters affect the formation of alkali compounds have been studied. However, these results could not be implemented in models that can be used by boiler manufacturers and operators. Knowledge and modeling of the emissions of heavy metals from new fuels is still rare. At the same time, knowledge about heavy metal emissions from biomass combustion are of more interest now than ever due to the new EU directive about allowed emissions for the twelve key elements (the " dirty dozen") mentioned above.

Metals transported from the environment to the biomass are contained as inherent material and can be organically associated, for example as chelates. Excluded minerals are mostly the dominant source of trace metals in woody biomass polluted with soil. Excluded minerals can make up to 80% of the total ash-forming matter in a woody biomass. However, although total amounts have been studied, little information is available in literature on the association of trace elements in biomass fuels and the influence this may have on their volatility in combustion and thus their presence in deposits and fine particulate emissions.

In recent years, also the understanding of the mechanisms responsible for submicron particle formation and deposit formation has increased, based on studies of the release of inorganic elements from annual biomass crops and wood gas-phase conversion of K/S/Cl, and formation of aerosols and deposits. While this work has contributed to a better understanding of issues related to particulate matter, the implications of fuel composition and combustion conditions are still not fully addressed and will be focus of this study.

3.1 Task 2.1: Formation of Ash and Volatilization of Heavy Metals

Formation of ash from the fuels studied as well as volatilization of heavy metals i.e. Pb, Zn, Cd, Cu during combustion, was modeled with global equilibrium analysis using thermodynamic data available at AAU. An excerpt of the results of these studies is presented below.

Table 3-1: Composition of waste wood as used in the calculations.

	g/100g		g/100g
H_2O	15.21	K	0.07
C	49.01	Air = N_2+O_2	Af = 1.2
H	6.13	Zn	0.01
O	42.81	Pb	0.01
S	0.04	Cu	0.1
Cl	0.31	Cd	0.0001

Thermodynamic equilibrium modeling was used for modeling the chemical interaction of the volatile ash fractions from waste wood with the combustion gases.

In the present study, the FACT53 database and the SGTE database for pure compounds were used to construct a tailor-made database for the stoichiometric compounds and the gas phase, and a tailor-made database was used for the solid and liquid solution phases. Certain solid solution and subsystems of the liquid phase also appear in the FTSalt and FTPulp databases in the Factsage software. The compounds of the C–H–O–N–S–Cl–Na–K–Zn-Pb-Cd-Cu system in the databases were used, except for gaseous nitrogen compounds, where only N2 was included. The formation of NOx compounds in biomass combustion is strongly dependent on kinetics and N-speciation in the fuel. Thermodynamic equilibrium calculations are therefore not suitable for modelling gaseous nitrogen chemistry. The solution phases of relevance are an alkali chloride solid solution, (Na,K)Cl; two alkali sulfate-carbonate solid solutions, $(Na,K)_2(SO_4, CO_3)$; glaserite (nonstoichiometric K3Na(SO4)2); and a multicomponent liquid phase, Na^+,K^+, Zn^{2+}, Pb^{2+}//SO_4^{2-}, CO_3^{2-}, S^{2-},Cl^-. Cd and Cu were not included in this liquid phase but were considered seperately.

The ash forming elements were assumed to be ideally mixed with the gas phase, allowing formation of carbonates and volatilization of alkali metals. In the calculations, the amount of carbon, nitrogen and oxygen was derived from the ultimate fuel analysis of waste wood to make the formation of a realistic gas

phase possible. An air factor of 1.2 for the combustion cases and atmospheric pressure were assumed. The calculations were done for a temperature range of 500-1200°C.

The role of chlorine and sulfur

It is well known that the chlorine and sulfur content in the fuel affects the volatilization of trace elements in combustion systems. The presence of chlorine considerably raises the gas phase concentrations compared to situations with no chlorine. Equilibrium predicts that the chlorine is present as hydrogen chloride (HCl) in combustion gases in a wide temperature range if no reactions with ash components occur. At lower temperatures the oxidation reaction

$HCl + 1/2\ O_2 \leftrightarrow Cl_2 + H_2O$

is shifted to the right making Cl_2 the more stable species. Introducing alkali metals complicates the picture drastically. Alkali metals may react with chlorine present, forming alkali chlorides. This may lead to a further shift of Cl_2 formation to slightly lower temperatures. These changes may also have a serious impact on the volatilization of trace metals.

Presence of sulfur will have the effect that the temperature range for HCl becomes broader and the Cl_2 formation is shifted to slightly higher temperatures. This is caused by formation of condensed potassium sulfate at lower temperatures, releasing chlorine to the gas phase. A small part of the potassium is in the form of gaseous K_2SO_4.

In the case of combustion of waste wood Figure 3-1 shows the distribustion of K, S and Cl. The diagrams clearly show the interactions between these three elements. At high temperatures KCl, SO_3 and HCl are the most stable compounds. Probably volatile K (in whatever reactive form) may react readily with HCl forming KCl. Upon cooling of the gases HCl remains stable under the entire temperature range studied. SO_3 will decrease at some 850°C and will be replaced by condensed sulfates.

The diagram for sulfur indicates the behavior of Zn forming $ZnSO_4$ and Pb forming $PbSO_4$ at low temperatures. Often reactivity of Pb and Zn may be considered comparable to that of K.

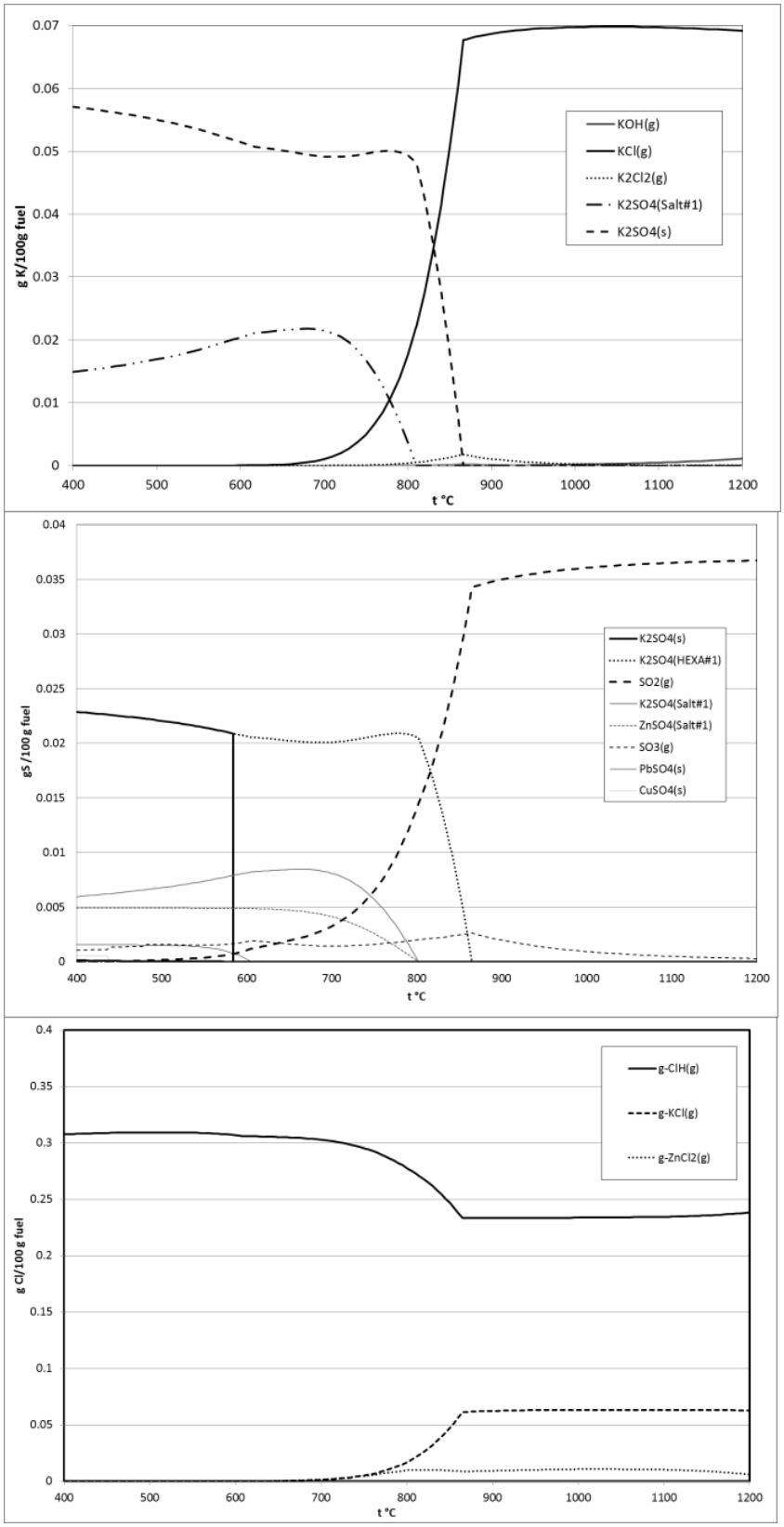

Figure 3-1: Distribution of K, Cl and S compounds: combustion of waste wood.

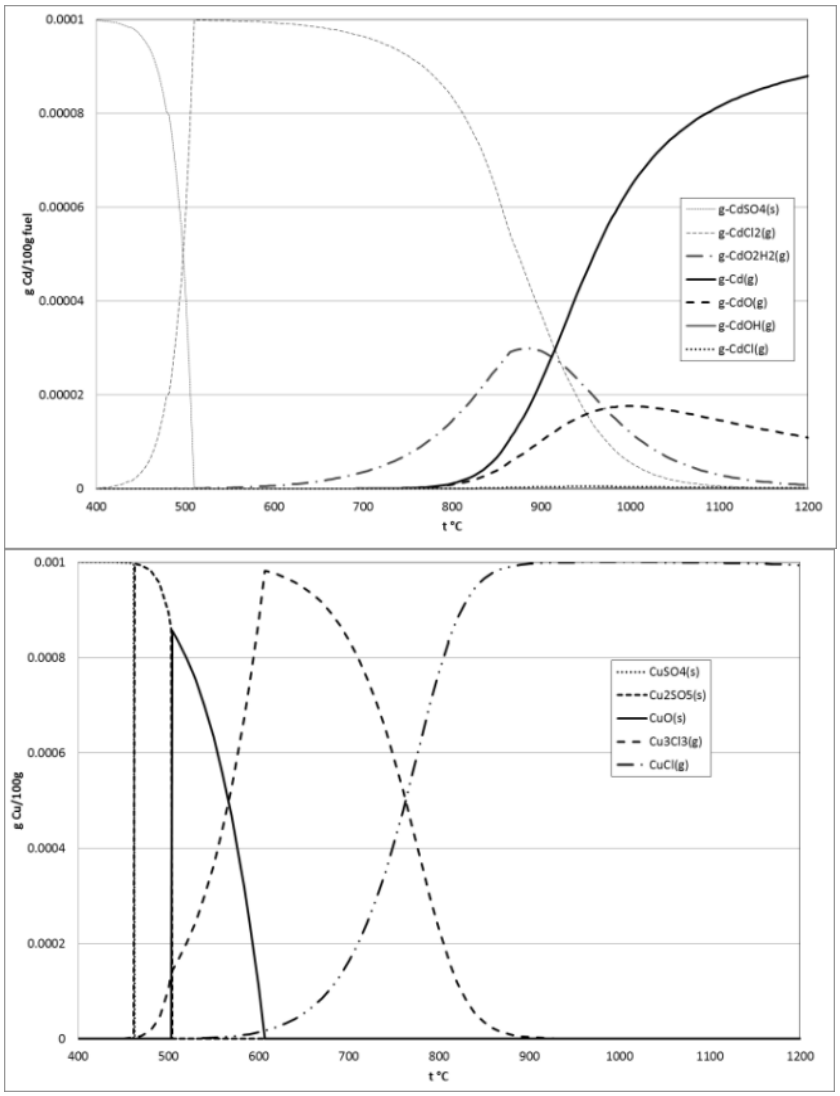

Figure 3-2a: Distribution of Cd and Cu compounds: combustion of waste wood.

Figure 3-2 shows the speciation of Cd calculated as if only chlorine, sulfur and alkaline metals would be present. At low temperatures $CdCl_2$ and $CdSO_4$ may be stable. At higher temperatures again Cd, Cd and $Cd(OH)_2$ could be the main stable species.

The speciation of lead and zinc shows that the amount of alkali metals was too low to counteract the chlorination of these metals. Above 400°C Pb-chlorides may be present either as molten salt or as gaseous $PbCl_2$ and PbCl. At temperatures above 800°C PbO becomes the most stable species. At low temperatures

(<600°C) solid $PbSO_4$ may be stable. $ZnCl_2$ is the most stable species at high temperatures whereas $ZnSO_4$ may be found at temperatures below 750°C.

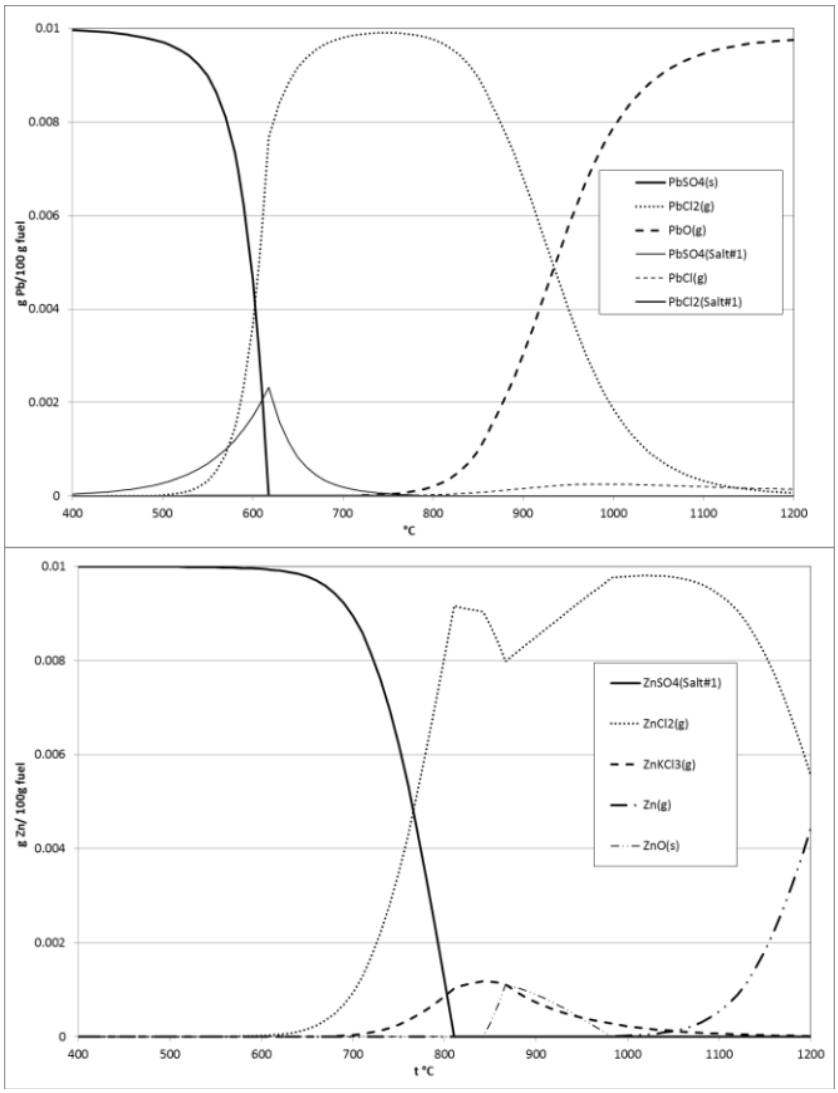

Figure 3-2b: Distribution of Pb and Zn compounds: combustion of waste wood.

With the low alkali content present in the waste wood considered also copper may be chlorinated at higher temperatures and becomes the most stable species already above 500°C. At lower temperatures copper may be stable in the form of sulfates or oxide.

Sensitivity studies

As indicated above the effects on the distribution shown are partly dependent on purely stoichiometric circumstances, i.e. the fuel composition in terms of K/2S+Cl and S/Cl ratios are important. Partly, the effects are governed by chemical equilibrium conditions, which make the role of temperature and condensation reactions important.

To show the influence of variation in fuel composition important variations such as in available S and Cl have been studied. Available S will be dependent on reactions with other metals in the fuel, such as Ca.

It is clear that alkali metals will compete for reaction with S and Cl with the trace metals studied here. This competition may be studied by variation of alkali metals, sulfur and chloride. The influence of variation in the alkali composition in relation to S and Cl can be considered as well. The ratio, expressed as $\frac{x_K}{2x_S+x_{Cl}}$, represents the availability of these most important anions for reaction with other elements such as Zn, Pb, Cu and Cd. The ratio can thus be considered being the **excess alkali value** (EAV) to catch S and Cl. The ratio is therefore defined as:

$$EAV = \frac{x_K}{2x_S+x_{Cl}}$$

In the study below input parameters are again retrieved from waste wood with the modification that in all cases 100ppm of trace metal was used. Calculations were carried out at 800°C a temperature most relevant to study the volatility of K, Cd, Cu, Zn and Pb in fluidized beds.

Competition between Sulfur and Chlorine, combustion conditions, 800°C

In the above described case the amount of chlorine was rather high, i.e. 0.31%wt. This high content made chloride formation possible for all elements studied. At 800°C Cu, Pb and Cd seem to form stable chlorides at all ratios of x_S/x_{Cl}. Chemistry of Zn and K can be rather similar. With increasing sulfur content both Zn and K may form $ZnSO_4$ and K_2SO_4 respectively through sulfation reactions of chlorides. This is shown through the decreasing $ZnCl_2$ and KCl and increasing $ZnSO_4$ and K_2SO_4 concentrations with increasing x_S/x_{Cl} (Figure 3-3 and 3-4).

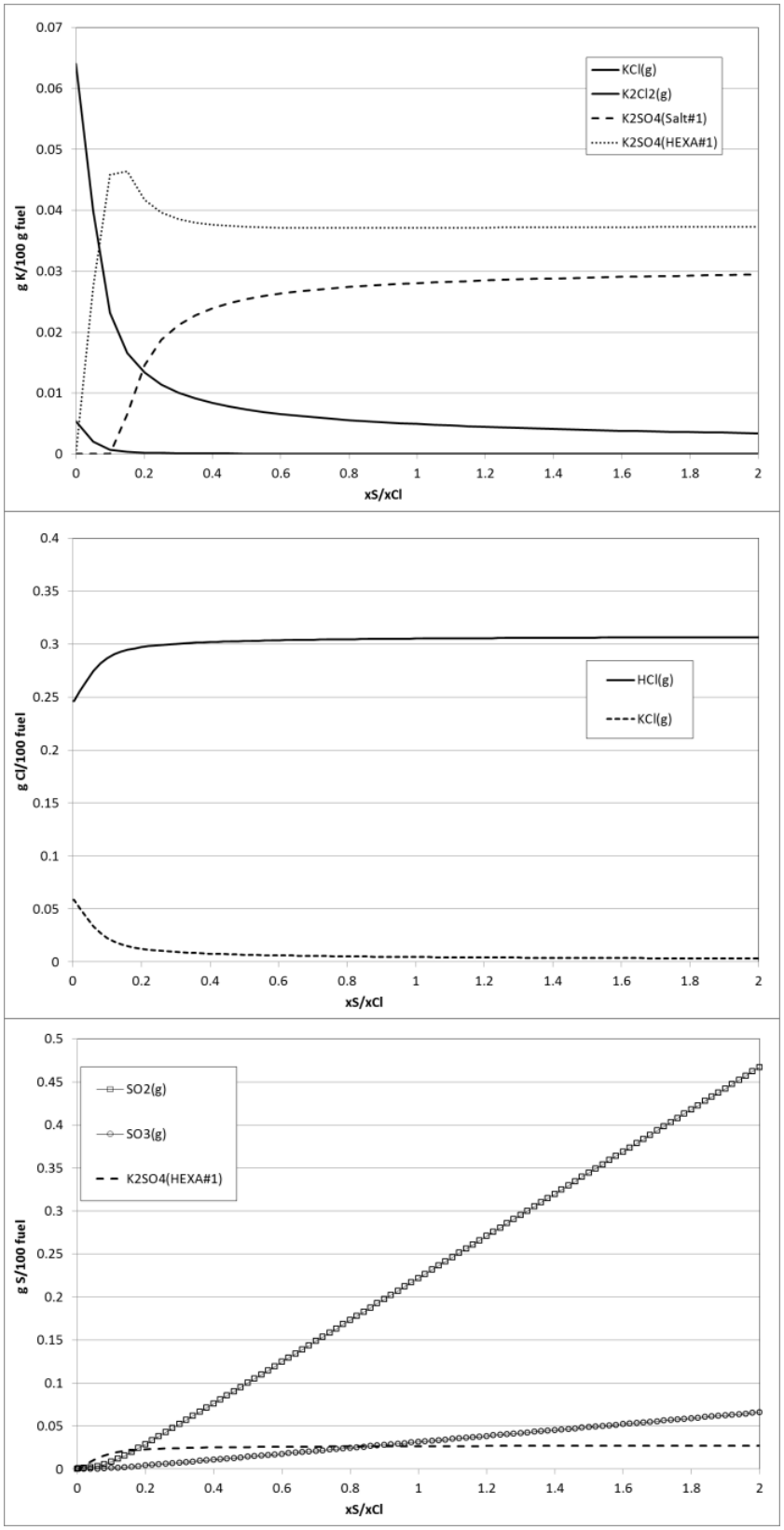

Figure 3-3: Distribution of K, S and Cl at 800°C as a function of xS/xCl.

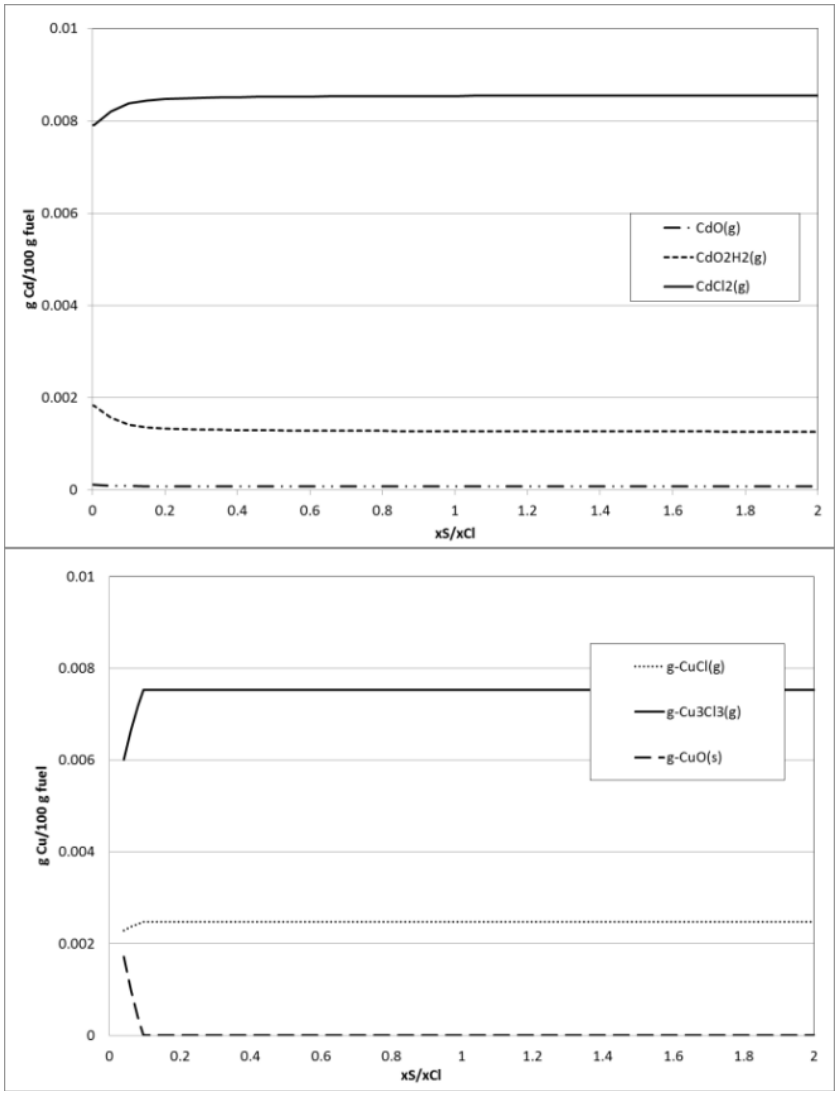

Figure 3-4a: Distribution of Cd and Cu at 800°C as a function of xS/xCl.

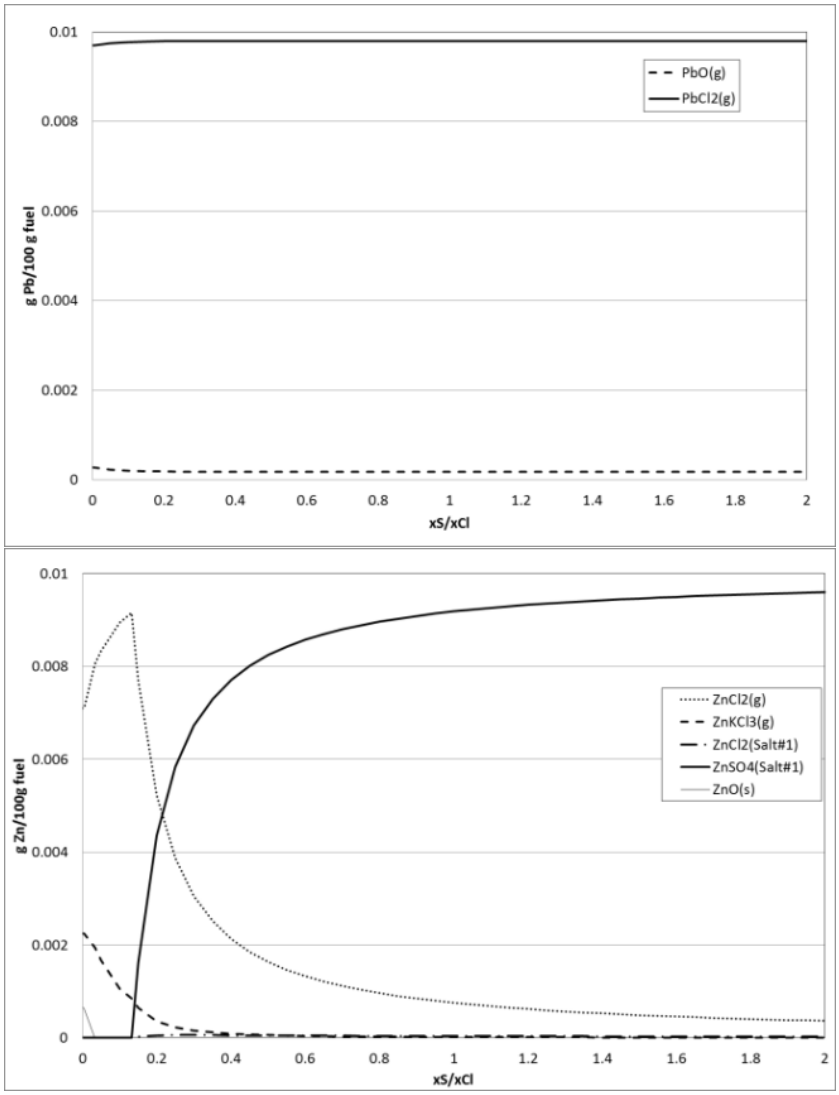

Figure 3-4b: Distribution of Pb and Zn at 800°C as a function of xS/xCl.

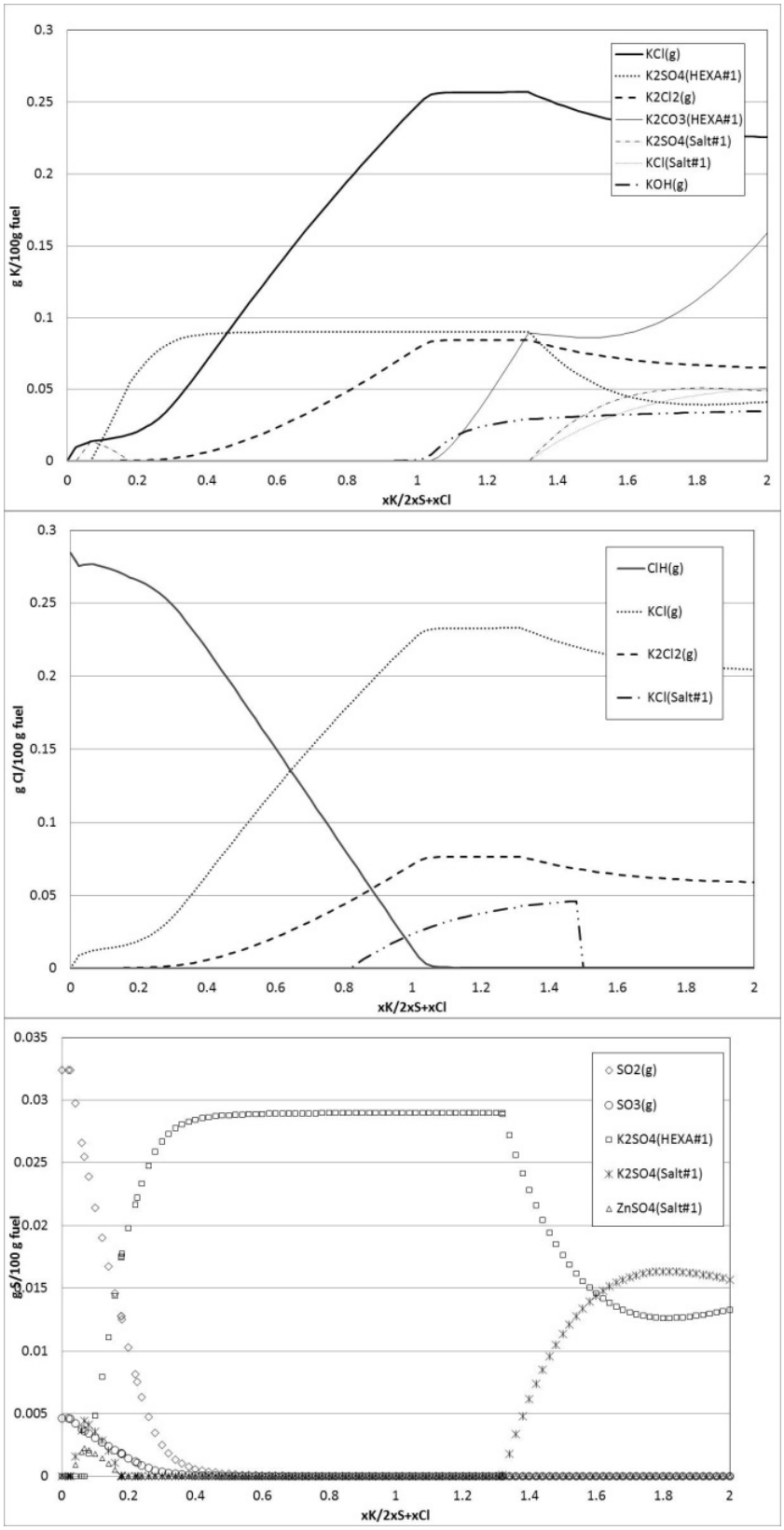

Figure 3-5: Distribution of K, S and Cl at 800°C as a function of xk/2xS+xCl.

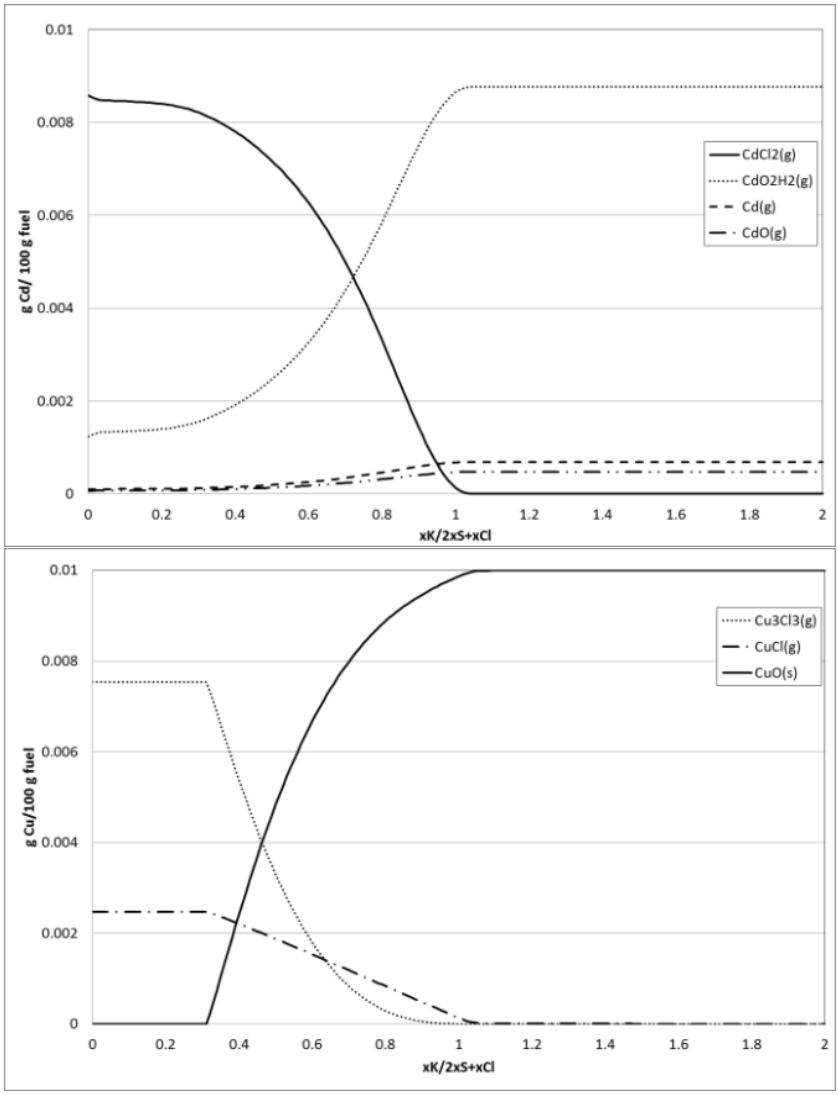

Figure 3-6a: Distribution of Cd and Cu at 800°C as a function of xK/2xS+xCl.

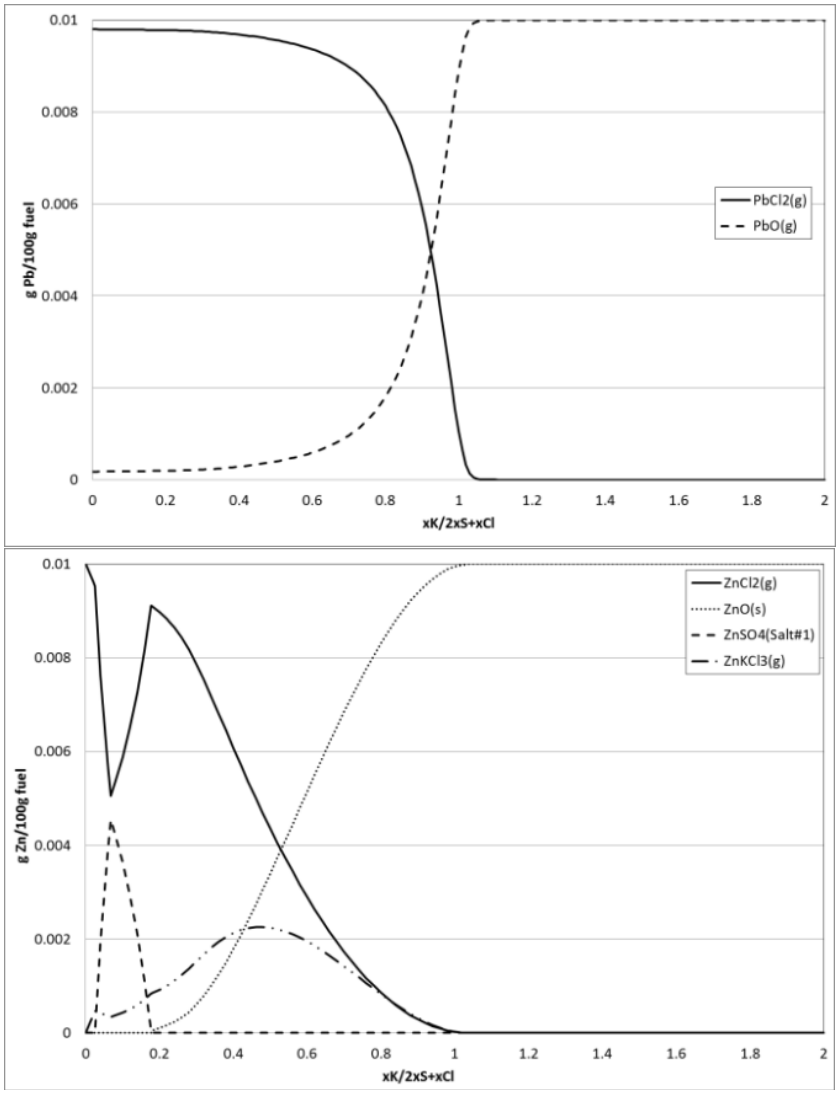

Figure 3-6b: Distribution of Pb and Zn at 800°C as a function of xK/2xS+xCl.

In Figures 3-5 and 3-6 show results from the calculations at 800°C are shown. Here the amount of an element in a compound is presented as function of the EAV. An EAV<1 represents cases where an excess of S and Cl form sulfates and chlorides. In this case chlorine will be present in the gaseous phase as HCl; S will be present both as condensed sulfates of K, as well as gaseous SO_2 and SO_3. Some $ZnSO_4$ might form at 0<EAV<0.2.

When EAV<1 Pb, Cd and Cu are expected to be present as gaseous chlorides. In cases where EAV >1 i.e. when alkali is presence in abundance gaseous KCl will be still present. Also K_2CO_3(s) and KOH may be formed, whereas the amount of sulfates present will decrease with increasing EAV, stabilizing at EAV>3.

The chemistry of different fuels

The table below shows the composition of K, Ca, S and Cl of the fuels studied. These elements are the most important to understand release of heavy metals. The influence of presence of Ca in the fuels will show in the S-chemistry. Calcium is well known to capture S forming $CaSO_4$. According to thermodynamic calculations $CaSO_4$ increases linearly until Ca/S =1 after which all S will be bonded effectively in $CaSO_4$. In reality this reaction will be kinetically restrained, but when only considering reactive calcium present in the fuel the reaction still can be considered relevant.

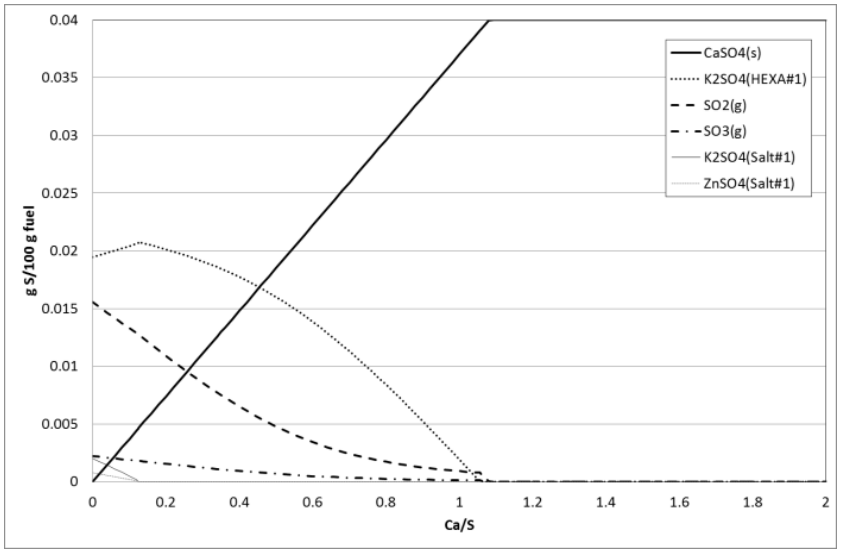

Figure 3-7: Calcium influences the effective S/Cl and EAV.

If Ca is ignored poplar, beech and bark all have a high S/Cl and EAV indicating that at 800°C both HCl and SO_2/SO_3 may be present as well as KCl, K_2CO_3, K_2SO_4 and KOH may be expected. In wood derived fuels all soluble alkali may be expected to participate in the lively chemistry. In bark and waste wood part of the K was bound to silicates and should be considered not released. This lowers the apparent EAV from 0.16 to 0.114 in waste wood and from 2.18 to 1.79 in bark. Waste wood clearly is an exception for a wood derived fuel caused by a very low S/Cl and EAV caused by the high chlorine content. Miscanthus contains a stoichiometric amount of K vs S and Cl with a surplus of S. Sludge on the other hand was low in alkali vs. S and Cl. Only 39% may be considered reactive which lowers the apparent EAV from 0.12 to 0.05. Chemistry from release of alkali and heavy metals studied can thus be read from the Figures 3-3 to 3-6 by using the EAV derived from reactive alkali.

All fuels, except Miscanthus contain much calcium. Calcium in wood derived fuels can be considered reactive in FBC and will be able to capture sulfur. This Ca can be considered substantially more reactive than addition of limestone would have been. Caused by the high surface area of oxalate particles and close contact with the fuel. Thermodynamic equilibrium calculations show that in these fuels when Ca/S>1 all sulfur will be bonded to Ca. This will represent the calculation cases where S/Cl=0 i.e. no S will be available for alkali and heavy metals. In that case K and the 4 heavy metals studied will be present as gaseous chlorides and the rest of excess chloride will be forming HCl(g). In Miscanthus Ca is not present for capturing all S. Some 40% of S may be captured as $CaSO_4$ lowering the effective S/Cl to some 2.1 (mol/mol) and the effective EAV to 2.2 (mol/mol).

To sum up this Task, thermodynamics showed that the fate of the heavy metals is dependent on other chemistry in the system. Chlorine and sulfur in the gas phase interact strongly with heavy metals and alkali metals. Variation in these three elements influences the partitioning of the heavy metals studied. Understanding this complex chemistry is vital for being able to interpret modeling results of more complex systems.

With interpretation of results of thermodynamic modeling as carried out in this task its drawbacks should be considered. At low temperatures chemical reactions are slow and especially simulation results of reactions involving solid species may be wrong or non-relevant.

In simulations using Fact sage databases it should be kept in mind than results may include system data that have not been proven experimentally. In Task 2.1 a data set is used for alkali, S, Cl, Zn and Pb that are considered reliable.

3.2 Task 2.2: Release of Ash in a Grate Furnace

The release of ash forming elements from the fuel to the gas phase as well as the melting behavior is key issues in biomass combustion processes. They influence the plant operation (regarding ash melting, deposit formation and corrosion) as well as the particulate emissions. Therefore, models which describe these processes represent an important tool for the modelling of the whole process. Hence, the objectives of Task 2.2 were to develop, test and validate models based on thermodynamic equilibrium calculations (TEC) which describe ash formation, ash composition, release of volatile and semi-volatile elements as well as ash melting based on fuel and ash composition data. The work was performed in close cooperation with WP5 from which data from ash melting studies as well as lab-scale reactor test runs were taken to calibrate and validate the models developed. The work performed within Task 2.2 can be divided into two main fields, namely (i) the investigation of the release behaviour of volatile ash forming species as well as (ii) the investigation of the ash melting behaviour of biomass ashes.

Release of volatile ash forming compounds during combustion

For the prediction of multi-phase equilibria and the identification and quantification of the liquid and solid phases of interest, the thermochemical software package FactSage 6.2 was applied. This package running on a PC operating under Microsoft Windows, consists of a series of calculation modules as well as databases and uses the image component method in Gibbs free energy minimization concerning thermodynamic equilibrium. The currently accessed databases are "solution databases" containing the optimized parameters for a wide range of solution phases and "pure compound" databases containing the data for over 4,500 stoichiometric compounds. For the application considered a selection of meaningful compounds and databases took place.

In order to exclude compounds present in minor concentrations in biomass ashes and to obtain more realistic results, extensive preparatory calculations have been performed. The compound selection was based on the following reactants: C, N,

O, Na, Mg, Al, Si, P, S, Cl, K, Ca, Mn, Fe, Zn, Pb and Cu. The calculations have been performed for dry fuels, oxidising atmosphere as well as the temperature range from 500°C to 1,600°C.

The thermodynamic model applied contains over 1,000 pure compounds and the following solid as well as liquid solution phases:

SLAGH: oxide liquid/glass containing fluoride and chlorides
SALTF: molten salt solution
OlivA: oxide solution (olivine)
SPINA: oxide spinel (cubic)
cPyrA: silica based solid solution
ACL_B: solid chloride solution
CSOB: solid alkali sulphate/carbonate
KSO: solid alkali sulphate/carbonate solution

The biomass combustion process can be divided into two phases, the volatilisation and the charcoal combustion phase. During the volatilisation phase volatile combustible compounds are released to the gas phase. In fixed-bed combustion systems usually temperatures significantly below 1,000°C and reducing atmospheres prevail during this phase. After all volatiles have been released from the fuel (i.e. almost no H and O is left in the fuel) charcoal combustion at oxidising conditions and temperatures higher than 1,000°C takes place. In order to also consider these process constraints in the TEC, a 2-step model has been developed and applied.

- Step I (devolatilisation phase):
  - input data: complete elemental fuel composition (taken from the fuel analyses of the SciToBiCom fuels applied during the lab-scale test runs within Task 5.4) and combustion air
  - reducing gas atmosphere (□<1) according to the lab-scale tests performed within Task 5.4 (□ determined for the volatilisation and charcoal gasification phase)
  - evaluation of the release data at 700°C since the lab-scale reactor tests performed within Task 5.4 have shown that this temperature seems to be a good approximation for an average temperature during the volatilisation phase

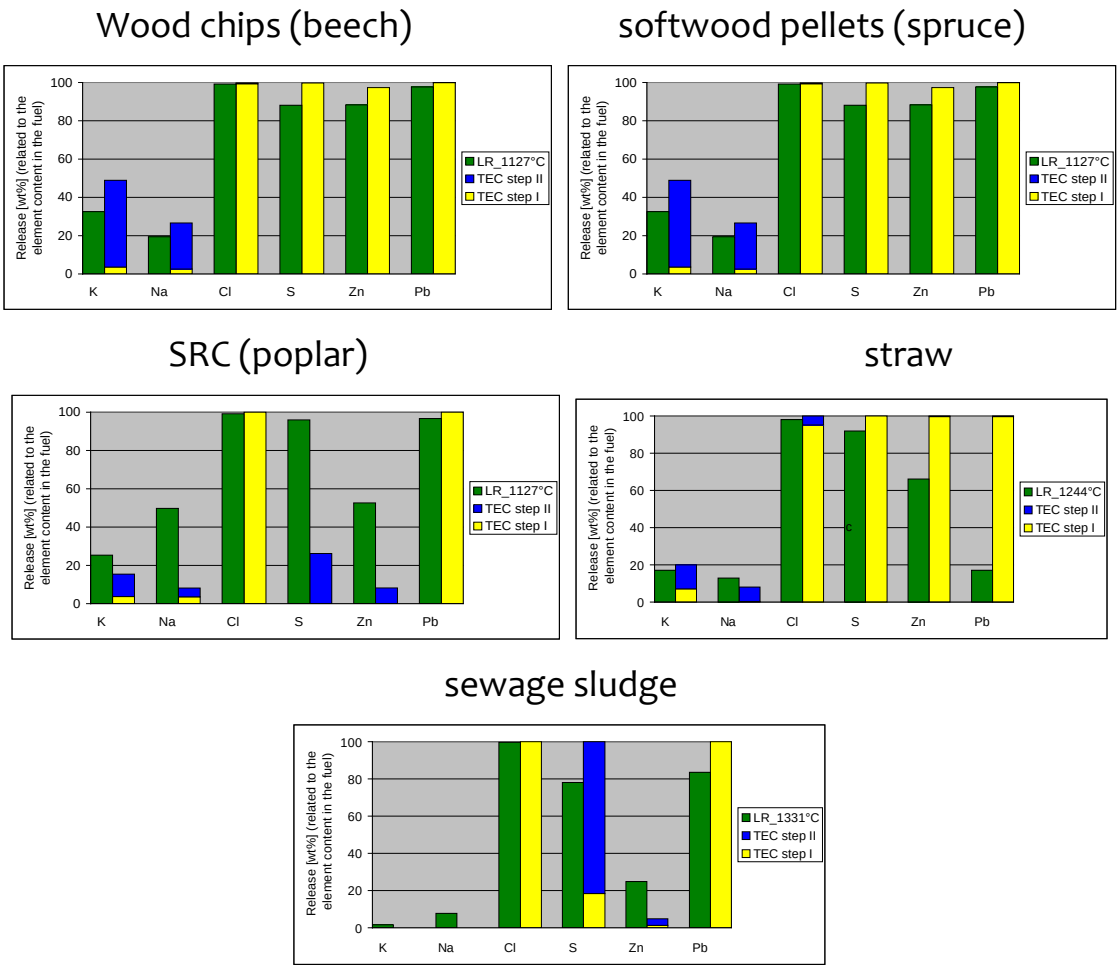

Figure 3-8: Comparison of element release data gained from TEC with results from the lab-scale reactor tests performed within WP5.

Explanations: LR … lab-scale reactor tests
wood chips (beech): step I: λ=0.89; step II: λ=1.71; LR_1127°C: release from LR (maximum bed temperature)
softwood pellets (spruce): step I: λ=0.70; step II: λ=1.26; LR_1301°C: release from LR (maximum bed temp.)
SRC (poplar): step I: λ=0.90; step II: λ=2.25; LR_1087°C: release from LR (maximum bed temperature)
straw: step I: λ=0.74; step II: λ=1.46; LR_1244°C: release from LR (maximum bed temperature)
sewage sludge: step I: λ=0.56; step II: λ=1.92; LR_1331°C: release from LR (maximum bed temperature) .

- Step II (charcoal combustion):
  - input: solid residues from step 1 (ash forming matter and charcoal) whereas the charcoal is assumed to be pure C and amounts to 15 wt% of the initial organic dry matter
  - oxidising gas atmosphere (□>1) according to the lab-scale tests performed within Task 5.4 (□ determined for the charcoal combustion phase)
  - evaluation of the release data at the maximum temperature measured during the lab-scale reactor tests performed within Task 5.4
- The total release of the elements considered is calculated as the sum of the release during step I and step II. The same model was applied for all calculation cases.

Moreover, as a consequence of another finding of the TEC performed so far, Al_2O_3 was excluded from the SLAGH solution in order to avoid an unrealistic overestimation of the slag stability at lower temperatures (up to 700°C).

In Figure 3-8, the element release ratios resulting from the calculations for wood chips (beech), wood pellets (softwood), SRC (poplar), straw and sewage sludge are compared with results from the lab-scale reactor test runs. Thereby, the element release calculated during step I and step II is displayed separately.

Regarding wood chips (beech) and SRC (poplar) K is mainly released as KOH and K within step I, whereas in step II it starts intensively to release at higher temperatures (beech: above 1,000°C / poplar: 1,200°C), mostly as gaseous K, K_2SO_4 and KO. For wood pellets (spruce) the K-behavior is similar to beech and poplar with a significant release during step II which starts at approx. 1,200°C as K (g) and KCl (g). For straw on the other side K is released within step I as KCl. Also during step II KCl is the dominating K-compound released. For sewage sludge K-release is generally very low what can be explained with nearly complete enclosure of the available K in the solid phase $KAlSi_2O_6$. While the TEC-results for sewage sludge and straw match well with the experimental data TEC predicts too high K-release ratios for wood chips and softwood pellets and too low K-release for SRC (poplar).

For Na about the same behaviour can be revealed from the TEC results as for K. For the wood fuels Na is released as NaOH (g) and Na (g) within step I and in higher amounts as NaOH and NaCl within step II. For straw Na is released as NaCl almost exclusively during step II. For sewage sludge the Na-release is very low in both steps which can be explained with the almost complete embedding of Na in the solid phase $NaAlSi_3O_8$. Compared with the experimental data for softwood

pellets, beech wood chips, straw and sewage sludge an acceptable agreement is achieved while TEC strongly underestimates the Na-release for poplar.

For all fuels investigated a good agreement between the calculated and the experimental Cl release could be achieved. The same is also true for Pb with the exception straw, where the Pb-release is strongly overestimated. For the S release on the other side good agreement for beech, softwood pellets and straw exists while TEC for SRC (poplar) significantly underestimated and for sewage sludge overestimate the release.

As it is generally known, Zn release in fixed-bed systems takes mainly place under reducing conditions, which is reflected by the results for beech, softwood pellets (spruce) and straw, where the release is mainly attributed to step I. However, for SRC (poplar) and sewage sludge by far too low and for straw too high release rates are predicted.

The comparison of the results gained from TEC with the experimental data shows that TEC is presently not suitable to model the release behaviour of ash forming elements correctly. This is most probably due to the combination of complex release mechanisms with adsorption and reaction mechanisms in the fuel bed respectively in the fuel particle. Moreover, it has to be mentioned that there is still a lack for reliable thermodynamic database values, especially concerning P-phases, which is of special relevance for P-rich fuels like sewage sludge. Moreover, the K-Si-Al-interactions do not get described correctly with TEC.

Prediction of the ash melting behaviour

As a second approach a TEC-model to predict the melting behaviour of biomass ashes has been developed and evaluated. Regarding the software as well as the databases applied, the same approach as for the release modelling was chosen. As input data the results of chemical analyses of the ashes gained from the SciToBiCom fuels by ashing them at 550°C under oxidising atmosphere have been taken. The calculations have been performed for oxidising gas atmosphere as well as atmospheric pressure. The temperature range investigated was between 500°C and 1,600°C.

The results of the TEC were compared with results from the standard ash melting test according to DIN 51730. The temperature at which 30 wt% of molten fraction occur according to TEC (T_{30}) was used as an indicator for the deformation temperature and the temperature at which 70% of the ash is molten (T_{70}) was used as an indicator for the flow temperature.

An in-depth analyses of the TEC results has revealed that a realistic prediction of the characteristic melting temperatures primarily depends on a reliable quantification of the molten solution phases SLAGH and SALTF over the temperature range of interest. The calculations showed that the assessment of these two phases was strongly influenced by the amounts of Al, Si and K in the ashes. By means of empirically estimated limits for the characteristic molar ratios of (Si+K+P)/(Ca+Mg), K/(Si+P) and Al/Si, it was possible to create an optimization method for the application of TEC which is summarized in the following.

The Si-reactivity (i.e. fraction of initial Si amount entering the calculation) was related to the molar ratio (Si+K+P)/(Ca+Mg). For ashes with values <0.94 a Si-reactivity of 10% was assumed. This primarily applies for pure wood ashes where the inclusion of typically sand-like contaminants combined with the low ash content of the corresponding fuels causes a significant share of the Si to be less reactive. This inert Si-fraction (approx. 90%) is supposed not to take place in the ash melting processes and thus an overestimation of slag formation can be avoided. For all other non-wood ashes the Si-reactivity was defined to be 100%, because the corresponding fuels exhibited high ash concentrations, making the Si fraction coming from external contaminants (e.g. sand, stones) of minor relevance.

Moreover, it is well known that the presently available thermodynamic data lead to a significant overestimation of slag formation for mixtures with low Al_2O_3 contents, especially at the lower end of the temperature range investigated. Therefore, based on the evaluation of a considerable number of calculations performed, Al_2O_3 was excluded from SLAGH in all calculation cases with a molar Al/Si ratio <0.2 in order to avoid these unrealistic slag formation predictions.

The molar K/(Si+P) ratio was used as determining criterion if the molten salt solution SALTF was used in the TEC model. For all ashes with molar K/(Si+P) ratios >1 SALTF was eliminated from the TEC model in order to avoid an overestimation of the SALTF phase (mainly composed of K-carbonates/sulfates) connected with an unrealistic drop of the melting temperatures estimated.

Figure 3-9 shows the trends of the percentage of molten fractions over temperature for the SciToBiCom fuels investigated. The melting curves presented, have been used for the estimation of the characteristic melting temperatures T_{15}, T_{30} and T_{70}.

It can be seen that all wood ashes (including bark ash) with the exception of waste wood showed a similar behaviour with a rather flat increase of molten phases over temperature. T_{70} is not reached within the temperature range

investigated. It is also worth to be mentioned, that for bark and softwood ash a low amount of molten phases even at 500°C already exists which is mainly due to the presence of SLAGH (mainly consisting of K, Al, Ca and Na-oxides). This molten phase is also stable at temperatures below 500°C. For waste wood a steep increase of the amount of molten fraction between 1,200 and 1,400°C can be seen and T70 is reached at about 1,320°C.

The decrease of the percentage of molten phases above 1,300°C observed in case of beech and poplar ash is attributed to the decomposition of the molten K_2CO_3, which is here the predominant molten phase, followed by evaporation of gaseous potassium components (K, K_2SO_4 and KO). For the ashes from bark, softwood and waste wood SALGH was the main molten phase with increasing amounts up to 1,400°C and leveling off afterwards. The untypical drop of the melting curve of softwood ash at 1,450°C can only be explained with the insufficiency of thermodynamic data for the equilibrium components at this temperature.

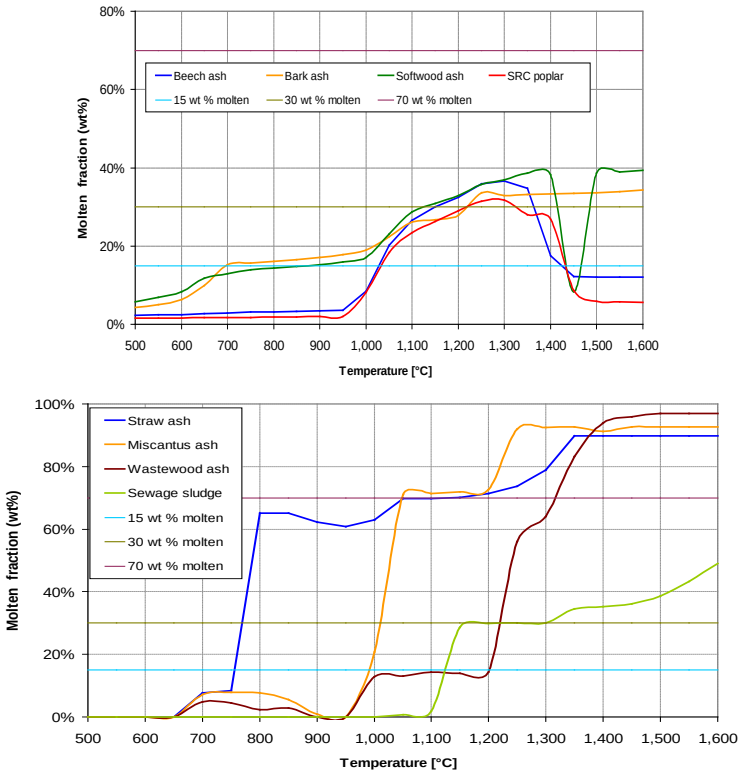

Figure 3-9: Calculated amount of molten fractions for the SciToBiCom fuel ashes according to TEC.

For non-wood ashes (straw, miscanthus) a strong propensity to slag formation between 750°C and 1,050°C was observed. This is in good agreement with literature findings as well as experimental results and can most likely be explained with the enhanced element ratio (Si+K+P)/(Ca+Mg) (mol/mol) in comparison to wood fuels which promotes slag formation.

The results of the TEC regarding the characteristic ash melting temperatures (T_{15}, T_{30} and T_{70}) for all ashes investigated as well as the experimental data obtained by STA (WP5) and the standard ash melting test according to DIN 51730 are summarized in Table 3-2.

		Straw ash	Miscanthus ash	Beech ash	Bark ash	Softwood ash	SRC poplar ash	Waste wood ash	Sewage sludge ash
Melting temp. T_{15} / TEC	°C	760	990	1050	710	890	1040	1200	1130
Melting temp. T_{30} / TEC	°C	770	1010	1150-1370	1230	1130-1420	1220 - 1330	1220	1180
Melting temp. T_{70} / TEC	°C	1160	1050	> 1600	> 1600	> 1600	> 1600	1320	> 1600
Melting Peaks / DSC	°C	900 - 1200	~ 850	> 1300	> 1300	> 1300	> 1300	850 - 1250	~1130
Deformation temperature acc. to DIN 51730	°C	850	820	1380	1310	1390	1390	1230	1080
Flow temperature acc. to DIN 51730	°C	1160	1070	1490	> 1500	1440	> 1500	1260	1260

Table 3-2: Comparison of relevant ash melting data achieved by TEC, STA and the standard ash melting test. Explanations: TEC … results from thermodynamic equilibrium calculations; DSC … results from the STA runs performed in Task 5.3.

In order to estimate the best evaluation method based on TEC that can reliably predict the deformation temperature (DT) according to DIN 51730, in a first step the theoretically evaluated temperatures T_{15} (at which 15 wt% of the overall ash is molten) have been compared with the experimentally measured data. Calculation results for the ashes of straw, waste wood and sewage sludge showed an acceptable match between T_{15} and DT. But particularly in case of pure wood ashes this agreement was not satisfying enough, i.e. T_{15} was too low. In a second step the deformation temperature was related to T_{30} (the temperature where an amount of 30 wt% of melt is formed). Following this way it was possible to improve the DT prediction for the bulk of ashes studied. For the ashes from straw, bark, waste wood and sewage sludge, the difference between the experimentally determined DT according to the standard test method and the corresponding calculated temperatures T_{30} ranges from 10°C to 120°C. Regarding T_{30}, beech, softwood and poplar ash showed no distinct value, but a temperature range (1,150-1,370°C, 1,130-1,420°C and 1,220-1,330°C respectively). In such cases the

upper end of the melting range should be taken as reference for the estimation of T_{30}. Only in case of miscanthus ash the difference between prediction (T_{30}) and experiment (DT) was higher than expected and amounted to 190°C.

The flow temperatures measured according to the standard ash melting test (DIN 51730) showed in general a good agreement with the TEC fusion temperatures at 70 wt% of molten fraction (T_{70}) for straw, miscanthus, beech, bark, poplar and waste wood ash. In case of softwood and sewage sludge ash, the T_{70} temperature seemed to be over-predicted compared to experimentally determined flow temperatures. Regarding the sewage sludge ash, the reason therefore could be a lack of correct thermodynamic data for P-rich phases. In the case of softwood and beech ash TEC shows a rather constant composition of the different phases at temperatures >1,500°C. Obviously, the model applied is not suitable to predict the melting process for this type of ashes at high temperatures correctly.

3.3 Task 2.3: Aerosol Formation

To assist the work packages related to deposition and corrosion in grate-fired and pulverized fuel fired systems and in gasification, S/Cl/K transformations in thermal processes has been characterized. The release of the elements S, Cl, and K from biomass combustion has been quantified as a function of fuel composition and temperature. A detailed chemical kinetic model for the gas-phase transformations of S, Cl, and K, emphasizing sulfation of KCl, has been validated against measurements from flames. A simplified aerosol formation model has been developed, based on aerosol theory, and sulfation of particulate KCl has been quantified and modeled.

In recent years, also the understanding of the mechanisms responsible for submicron particle formation has increased, based on studies of the release of inorganic elements from annual biomass crops and wood, gas-phase conversion of K/S/Cl, and formation of alkali sulfate aerosols. While this work has contributed to a better understanding of issues related to particulate matter, there is still uncertainty about the sulfation mechanism and the implications of fuel composition and combustion conditions are still not fully addressed.
The purpose of this task is to develop a simplified model for formation of aerosols for use in CFD. The proposed work will involve the following activities:

- Development of a simplified model for release of the elements S, Cl, and K/Na from biomass combustion as function of fuel composition and temperature. The model will be based on previous release experiments performed at DTU.
- Laboratory experiments on sulfation of KCl
- Development of a simplified model for the fate of S, Cl and alkali elements in the freeboard, based on earlier work at DTU
- Development of simplified model for aerosol formation for use in CFD

In the following the results of each subtask are described. Most of the results have been or are in the process of being published as articles and the present report provides only an abbreviated presentation.

Release of the elements S, Cl, and K/Na from biomass combustion

Currently, a broad variety of biomass sources are being utilized for heat and power production, mostly in small-scale (< 30 MW_{th}) dedicated grate-fired plants. This includes stemwood-based assortments as well as other novel fuels, commonly known as 'opportunity sources'. The novel biofuel types include energy crops (e.g., short rotation coppice, perennial grasses and herbaceous species), which are foreseen as an opportunity to overcome fossil fuel disadvantages and increasing energy demands. The use of the novel fuels results into a broad variety of properties influenced by the biofuel production related factors. The latter includes genotype, growth conditions attributed to geographical origin, soil and climate characteristics, and cultivation (e.g., fertilizers and pesticides), as well as harvest time and procedure, fuel handling (i.e., collection, transport and storage), pre-treatment (i.e., particle size reduction and drying), and densification processes (e.g., pellets and briquettes production). The aforementioned factors influence the biofuel chemical composition with respect to proximate, ultimate and ash matter compositions.

The incombustible fraction (ash) in biofuels may be retained in the fuel bed or may be vaporized (released) from the fuel bed to the gas phase during thermal conversion of biofuels. Slagging, fouling, corrosion and erosion, as well as aerosols and acidic pollutants formation are some of the potential problems associated to the incombustible material affecting the reliability level of conversion plants (see [7]). Because of the recent incorporation of the opportunity biofuels into the energy sector, the knowledge of ash chemistry and partitioning of the major ash-forming elements during thermochemical conversion is limited for energy crops. Therefore, gaining specific knowledge concerning the ash chemistry and factors influencing how the troublesome

elements existing in the novel fuels interact will provide valuable information on operation and design features of combustion systems.

In this Task, we combine novel data for the release of K, Cl, S, and P to the gas phase during combustion of two pelletized energy crops (a herbaceous biomass, *Brassica carinata*, and a short rotation coppice, *Populus sp.*) with release data obtained earlier at DTU from agricultural residues and perennial wood in order to assess factors influencing the conversion of K, Cl, S and P, but also to gain knowledge based on a more general ash composition perspective.

Fuel characterization

Figure 3-10 show the main properties of the selected fuels. Despite a significant variation in ash content among the fuels considered (i.e., from 0.5 wt%, d.b. in beech up to 10 wt%, d.b. in brassica), the majority of the samples can be characterized as ash rich fuels. In Figures 3-15-b and -c, the relative molar content of alkalis (dominated by K and Ca), Si and P in the fuels is compared in two ternary diagrams. Three fuel categories can be identified, i.e., Group A, Group B and Group C. As is shown in Figure 3.15-b, these groups all have high content of alkalis (K+Na+Ca+Mg) and Si, compared to P. Group A exhibits between 25-50 molar % of Si, and around 50-75 molar % of alkalis. Group B contains fuels with around 10-25 molar % of Si, and 75-90 molar % of alkalis. Finally, Group C includes fuels with < 10% Si, (see Figure 3.15-b) and 90-100 molar % of alkalis. Comparison of alkalis distribution is shown in Figure 1-c. As seen, Group A is characterized by alkaline earth content (Ca+Mg) around 10-30%, the lowest proportion among fuels. In the other two groups, their proportion is larger than 30%, even richer than 70% particularly to bark in Group B. Regarding the volatile elements S and Cl, Group A shown the highest contents (see Figure 2.0.1-a). The amount of S in poplar (Group B) was larger than the one expected due to the use of lignosulfonate during the densification process.

Experimental

The brassica and the poplar used in this study were both cultivated and pelletized in Spain. Biomass raw materials used in the pelletizing process consisted of brassica straw (grains included) and poplar stem (branches, leaves and bark were not included). Pellets had a diameter of 6 mm and a length of 15–20 mm.

A laboratory-scale fixed-bed reactor was used to conduct release experiments under combustion conditions (i.e., an initial pyrolysis stage in N_2, followed by oxidizing conditions), between 500 °C and 1100 °C. The facility, which included a

gas mixing system, a two-zone electrically heated horizontal tube reactor, a gas conditioning system (cooling and filtration), standard gas analyzers for O_2, CO, CO_2, NO and SO_2, two thermocouples placed inside the reactor, and a data acquisition system, facilitated release experiments under well-controlled conditions in the reactor (see [1]).

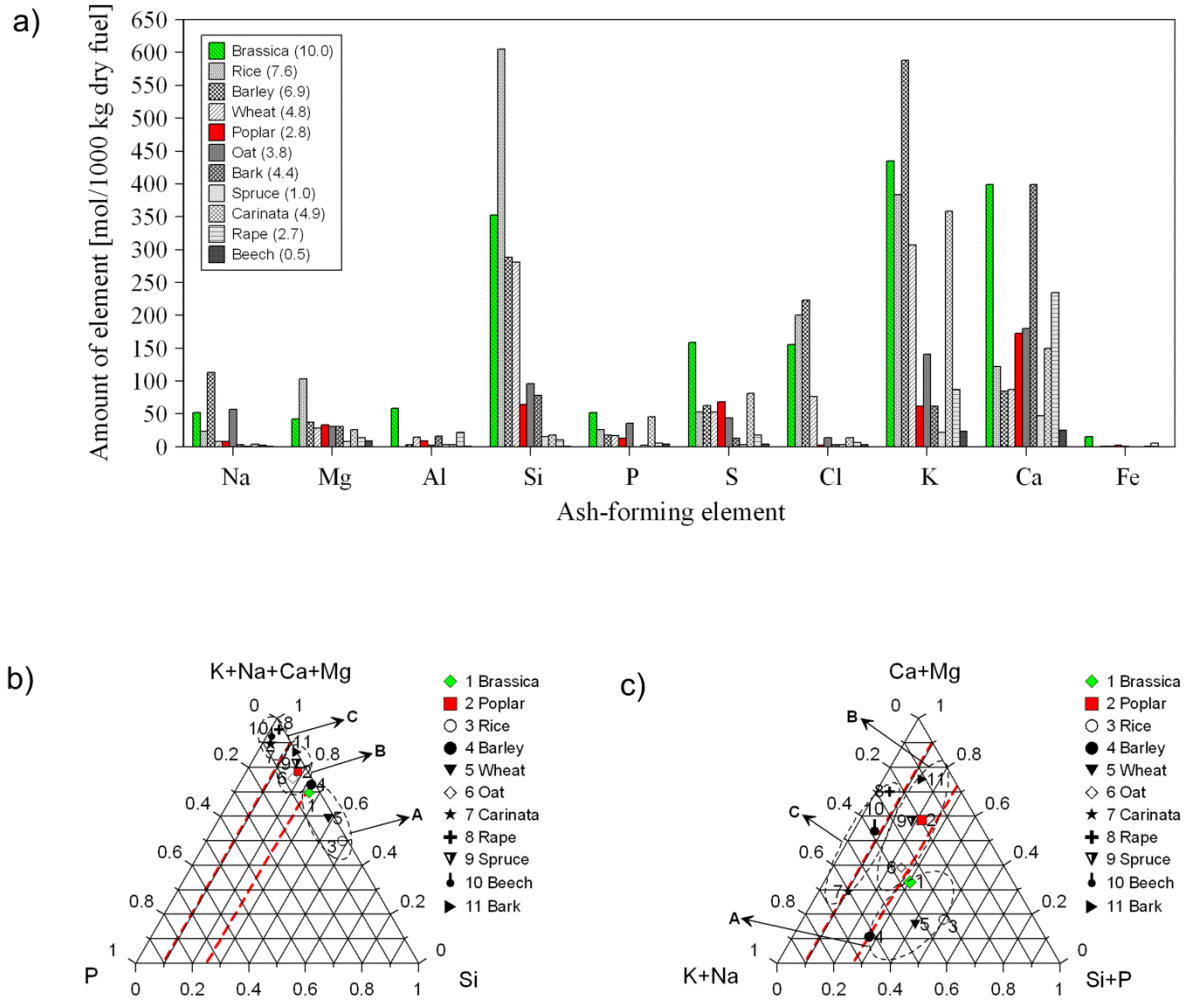

Figure 3-10: Proportion of main ash-forming elements in the fuel samples. Data for agricultural residues and perennial woody fuels were obtained from references [13, 14]. Figure (a) Amount of ash-forming elements is given as mol of element in dry matter of fuel. Values in parenthesis represents the amount of ash given in weight percent dry base (wt%, d.b.) corresponding to the fuel "i". Figures (b) and (c) Alkalis, P and Si relative molar concentration in fuels. Contents in X, Y and Z axis are given in molar fractions and normalized to 100%.

The release quantification method applied in this study was similar to the ones developed at DTU by van Lith *et al.* (method A) and Knudsen *et al.* (see [1]), at combustion conditions that resemble those of the fuel-bed of a grate-fired plant. To avoid ash-forming elements reacting with the crucible material, a crucible made of a Pt/Au (95/5 wt%) alloy was applied. After complete burnout, the amount of residual ash was quantified and chemically characterized. The total amount of fuel sample used to the release experiments is shown in Table 1. After each experiment, the solid residue in the Pt/Au crucible was weighed, manually removed, and saved for chemical analysis. The concentrations of the inorganic elements in both the fuel sample and the residual ash collected from the crucible were determined by an Inductively Coupled Plasma-Optical Emission Spectroscopy (ICP-OES) technique. The chemical composition of the residual ash was also analyzed semi-quantitatively by means of Scanning Electron Microscopy (SEM), equipped with Energy Dispersive Spectroscopy (EDS), and, finally, assessed qualitatively with Powder X-Ray Diffraction (P-XRD) to gain information about the presence of crystalline phases in the samples.

Results

The release of K, Cl, and S as a function of temperature for the selected fuels is presented in Figure 3-15. Data for the novel fuels are depicted, side-by-side with release data for other biofuels (within A, B and C groups) obtained in earlier work. The release of inorganic elements depends on the fuel composition. Further, the reaction paths and the final level of release of ash-forming elements are dependent on the local environment in the combustion unit. The experimental data gained within this work are analyzed in terms of fuel categorization (i.e., groups A, B and C). The reaction paths and elemental speciation are discussed based on chemical characterization of solid residues and release of ash-forming elements, as well as on literature results. Generally, the release trend for the elements was similar among fuels within each group, but differed among A, B and C groups.

According to Figure 3-11a, the release of K was insignificant up to 700 °C, while it gradually increased at higher temperatures. Regarding the two tested energy crops, at 1100 °C around 60% and 40% of K was released for brassica and poplar, respectively. In general, a rising temperature significantly increased the K-release for Group C fuels, whereas it was less notorious for A and B groups.

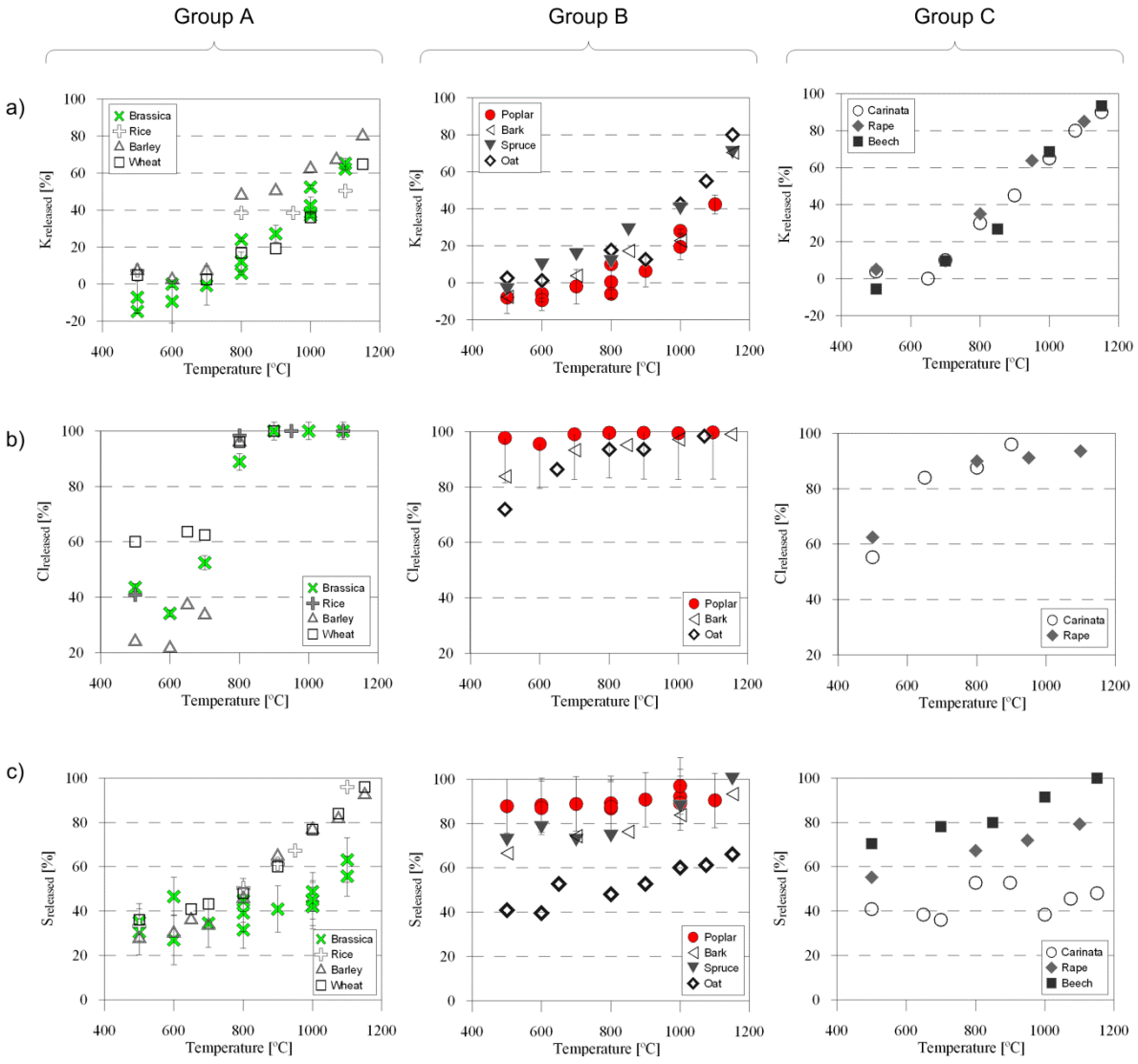

Figure 3-11: Percentage of K, Cl and S from the fuel bed to the gas phase as a function of the combustion temperature for the tested fuels and data from references. Uncertainties are shown for the energy crops experiments.

Data from chemical fractionation indicate that 80-90% of the K content in biomass fuels occurs in the form of easily mobile species. Based on the experimental results, the relative molar ratios Cl/K, K/(2S), S/Ca, and K/(2S+Cl) based on the original fuel matrix composition were assessed for all the biofuels (see [7]). These ratios were selected because they are considered as useful tools to understand the ash behavior and elemental release tendencies among groups. The concentration of K relative to (2S+Cl) is generally larger than one. Comparison of data from Figures 3.11-a, -b and –c below 700 °C suggest dechlorination and desulfurization in absence of K-release, further increasing the

K/(2S+Cl) ratio. The surplus of K with respect to Cl and S suggests that other chemical forms of K were available in the ash, presumably carbonates. Above 700 °C, the release of K significantly increased for each fuel group, as shown in Figure 3-11a, accompanied by relative losses of Cl and S (see Figures 3-11b and 3–11c, respectively) in the temperature range 700-1100 °C. The metal chloride vapor pressure becomes significant between 700 °C and 800 °C, thereby facilitating K-sublimation. Solid K-carbonates are stable until their decomposition at temperatures over 850 °C. Concerning alkali sulfates, they are expected to be released at considerably high temperatures. A surplus of K might cause interactions among silicates and K, resulting in partial retention of the alkali metal.

In contrast to K, Cl was almost completely released below 700 °C, for fuels within groups B and C. For Group A, the Cl release was relatively low at these temperatures. Complete release of Cl was observed for nearly all the fuels within the three groups above 700 °C. Chemical fractionation studies indicate that Cl is largely present as water soluble components or loosely bound to organic exchange sites (ion exchangeable matter). Both inorganic and organic forms of Cl are very reactive and susceptible to vaporization. Nevertheless, only minor amounts of Cl are expected to be released from organic structures because the water soluble forms are the predominant fraction in most biofuels. As mentioned in the preceding section, the salt of this element, i.e., KCl(s), is vaporized in the interval 700-800 °C. Consequently, the Cl-release at low temperature can be attributed to interactions of KCl with the organic fuel matrix, releasing Cl as HCl or CH_3Cl. Since the release pattern for Cl among the fuels differed quite a lot below 800 °C, also within groups, it is likely that the Cl-release is affected by factors related to the composition of the organic matrix. It has been proposed that the availability of proton-donating sites (e.g., H_2O molecule, carboxylic or phenolic groups) govern interactions among the inorganic Cl and the organic groups and thereby limit the low-temperature release of Cl. This is supported by the results of Figure 3-10, showing that the fuels of Group A, characterized by the highest Cl content, generally exhibit the smallest release of Cl below 700 °C. The Cl-rich Group A fuels also yielded a high ash and alkaline earth metal contents. Above 700 °C, the Cl-release can be largely attributed to metal chloride sublimation.

According to Figure 2.0.2-c, the S-release was significant for all the biofuels, ranging from 40% up to nearly 100%, at temperatures below 800 °C. The release of S from poplar was almost 100% even at 500 °C. For brassica, it gradually increased

from 30% up to about 60%, in the temperature range 500-1100 °C. In general, the largest S-losses were observed for Group B fuels, in the entire temperature range, i.e., 500-1100 °C. However, significant differences in the S-release were observed within each fuel group. The loss of S below 500 °C can be attributed to devolatilization of organically associated S in the fuel. Therefore, differences in the relative amount of S released, at low temperature, are most likely related to organic and inorganic proportions of S. Reactions of organic S with Ca or K may retain S as sulfates, i.e. K_2SO_4 or $CaSO_4$. The sulfates may decompose at temperatures exceeding 900 °C. For Si-rich fuels, release of S may occur at lower temperature as consequence of silicates and alkali interactions, but this reaction is limited compared to salt sublimation or decomposition according to experimental data.

Sulfation of particulate KCl.

The sulphation of particulate alkali chlorides proceeds as a gas-solid reaction that may involve SO_2 or SO_3:

$$2KCl(s) + SO_2 + \tfrac{1}{2}O_2 + H_2O \rightarrow K_2SO_4 + 2HCl \quad (1)$$
$$2KCl(s) + SO_3 + H_2O \rightarrow K_2SO_4 + 2HCl \quad (2)$$

These reactions are believed to be slower than the homogeneous sulphation occurring in the gas-phase (see [8]). Presumably the in-flight sulphation of particulate KCl is limited in a furnace where the residence time in suspension is of the order of a few seconds, but little is known. There are only few reported experiments on sulphation of solid alkali chlorides (NaCl(s), KCl(s), and $CaCl_2$ (s)), mostly obtained for SO_2 concentrations of 3000 ppm and larger; i.e., considerably above the levels typically found in combustion systems. For this reason, rate coefficients may not extrapolate well to practical conditions. The objective of Task 2-3 is to study the sulphation of particulate KCl by SO_2 in the temperature range 673-1023 K and with reactant concentrations representative of combustion of biomass and waste.

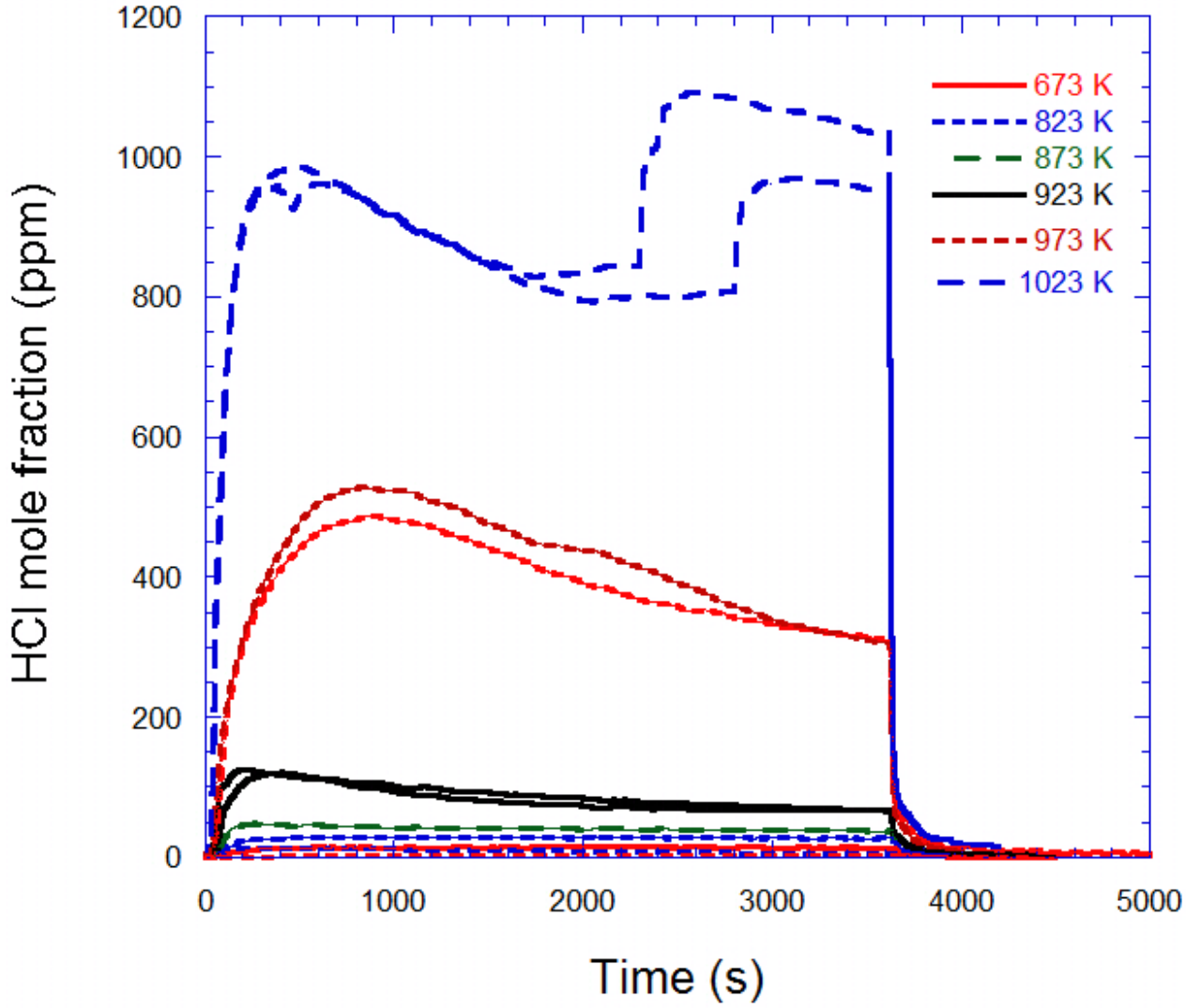

Figure 3-12: Measured HCl concentrations as a function of temperature and reaction time. Temperature: 673-1073 K; gas composition: 959-965 ppm SO2, 4.8% O2, 3.9-4.6% H2O, balance N2.

The experiments were conducted in a fixed bed quartz reactor, with solid KCl placed on a porous quartz plate in an isothermal zone. Reactant gases (SO_2, O_2, and H_2O in N_2) were introduced separately into the reactor and mixed just above the porous plate. The product gas was analyzed for HCl and SO_2. Temperature (623-1023 K) and reactant concentrations (500-3000 ppm SO_2, 1-15% O_2, 4-15% H_2O) were varied. The progress of reaction was based on the HCl measurements. Figure 3-12 shows the measured HCl profiles for the different temperatures. The reaction rate was determined as dX/dt, where X is the fractional conversion of KCl.

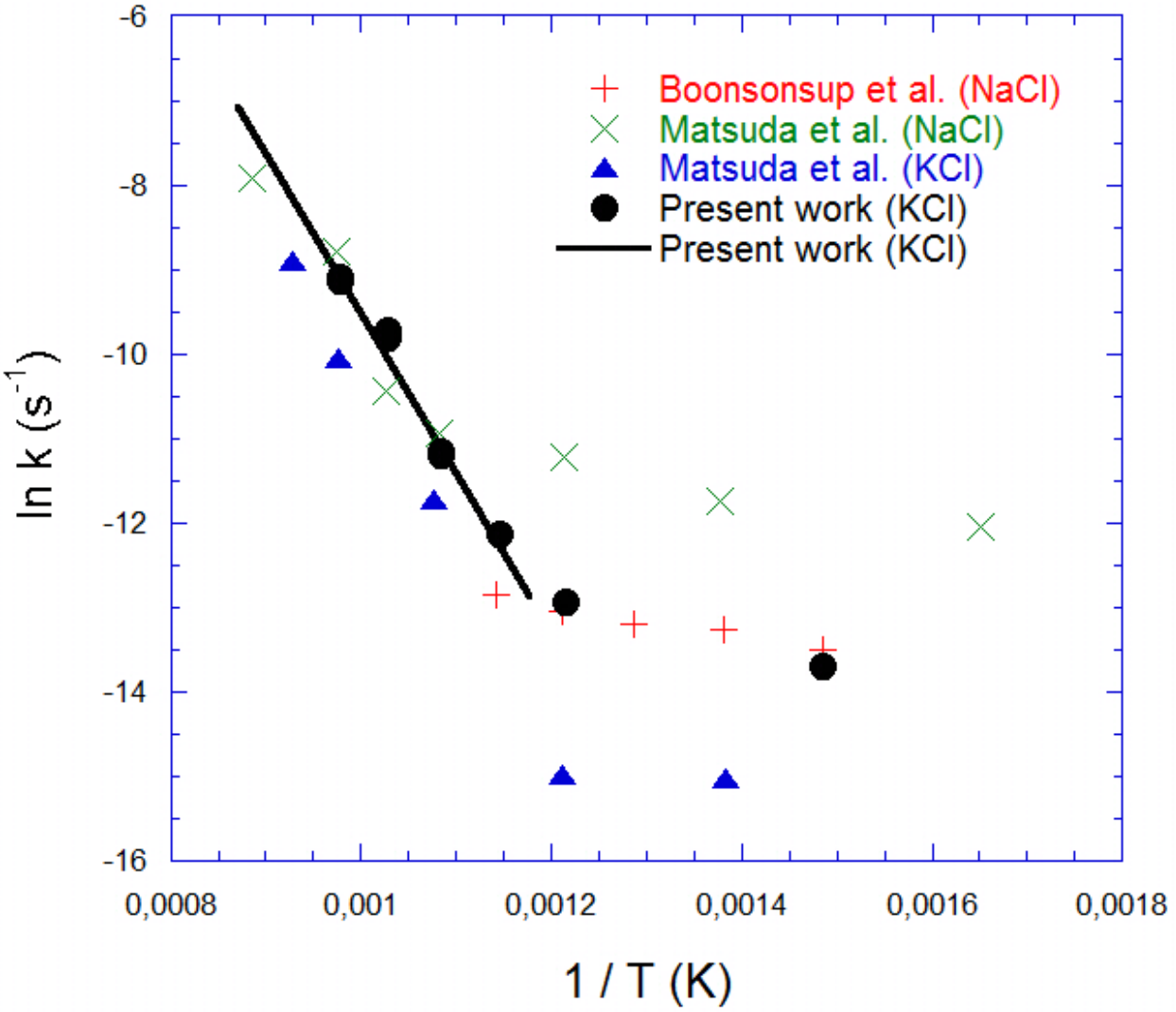

Figure 3-13: Arrhenius plot for the rate constant of sulphation of KCl and NaCl with SO2. Nominal conditions for the comparison: SO2: 9000 ppm; O2: 5.0%; H2O: 10%; N2: balance. Literature data from Boonsongsup et al. for NaCl, and Matsuda et al. for NaCl and KCl. The present data for KCl were obtained at conditions with 959-965 ppm SO2, 4.8% O2, and 3.9-4.6% H2O. To extrapolate to the conditions of the figure, SO2 was corrected for according to the Langmuir-Hinshelwood expression (high temperature) and to $(Y^{SO2})^{0.2}$ (low temperature), respectively, while no corrections were made for O2 and H2O.

At the lowest temperatures, the amount of HCl generated is comparatively small and the reaction rate we derive is more uncertain. Above 900 K, the formation of HCl increases rapidly with temperature. At 1023 K, a second peak in HCl is observed after approximately 2500 s reaction time, indicating a sudden increase in the reaction rate. We attribute this phenomena to a phase transition from a

solid to a melt, possibly due to the formation of an eutectic mixture of KCl and K_2SO_4.

Based on the experimental results and assuming that the reaction proceeds according to a shrinking particle model, the rate of the sulphation reaction can be described by the expression in the temperature range 873-1023 K:

$$dX/dt = 2.7x10^7 exp(-18900/T)(1-X)^{2/3} \times Y_{SO_2})/(1+708Y_{SO_2})x(Y_{O_2})^{0.37}$$

Here, Y_A denotes the mole fraction of A. The model compares well with literature data for sulphation of KCl and NaCl (see Figure 3-13), and comparison of predictions with literature data indicate that it may be applied even at higher SO_2 concentrations and temperatures than those of the present study (see [8]).

Model for the gas-phase interactions of S, Cl and alkali elements.

The gas-phase sulfation of KCl during biomass combustion has implications for operation and emissions: it reduces the rates of deposition and corrosion, it increases the formation of aerosols, and it leads to higher concentrations of HCl and lower concentrations of SO_2 in the gas phase. Rigorously homogeneous systems are required to characterize the gas-phase formation of alkali sulfates. In this Task, we have measured the temperature and gas-phase concentrations of KCl and HCl, and detected the presence of aerosols in the post-flame region of a range of hydrocarbon flames seeded with KCl, with and without the addition of SO_2, and compared the results to modeling predictions, using a detailed chemical kinetic model for gas-phase S/Cl/K interactions.

The chemical composition of biomass leads to a number of challenges, including enhanced levels of submicron aerosol particles, deposits, corrosion, and emissions of harmful gases. These problems arise mainly from the relatively high concentrations of potassium, chlorine and sulfur in herbaceous biomass. These elements are partly released to the gas phase during combustion of the biomass.

Potassium is mainly released as KCl or KOH, chlorine as HCl or KCl, and sulfur as reduced species or as SO_2. These inorganic species are subsequently involved in gas-phase and gas-solid reactions that determine the partitioning of sulfur and

chlorine among SO_2, HCl and alkali salts, but details of the chemical processes involved are unclear.

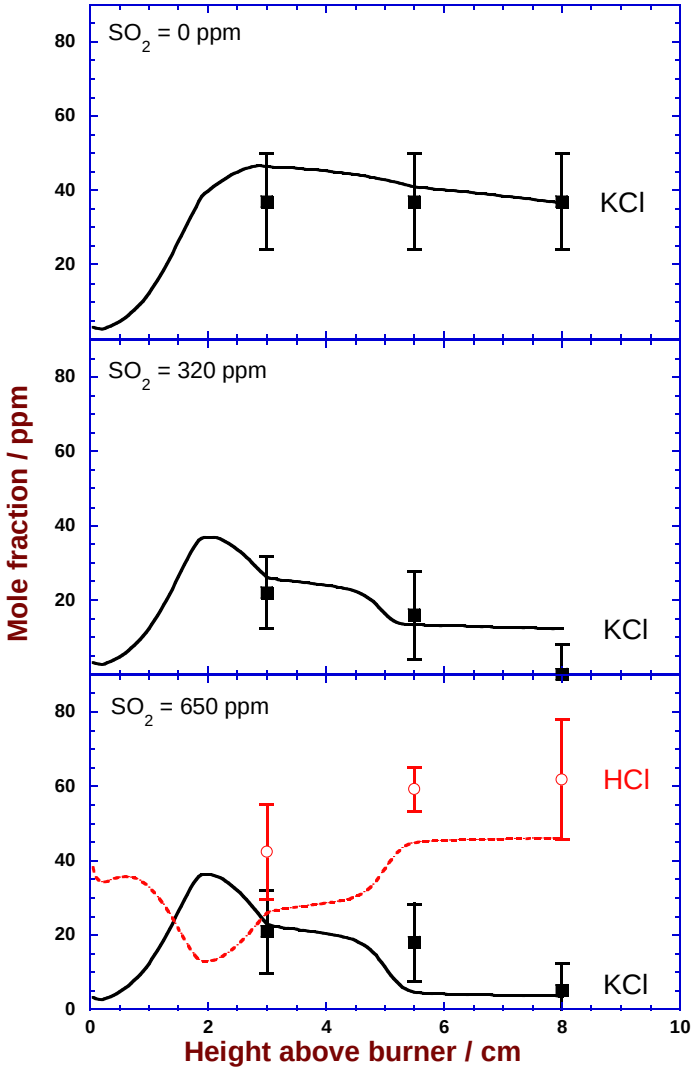

Figure 3-14: KCl and HCl concentration profiles as a function of height above burner and concentration of SO_2 (0, 320, and 650 ppm, fully mixed) for the medium-temperature flame [9]. Experimental data are shown as symbols, while predictions from the model are shown as lines.

High-temperature chlorine corrosion of the superheater tubes is a concern in biomass-fired plants. The superheater temperature should be as high as possible to obtain a high electrical efficiency, and steam temperatures of 800 K or higher are desirable. The presence of alkali chlorides in deposits formed on the superheater surfaces strongly promotes corrosion of the metal, while alkali sulfates are much less corrosive. It is, therefore, essential to reduce the amount of KCl that is deposited onto the tubes. It is believed that alkali sulfates form in both homogeneous and heterogeneous reactions between alkali chlorides (in solid, molten, or gaseous form) and gaseous sulfur oxides (SO_2 or SO_3). Gas-phase sulfation of alkali metals is followed by homogeneous nucleation.

In this task, we focus on the formation of K_2SO_4 in the gas phase. The experiments have been designed to ensure that no wall-based reactions or other heterogeneous reactions contribute to the sulfation of KCl to form K_2SO_4. This has been achieved by using a setup in which the sulfation takes place downstream of a flame in an environment that is free of surfaces. KCl was seeded into a number of small, premixed $CH_4/O_2/N_2$ jet flames. Each jet flame was surrounded by six co-flow holes that supplied N_2, and SO_2 could be seeded into this co-flow. The temperature in the post-flame region was measured, and gas-phase KCl, HCl, and aerosols were detected here, with and without the seeding of SO_2. The results were compared with a kinetic model from previous work [9].

The model used in this study is based on the reaction mechanism proposed by Hindiyarti et al. (see [9]), which describes gas-phase interactions between potassium, chlorine and sulfur. The model has been extended here to include a description of the homogeneous nucleation of K_2SO_4. The S/H/O subset provides a satisfactory description of SO_2 oxidation in the absence of chlorine and alkali metals. The formation of SO_3 proceeds primarily through reaction of SO_2 with O and OH radicals, either directly or through an $HOSO_2$ intermediate. The full mechanism predicts KCl sulfation rates that agree reasonably well with rates observed in laboratory flow reactors and in entrained-flow reactors (see [9]). The main reaction sequence by which it is proposed that K_2SO_4 forms is: $KCl + SO_3 (+M) = (KO_2)S(O)Cl (+M)$ (R1), $(KO_2)S(O)Cl + H_2O = KHSO_4 + HCl$ (R2), and $KHSO_4 + KCl = K_2SO_4 + HCl$ (R3). The chemical kinetic model is combined with the simplified aerosol formation model described below.

Figure 3-14 compares measured and predicted concentrations of KCl and HCl as a function of the height above the burner for both doped and un-doped flames at medium temperatures. The SO_2 levels used correspond to 0, 320 and 650 ppm

after mixing. Presence of SO_2 has a great impact on the concentration profile of KCl. In the absence of SO_2, the level of KCl is independent of height, while 60-100% of the KCl in the post-flame region is consumed in the doped flames. The presence of significant levels of HCl confirms that the loss of KCl is due to sulfation. This is further supported by the detection of aerosol formation (by elastic scattering) [9]; the temperature is too high for homogeneous nucleation of KCl.

The model predicts results that agree well with experimental data, even though it underpredicts slightly the concentration of HCl (Figure 3-14). The model predicts that concentrations of chlorine species other than KCl and HCl are insignificant. The agreement between predictions and experimental observations are satisfactory over the whole range of flames [9].

The developed model, combined with a good understanding of the aerosol formation (see below), makes it possible to improve the designs of biomass boilers to achieve less corrosion of superheaters. It will also be possible to estimate emissions of SO_2, HCl, and submicron particles with higher accuracy. A first attempt to combine the kinetic model for sulfation with an ash deposition model using computational fluid dynamics (CFD) techniques was reported very recently by Garba et al. (see [9]). The model was able to adequately reproduce the deposit position and shape in a 10 MW test furnace, but requires improvements for quantitative predictions.

Simplified model for aerosol formation.

Both KCl and K_2SO_4 formed in the gas phase will condense when they reach a sufficiently high saturation level. The aerosol formation can be predicted from aerosol theory, but it is computationally challenging. In Task 2-4, we have developed a simplified expression for homogeneous nucleation of K_2SO_4. Nucleation of KCl is less important since this component preferentially condenses on existing surfaces, i.e. K_2SO_4 aerosols or fly ash.

For K_2SO_4, a saturation level sufficiently high for homogeneous nucleation in biomass combustion occurs at temperature between 1030 and 1130 K (see [9]). The homogeneous nucleation is followed by a rapid heterogeneous nucleation on the particles that have formed, resulting in the almost instantaneous formation of a K_2SO_4 aerosol. The present model describes the nucleation process by a simplified, irreversible first-order reaction:

$$K_2SO_4 \rightarrow K_2SO_4 \text{ (aerosol)}$$

This makes it simple to implement the loss of gas-phase K_2SO_4 in a full chemical kinetic model or in CFD. The simplified reaction describes both the homogeneous nucleation and the subsequent heterogeneous condensation. The rate constant for the nucleation reaction, $k_{nucleation} = 1 \times 10^{-61} \exp(150000/T)\ s^{-1}$, has been derived from aerosol theory (see [9]), and describes a very fast rate in the relevant temperature range. It should be emphasized that the rate constant can only be used in a limited temperature window and cannot be extrapolated to temperatures below 900 K. This expression is used in the calculations shown in Task 2-3.

References:

1. Daniel Lindberg, Rainer Backman , Patrice Chartrand Thermodynamic evaluation and optimization of the (Na_2CO_3 + Na_2SO_4 + Na_2S + K_2CO_3 + K_2SO_4 + K_2S) system, The Journal of Chemical Thermodynamics, **39(6)**, 2007, Pages 942–96
2. Daniel Lindberg, Rainer Backman, Patrice Chartrand, Mikko Hupa, Towards a comprehensive thermodynamic database for ash-forming elements in biomass and waste combustion — Current situation and future developments, Fuel Processing Technology, Available online 28 September 2011, In Press, Corrected Proof
3. Daniel Lindberg,Rainer Backmana, Patrice Chartrand, Thermodynamic evaluation and optimization of the (NaCl + Na_2SO_4 + Na_2CO_3 + KCl + K_2SO_4 + K_2CO_3) system, The Journal of Chemical Thermodynamics, **39(7)**, 2007, Pages 1001–1021.
4. Daniel Lindberg, Report 07-03, Thermochemistry and melting properties of alkali salt mixtures in black liquor conversion processes, 2007, Academic dissertation, Åbo Akademi University, ISBN 978-952-12-1886-6.
5. Christian Robelin, Patrice Chartrand, Thermodynamic evaluation and optimization of the (NaCl + KCl + $MgCl_2$ + $CaCl_2$ + $ZnCl_2$) system, The Journal of Chemical Thermodynamics, **43(3)**, 2011, Pages 377–391.
6. Appearance of trace metals in co-firing fuels, Maria Zevenhoven, Rainer Backman, Bengt-Johan Skrifvars and Mikko Hupa, Proceedings of the 18th International FBC conference, Toronto , Canada, 2005

7. M. Díaz-Ramírez, F. Frandsen, P. Glarborg, F. Sebastián and J. Royo, ”Factors Controlling the Partitioning of K, S, P and Cl during Opportunity Fuel Combustion”, submitted for publication (2012).

8. L.W. Sengeløv, T.B. Hansen, C. Bartholomé, K.H. Pedersen, F.J. Frandsen, A.D. Jensen, P. Glarborg, “Sulphation of condensed potassium chloride by SO_2”, submitted for publication (2012)
9. B. Li, Z. Sun, Z. Li, M. Aldén, J.G. Jakobsen, S. Hansen, P. Glarborg; “Post-flame gas-phase sulfation of potassium chloride”, Combust. Flame, accepted (2012)

4. WP3: Combustors – Technology Dependent Models

By Dr. Robert Scharler, BE2020+

Optimizing and designing thermal conversion processes of solid biomass require understanding and description of the conversion of single fuel particles itself as well as their interaction with the other particles, with gas phase and with the furnace walls in different biomass combustion plants. The conversion steps of biomass, drying, pyrolysis and char conversion occur in sequences for thermally small particles. For thermally large particles the conversion steps may overlap because of intra-particle temperature gradients. Several single particle models applied to CFD, both for thermally small and thermally large particles, have been reported and evaluated in literature. Using single particle models for certain biomass materials require parameters describing the pyrolysis and the char conversion. In this field, much work has been done for pulverized biomass fuels. Determining parameters for thermally large particles is less frequent. In fact, very little work has been done to incorporate thermally large biomass particles into combustion models.

Moreover, experience gained from CFD modeling of biomass combustion plants showed that a number of sub-processes of turbulent reactive multiphase flows are still not sufficiently described to model fluidized bed combustion and grate furnaces with sufficient accuracy. Therefore, within WP3 sub-models were developed, linked and validated in order to enhance the modeling capabilities of CFD codes and to improve their validity and prediction accuracy for biomass grate furnaces (WP 3.1 and WP 3.2) and biomass FBC plants (WP 3.3, 3.4 and 3.5) based on the modelling work in WP 1 and 2 as well as the experimental work in WP 4 and 5.

4.1 Task 3.1: Development of Generic Release Model for Ash Forming Elements and Link with Fixed Bed Combustion Model

One major objective of Task 3.1 was to develop a release model describing the release of ash forming elements from packed beds in dependence of relevant

influencing parameters like stoichiometry, fuel composition and fuel moisture as a basis for CFD modeling of fine particle formation, ash deposit formation and corrosion. It was intended that the release model will be based on thermodynamic equilibrium calculations performed within task 2.2. Here, a 2-step approach for the release of the ash forming elements in the pyrolysis zone and the char burnout zone was developed. An in-house developed 3D packed bed combustion model of BE2020+/TUG was used to provide profiles of particle and flue gas temperatures as well O_2 concentrations along the grate and to locate the pyrolysis and char burnout zone as input parameters for the 2-step ash release model. A simulation for a 20 kW pellet underfeed stoker was performed in order to test this approach (see Figure). In Figure, the results concerning the averaged radial profiles of particle temperatures, O_2 concentrations as well as pyrolysis and char burnout rates at different levels above the grate are shown.

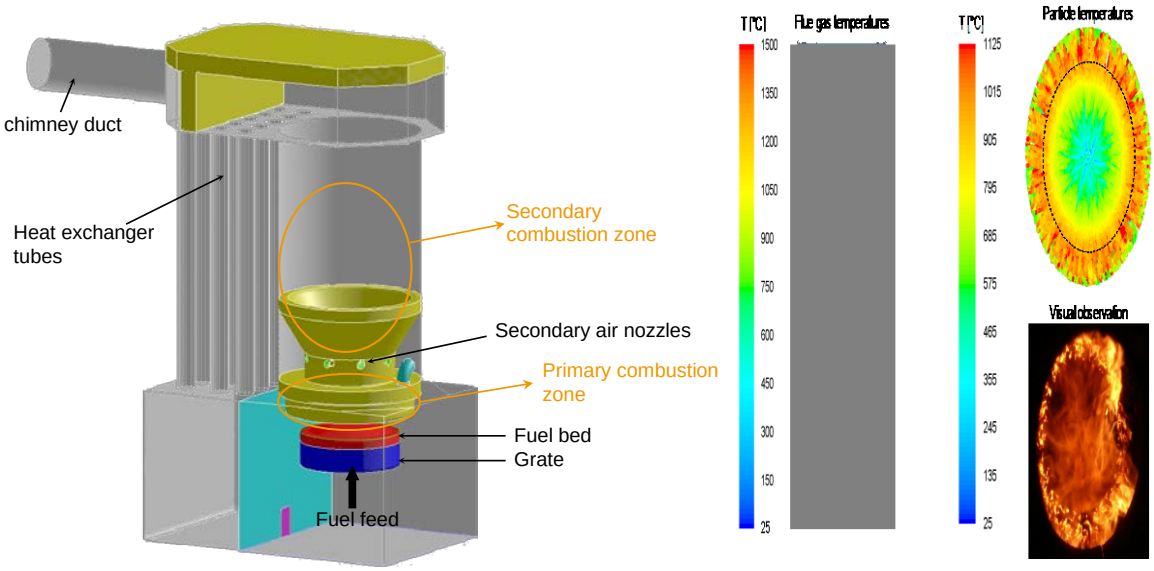

Figure 4-1: CFD model underfeed stoker furnace (left) and packed bed model result (top right) compared with observation (bottom right). Explanations: Operating data: Biomass fuel: softwood pellets; moisture content= 8.12 wt.% (wet base); λ_{total}= 1.58; λ_{prim}= 0. 64, no flue gas recirculation

Since the results of Task 2.2 showed that the approach based on thermodynamic equilibrium calculations is not able to predict the release of ash forming volatiles appropriately which is supposed to be mainly due to secondary reactions of the ash forming elements within the fuel bed, it was finally not linked with the packed bed model. It showed that a prediction of ash release would only be possible by the link with reaction kinetics. However, since they should comprise heterogeneous reactions in the packed bed as well and such data are not

available, this is currently not possible. At the present state, the results from packed bed modeling can be combined with experimental data from WP5 (TGA and lab-scale packed bed experiments). The location of the release stage during pyrolysis and char burnout can be determined by the packed bed model whereas the total release rates have to be taken from the experiments.

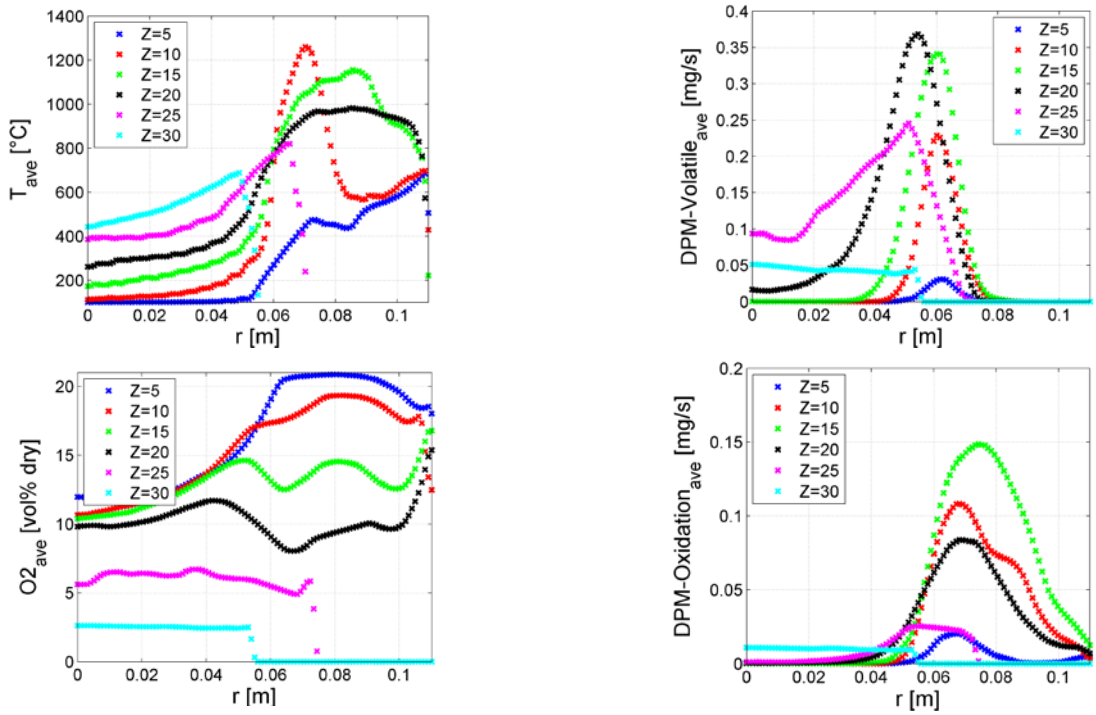

Figure 4-2: Averaged radial profiles of particle temperature T, gas O_2 concentration, pyrolysis rates (DPM-Volatile) [mg/s] and char burnout (DPM-Oxidation) [mg/s] at different heights above the grate.

4.2 Task 3.2: Advanced CFD Models Considering Streak Formation and Low-Turbulence Regimes

Development of gas phase combustion model suitable for low and high turbulence conditions

Especially in the small size-range < 500 kW_{th} and in the region above the fuel bed the gas phase mixing and reaction progress is highly influenced by laminar and low turbulent zones. Here, the gas phase combustion models, which are originally developed for highly turbulent flows, are not valid anymore, leading to wrong

predictions of the reaction progress and wrong concentrations of gas species (CO, NO_x species etc.). Therefore, a CFD gas phase reaction model which is applicable in the whole Reynolds range from laminar to turbulent flows has been developed. The model development was supported by experimental data from literature for different jet flames. Moreover, since a good prediction of flow, mixing and the turbulence properties is important for a good prediction of gas phase combustion, a turbulence model suitable for low-Re flows was selected by a comparison with cold flow experiments with a flame reactor of BE2020+/TUG (species concentration measurements and velocity measurements).

Streak formation modeling

Moreover, state-of-the-art packed bed models supply continuous concentration profiles as boundary conditions for subsequent CFD-simulations of gas phase, leading to premixed combustion conditions. However, in reality the "porous" nature of the packed bed leads to streak formation. In order to account for the influence of the streaks on gas phase combustion, a gas streak model based on a correlation between the local gas residence time and a mixing time has been developed by BE2020+/TUG. The cold-flow reactor experiments as well as a numerical case study with an ideally packed bed supported the model development and were used to calibrate the model constants. Finally, the gas streak formation model and the newly developed gas phase reaction model were tested with an in-house developed packed bed combustion model of BE2020+/TUG. Simulations of a 20 kW pellet underfeed stoker furnace were performed for model evaluation.

Selection of turbulence model

A good prediction of flow field, turbulence and mixing behaviour is an important basis for gas phase combustion modeling. In biomass grate furnaces, the low turbulent regions especially above the fuel bed and in small-scale plants need special attention in modeling. Therefore, different turbulence models implemented in Fluent have been tested for low-Re flows by a comparison with cold-flow reactor experiments with the flame reactor of BE2020+/TUG. Concluding, for the low-Re experiments, the Realizable k-ε model yielded mesh-dependent results and had the lowest accuracy on the coarser tetrahedral mesh. The RNG k-ε model yielded the best results but showed problems concerning the convergence behavior. The Standard k-ω model and the SST k-ω model both gave

reasonable agreements with the experiments with less grid dependency for the SST k-ω model.

Additionally, the turbulence models were also investigated for a high-Re non-reacting propane jet from literature since the finally selected turbulence model should be able to give good results for both low and high-Re flows. For the highly turbulent propane jet from literature, the Reynolds Stress model (taken as additional reference) yielded the best agreement with the measurements, followed by the Realizable k-ε model, the SST k-ω model and the RNG k-ε model, all with reasonable agreement. The agreement of the Standard k-ω model with the experiments was poor. Concluding, the SST k-ω model and the RNG k-ε model yielded reasonable results both for low-Re and high-Re flows and hence can be taken as a basis for gas phase combustion modelling in low to highly turbulent flows. However, it has to be considered that the RNG k-ε model may lead to considerable convergence problems. Therefore, within this project the SST k-ω model has been selected for simulations of biomass combustion plants.

Development of gas phase combustion model suitable for low and high turbulence conditions

The Eddy Dissipation Concept (EDC), which enables the consideration of the complex interaction of turbulence and detailed reaction kinetics, was taken as a basis for the development of a general gas phase combustion model applicable for the whole Reynolds range of flows. However, gas phase combustion models like the Eddy Dissipation Concept (EDC) are originally developed for high Reynolds conditions. The Eddy Dissipation Concept (EDC) of [Magnussen, 1981] is based on the turbulent energy cascade, which means that larger eddies break up into smaller eddies and the reactions take place in the so-called fine structures, where the fluid is mixed on a micro-scale.

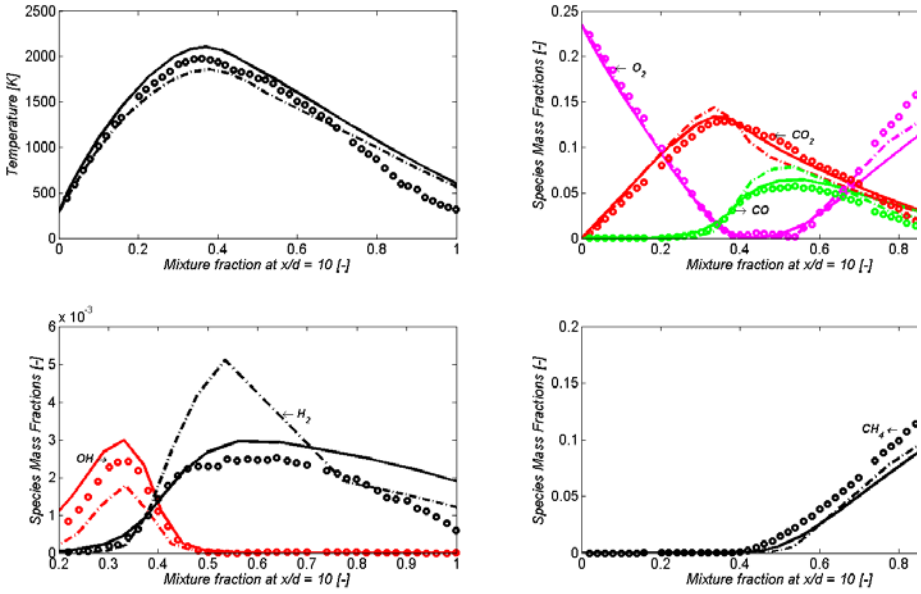

Figure 4-3: Laminar flame A (Re = 1100) – temperatures [K] and species mass fraction [-] at normalised axial distance x/d = 10. Explanations: solid line : Finite rate kinetics model; dash dotted line : Hybrid model; circles: experiment; simulation with modified SST k-ω turbulence model; differential diffusion model and DRM-22 reaction mechanism.

The model development was done based on the simulation of measured jet flames from literature (Sandia flame D as well as flame A with a jet Re number 1100 and flame B with a jet Re number 8200 by [Barlow et al., 1998]). Since it is well-known, that k-ε models over-predict the spreading rate of round jets, the model constants were modified based on the comparison with results from a non-reacting propane jet from literature [Schefer et al., 1985] in order to minimize additional effects influencing gas phase combustion modeling. Furthermore, at low-turbulent combustion regimes the description of the reaction kinetics is of high relevance since it has a considerable influence on the simulation results. Hence, the reduced DRM-22 reaction mechanism was selected based on the simulation of Sandia flame D since the description of reaction kinetics is of high importance in low-Re flows. At low-Re conditions the influence of molecular diffusion on mixing becomes comparable to the influence of turbulent viscosity.

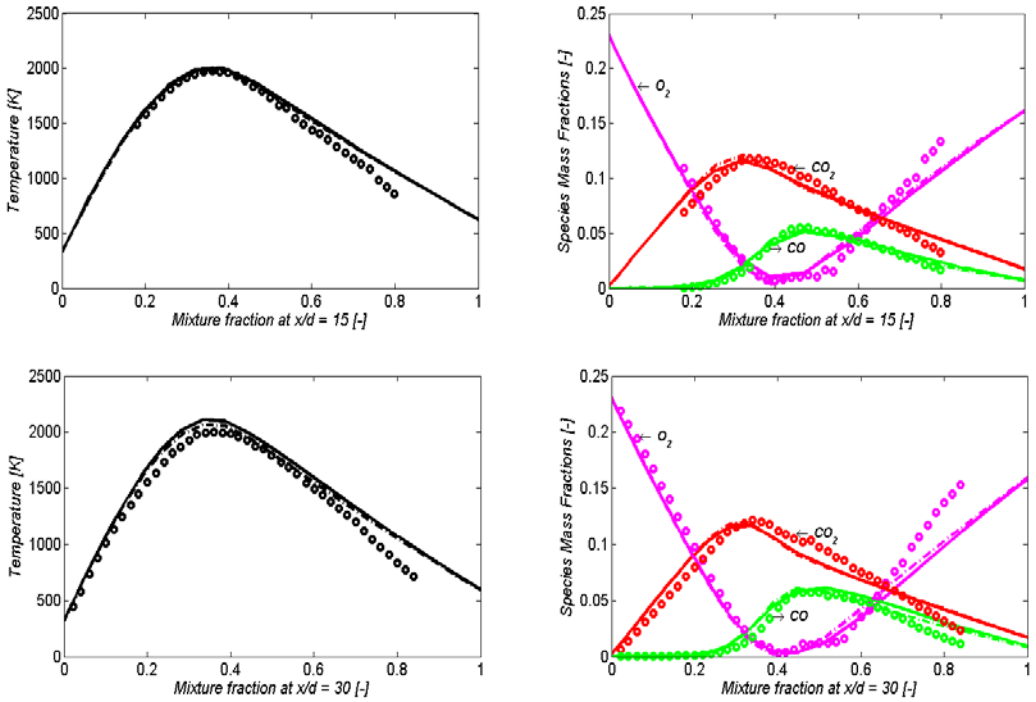

Figure 4-4: Moderately turbulent flame B (Re = 8200) - temperatures [K] (left) and species mass fraction [-] (right) at different normalised axial distances. Explanations: solid line: Standard EDC; dash dotted line: Hybrid model; circles: experiment; simulation with modified SST k-ω turbulence model; differential diffusion model and DRM-22 reaction mechanism.

Therefore, the diffusion of each gas species in the mixture was taken into account and compared with the conventional approach (constant value for the diffusion of the species in the mixture) for the simulation of flame A (Re = 1100) and B (Re = 8200). In a next step, the limitation of the EDC in low turbulence conditions was investigated for flame A (jet Re number 1100) and flame B (jet Re number 8200). While the EDC together with the differential diffusion approach gave a good agreement with measurements for flame B with moderate turbulence, it failed to predict laminar flame A. With finite rate kinetics good results could be achieved for flame A. Since it could be shown that the EDC is not valid below turbulent Re numbers of 64, a hybrid EDC / finite rate kinetics model was introduced. This model calculates the reaction rates with finite rated kinetics and the EDC and finally an effective reaction rate with a weight function in dependence of the turbulence Reynolds number. The new hybrid model was applied for the simulation of flame A and B to validate it for laminar to moderately turbulent flows (see Figure 4-3 and Figure 4-4). It could be shown that for flame B a very good agreement with the measurements could be

achieved. Also for flame A, a good agreement with the measurements could be achieved. However, the agreement was slightly worse than with pure finite rate kinetics since the influence of the EDC was too strong. Therefore, the weight function was modified in order to achieve a sharper transition between around Re_t = 64.3 with a stronger influence of the finite rate kinetics model in the lower Re region.

Streak formation modeling

A streak formation model has been developed by BE2020+. The model is based on a mixing time where the gas streaks are fully mixed and a linear correlation with the residence time of the flue gas arising from the fuel bed. In order to describe the mixing process, a criterion has been developed to calculate the mixing state (MS):

$$MS=\left(1-\frac{(C_{fm}-C(t))}{C_{fm}}\right)$$

Here, C_{fm} is the tracer gas (CO_2) concentration in the fully mixed gas and C(t) is the local tracer gas (CO_2) concentration in dependence of mixing time. The residence time which is necessary to reach the defined mixing state (e.g. 0.99 or 1) is the mixing time t_{fm}. Finally, the mixing function is the combination of the mixing time t_{fm} and the gas residence time t_{gas}:

$$MF=MIN\left(\frac{t_{gas}}{t_{fm}};1\right)$$

MF = 0 (completely unmixed)

MF = 1 (completely mixed)

As a first approximation, a linear correlation between the gas residence time t_{gas} and the mixing function MF was chosen. First, the model was successfully tested by the simulation of cold flow reactor experiments. The mixing time was calculated with a detailed simulation with resolved nozzles and additionally with empirical correlations from literature, which are in good agreement with the simulated values. The simulation of the flame reactor without resolved nozzles showed a good agreement concerning the mixing progress with the simulation with resolved nozzles.

In a next step, a CFD-based case study with an ideally packed bed with spheres as fuel particles and non-reacting flow was performed in order to numerically derive the mixing time. The volatiles were represented by CO_2 released from the surface of the particles in the bed. The volatiles release rate from a single particle was

approximated by the value calculated by an in-house developed layer model for single particle conversion. In this parameter study, the following influencing parameters have been investigated for a packed bed:

- Bed height: variation by the particle layers (from 3 to 10 layers)
- Volatiles mass flow rate: The release rates of the variations are normalised with the values estimated by the layer model (varied between a factor from 1 to 1.7)
- Bulk flow velocity of primary air below the bed (1 – 7 m/s)

The study has been performed for pellets as fuel. However, the simulation results can be applied for all particle sizes by applying the particle Reynolds number for the look-up table where the results are summarized. Here, two parameter studies with an ideally packed bed were performed in order to calculate the mixing time in dependence of primary air flow through the bed, volatiles release and bed height. The first study showed a strong effect of the number of layers (bed height) on mixing. Hence, it was considered as an independent parameter. Afterwards, two bed heights with different numbers of particle layers (5 and 10 layers) were chosen to investigate the influence of primary air velocity and volatiles release rate.

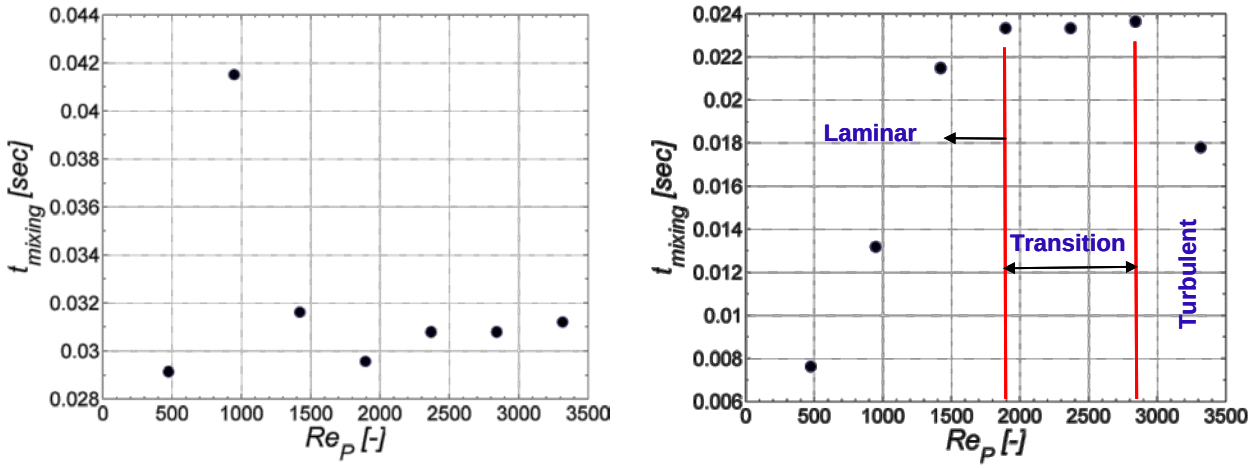

Figure 4-5: Mixing time [-] for different particle Reynolds numbers (left: 5 layers, right: 10 layers).

The results showed a negligible effect of the volatiles release on mixing. However, the primary air velocity and the particle Reynolds number respectively, had a significant effect on the mixing time. While for 5 layers, a constant value for the mixing time can be assumed as an approximation, for 10 layers a trend

concerning the mixing time in dependence of the particle Reynolds number was found (see Figure 4-5). The results of the case study serve as look-up table for the calculation of the mixing time in dependence of the different influencing parameters. A linear interpolation is applied for the dependence of particle Reynolds number (primary air velocity and particle size) in order to retrieve the mixing time on the bed surface as a basis for the calculation of the mixing function. Furthermore, a linear interpolation is currently being applied for the dependence of the number of layers (bed height). A further parameter study is being performed with 15 particle layers as a basis for a second order interpolation.

Link to an in-house developed 3D packed bed model and test for an underfeed stoker furnace

The hybrid EDC / finite rate kinetics model and the streak formation model have been linked with an in-house developed 3D packed bed model. Here, movement and conversion of the particles are modeled in a 2-step approach: First, the movement of the particles is calculated with a cold-flow simulation by using the Euler-Granular model, which enables to consider inter-particle interactions (particle-particle collisions). Based on the simulated packed bed flow field, the conversion of the individual particles is calculated along the particle trajectories with the Lagrangian Discrete Phase Model of Ansys / Fluent. For the conversion of thermally thick particles a Layer Model was developed and successfully validated by BE2020+ [Mehrabian et al., 2012]. The packed bed model was linked with CFD gas phase models specially adapted for biomass grate furnaces including the Eddy Dissipation Model and a global 4-step reaction mechanism (EDM) and successfully tested for a 20kW pellet underfeed stoker furnace ([Mehrabian et al., 2011] see Figure).

First, the hybrid EDC / finite rate kinetics model (Hybrid) together with the packed bed model was tested by a simulation of the 20kW pellet underfeed stoker furnace and compared with the simulation by [Mehrabian et al., 2011]. The C-H-O subset of the skeletal Kilpinen97-mechanism usually applied at BE2020+ for NO_x simulations in biomass grate furnaces (28 species and 102 reactions in total, 12 species and 25 reactions of the C-H-O subset) was selected as reaction mechanism [Kilpinen, 2005].

In a next step, the simulation of the furnace and comparison with the basic simulation was done by additionally applying the streak formation model (Hybrid/streak formation). In order to save computing time during the first tests,

the packed bed simulation of [Mehrabian et al., 2011] was fixed, which means that the influence of changing gas phase reactions on packed bed conversion was not considered. It could be shown that a major part in the reaction zone above the bed is located in low-Re regions and influenced by streak formation (see

Figure). The Hybrid EDC / finite rate kinetics model which captures the whole Re-range should result in an improved combustion prediction:

- compared to the EDM and the EDC, since both are developed for high-Re flows.
- compared to the EDM with a poor prediction in kinetically influenced combustion regions.

Moreover, the streak formation model should lead to an improved prediction of gas phase combustion above the fuel bed since a part of the reaction zone is located in the region where the streaks are mixed.

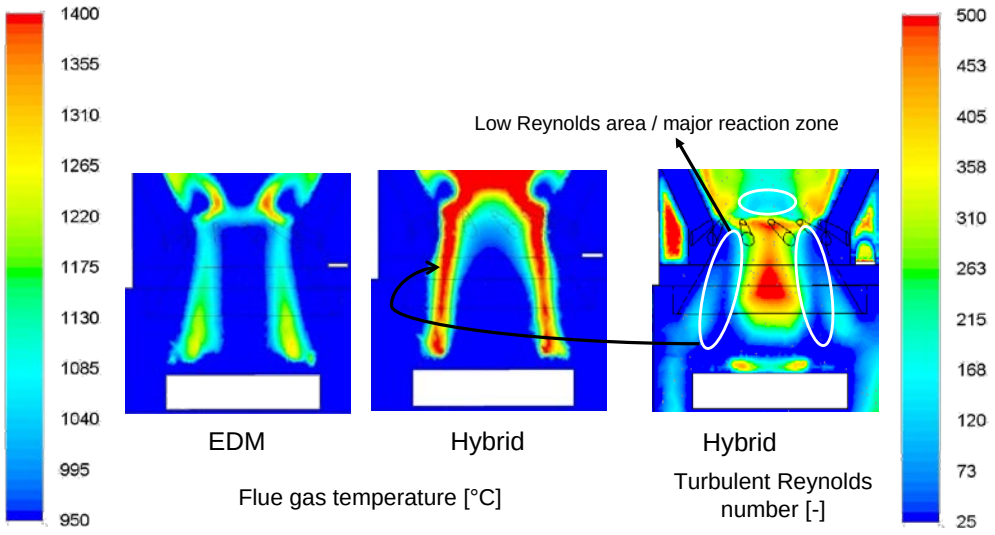

Figure 4-6: Iso-surfaces of flue gas temperature [°C] and turbulent Reynolds number [-] in a vertical cross-section through the furnace (till the upper edge of the refractory lining). Explanations: Hybrid… hybrid EDC / finite rate kinetics.

Concluding, the milestones of WP3, "Gas phase reaction models (eddy break-up models) extended to low-turbulence regimes in grate furnaces" and "CFD model for gas streaks arising from packed beds" could be successfully achieved and new models for an improved prediction of flue gas mixing and combustion in fixed

bed biomass combustion plants are available. In the future, further validation simulations as well as a subsequent application for real-scale plants are foreseen.

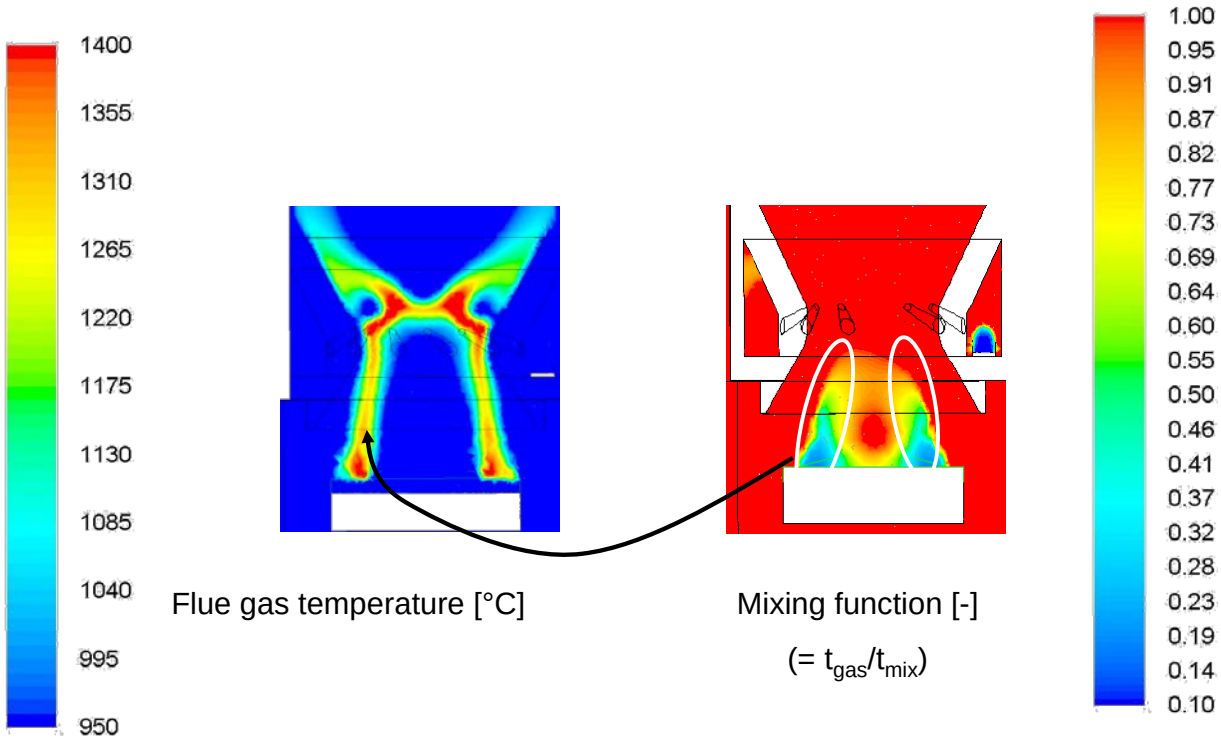

Figure 4-7: Iso-surfaces of flue gas temperature [°C] (left) and mixing function [-] (right) in a vertical cross-section through the furnace (up to the upper edge of the refractory lining). Explanations: simulation have been performed with the hybrid EDC / finite rate kinetics.

4.3 Task 3.3: Development of Particle Models

Single particle models

In this Task, available single particle models have been applied and modified to be applicable in CFD. The nitrogen oxide release model is new and has for the first time been validated within this project in Task 4.2.

Drying and pyrolysis model

During combustion and gasification of solid biomass the drying and pyrolysis occurs partly or entirely simultaneously (Thunman et al.). In fluidized beds and in grate furnaces biomass particles are generally larger than 1 mm. Therefore, the particles are characterized by significant temperature gradients during the heating of the particle. The pyrolysis and the drying takes place at different temperatures and, as a consequence, the conversion phenomena take place simultaneously. The conventional approach to model overlapping of drying and pyrolysis is to discretize the biomass particles into a large number of isothermal layers. The temperature of a layer determines whether water evaporation of devolatlization occurs in that layer. This approach is, however, computationally expensive and, therefore, this types of particle sub-models cannot be included into a CFD-code. In order to make the single particle modeling more time efficient, without significantly reducing the accuracy of the modeling results, the number of isothermal layers can be highly reduced. Thunman et al., Saastamoinen et al. and Järvinen et al. divided large particles into 2-4 layers when modeling the conversion of large biomass particles. According to them, the simplifications make the model computationally fast enough to be included as a sub-model into a CFD code. In this project, the drying and pyrolysis model of Järvinen et al. has been used. This model is developed for combustion of black liquor. In this project, this model has been modified to be suitable for solid biomass particles.

In the model, the particle is divided into three layers. In the innermost layer drying takes place. The second layer is dry and pyrolysis takes place. The third and outermost layer consists of char and ash. For simplification, the char is not assumed to react during the pyrolysis. Thus, overlapping of drying and pyrolysis is taken into account, but the possible overlapping of pyrolysis and char conversion is not considered.

The characteristic external diameter of the particle is calculated as

$$d_p = d_{p,0}\left(1-U\right)^{\alpha} \qquad (1)$$

Here $d_{p,0}$ is the initial particle size; *U* is the fractional degree of conversion; and α is an empirical parameter.

Char oxidation model

In this project, the char oxidation model by Baum and Street has been used. The oxidation rates are predicted with a model based on apparent kinetics and external diffusion

$$\frac{dm_p}{dt} = S_p A_a e^{-E_a/RT_p}\left(P_{O_2,\infty} - \frac{dm_p}{dt}\frac{1}{S_p D}\right)^n \qquad (2)$$

Here, m_p is the mass of the particle (kg); $P_{O_2,\infty}$ is the oxygen partial pressure in the bulk gas (Pa); A_a is the apparent pre-exponential factor (kg/m^{2}sPa^n); E_a is the apparent activation energy (kJ/mol); D is the external diffusion rate coefficient (m/s); and S_p is the external surface area of a spherical particle (m^2). The evolution of the external diameter is modeled as

$$d_p = d_{p,0}(1-U)^{\beta} \qquad (3)$$

The char particle temperature is calculated from

$$m_p c_p \frac{dT_p}{dt} = hS_p(T_\infty - T_p) - f_h \frac{dm_p}{dt} H_{reac} + S_p \varepsilon_p \sigma(\theta_R^4 - T_p^4) \qquad (4)$$

Here c_p is the heat capacity of the particle (J/kgK); h is the convective heat transfer coefficient (W/m^{2}K), calculated using the correlation $Nu\, k_\infty / d_p$; f_h is the fraction of the heat that the particle absorbs from the heat released by the surface reaction H_{reac} (J/kg); ε_p is the emissivity of the particle surface; σ is the Stefan-Boltzmann constant; and θ_R is the radiation temperature. It is important to note that the model is a function both of chemical kinetics and external mass transfer. For high kinetic rates, i.e. $A_a e^{-E_a/RT_p}$ >>D, the rate is independent of the kinetics and, therefore, the conversion is limited by external mass transfer.

Char gasification model

Generally char gasification is much slower than char conversion. One approach to model kinetically limited char gasification is by using the random pore model (Bhatia). Here, the conversion rate can be modeled as

$$\frac{dX}{dt} = kP_{CO2}{}^n(1-X)\sqrt{1-\psi\ln(1-X)} \qquad (5)$$

where

$$X(t) = \frac{m_0 - m(t)}{m_0 - m_{ash}} \qquad (6)$$

Here, *k* is the kinetic rate constant, *m* is mass, ψ is structural parameter, and *n* is apparent reaction order assumed to be one.

Nitrogen oxide (NO) release model

During char oxidation, the oxidation of char-N and char-C can be assumed to be non-selective. Therefore, the rate of char-N oxidation can be obtained from the rate of carbon oxidation and the N/C ratio in the char. The formed NO is partly reduced. For biomass char particles there is no CFD-applicable model for this NO reduction. Therefore, a new NO reduction model as been developed. The NO release from a char particle during oxidation is expressed as:

$$\dot{m}_{NO} = \frac{M_{NO}}{M_N}\frac{f_N}{f_C}\dot{m}_{C,\exp t} - p_{NO,\max}^{n} S_{char} A_{NO} e^{-E_{NO}/RT_p} \qquad (7)$$

Here the first term on the right hand side is the formation of NO and the second term is the reduction of NO. *M* is molar mass; *f* is mass fraction; S_{char} is the external surface area of the char particle calculated from the diameter in Eq. 3 in this chapter. *A* and *E* are apparent kinetic parameters and $p_{NO,\max}$ is defined as

$$p_{NO,\max} = \frac{x_N}{x_C} p_{O_2,\infty} = \frac{M_C}{M_N}\frac{f_N}{f_C} p_{O_2,\infty} \qquad (8)$$

Here, x_N and x_C are molar fractions of nitrogen and carbon in the char.

4.4 Task 3.4: Conversion of the Particle Model into a CFD Sub-Model

The generic biomass particle model has been converted into a CFD sub-mode. It was found that the model with distinct temperatures for drying and devolitilazation had all the necessary features for modeling various biofuels. The effort put on this task mainly involved validation of the coupling with the CFD code used. Although the particle models were tested in Task 3.3, a few problems were encountered. E.g., in CFD calculation unexpected time histories of the temperature field were encountered that required modification to the model in order to make it numerically more stable. In addition, it was necessary to increase the numerical efficiency of the particle mode, involving a more efficient solution strategy to the temperatures of the char conversion layer of the particle. A significant amount of work also had to be put on validating the coupling with the radiation model in the CFD code that did not need to be addressed in Task 3.3.

4.5 Task 3.5: CFD Studies of Combustion of Biomass Mixtures

Bubbling fluidized bed (BFB) is frequently used for biomass combustion. Biomass differs from coal in several ways; the volatile yield is typically high and the char is more reactive. As a consequence there is a need for tailor made models when applying computational fluid dynamics (CFD) modeling to study the behavior of such combustors. These include models for the conversion of the large biomass particles and for their behavior in the bubbling bed. Frequently, the bubbling bed is modeled using simplified boundary conditions that are neither sensitive to the fuel properties nor to the design of the air distributor type nor to the bed material. Another option is to use multi-phase models to model the bed. This approach is, however, associated with large computational expensive, especially since the bed processes are non-stationary.

Brief description of FBC boiler used as case study

A 107 MW_{th} commercial BFB boiler was used as validation and test case. The total height of the BFB boiler was approximately 40 m. The boiler had been used in an extensive measurement campaign and results from gas composition measurements, fate of some ash forming elements and temperature measurements were published elsewhere (Vainio *et al*. 2011a, Vainio *et al*. 2011b, Brink *et al*. 2011). The main fuel was bark. Measurements from three different operational conditions were available. In the first case the bark was only fuel. In the second case, a mixture of bark and sludge was used. In the third case a mixture of bark, sludge and refuse derived fuel was used. In all cases bark was the dominating fuel. Fuel analyses showed that all the fuel had very similar heating values on dry ash free bases. The sludge was added to the fuel in such a way that it mainly wetted the main fuel. The refuse derived fuel had a size distribution similar to the bark. However, here too the ash content was slightly higher as compared to the bark. Analyzing the fuel showed that a large fraction of the "ash" actually was made up of construction waste such as bricks, masonry and tiles.

Description of the numerical models

The mathematical model used was based on the commercial CFD code, Ansys-FLUENT. The time averaged conservation equations for mass, momentum, enthalpy and species are solved for gas flow. Turbulence was modeled with the k-ε model. Species and chemical reactions are modeled using the Eddy Dissipation Combustion Model of Magnussen and Hjertager (1976) as implemented in Ansys-FLUENT for a single reaction, having the possibility of chemical reaction rate limitations included. The discrete phase equations in this model are formulated in a Lagrangian form. The behavior of the particles in the splash region is described using a stochastic tracking approach (Brink *et al*. 2009), where the initial velocities and directions are chosen such that the effective dispersion coefficient is that of a typical bubbling bed. This calls for tracking the Lagrangian particle until complete burnout. This easily leads impractical tracking times. To avoid such long computational times, a few criteria were added. The Lagrangian paraticle tracking was interrupted if the particle conversion time used a predefined maximum value. Also a criterion was tested based on the char conversion degree. However, this approach could not be used if also the ash residue was to be tracked in the boiler.

The heat transfer in the splash zone is modeled using an effective thermal conductivity. Estimating the effective thermal conductivity in the splash zone, the relation between the dispersion coefficient and the thermal conductivity is utilized:

$$D = k/\rho c_p \qquad \text{Eq. (1)}$$

together with the assumption that the thermal dispersion follows the dispersion of solids. The largest measured dispersion of solids are around 0.02 – 0.03 m^2/s (Leckner 1998). The dispersion coefficient of solids can also be calculated following Kunii and Levenspiel (1991). Following Kunii and Levenspiel (1991) the horizontal dispersion coefficient for deep beds may be calculated as

$$D_{s,horizontal} = 3\delta\alpha^2 U_{mf} d_b / 16(1-\delta)\epsilon_{mf} \qquad \text{Eq. (2)}$$

and the vertical dispersion coefficient calculated as

$$D_{s,vertical} = f_w^2 \epsilon_{mf} \delta d_b U_b^2 / 3U_{mf}. \qquad \text{Eq. (3)}$$

The equations above include several parameters that can be estimated using equations also presented in Kunii and Levenspiel (1991). This opens up the

possibility for estimates of the dispersion coefficients of solids based on the actual boiler design and bed material.

Solving Eq. 1 for thermal conductivity one obtains

$$k_{splash} = \rho_{splash} c_{p,splash} D_{splash}.$$

This equation includes two unknowns: the density of the splash zone and the heat capacity of the splash zone. Here it is assumed that both are related to the fraction of solids in the splash zone:

$$c_{p,spash} = c_{p,sand}\epsilon_{splash} + c_{p,air}\left(1 - \varepsilon_{splash}\right) \qquad \text{Eq. (4)}$$

and

$$\rho_{spash} = \rho_{sand}\epsilon_{splash} + \rho_{air}\left(1 - \varepsilon_{splash}\right). \qquad \text{Eq. (5)}$$

The fraction of solids at the interface between the bed and the splash zone can be calculated estimated using standard equations. The fraction of solids in the splash zone is more difficult to resolve. The height of the splash zone can be estimated solving the equation of motion of an ejected spherical inert particle in the splashing region, neglecting the drag force.

Figure 4-8A shows the temperature distribution on a plane in the center of the boiler and on a plane located at the elevation of the start of the splash zone. In this case only bark was fired. Fig 3.5.1a shows the results obtained without an enhanced thermal conductivity in the splash zone region. In this case the whole bed has an unrealistically low temperature. Because of the low temperature, the drying becomes very slow and takes place in the entire splash zone. Because of the low temperature, almost no combustion of volatiles takes place in the bed. Instead, high temperature regions are found around the secondary air inlets, where the turbulent mixing is high. Fig 4-8B shows the result obtained with a splash zone of 0.5 m. The figure shows that the drying is very local, and that the predicted temperatures are unrealistically low. However, in this case, parts of the bed have a more realistic temperature. In fact, the predicted temperatures close to the wall is too high. Fig 4-8C shows the case with a 1 m high splash zone. This case is rather similar to the case shown in Fig 4-8B, although the temperature in the cold spots where more of the drying occurs has been slightly raised. These results indicates that assuming that only the splash zone is the active part of the bed, is not a very realistic assumption.

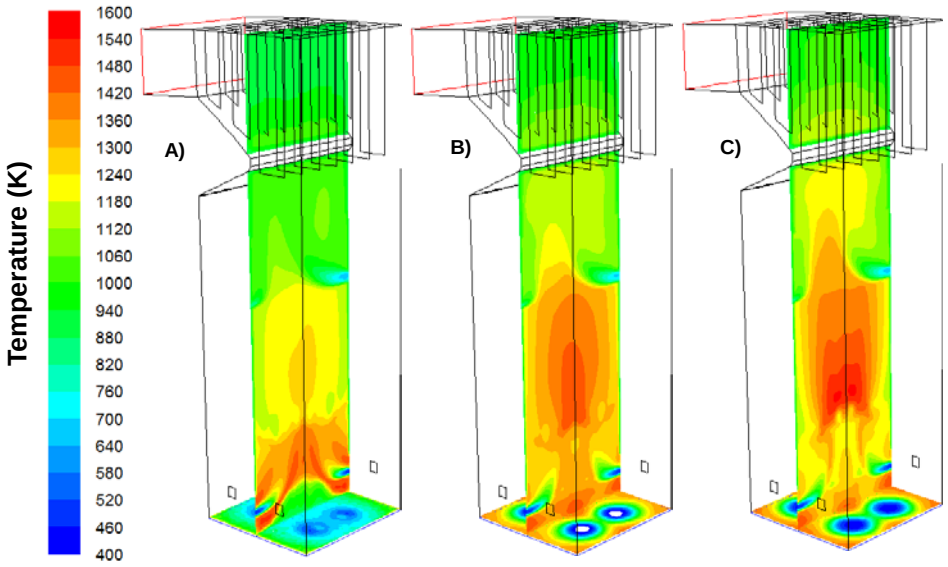

Figure 4-8: Temperature predictions obtained applying a splash zone model. A) No enhanced heat transfer in splash zone. B) Enhanced heat transfer in a 0.5 m high splash zone. C) Enhanced heat transfer in a 1.0 m high splash zone.

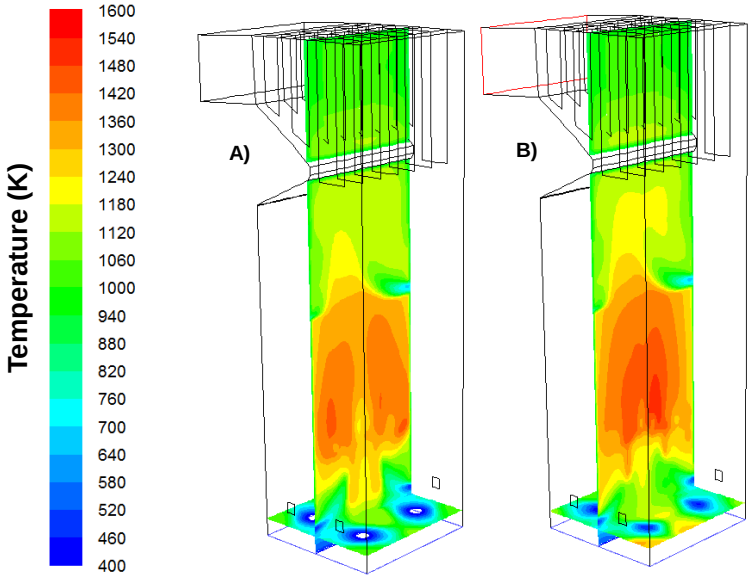

Figure 4-9: Temperature predictions obtained applying a splash zone model and a bed model. A) Enhanced heat transfer in a 0.5 m high splash zone on top of a 1.0 m bed. B) Enhanced heat transfer in a 1.0 m high splash zone on top of a 1.0 m bed.

Fig 4-9 shows results obtained with a 1 m bed added below the splash zone. In the model, the thermal conductivity of the bed is assumed to be the same as for the lowest part of the splash zone. Further, it is assumed that the fuel particles do not enter the bed; they only appear in the splash zone. The figure show that the

appended bed contributes to a more uniform temperature in the splash zone. However, the temperature variation is still large, and cold spots occur where the fuel particles are landing.

The bed model version with an enhanced heat transfer in a 1.0 m high splash zone on top of a 1.0 m bed was used to model the bark + sewage sludge in two different ways. First, the fuel was modeled as a single food having measured average properties for fuel size distribution, fuel composition and moisture content. Secondly, the bark + sewage sludge case was modeled as two separate fuels, each having separate particle size distributions, fuel properties and moisture contents. Figure 4-10 shows the particle size distributions of bark, of the sewage sludge + bark mixture and of the sewage sludge. Here the particles size distribution of the sewage sludge has been calculated using the particle size distribution of the bark and the bark + sewage sludge mixture, taking the fraction of each of the fuels in the mixture into account. The figure shows that the sewage sludge consists of smaller particles. The particle size distribution of the sewage sludge was not available. However, the result is in line with visual observation made during the measurement campaign made earlier.

Figure 4-11 shows H2O concentrations in the free board using the two approaches. The figure shows only minor differences. In this case, this is to be expected since in both cases the same amount of water is entering with the fuel. The only major difference between the two cases is that in one case all particles have a moisture content of 54.4%, whereas in the second case 84% of the particles have a moisture content of 52.3% and 16% of the fuel has a moisture content of 75.6%. Nevertheless, adding up to two fuels in the latter case will yield an identical average moisture content, fuel property as well as particle size distribution.

The predicted temperatures in the bed region showed some discrepancies compared to observation using an IR-camera. A possible reason for this is uncertainties in the initial mass dispersion rate of the fuel.

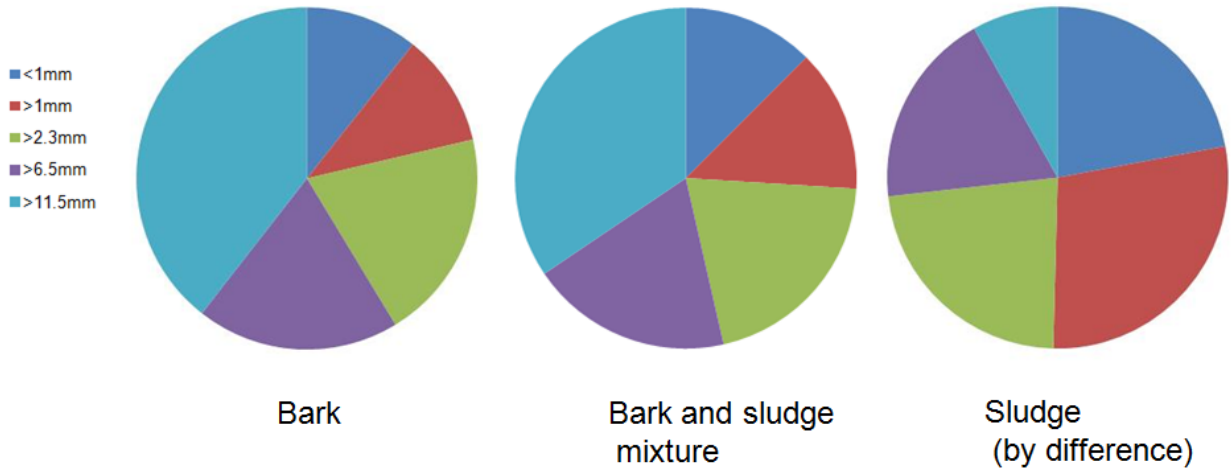

Figure 4-10: Particle size distribution of the fuels used in the calculations.

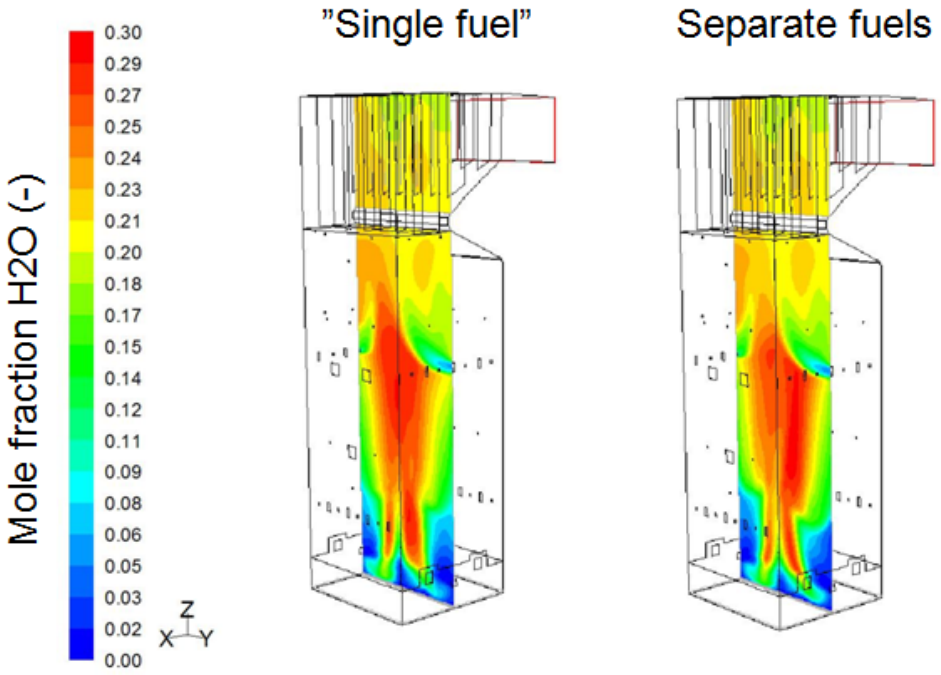

Figure 4-11: Calculated H2O concentration at the centerline of the boiler obtained two alternative ways to describe firing of a fuel mixture.

References:

Barlow, R.S., Frank, J.H., 1998: Effects of Turbulence on Species Mass Fractions in Methane/Air Jet Flames. In: Proc. Combust. Inst, Vol. 27, pp.1087–1095

M.M. Baum, P.J. Street. Predicting the combustion behaviour of coal particles. Combustion Science and Technology Volume 3, Issue 5, 1971pages 231-243

K. Bhatia, D. D. Perlmutter, A random pore model for fluid-solid reactions: I. Isothermal, kinetic control AIChE Journal, Volume 26, Issue 3, pages 379–386, May 1980

Brink, A., Koschack, R., Laurén, T., Hupa, M.: 9th European Conference on Industrial Furnaces and Boilers, (2011).

Kunii Daizo, Levenspiel Octave. Fluidization engineering. USA: Butterworth–Heinemann, 1991.

Mika Järvinen, Christian Mueller, MikkoHupa, Carl-Johan Fogelholm, *Predicting the combustion behaviour of coal particles, Combustion Science and Technology Volume 3, Issue 5, 1971, pages 231-243.*

M. Järvinen, C. Mueller, M. Hupa, C.-J. Fogelholm. A CFD-applicable discrete combustion model for thermally large particles. Progress in Computational Fluid Dynamics Volume 11, Number 6/2011 Pages 373-387.

Kilpinen, P., 2005: KILPINEN97_Skeletal_NH3_HCN_CO_H2, Skeletal mechanism for oxidation of NH3, HCN, CO, and H2 based on the full KILPINEN97 mechanism Internal report, 24.11.2005. Available from the author on address: Pia.Kilpinen@uku.fi or Pia.Kilpinen@abo.fi

Leckner, B.: Prog. Energy Combust. Sci. 22 (1998), pp. 31-61.

Magnussen, B. F., 1981: On the Structure of Turbulence and a Generalized Eddy Dissipation Concept for Chemical Reaction in Turbulent Flow. Nineteenth AIAA Meeting, St. Louis.

Magnussen, B.F., Hjertager, B.H.: In Sixteenth Symposium (International) on Combustion (1976), pp. 719-729.

Mehrabian Ramin, Stangl Stefan, Scharler Robert, Obernberger Ingwald, Weissinger Alexander, 2011: CFD simulation of biomass grate furnaces with a comprehensive 3D packed bed model. In: Proc. of 25th German Flame Day Conf., Sept. 2011, Karlsruhe, Germany, ISBN 978-3-18-092119-8, pp. 189-204, VDI Verlag GmbH Düsseldorf (Ed), Germany.

Mehrabian R., Zahirovic S., Scharler R., Obernberger I., Kleditzsch S., Wirtz S., Scherer V., Lu H., Baxter L.L., 2012: A CFD model for thermal conversion of thermally thick biomass particles, Fuel Processing Technology 95 (2012), pp. 96–108.

J.J. Saastamoinen, *A CFD-applicable discrete combustion model for thermally large particles, Progress in Computational Fluid DynamicsVolume 11, Number 6/2011, Pages 373-38.7*

J.J. Saastamoinen. Simplified model for calculation of devolatilization in fluidized beds. Fuel, Volume 85, Issues 17–18, December 2006, Pages 2388-2395

Schefer, R. W., Johnston, S. C., Dibble, R. W., Gouldin, F. C. and Kollmann, W., 1985: Nonreacting Turbulent Mixing Flows: A Literature Survey and Data Base, Sandia Report SAND86-8217, Sandia National Laboratories, Livermore, CA.

H. Thunman, K. Davidsson, B. Leckner. Separation of drying and devolatilization during conversion of solid fuels.Combustion and Flame, Volume 137, Issues 1–2, April 2004, Pages 242-250

H. Thunman, B. Leckner, F. Niklasson, F. Johnsson**.** Combustion of wood particles—a particle model for eulerian calculations**.** Combustion and Flame, Volume 129, Issues 1–2, April 2002, Pages 30-46

Vainio, E., Yrjas, P., Zevenhoven, M., Brink, A., Laurén, T., Hupa, M., Kajolinna, T., Vesala, H.: Fuel Processing Technology (2011a), in press.

Vainio, E., Brink, A., Yrjas, P., Hupa, M., Kajolinna, T., Vesala, H.: 9th European Conference on Industrial Furnaces and Boilers, (2011b).

5. WP4: Advanced Characterization – Combustion and NOx Related Issues

Coordinated by Prof. Terese Løvås, NTNU

For the low temperature (i.e. 600-900°C) conditions NOx are almost exclusively formed through a mechanism known as the fuel-NOx mechanism in waste (fractions) and biomass combustion. In this mechanism, nitrogen contained in the fuel is primarily released during devolatilisation as NH3 and HCN. NH3 and HCN may then be oxidised to NO, NO2, N2O and N2 through a number of reaction paths. Several theoretical studies show that the main oxidation routes of NH3 lead to NO and N2 while HCN is the main precursor for N2O.

The experimental data from literature concerning NH3, HCN and NH3/HCN ratio in the pyrolysis gases are quite diverse. NH3 is often reported to be the main N-containing component in the devolatilisation gas. However in other studies HCN appears to be released in equal amounts as NH3 or even to be the main N-compound in the pyrolysis gas. The contribution in this particular project is the particular selection of materials, process conditions and the experimental techniques proposed. The cooperation and discussions between the partners in the project are also very important for the outcome.

For modeling purposes not only NO_X formation should be understood, also release and formation of other gaseous compound should be taken into account. In this field, a lot of work has been done for pulverized biomass fuels. Determining parameters for thermally large particles have mostly been done based on thermally small particles. In fact, very little work had been done on determining parameters based on thermally large biomass particles.

Accordingly the objectives of WP4 were:

- Studying operating parameters influencing N-release. This was performed in a lab-scale multifuel reactor using micro gas chromatograph (GC), Fourier transform infrared spectrometer (FTIR) and a portable gas analyzer for flue gas analysis.
- Study of NO_x release in single fuel reactor (TGA conditions).
- Determination combustion characteristics a single particle furnace equipped with a video camera and on-line gas analysis featuring realistic heating rates.

5.1 Task 4.1: Operating Parameters Influencing N-Release

In large industrial boilers, particles from incomplete combustion are generally low due to favorable combustion condition. However for each type of biomass, based on the source, characteristics and chemical composition, special care should be taken with certain emissions and residues as they can cause environmental problem. For example sewage sludge needs consideration regarding the high ash content and the problems regarding ash removal from the reactor. Parallel studies on the same fuel batch show that straw needs care due to a low ash melting temperature and high alkali content which may cause damages to the tubes and walls via agglomeration, corrosion, deposition and fouling. This is confirmed by others for varying types of reactors. Furthermore, peat, sewage sludge and straw have all high nitrogen content that results in a high NOx emission level. It is difficult to reduce all the mentioned pollutants simultaneously. There is e.g. a trade-off between NOx emissions and unburnt hydrocarbons and carbon.

Formation of NOx is through 4 different processes: thermal NOx (Zeldovich mechanism), N2O-intermediate mechanism, prompt NO (Fenimore mechanism), and fuel-N conversion. In solid fuels fired systems, fuel-NO accounts for more than 80% of the total NOx and NOx is mainly produced by conversion of volatile nitrogen containing species such as NH3 and HCN, while remaining char-N oxidation in the reactor bed accounts for a minor part of the total NO. In addition, thermal NOx formation becomes important at temperatures above 1400 °C, which is far from the typical temperature range (800-1200 °C) of biomass combustion systems.

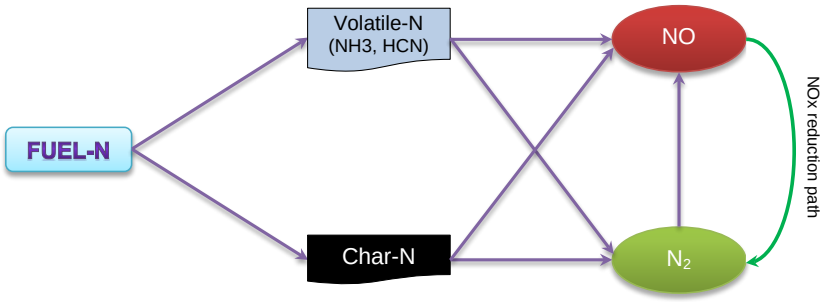

Figure 5-1: Simple fuel nitrogen conversion path diagram.

Experimental investigations are needed to characterize the release of nitrogen containing species from different solid biomass fuels to establish input for CFD modeling studies. Figure 5-1 shows the conversion path for fuel-nitrogen in a conventional biomass combustion system.

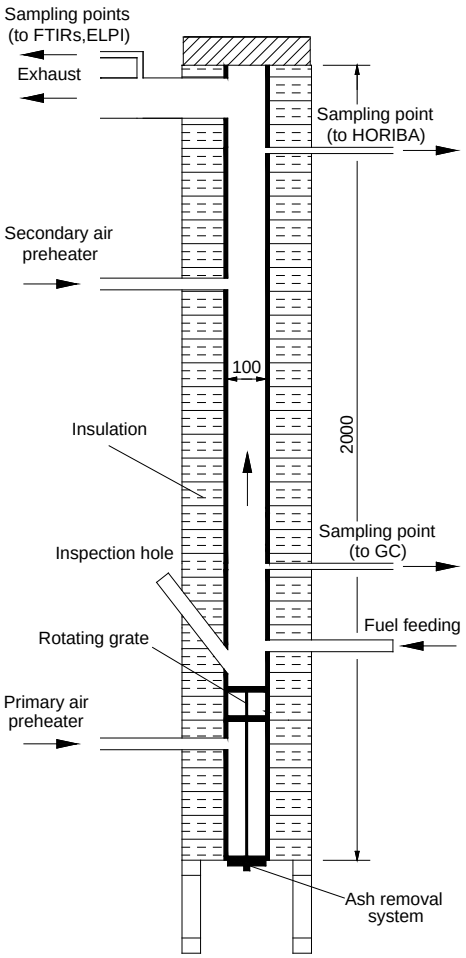

Figure 5-2: Schematic drawing of the reactor.

Major technologies to reduce the NOx emissions, based on the fuel composition and combustion system are divided into two categories: primary measures and secondary measures. Primary measures reduce the emissions within the combustion chamber or before fuel feeding, so the formation of NOx will be prevented as much as possible before the flue gases leave the reactor. These measures include staged air and staged fuel combustion, modification to the fuel composition by fuel blending, co-combustion, improvements to the combustion

chamber, flue gas recirculation, fuel pretreatment, etc. Staged air combustion is widely applied in biomass combustion applications, both in small scale and large scale. Fuel staging follows a concept similar to air staging, but with addition of the fuel to the reactor in two stages. The combustion tests were carried out in SINTEF Energy Research's multifuel reactor, which is an electrically heated isothermal high temperature reactor. A schematic drawing is presented in Figure 4-2. The reaction section, located above the grate, is 1.6 m long, while the section below the grate is 0.4 m long. The lower part of the multifuel reactor is the section containing the grate, which has two levels (10 cm apart), a primary grate and a final burnout grate and an ash collection system with an ash bin. The reactor setup thus combines two possible reduction technologies simultaneously, staged air through the secondary air feed and staged fuel combustion through the 2-level grate which enables a possible fuel staging effect.

In the following subsections different strategies for NO_x reduction through controlling operating parameters will be presented. The ERA-net fuels discussed in Chapter 6 were used as well as other types of biofuels for comparison.

Fuel Mixing and Staged Air Ratio

In this set of studies, we investigated NOx, and N2O, emissions for different biomass fuels and fuel mixtures thereof as pellets both with and without air staging in a grate fired multifuel reactor at a constant reactor set point temperature of 850 °C. The fuels investigated are wood, demolition wood, coffee waste, straw, tops and branches, sewage sludge, peat, and selected mixtures of these. Details of these studies can be found in the selected publications, and only the trends are reported here.

A large NOx reduction potential, up to 91% and corresponding to less than 20 ppm NOx at 11% O2 for a fuel containing about 3 wt% fuel-N, using air staging was found at the optimum primary excess air ratio. However, the reduction level depended on the excess air ratio at the first stage. An optimum primary excess air ratio of about 0.9 was found for the reactor in the primary zone (fuel rich condition), see Figure 5-3. However, low ash melting characteristics of some of the fuels, particularly straw, caused this value to be somewhat higher due to sintering on the fuel grate.

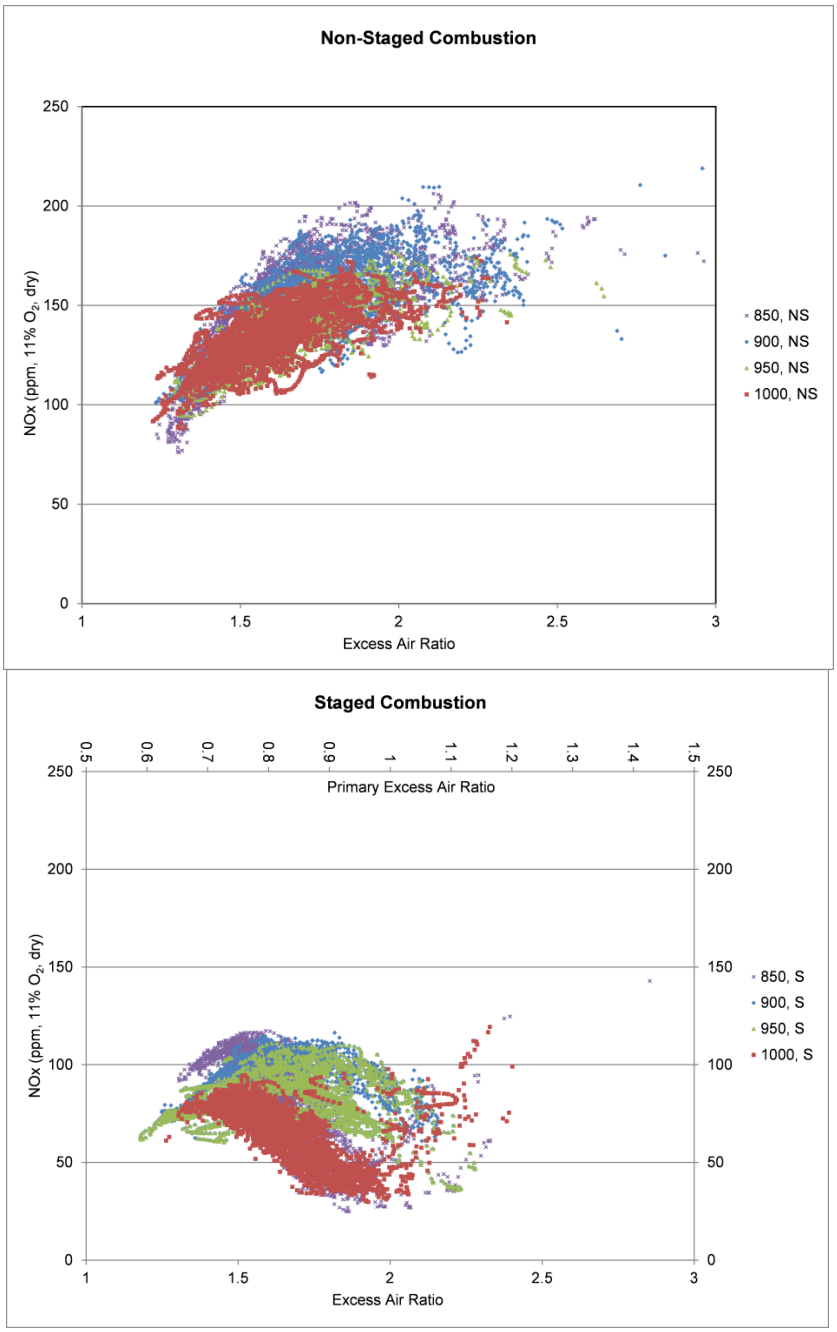

Figure 5-3: NOx as ppm corrected to 10% O2 in the dry flue gas for staged air combustion and non-staged combustion as function of excess air ratio at different temperatures.

The effect on N2O, however, is adverse at the selected set point temperature and the optimum primary excess air ratio for NOx reduction, with an increase in the N2O emission level of up to 635%. The NOx emission level increases with increasing fuel-N content, while the conversion factor for fuel-N to NOx

decreases with increasing fuel-N content. Fuel mixing has a positive influence on the NOx emission level, but a negative influence on the overall conversion factor for fuel-N to NOx and N2O. The general conclusion is that air-staging can be effectively used in a grate combustion reactor in order to reduce NOx emissions. Wood pellets with the lowest nitrogen content showed less reduction potential, while a blend of peat and sewage sludge, which had high fuel-N content, only converted about 2% of the fuel-N to NOx and N2O, the rest being converted directly to N2, and a minor part remained in the ash.

Figure 5-4 shows the fuel-N conversion and the effect of fuel-N content in different fuels and mixtures. Sewage sludge, having low VM and high ash content, is suggested as a favorable fuel to be blended with straw, showing high NOx reduction and low fuel-N conversion. Grot, however, with high VM and low ash content, did not show desirable NOx reduction and also made the combustion more unstable. The reduction potential for grot and sewage sludge mixtures was about 50% and 80%, respectively.

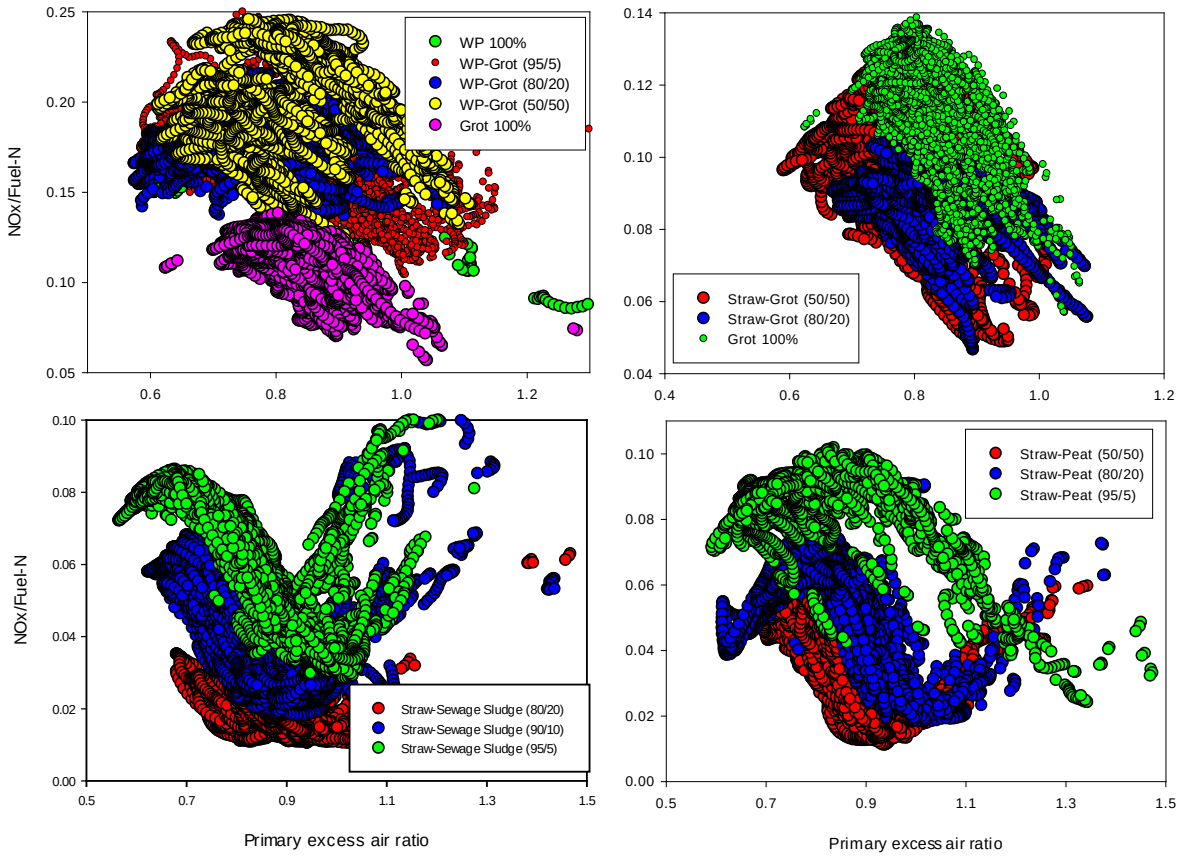

Figure 5-4: Fuel-N conversion and the effect of fuel-N content.

It is also found that fuel type influences the flue gas composition, especially the SOx and NOx levels depending on the fuel S and N levels. Further, higher probability of corrosion is expected in a plant fuelling forest residues compared to virgin wood, due to higher alkali content of the fuel. Air staging reduces HCl emissions somewhat, but does not have a clear effect on SOx. Fuel mixing increases the small particles (aerosols at a range of 0.04–0.1 μm) emission in staged experiments, a behavior that is not noticed during experiments without air staging.

Temperature Effects

Experiments were carried out on demolition wood pellets showing that primary excess air ratio is the most important parameter which can be optimized for maximum conversion of fuel-N to N2, hence reducing the NOx level. The effect of two-stage combustion of biomass is significant for reduction of NOx emission levels. Staged air combustion can reduce the emission level by 50–75% in average, and up to 85% at the optimum conditions.

The maximum NOx reduction happens when the primary air is injected at a primary excess air ratio of 0.8–0.95 and the total excess air ratio is 1.6–1.9 for staged air combustion. The average N2O level increase for the different temperatures is 75–1660%, but with a low amount of N2O at high temperatures.

The NOx emission level is not affected significantly by the reactor temperature neither in non-staged nor staged air combustion when temperatures are kept below 1000 °C in the reactor, see Figure 4.5. Yet, the effect of temperature on the N2O level is considerable. As expected, at high temperatures, N2O emissions almost disappear. The results point to that the effects of moderate temperature and staged air combustion are counteractive for N2O, meaning a negative influence on N2O for staged air combustion. Therefore, to minimize N2O emissions and reduce emissions of unburnt, temperatures of above 900 °C are beneficial for staged air combustion.

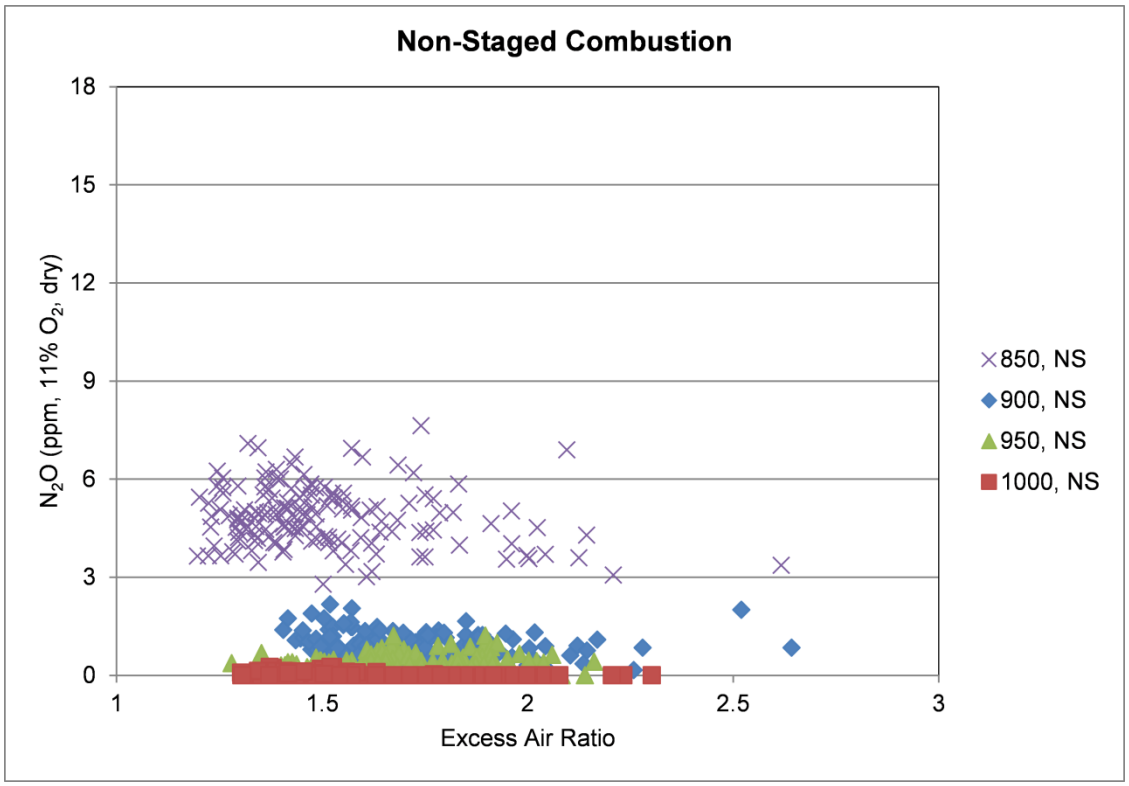

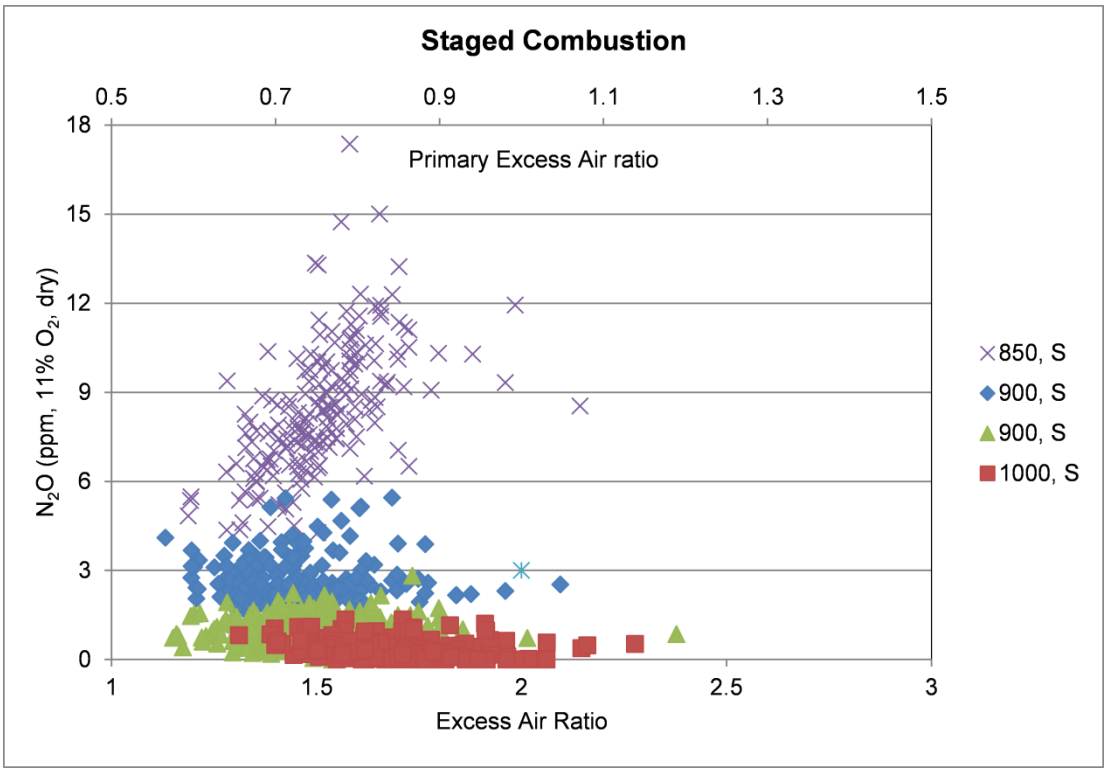

Figure 5-5: N2O as ppm corrected to 11% O2 in the flue gas for staged air combustion and non-staged combustion as a function of excess air ratio at the different temperature levels.

The CxHy emission level is almost independent of the combustion condition (staged air combustion or non-staged combustion), and is below 4 ppm at 11% O2 in dry flue gas. CO emissions increase for staged air combustion compared to non-staged combustion by a factor of about 1.5 at a given temperature. Increasing temperature decreases the CO emission level in the whole temperature range of 850–1000 °C.

5.2 Task 4.2: Combustion Characteristics

For the thermogravimetric analysis, a TA Instruments SDT Q600 is used. Figure 5-6 shows the setup. The microbalance consists of two horizontal beams for thermogravimetry and differential thermo analysis. A platinum crucible (6 mm diameter) is filled with 11 ± 1 mg biomass, which means approximately one third of the total crucible volume. In the experiments, the sample is heated to a temperature of 700°C, 800°C or 900°C. At these temperatures, isothermal char gasification experiments are performed. Thus, for one fuel sample isothermal char gasification runs are performed separately at 700°C, 800°C and 900°C. The heating rate is 180 K/min. During the heating of the particles, surrounding gas is nitrogen. Then, a mixture of 90 vol.% CO2 and 10 vol.% N2 is added, and the char gasification tests begin.

Table 5-1

	[a] VM	[b] FC	[c] ASH	[d] ψ	[e] E_{CO2}
Spruce Bark	74.5	21	4.5	0	130
Danish Straw	78.5	16	5.5	3.7	170
Miscanthus	81.4	16.6	2	24.6	170
Sewage Sludge	56.2	2.9	40.9	1	165

[a] Volatile matter (%)
[b] Fixed carbon content (%)
[c] Ash content(%)
[d] Structural parameters (-)
[e] Activation energy (kJ/mol)

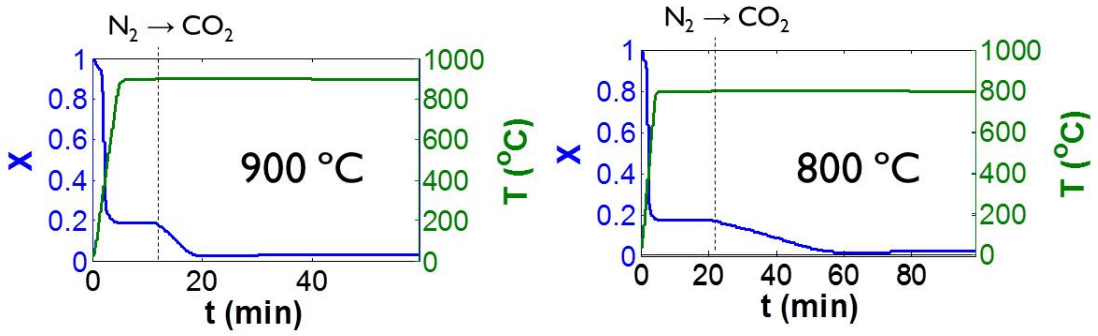

Figure 5-6: Raw data from TGA tests.

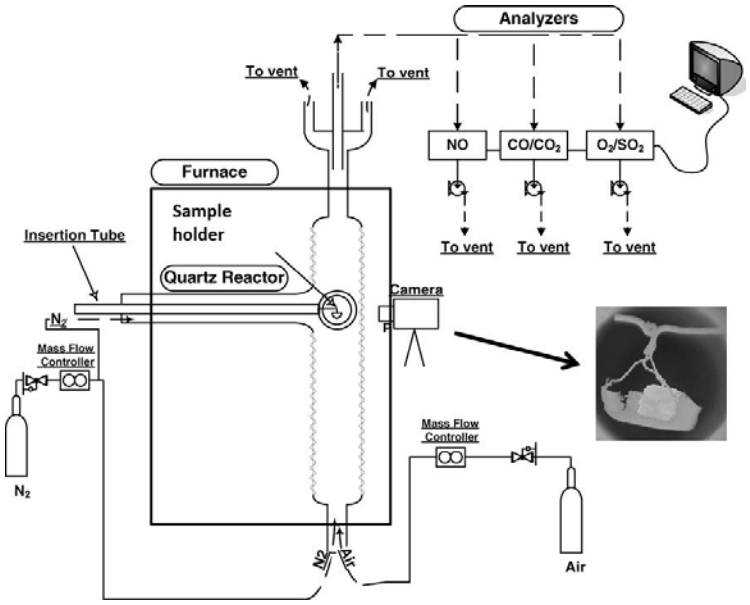

Figure 5-7: Åbo Akademi single particle reactor

Figure 5-6 shows raw data from the TGA tests at 800°C and 900°C. In the figure the dashed line is the point for when CO2 is introduced to the TGA. It can be seen that the char is gasified in around 8 minutes (12 to 20 minutes) at900°C and in around 40 minutes (20 to 60 minutes) at 800 °C. Here it is important to note that the gasification is expected to be entirely controlled by chemical kinetics and, therefore, the char conversion time is independent on the initial char mass. The fuels investigated in the TGA are listed in Table 5-1.

Combustion experiments of biomass pellets were performed in the Åbo Akademi Single Particle Reactor (SPR). A detailed description can be found elsewhere

(Giunotoli). A brief description is given here. The SPR consists of a quartz tube inserted in an electrically heated ceramic furnace. Gas mixtures of synthetic air and nitrogen were fed from the bottom of the reactor system. The gas flow was 220 dm3/h which corresponded to a gas velocity of around 0.1 m/s in the investigated temperature range.

Table 5-2

	[a] VM	[b] FC	[c] ASH	[d] α	[e] β
Wood	83.7	15.6	0.7	0.07	0.33
Straw	77	18.7	4.3	0.07	0.33
Olive	72.6	20.2	7.2	0.07	0.33

[a] Volatile matter (%)'
[b] Fixed carbon content (%)
[c] Ash content(%)
[d] Area evolution parameter during pyrolysis
[e] Area evolution parameter during char conversion

The gas flow was chosen such that the temperature of the gas corresponded to the reactor temperature at the position of the fuel particle. The sample was inserted by using a movable probe which manually was inserted from a cold environment into the hot reactor within a fraction of seconds. The sample holder consisted of a thin net on which the pellets were placed on. The outlet gas of the reactor system was analyzed with commercial analyzers for the measurement of CO, CO2, and NO. Figure 4 shows an example of raw data from the analyzers. The peak in the figure corresponds to the devolatilization, and the remaining tail corresponds to the char conversion. In the example, the maximum molar fraction of CO2 is around 0.12 during the devolatilization, and around 0.01 during the char conversion. The maximum CO molar fraction is for the same condition (not shown here) around 0.001 during the devolatilization, and below 0.0001 during the char conversion. Thus, more than 99% of the char carbon is oxidized to CO2 in the reactor system. Figure 5-8 also shows the deconvoluted signals. The lowest value of the deconvoluted NO curve, immediately after the peak, is taken as the starting point for the char combustion. This point is marked in the figure. In the experiments, the development of the external surface area was estimated from video uptakes of the combustion process.

The experiments were conducted at 1073, 1173 and 1323 K and with 10 vol.% O2. At 1173K, experiments were also performed with 3 and 19 vol.% O2. The NO and C

release rates can be calculated from molar fractions of CO, CO2 and NO measured at the analyzers:

$$\dot{m}_{NO,\exp t} = \frac{\dot{V}_{gas}\, p}{RT} M_{NO}\left(x_{NO}(t)\right) \qquad (1)$$

$$\dot{m}_{C,\exp t} = \frac{\dot{V}_{gas}\, p}{RT} M_{C}\left(x_{CO_2}(t) + x_{CO}(t)\right) \qquad (2)$$

Here, $\dot{m}$ is mass stream from the char particle (kg/s); $\dot{V}_{gas}$ is volume flow of gas (m3/s); p is pressure (Pa); M is molar mass (kg/mol), R is the universal gas constant (J/molK); T is temperature (K); and x is molar fraction.

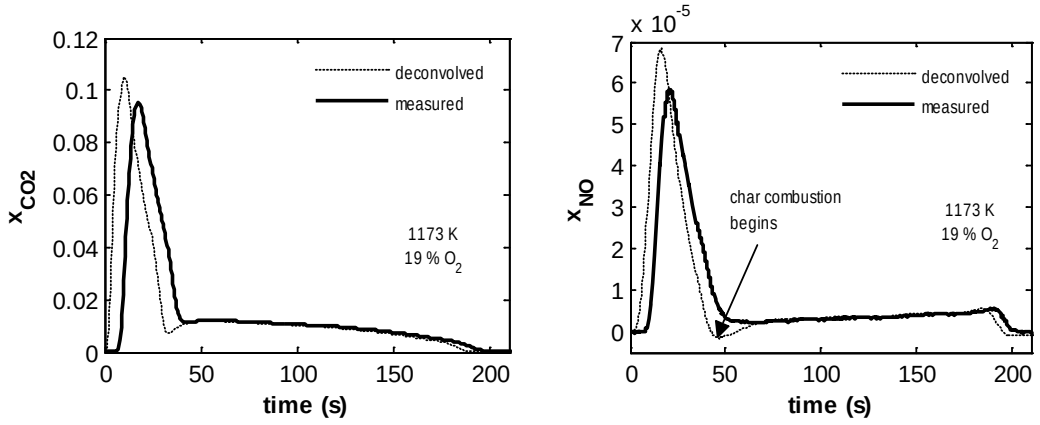

Figure 5-8: Raw data from the Single Particle Reactor. Deconvoluted signals of the CO2 and NO signals are included.

Kinetic parameters and area evolution parameters in models presented in Task 3.1 have been determined with multivariable optimization methods developed within this project [9]. Parameters are determined by fitting modeled conversion rates to experimentally determined conversion rates. The optimization methods are based on the brute force method since the optimization problems are non-convex.

The fuels investigated in the SPR are listed in table 2 and table 3. The fuels in table 2 have been used to investigate the change of the external surface area on pyrolysis and char oxidation rates and the fuels in table 3 have been used to investigate NO release rates at combustion conditions.

Table 5-3

	[a] VM	[b] FC	[c] ASH	[d] A_{NO}	[d] E_{NO}	[d] n_{NO}
Spruce Bark	74.5	21	4.5	1.94E-05	41	0.9
SRC poplar	82.3	16	1.7	7.89E-06	41	0.85
Danish straw	78.5	16	5.5	2.25E-05	43	0.7
Torrefied wood	72.5	27	0.5	2.04E-05	50	1

[a] Volatile matter (%)'

[b] Fixed carbon content (%)

[c] Ash content(%)

[d] Kinetic parameters - A (kg/m^{2}sPa^n)and E (kJ/mol) - and reaction order *n*

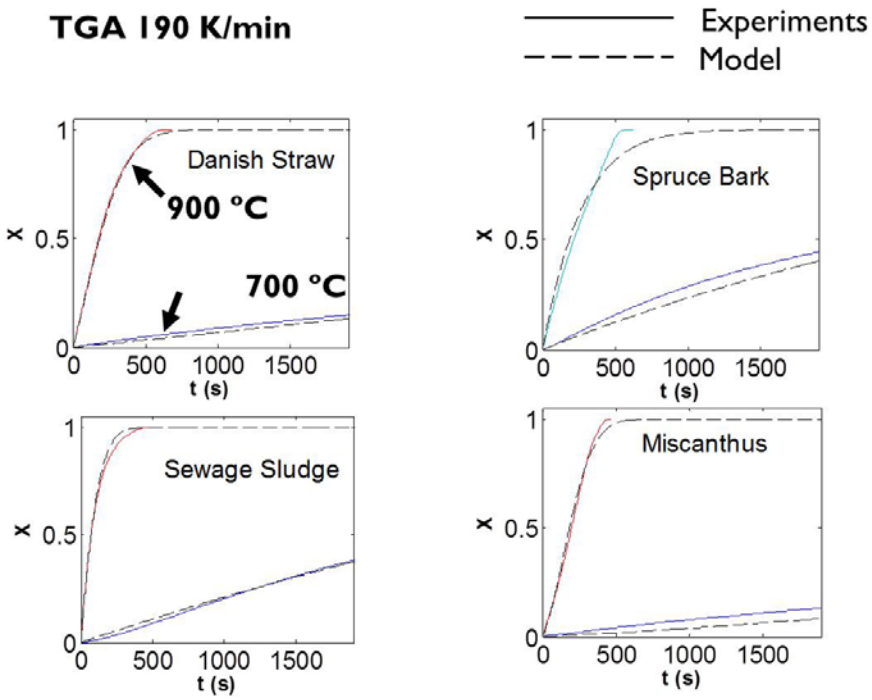

Figure 5-9: Modeled and experimental char gasification profiles from TGA tests.

Figure 5-9 shows modeled and experimental char gasification profiles from the TGA tests. It can be seen that the modeled profiles are in very good agreement to the experimental profiles. The determined parameters used in the model are present in Table 1. The activation energies are in the range of 150 kJ/mol and are in good agreement to reported values (Di Blasi). In the figure it can be seen that the conversion is significantly faster at 900 °C than at 700° C. This can be

explained by the high activation energies and that the gasification is limited by chemical kinetics.

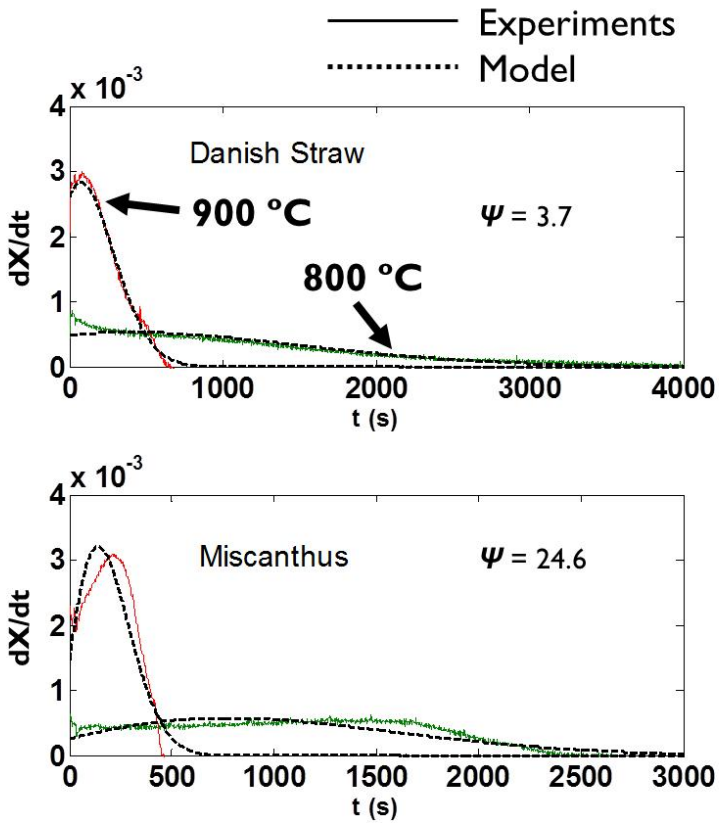

Figure 5-10: Modeled and experimental char gasification rates from TGA tests.

Figure 5-10 shows modeled and experimental gasification rates of the Danish straw char and the Miscanthus char straw. It can be seen that the agreement between the modeled and experimental rates is good. For the Danish straw char, the structural parameter ψ is low (3.7) and for the Miscanthus char ψ is high (24.6). In the first case, the internal specific surface area is almost proportional to the instantaneous char mass. Therefore, the gasification rate is highest in the beginning. In the second case the internal surface area grows significantly as function of conversion during the initial conversion stage. Therefore, the rate increases initially as a function of conversion although the mass of the char is decreasing.

Figure 5-10 shows modeled and measured conversion times of the biomass particles available in Table 5-3. It can be seen that both the devolatilization/pyrolysis times and the char oxidation times are predicted

accurately. The external surface area parameters used in the model are listed in Table 5-3.

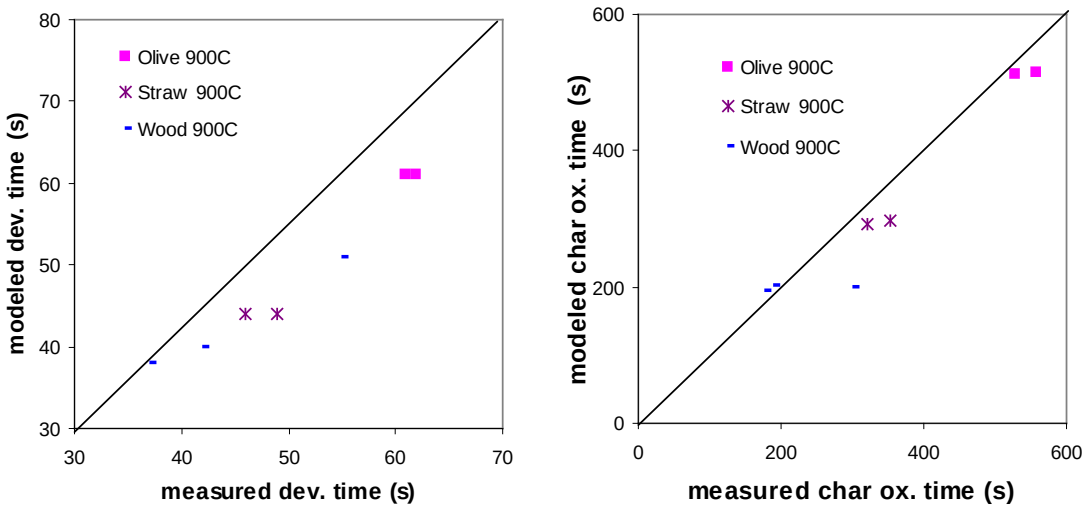

Figure 5-11: Modeled and experimental devolatilization/pyrolysis and char oxidation times.

In order to evaluate the influence of changes in the external surface area on devolatilization and char oxidation rates the following test is performed: the predicted devolatilization and the char oxidation times are compared using various values of α and β. A small value of α corresponds to a large initial char particle size, and a large value of α corresponds to a small char particle size. Since the char combustion is partly of fully limited by external mass transfer in the experiments, the char oxidation time is therefore limited by how the particle shrinks during devolatilization. Figure 5-12 shows predicted char oxidation times with various values of α. It is seen that decreasing α reduces the char oxidation time and vice versa. The char oxidation times illustrated in Figure 5-12 are predicted with β = 0.33, which, corresponds to mass transfer limited conversion. Figure 5-11 shows the corresponding char oxidation times for various values of β. It is clear that reducing β increases the char oxidation rate, and the char oxidation time decreases. This can be explained by that a smaller value of β gives that the external surface area decreases throughout the conversion. Since the predicted char oxidation times generally are smaller than experimental char oxidation times with β = 0.33, it is likely that β = 0.33 is reasonable since reducing β will overestimate char oxidation rates and thus decrease the time for char oxidation.

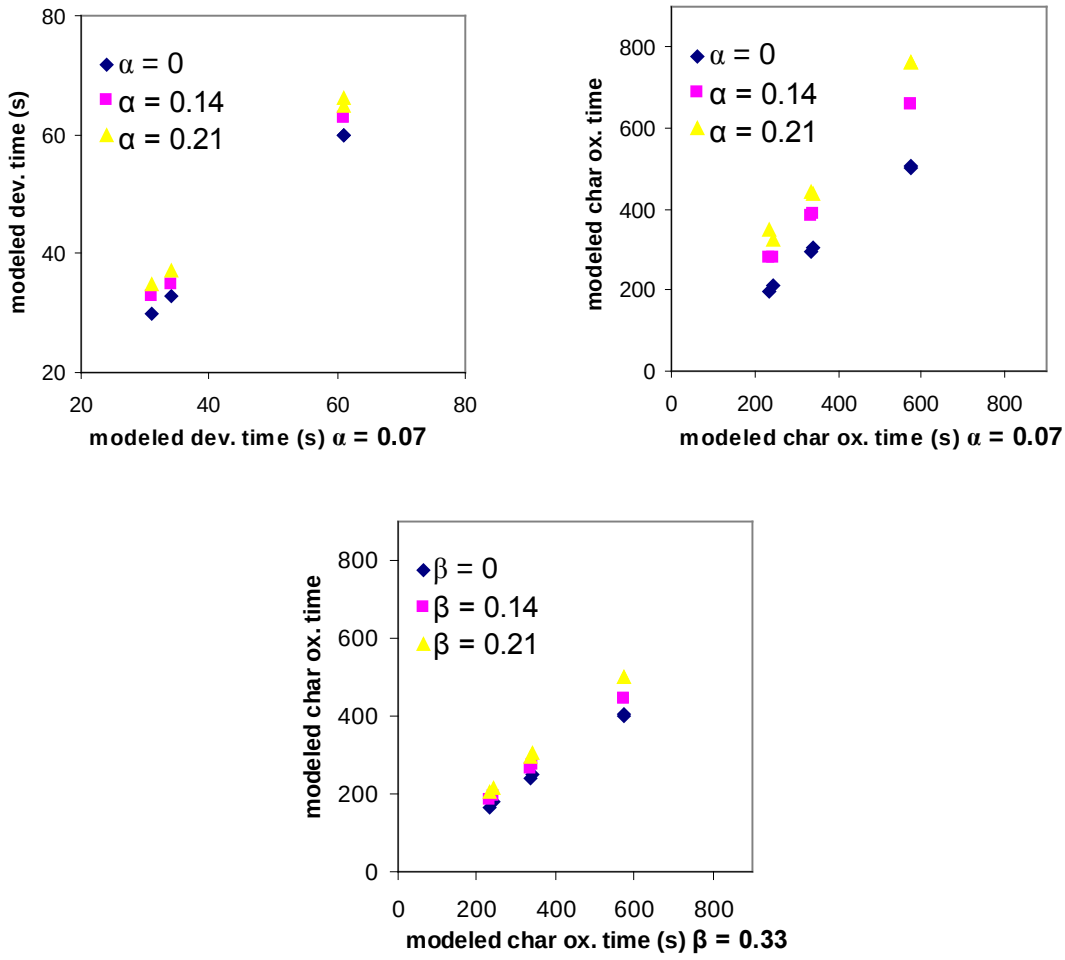

Figure 5-12: Modeled devolatilization/pyrolysis and char oxidation times with different evolution of the external surface area.

Figure 5-13 shows modeled and experimental NO release curves of the biomass chars in Table 5-3.

It can be seen that the NO release generally increases as a function of burnout. Thus, even though the particle decreases in mass and size, the NO release increases. It can be seen that the modeled NO release in some cases starts at zero, while it sometimes starts at a higher value. This is because the entire formed NO is reduced according to the model. In all of the shown figures the general agreement between the modeled NO release rates and the experimental NO release rates are good.

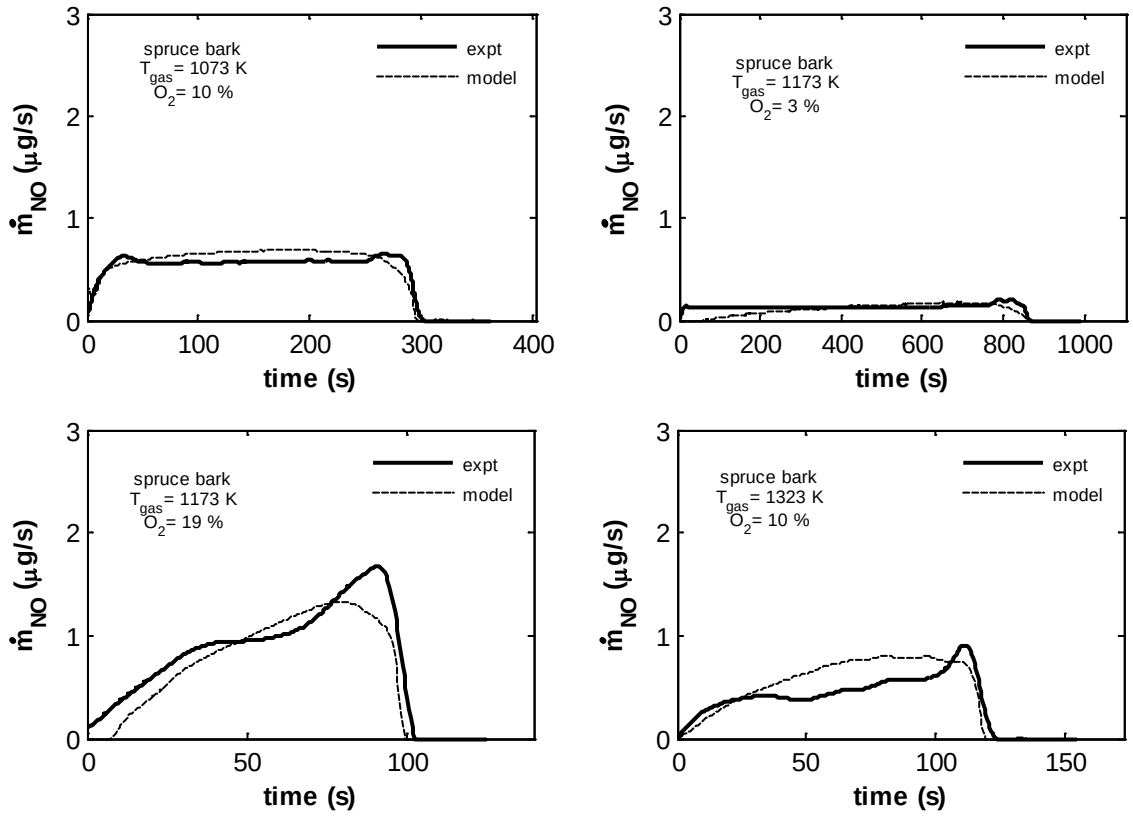

Figure 5-13: Modeled and experimental NO release rates for char particles of spruce bark.

Figure 5-14 shows experimental and modeled amounts of released NO from the biomass chars. In all cases, the agreement between the modeled and experimental amounts of released NO during the char combustion is good. At 1073 K and 10 vol.% O2, the lowest value of the percentage of char-N being released as NO is observed for the Danish straw, 23%, and the highest value is observed for the torrefied wood char, 56 %. At 1373 K, and 10 vol.% O2, the corresponding values are 15 % (Danish straw char) and 24 % (torrefied wood char). This is equivalent to that NO corresponding to 5-13% of the initial fuel-N nitrogen is released at 1073 K, and that NO corresponding to 3-5% of the initial fuel nitrogen is released at 1373 K during the char combustion stage. Based on these results, the Danish straw char has the best potential to reduce the formed NO, even though the potential is nearly as good for the other chars.

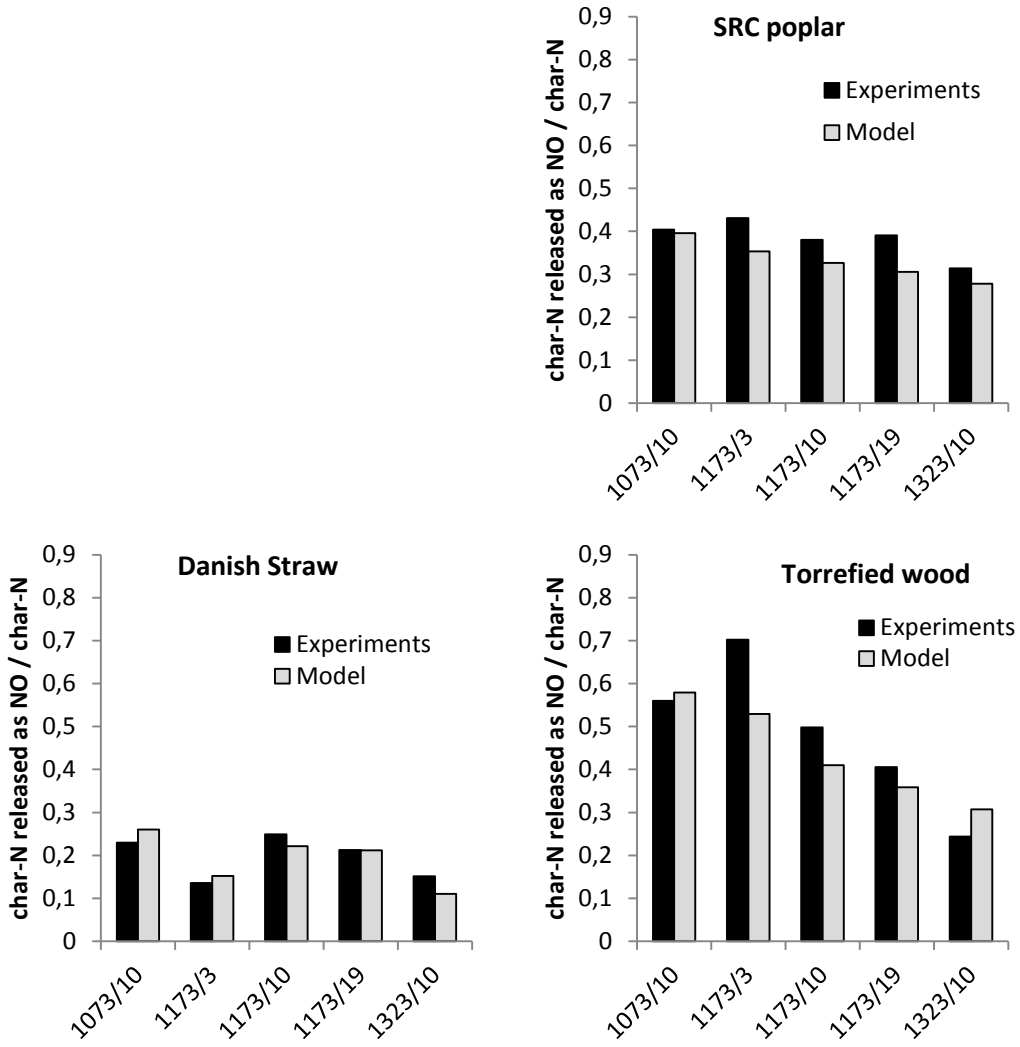

Figure 5-14: Modeled and experimentally measured amount of NO released during char combustion of biomass particles. The numbers on the x-axes refer to temperature (K) and vol. % oxygen in the surrounding gas.

Input parameters to various models have been determined from single particle experiments and from TGA experiments. The parameters are given in Table 1-Table 3. NO release from combustion of biomass particles have been modeled and compared to measurements.

References

1. Ehsan Houshfar, Judit Sandquist, Wilson Musinguzi, Roger Antoine Khalil, Michael Becidan, Oyvind Skreiberg, Franziska Goile, Terese Lovas, Lars Sorum. COMBUSTION PROPERTIES OF NORWEGIAN BIOMASS: WOOD

CHIPS AND FOREST RESIDUES. Applied Mechanics and Materials, 110–116, pp. 4564–4568, 2012. [DOI: 10.4028/www.scientific.net/AMM.110-116.4564]

2. Ehsan Houshfar, Oyvind Skreiberg, Terese Lovas, Dušan Todorović, Lars Sorum. EFFECT OF EXCESS AIR RATIO AND TEMPERATURE ON NOx EMISSION FROM GRATE COMBUSTION OF BIOMASS IN THE STAGED AIR COMBUSTION SCENARIO. Energy & Fuels, 25 (10), pp. 4643-4654, 2011. [DOI: 10.1021/ef200714d]
3. Ehsan Houshfar, Oyvind Skreiberg, Dušan Todorović, Alexandra Skreiberg, Terese Lovas, Aleksandar Jovović, Lars Sorum. NOx EMISSION REDUCTION BY STAGED COMBUSTION IN GRATE COMBUSTION OF BIOMASS FUELS AND FUEL MIXTURES. Fuel, In Press, 2012. [DOI: 10.1016/j.fuel.2012.03.044]
4. Ehsan Houshfar, Terese Lovas, Oyvind Skreiberg. EXPERIMENTAL INVESTIGATION ON NOx REDUCTION BY PRIMARY MEASURES IN BIOMASS COMBUSTION: STRAW, PEAT, SEWAGE SLUDGE, FOREST RESIDUES, AND WOOD PELLETS Energies, 5 (2), pp. 270–290, 2012. [DOI: 10.3390/en5020270]
5. Ehsan Houshfar, Roger Antoine Khalil, Terese Lovas, Oyvind Skreiberg. ENHANCED NOx REDUCTION BY COMBINED STAGED AIR AND FLUE GAS RECIRCULATION IN BIOMASS GRATE COMBUSTION. Energy & Fuels, In Press, 2012. [DOI: 10.1021/ef300199g]
6. Giuntoli J, de Jong W, Verkoojien AHM, Piotrowska P, Zevenhoven M, Hupa M., *Combustion characteristics of biomass residues and biowastes: fate of fuel nitrogen*, Energy and Fuels 2010; 24: 5309-5319.
7. Colomba Di Blasé, *Combustion and gasification rates of lignocellulosic chars,*Progress in Energy and Combustion Science, Volume 35, Issue 2, April 2009, Pages 121-140. Oskar Karlström. Anders Brink, Mikko Hupa, Leonardo Tognotti, *Multivariable optimization of reaction order and kinetic parameters for high temperature oxidation of 10 bituminous coal chars*, *Combustion and Flame, Volume 158, Issue 10, October 2011, Pages 2056-2063.*
8. Oskar Karlström, Anders Brink, Mikko Hupa, *Time dependent production of NO from combustion of large biomass char particles, Fuel, In Press, Corrected Proof, Available online 27 June 2012.*
9. Oskar Karlström, Anders Brink, Mikko Hupa, *Influence of change in the external surface area on combustion rates of biomass pellets*, *European Combustion Meeting 2011, Wales.*

6. WP5: Advanced Characterization – Ash Related Issues

Coordinated by Dr. Thomas Brunner, BE2020+/TUG

Ash related issues such as ash melting on grates of fixed-bed combustion systems, bed agglomeration in fluidized bed combustion systems, deposit formation and corrosion as well as particulate emissions may cause severe problem during the combustion of new biomass fuels (e.g. agricultural fuels, energy crops, etc.). Therefore, advanced fuel characterization with special respect to ash related issues are a task of outstanding relevance. During combustion easily volatile elements (K, Na, S, Cl as well as easily volatile heavy metals) are partly released from the fuel to the gas phase. There they undergo chemical reactions and the resulting compounds (alkali and heavy metal sulfates, chlorides and oxides) either form particles or directly condense on heat exchanger surfaces. The release of the relevant elements thereby strongly depends on their association in the biomass fuel. With state-of-the-art fuel characterization methods the release behavior of easily volatile ash forming species cannot be predicted and therefore, new advanced fuel characterization methods are needed. Moreover, the melting behavior of the residual ashes is of relevance since it influences slagging as well as bed agglomeration. With state-of-the-art methods ash melting can also not be predicted with sufficient accuracy since the constraints (temperatures, heating rates, gas atmospheres) in real-scale applications are not correctly considered in the testing standards. Therefore new, advanced fuel characterization methods are also needed concerning this issue.

Accordingly the objectives of WP5 were:

- Advanced characterization of biomass fuels according to fuel indexes and chemical fractionation.
- Determination of the association of ash forming matter in biomass fuels with emphasis on volatile alkali compounds and heavy metals.
- Advanced characterisation of biomass fuels by µTGA and macro-TGA, TGA/DSC and XRD analysis of ashed fuel samples.
- Performance of lab-scale combustion tests as innovative method for fuel characterisation and in order to gain basic data concerning the release behavior of alkaline metals, S, Cl and heavy metals.
- Determination of release curves for alkaline metals and heavy metals.

- Establishment of an advanced fuel database for conventional and new biomass fuels investigated within the project.
- Determination of release curves for alkaline metals and heavy metals.
- Establishment of an advanced fuel database for conventional and new biomass fuels investigated within the project.

		Wood pellets (softwood)	Wood chips (spruce)	Wood chips (beech)	Bark (spruce)	Waste wood (Q1-Q4)	Miscanthus	SRC (poplar)	Sewage sludge	Torrified softwood	Straw
moisture content	wt% w.b.	7.10	13.83	7.43	12.76	13.23	9.72	8.30	9.00	2.11	10.03
ash Content	wt% d.b.	0.43	0.34	0.64	4.98	1.70	2.26	1.75	41.43	0.48	5.57
CO2-free ash content	wt% d.b.	0.33	0.24	0.45	3.62	1.53	2.17	1.32	41.05	0.38	5.42
sum of oxides	wt% d.b.	0.34	0.25	0.44	3.38	1.56	2.20	1.38	39.92	0.37	5.55
Carbon	wt% d.b.	49.53	48.88	48.50	49.66	49.01	47.97	48.48	29.47	56.80	45.93
Hydrogen	wt% d.b.	6.13	6.23	6.05	5.63	6.13	5.92	6.06	4.43	5.68	5.86
Nitrogen	wt% d.b.	0.10	0.02	0.06	0.34	1.33	0.28	0.36	4.35	0.03	0.64
Sulphur	mg/kg d.b.	50	43	92	301	370	392	289	12,300	39	1,110
Chlorine	mg/kg d.b.	16	27	37	99	3,100	1,810	156	841	11	1,900
Silicon	mg/kg d.b.	299	69	53	3,180	1,710	4,500	375	45,000	83	14,000
Calcium	mg/kg d.b.	950	1,040	1,340	12,900	3,200	1,300	4,120	35,400	1,160	4,330
Magnesium	mg/kg d.b.	122	106	284	813	443	552	464	5,800	243	792
Aluminium	mg/kg d.b.	90	26	18	733	449	83	92	16,800	16	61
Iron	mg/kg d.b.	53	21	16	528	363	84	139	58,800	253	84
Manganese	mg/kg d.b.	94	76	49	675	79	66	5	696	75	23
Phosphorus	mg/kg d.b.	38	31	53	335	93	201	726	36,600	60	947
Potassium	mg/kg d.b.	507	358	1,280	1,840	703	4,850	2,860	3,580	574	9,040
Sodium	mg/kg d.b.	15	7	10	99	326	27	41	1,990	6	114
Copper	mg/kg d.b.	0.42	0.70	0.92	3.56	8.65	1.62	2.97	316.00	1.35	2.59
Zinc	mg/kg d.b.	12.40	7.60	3.06	82.40	62.80	10.30	24.50	994.00	28.40	7.51
Lead	mg/kg d.b.	0.14	0.17	0.14	0.76	132.00	0.28	0.38	25.84	0.61	0.44
Cadmium	mg/kg d.b.	0.12	0.09	0.05	0.85	0.19	0.11	0.49	0.90	0.19	0.15

Table 6-1: Chemical composition of the SciToBiCom fuels. Explanations: w.b. … wet basis; d.b. dry basis; CO_2-free ash content … ash content based on oxides

At the kick-off meeting a list of fuels to be investigated within the project was defined. According to this list the SciToBiCom fuels are:

- Wood pellets (softwood)
- Wood chips (softwood/spruce)
- Wood chips (hardwood/beech)
- Bark (spruce)
- Straw
- Waste wood (Q1 to Q4 according to Austrian regulations)
- Miscanthus
- SRC (poplar)
- Sewage sludge
- Pellets from torrefied wood

The fuels were collected by DTU (straw) and BE2020 (all other fuels). They were analysed by BE2020 regarding the parameters ash content, moisture content, C, H, N, S, Cl, Si, Ca, Mg, Fe, Al, Mn, P, K, Na, Cu, Zn, Pb and Cd. Then, sub-samples were distributed among the partners according to their needs regarding mass and fuel particle size. Thereby it was secured that the experimental work within WP5 was performed with comparable fuel samples.

In Table 6-1, the chemical compositions of the fuels are presented. The methods applied for the analyses can be taken from [Sommersacher et al, 2012].

6.1 Task 5.1: Advanced Fuel Characterization Based on Fuel Indices

As mentioned in the introduction, possible ash related problems (ash melting on grates, bed agglomeration in fluidized bed combustion systems, deposit formation and corrosion, particulate emissions) as well as problems regarding SO_x and HCl emissions are often associated with the utilisation of new biomass fuels. With state-of-the-art fuel characterisation methods these issues cannot be sufficiently covered and therefore, new and advanced fuel characterisation methods are needed. One option to gain quick first indications regarding the problems mentioned is the development, evaluation and application of fuel indexes. Within SciToBiCom, BE2020+ focused at investigations regarding the applicability of certain fuels indexes for fixed-bed biomass combustion systems.

Proximate and ultimate analysis of the fuels investigated (ash content, contents of N, S, Cl, major and minor ash forming elements – see Table 6-1) formed the basis for the work presented. These analyses results were applied for the calculation and evaluation of fuel indexes. The fuel indexes are defined by considering the physical behaviour and chemical reactions of dedicated elements during biomass combustion, known interactions of different ash forming elements during thermal biomass conversion and correlations and experiences gained from pilot and real-scale combustion as well as lab-scale combustion tests with conventional and new biomass fuels. Data derived from combustion tests performed at BIOENERGY 2020+, the Institute for Process and Particle Engineering, Graz University of Technology (IPPE/TUG), and BIOS BIOENERGIESYSTEME GmbH, Graz, were considered.

Fuel indexes as a tool for advanced fuel characterisation have a long history in coal combustion. Accordingly, in a pre-evaluation step existing empirical correlations for coals were tested regarding their applicability for biomass fuels.

It was seen that indexes developed for coal can not be applied for biomass which is mainly due to the different associations of minerals and metals in biomass and coal.

Far less empirical correlations or fuel indexes predicting combustion related problems have so far been found in literature for biomass [Visser et al., 2004], [Gilbe et al., 2008], [Lindström et al., 2008]. For fluidized bed combustion systems the indexes (Ka+Na)/(2S+Cl), (Ka+Na+Si)/(Ca+P+Mg) and K/Si have been investigated. The index (Na+K)/(2S+Cl) is based on the general observation that the initial gas phase alkali concentration is attributable to the alkali concentration in the fuel. A molar (Na+K)/(2S+Cl) ratio >1 reflects the chance that the excess alkali over the sum of S and Cl would stay in the bed and may react with silicates. The formation of alkali-silicates is often observed and leads to sintering or de-fluidization. The index (K+Na+Si)/(Ca+P+Mg) is applied to describe the probability of the formation of a non-sticky outer coating on a bed material particle. Also a third agglomeration indicator, the molar K/Si ratio, was introduced. To describe slagging tendencies and the K retention in fixed-bed combustion the molar amounts of Si-(Cl+Ca+Mg) in the fuel have been investigated. The molar Si/(Ca+Mg) ratio has been reported to predict the slagging tendency for residential heating appliances.

Within SciToBiCom the investigation of the fuel indexes has been performed for the broad spectrum of the SciToBiCom fuels ranging from different types of wood to herbaceous and agricultural biomass as well as sewage sludge. Summing up the following results could be achieved. More detailed information has been published in [Sommersacher et al., 2012].

Fuel indexes, which allow for accurate qualitative predictions, are the molar 2S/Cl ratio regarding corrosion risks and the molar (Si+P+K)/(Ca+Mg) ratio regarding the prediction of the ash-sintering temperature. Indexes which can be applied with some restrictions regarding other constraints are the sum of K, Na, Zn and Pb regarding the aerosol formation potential, the molar ratios of Si/(Ca+Mg) and (Si+P+K)/(Ca+Mg) regarding ash melting properties, as well as the molar ratio of (K+Na)/[x*(2S+Cl)]) regarding HCl and SO_x emissions.

During combustion, easily and semi-volatile elements (K, Na, S, Cl, Zn and Pb) are partly released from the fuel to the gas phase, where they undergo chemical reactions and finally contribute to problems concerning emissions, deposit formation and corrosion. With decreasing molar 2S/Cl ratios in the fuel, for instance, the amount of alkaline chlorides in aerosol emissions and consequently also in ash deposits on heat-exchanger surfaces increases (see Figure). According

to literature, a molar ratio of 2S/Cl <8 increases the risk of high temperature Cl corrosion. A ratio below 4 indicates high corrosion risks.

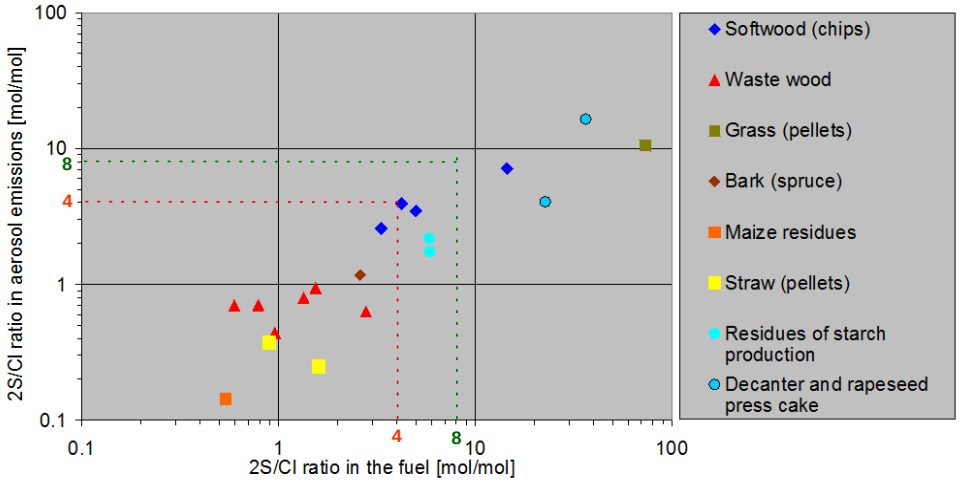

Figure 6-1: Dependency between the molar ratios of 2S/Cl in fuels and aerosol particles. Explanation: >8: low corrosion risk; <4: high corrosion risk; data taken from the BE2020 and IPPE/TUG databases.

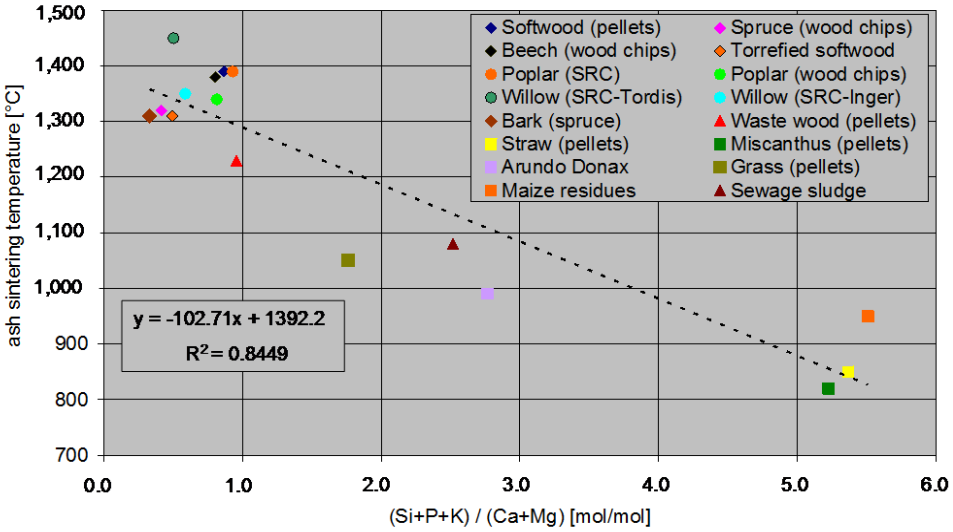

Figure 6-2: Molar (Si+P+K) / (Ca+Mg) ratio versus ash-sintering temperature for different biomass fuels. Explanation: the correlation is statistically significant ($p<0.05$); the data gained from the SciToBiCom fuels have been supplemented with database values from BE2020 and IPPE/TUG for other fuel assortments

The molar ratio of (Si+P+K)/(Ca+Mg) is an indicator which can generally be applied regarding the pre-evaluation of ash-melting tendencies and is also valid

for P-rich fuels. For values <1 no ash melting problems have to be expected while with increasing value of the index the ash melting temperatures decrease. Also the molar Si/(Ca+Mg) ratio can provide first information about ash-melting tendencies, however, it can only be applied for P-poor fuels. Moreover, the molar (Si+P+K) / (Ca+Mg) ratio may also be used as a first indicator for the K-release to the gas phase.

The sum of K, Na, Zn and Pb (in mg/kg dry fuel) describes the potential for aerosol and deposit formation, which increases with rising values of this index.

The molar ratio of (K+Na)/[x*(2S+Cl)], where x represents the ratio of the average K- and Na-release in relation to the average S- and Cl-release from the fuel to the gas phase, provides a first prediction concerning the HCl and SO_x emissions expected. For values >0.5, it is very likely that most of the S and Cl will be embedded in the ashes.

The fuel indexes calculated for the different SciToBiCom fuels as well as background information concerning the combustion related evaluation of these fuel indexes has been integrated into the SciToBiCom advanced fuel database (Task 5.6).

6.2 Task 5.2: Advanced Fuel Characterization Based on Chemical Fractionation, SEM and Other Techniques

Chemical fractionation is a method based on selective leaching by water, ammonium acetate and hydrochloric acid. The method was originally developed by Benson and Holm (1985) for the characterization of coal. Baxter (1994) used a modified version for the characterization of 7 biomass fuels. At Åbo Akademi University the method has been further developed for biomass and waste characterization. This method can be helpful when determining how ash-forming elements are bound in the fuel.

Figure 6-3 presents a simplified scheme showing that the stepwise leaching distinguishes between different types of ash-forming matter in a fuel according to their solubility in different solvents.

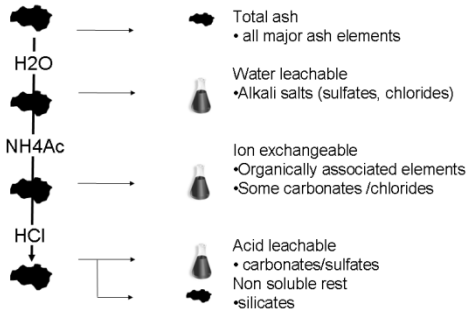

.

Figure 6-3: Simplified scheme of the fractionation procedure.

Fuel samples were milled to a particle size below 5 mm to facilitate handling and acceptable leaching times. Too small particles have shown to clog filters, whereas too large particles demand a too long leaching time. Increasingly aggressive solvents, i.e. water (H_2O), 1M ammonium acetate (NH_4Ac) and 1M hydrochloric acid (HCl) leach samples into a series of four fractions (including the unleached residue) for analysis. The amounts of leaching agents as suggested by Baxter (1994) and Benson et al. (1985) cannot be applied when leaching dry biomass fuels. It is difficult to achieve proper mixing for most fuels. Instead, an excess of water (up to 500ml/50g fuel for agricultural residues) should be used in the first step, firstly to achieve proper wetting of the samples, secondly to achieve proper leaching. These problems are not encountered in the other leaching steps, since the solid samples here are already thoroughly wet from the previous steps and extensive washing.

The increasingly aggressive solvents leach samples into a series of four fractions (including the unleached residue). The untreated samples, the liquid fractions and the remaining solids were analyzed by an external laboratory according to Swedish standards. Depending on the metals analyzed the solids residues were ashed and dissolved in hydrochloric acid, in HNO_3/H_2O_2 or molten with $LiBO_2$ and dissolved in HNO_3. In most cases ICP-AES or ICP-SFMS was used as analytical technique for the dissolved solids as well as the leachates.

Typical main ash-forming components, which are leached out by water include alkali sulfates, -carbonates, -phosphates and -chlorides. Elements leached out by NH_4Ac are believed to be organically associated, such as Mg, Ca as well as K and Na. HCl leaches the carbonates and -sulfates of alkaline earth and other metals. Silicates and other minerals remain mainly in the insoluble residue. Heavy metals

are usually leached out at low pH, with an exception of Zn, Pb and Mn that also may be present in water soluble and/or ion exchangeable forms
Fuels analysed were:

1. Danish straw,
2. Miscanthus,
3. Beech
4. Poplar,
5. Wood waste,
6. Torrefied wood and
7. Sewage sludge
8. Bark (from a boiler in Finland)

Danish straw and Miscanthus:

The solubility of Danish straw and Miscanthus exhibits typically the leaching of agricultural residues and grasses. Both fuels are relatively high in silicon, potassium and chlorine. Silicon is found present as insoluble minerals embedded in the skeleton of the straw. In straw as much as 25% of the silicon may be found soluble either in water or acetate, probably as soluble potassium silicates. Potassium may be found mainly water soluble in connection to phosphates, chlorides and sulfates. Part of sulfur is non-soluble indicating organic association. Phosphorous may be present organically associated or as water soluble alkali salts. Calcium seems to be present as either water soluble compounds, organically associated, as carbonates and as sulfates.

Heavy metal concentrations in Danish straw were low. Mn (≈20 ppm), was soluble in all solutes. The same leaching behavior was found for Zn (≈7 ppm) and Cu (≈5 ppm). Other heavy metals were present in neglectable concentrations. In Miscanthus, Mn was present in higher concentrations when compared to straw, some 70 ppm versus 20 ppm. The solubility of the heavy metals was comparable to that in straw. Water soluble Zn may origin from water soluble fertilizers often containing easily soluble Zn-compounds.

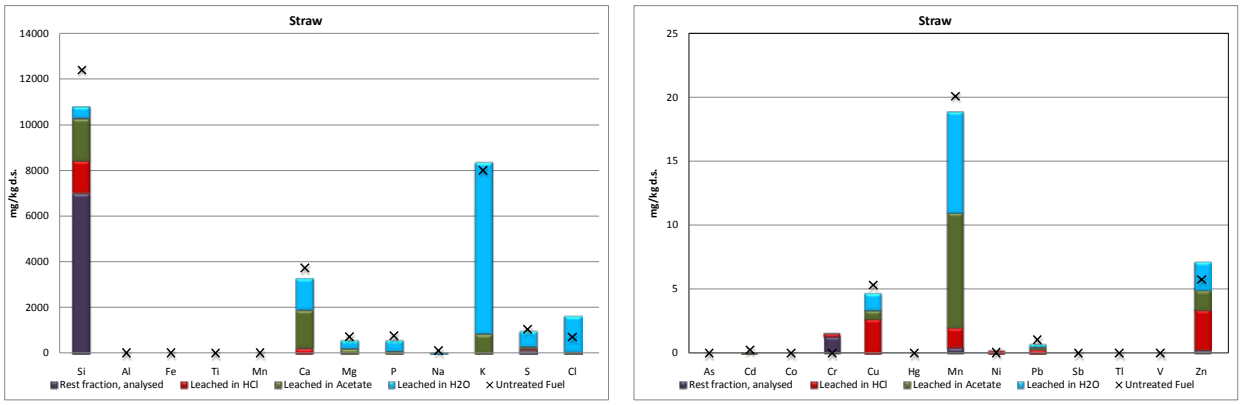

Figure 6-4: Leaching results of main ash forming matter and heavy metals in Danish straw.

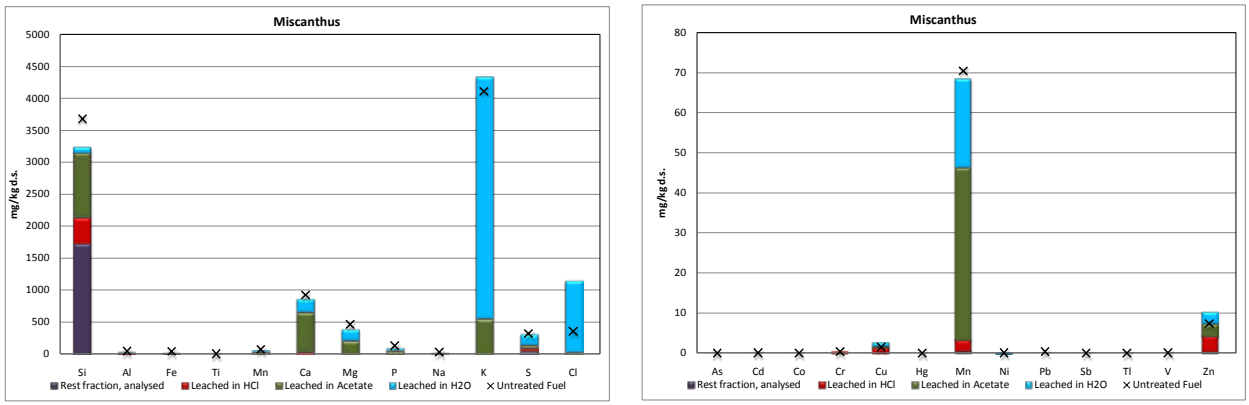

Figure 6-5: Leaching results of main ash forming matter and heavy metals in Miscanthus.

Beech and Poplar:

Both Beech and Poplar were fuels low in ash indicating a low contamination of soil particles. This shows also in the leaching results, where non dissolved mineral matter was neglectable. Ash forming matter exhibited a typical leaching behavior for clean wood. Potassium and calcium were mainly found water soluble or present in an ion exchangeable form. Calcium oxalate may also be found soluble at low pH. Phosphorus may be present either as alkali salts or organically bound.In Beech Mn was the heavy metal present in the largest amounts (≈53 ppm) whereas Zn was the heavy metal present in poplar (≈25 ppm). Mn in Beech was found mainly ion exchangeable. Zinc in Beech was found mainly acid soluble whereas it was found in all three solutes when leaching Poplar.

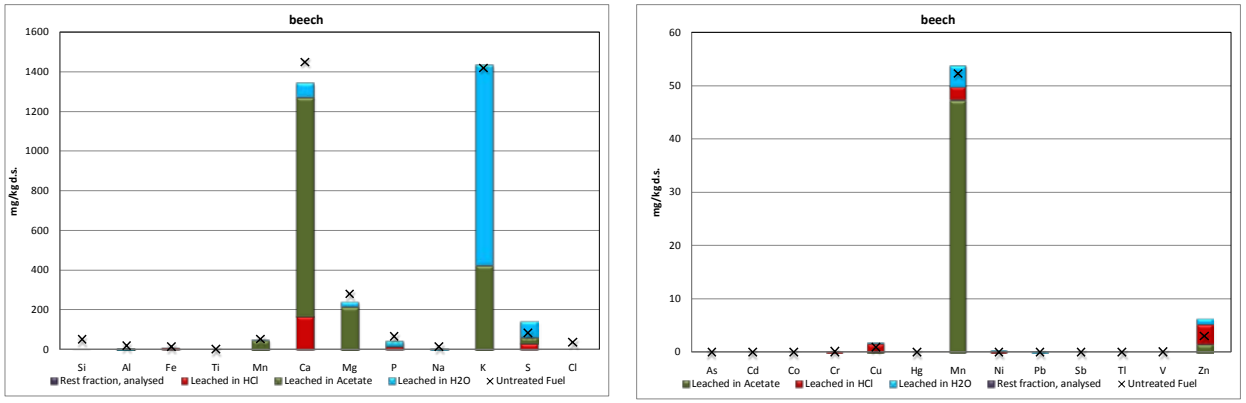

Figure 6-6: Leaching results of main ash forming matter and heavy metals in Beech.

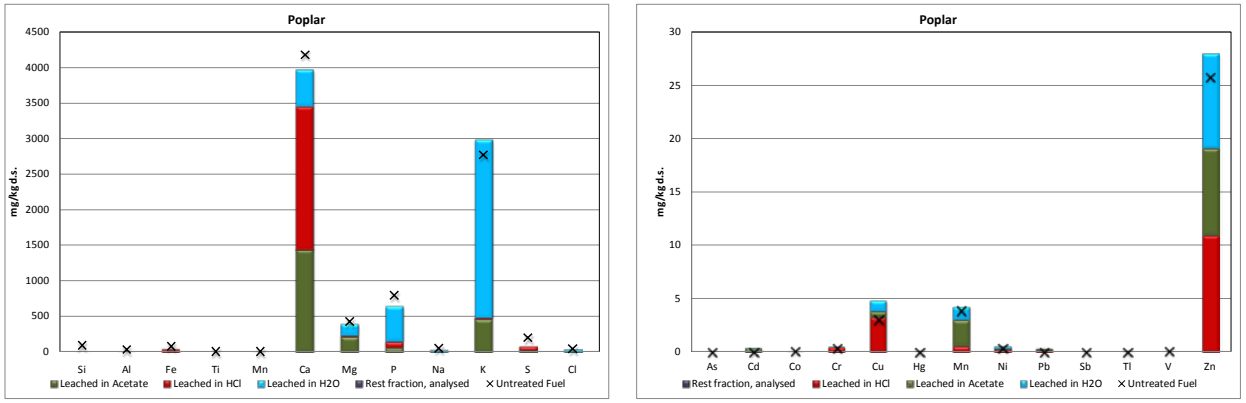

Figure 6-7: Leaching results of main ash forming matter and heavy metals of Poplar.

Waste wood

Waste wood exhibits the leaching behavior of regular wood. Chlorine is mainly water soluble. Sulfur may be present as water soluble alkali salts or organically bonded in the fuel and being thus insoluble. Wood waste is often contaminated with sand or other silicates, indicated by the rather large fraction of ash forming matter that was found in the rest fraction. Calcium exhibits a, for wood, typical leaching behavior and was found in all three solutes. Calcium may be present as water soluble calcium salts, organically associated calcium that can be replaced by NH_4^+ and acid soluble CaC_2O_4 or $CaCO_3$.

The main difference between clean wood and wood waste is the presence of heavy metals. The wood may have been contaminated with paint, spikes and other metal parts.

Most heavy metals are mainly acid soluble or non-soluble at all. Exceptions form Zn and Mn that may be present in ion exchangeable or water soluble forms as well and may be present included in the wood structure itself.

The results described above clearly illustrate the inhomogeneity of this kind of waste fuel. Spreading in leaching data may be expected in the fractions representing the contamination of wood.

Solid fuels were analyzed twice at ALS as well as in Graz at BE2020+. Main ash forming matter as analyzed from Graz seem to fit the leaching data best. Untreated fuel analyses have been carried out twice at the Swedish laboratory, the second time with acceptable results.

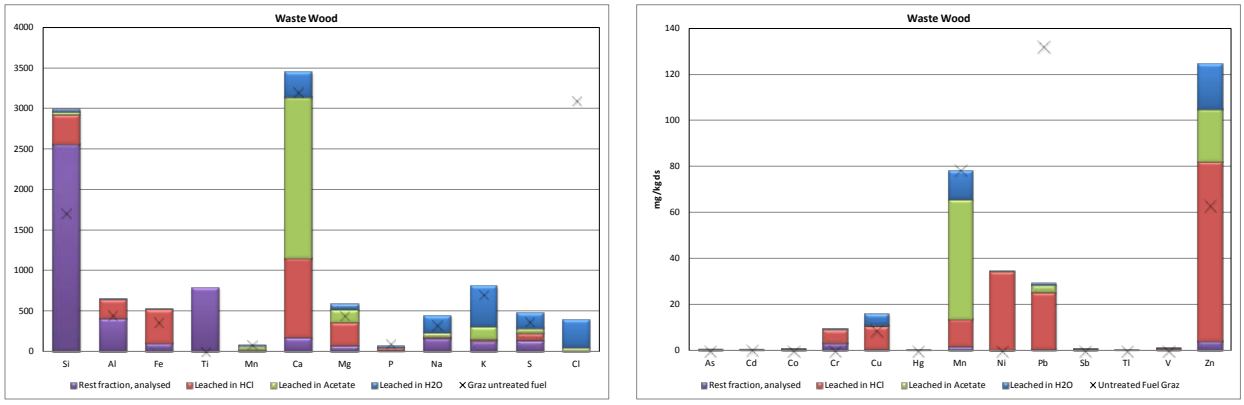

Figure 6-8: Leaching results of main ash forming matter and heavy metals of waste wood.

Torrefied wood

Torrefied is a wood that has been pyrolysed at low temperatures. This implies that volatile matter has been removed from the fuel matrix and char and ash forming matter remain behind. The chemical fractionation results show typical leaching results of ash forming matter from wood, although concentrations present in the fuel are substantially lower when compared to poplar or beech. Also here analyses as carried out in Sweden were repeated to verify results (see table with fuel analyses).

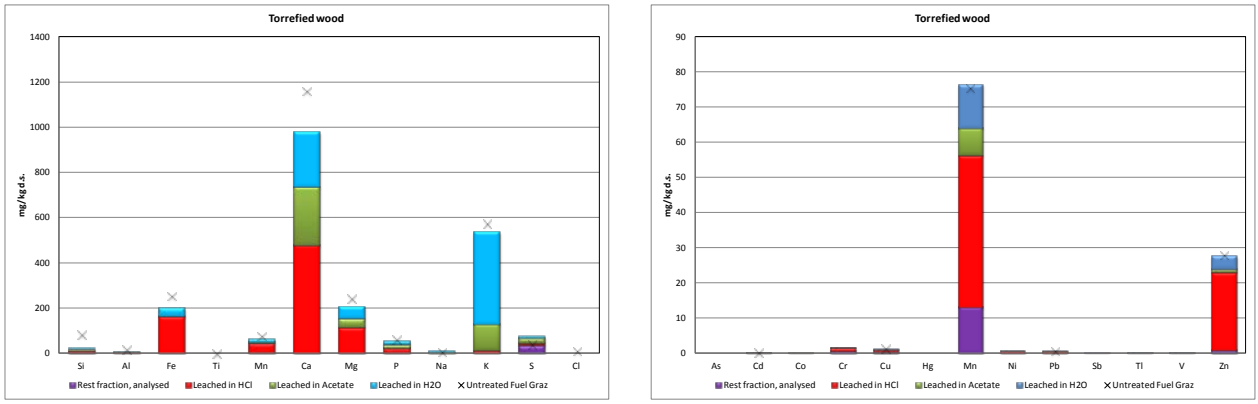

Figure 6-9: Leaching results of main ash forming matter and heavy metals of torrefied wood.

Sewage sludge

Sewage sludge was highest in ash content when compared to the other fuels described in this report. Sludges from waste water treatment plants contain either a substantial amount of aluminum- or iron sulfate that has been added to the waste water stream for precipitation of phosphates.

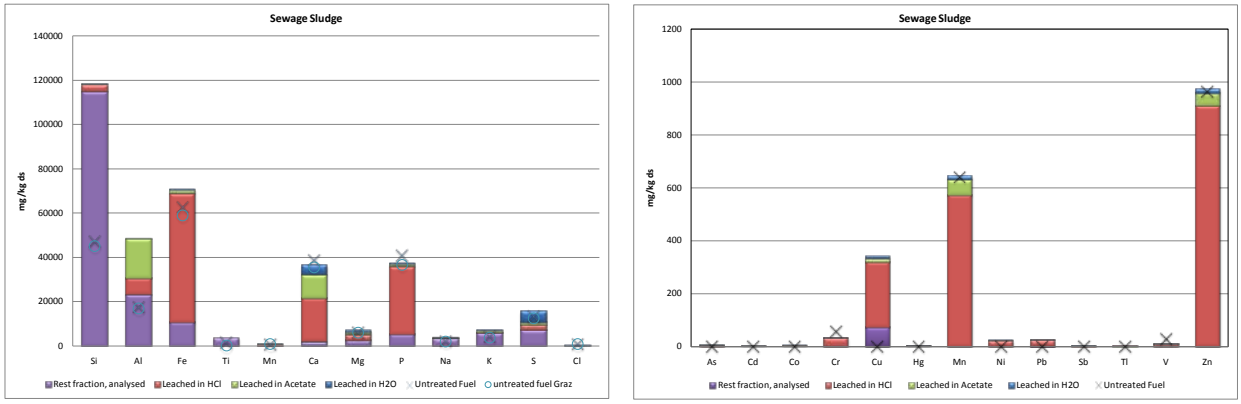

Figure 6-10: Leaching results of main ash forming matter and heavy metals in sludge.

The sewage sludge as analyzed here contained iron that was mainly leached at low pH. In combination with acid soluble phosphorus this indicates the presence of iron phosphate Non soluble silicates and aluminum indicate the presence of zeolites. Zeolites have been found to play a role in potassium capture during combustion. After the waste water treatment sludge has been dewatered and a

large fraction of potentially water soluble ash forming matter was removed at this stage leaving only a small fraction of soluble soluble material behind.

Bark (from a boiler in Finland 102209)

The bark analysed within this project had a composition similar to the barks analysed before at ÅA. Si, Ca and K were the main ash forming matter present in the highest concentrations.

Silicon was found in soil impurities. Calcium may be soluble in either water, acetate or hydro chloric acid, indicating the presence of water soluble salts, Ca-oxalate and ion exchangeable forms of calcium. Potassium was found mainly soluble in water and acetate indicating the presence of simple soluble salts. Part of sulfur and phosphorus was found insoluble, indicating presence of covalently bonded S and P in the organic fuel matrix.

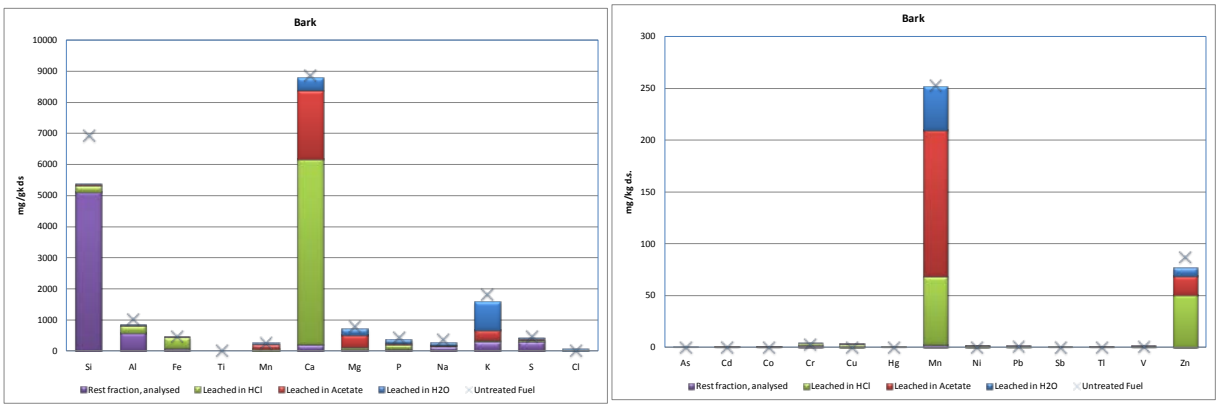

Figure 6-11: Leaching results of main ash forming matter and heavy metals of bark

SEM analyses of ashed fuels

Fuel samples were ashed in a laboratory furnace in an atmospheric atmosphere at 500, 700 and 900°C respectively during 15 minutes. Fuels as well as ashes retrieved were mounted on carbon tape, coated and subjected to SEM_EDX analyses using a a LEO Gemini 1530 with a Thermo Scientific UltraDry Silicon Drift Detector (SDD). Overall analyses were carried out at a magnification of 30x. Image mapping was carried out at a magnification of 500x after which phase maps were calculated and spot analyses were done

Agricultural Residues

After ashing particles high in Si and K can be detected in agricultural residues. These have molten at higher (see Figure 6-12) temperatures. At an ashing temperature of 900° these particles are clearly dominating. Also P rich particles (combined with Si, Ca and K) may be present.

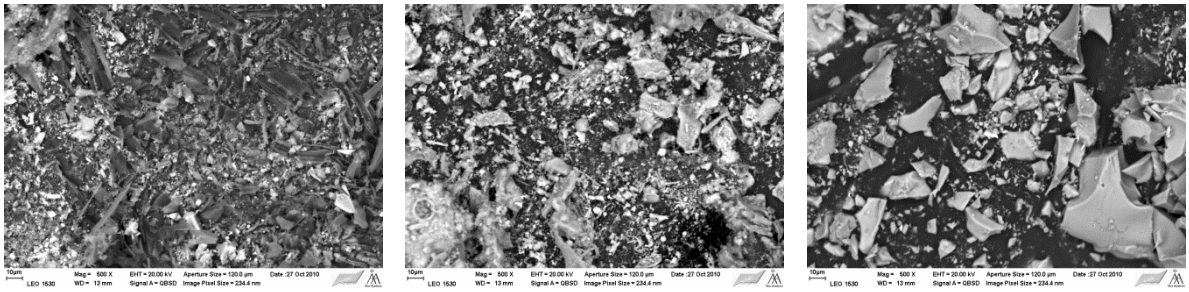

Figure 6-12: Miscanthus ashed at 500 (left), 700(centre) and 900°C (right) during 15 minutes

Wood Derived Fuels

Overall analyses of beech show that ash mainly contains sand and Ca_K_P rich particles Discreet particles can be noticed rich in Ca-P and S. Mineral phases as found in beech, poplar and torrefied wood are either richer in Ca or K in combination with Ca/K-P and S. Besides the typical wood phases wood waste also contains Si, Al, Fe and Ti. And can thus be considered a polluted wood.

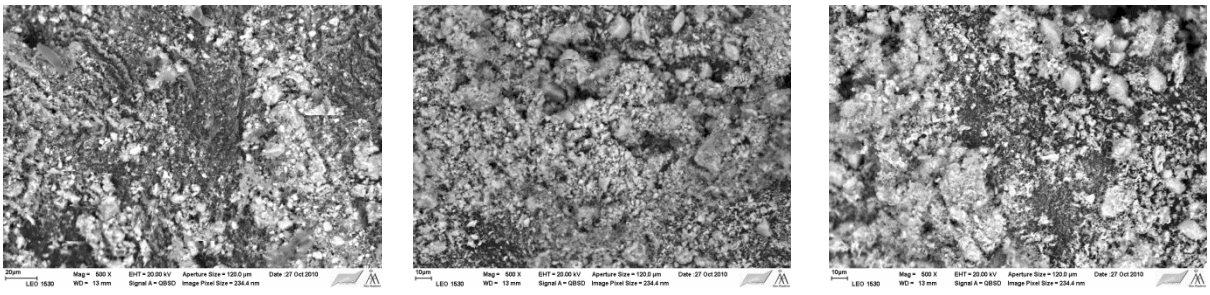

Figure 6-13: Poplar ashed at 500 (left), 700(centre) and 900°C (right) during 15 minutes

Sludge

SEM analyses of sludge show that this ash rich fuel contains phases rich in Si, Ca, Fe, P and or S. These seemed present in the same particles impossible to distinguish which compounds were present in small particles covering larger ones. Since $FeSO_4$ was present in the sludge as a P-capturing additive Fe-S and Fe-

P rich particles are to be expected. Also some Ca-P and Ca-S rich particles may have formed during ashing.

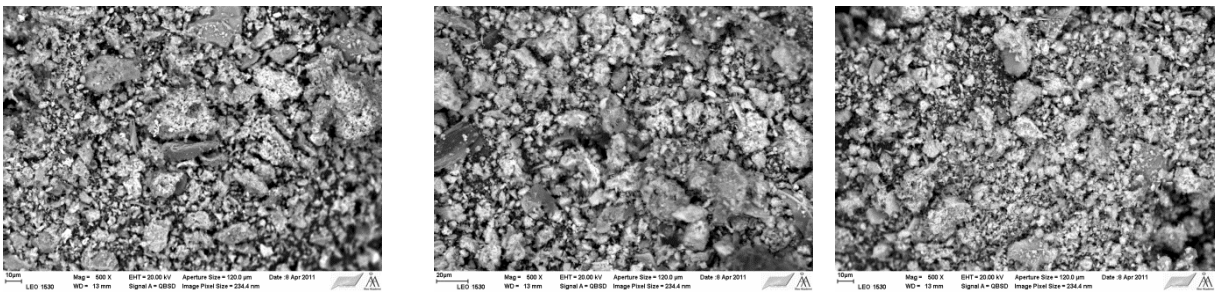

Figure 6-14: Sludge ashed at at 500 (left), 700(centre) and 900°C (right) during 15 minutes

t of view is potassium. Potassium is the root cause to bed sintering, fouling and corrosion when using biomass based fuels. K is present in the fuel in different forms, and it is of vital interest to identify these forms. Here, the selective leaching analysis of the ash forming matter is very useful. The insoluble part of the potassium is most often in the form of silicate contaminations of the fuel (clay etc). This part of potassium is in a very inert form and does not take part in the lively chemistry of the more reactive forms of potassium. In biomass based fuels K is mostly in soluble form. It can be present either in ionic form in salts in the aqueous fluids of the plant, or as directly organically bound K ions These potassium compounds will be effectively released in combustion and thus be easily available to any further reactions in the flue gases

Calcium is the element present in the highest concentration in woody biomasses. It is partially organically bonded and thus exchangeable in the ammonium acetate leaching. It is also present as crystalline salt particles, mostly calcium oxalate – especially in biomasses having a high content of Ca, such as bark . This fraction of Ca is found mainly in the acid soluble fraction of the leaching test. The organic calcium compounds will be converted to calcium oxide. Calcium oxide has a low vapor pressure and a high melting point. Consequently, organic calcium in biomass is released in combustion as small solid particles, CaO(s). Calcium oxalate (several crystalline forms containing crystal water) in the biomass will also form finely divided small oxide particles under hot furnace conditions.

Chlorine is present in biomass fuels as chloride salts. These salts may vaporize at combustion as alkali chlorides (KCl(g), NaCl(g)) or decompose and release the Cl which rapidly converts to HCl(g). Most (all) chloride salts in fuels are soluble and show up in the soluble fraction of the leaching test Some part of Cl may also be present as organic chlorine compounds. The most important of these are waste

derived fuels containing rests of polyvinyl chloride (PVC) polymers. The Cl in PVC is insoluble in the leaching test and will stay in the rest fraction.

Sulfur is present in biomasses as both inorganic sulfate anions and as organic sulfur. According to recent studies roughly ¾ of the sulfur in woody biomasses is organically bound and ¼ as soluble alkali sulfates. The organic sulfur will be fully released in combustion – primarily as H_2S and other reduced gaseous species which then oxidize to SO_2. The fate of the sulfur in alkali sulfate is not clear. It may stay connected to the alkali sulfate, but it also may be released due to some decomposition reaction of the alkali sulfate.

Phosphorus may be present in biomass fuels as either soluble phosphate salts, or in organic molecules containing phosphorus. In woody biomass around 3/4 of the phosphorus is inorganic and some 1/4 organic. However, in other biomasses this ratio may be different. In some annual plants the phosphorus content may be very high. The release and fate of the various phosphorus compounds in combustion furnaces and flue gases is not well studied. However, it is clear that both alkali and calcium phosphates may form

6.3 Task 5.3: TGA/DSC and XRD Analysis of Ashes

A good knowledge of the melting behavior of biomass fuel ashes is of great relevance to avoid operational problems in biomass-fired boilers. The occurrence of melt is believed to enhance both, stickiness propensity of ash particles to heat-exchange surfaces and cohesive strength of deposits built.

Therefore, the objectives of Task 5.3 were to investigate the ash melting behavior of ashes derived from the SciToBiCom fuels using a TGA/DSC-method (thermogravimetric analysis/differential scanning calorimetry) as a kind of simultaneous thermal analysis (STA). The data gained should also act as one basis for the calibration of thermodynamic equilibrium calculations regarding ash melting performed within Task 2.2.

The biomass samples were firstly dried and ashed at 550°C using a muffle furnace that was supplied with air. After milling in a planetary mono mill (material: silicon-carbide) the samples were divided and sub-samples were subjected to ultimate chemical analysis, standard ash melting tests according to DIN 51730 as well as thermoanalytical investigations by means of STA technique.

For thermoanalytical investigations a Netzsch STA 409 CD thermal analyzer using TGA/DSC configuration (thermogravimetric analysis/differential scanning calorimetry) was applied. This study has mainly been focused on receiving information on ash melting as a function of temperature, whereby ash melting processes were identified as the distinctive endothermic peaks of the DSC curves recorded. A clear separation from simultaneously running evaporation reactions was partly not possible, but it did not significantly affect the determination of melting characteristics.

During the experiments, the ash samples have been placed in a Pt/Rh crucible and a reference material in the reference crucible on top of the sample carrier. To obtain a more uniform heat distribution inside the crucibles, they have been covered with lids. A hole in the middle of the lids allows the vapor exchange between sample and gas atmosphere. The output information from each test is sample mass (TGA), and heat flow (DSC), as a function of temperature. The DSC signal describes the heat flow required to keep the sample and reference at the same temperature. A difference in heat flow corresponds to exothermic or endothermic reactions inside the samples, e.g., changes of state (such as melting), changes of phases and other physical properties like heat capacity and thermal conductivity. Melting processes have been determined as the endothermic peaks in the related DSC curves.

The STA measurements were performed under the following conditions:

- Sample preparation: ground in a mortar to ensure homogeneity
- Sample mass: about 20 mg
- Sample holder: TGA/DSC, Pt/Rh crucible
- Temperature range: 25 to 1,300 °C
- Heating rate: 10 K/min
- Atmosphere: synthetic air
- Gas flow rate: 100 ml/min (at 0°C and 1 atm)
- Measurement: weight loss and heat flow over time

In order to check the reproducibility of the instrument and the sample homogeneity, the majority of the measurements has been repeated twice and in few cases three times.

To demonstrate the results from the STA measurements, the test runs for the straw and beech ashes are presented in Figure.

Straw has a typical ash composition with silicon and potassium as the dominant elements (22.4 and 17.0 wt% d.b. respectively) and contains smaller amounts of chlorine and sulfur (1.87 and 1.45 wt% d.b. respectively). The mass changes up to

400°C are generally assumed to be evaporation processes of physically and chemically bound H_2O (crystal water). In case of straw ash the mass loss of 3.82 wt% (w.b.) can be attributed to this process.

The STA curve that is observed shows further in the temperature range of 400 to 850°C a mass loss of 3.33 wt% w.b. characterized by an endothermic peak at 669°C, which is caused by $CaCO_3$ decomposition and release of CO_2. The mass decrease observed in the temperature segment from 850 to 1,150°C may primarily be attributed to KCl evaporation which is in good agreement with the existing literature data. In this temperature segment simultaneously the initial melting of the ash sample occurs. The endothermic peaks at 905°C and 1,037°C, along with the peak at 1,149°C, can be assigned to different stages of ash melting. The mass loss above 1,150°C may be explained by K_2O release most probably caused by the decomposition of slag silicates.

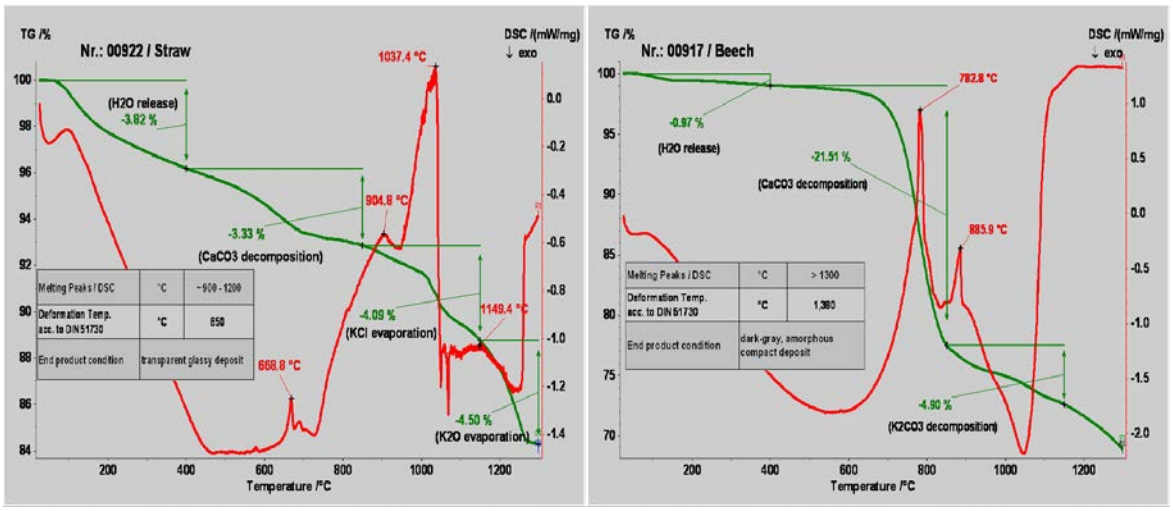

Figure 6-15: Results of simultaneous thermal analysis (STA) for straw ash and beech ash. Explanations: TG (thermogravimetric analysis) ...mass loss in % w.b.; DSC... differential scanning calorimetry; sample mass….straw: 20.51 mg; beech: 20.81 mg.

For beech ash two endothermic peaks appear within the temperature segment between 400°C and 1,150°C, accompanied by mass losses of 21.51 wt% and 4.90 wt% w.b. respectively. The first peak appears at 783°C and is attributed to the decomposition of $CaCO_3$. The most likely explanation for the second endothermic peak at 886°C is the decomposition of K_2CO_3, which is characteristic for ashes with low silicon contents. No melting processes were identified during this STA test, what has been expected due to the low molar ratio of Si/(Ca+Mg) (0.05 mol/mol).

The results from the TGA/DSC measurements generally showed a good reproducibility, verifying the quality of this method for studying the temperature generated transformations of biomass ashes. The TGA curves for the single measurements with one fuel (mass loss of initial weight in %) showed nearly identical matches in all cases. Also the DSC curves demonstrate in most cases a satisfying reproduction of enthalpy changes (endothermic peaks). However, a certain difference was observed with ashes from straw and waste wood, probably caused by the strong change in physical properties of the ashes (thermal conductivity, swelling/shrinkage of the sample, etc.) during the test runs.

Based on chemical analysis of the input material (ashed fuels) weight losses in the characteristic temperature segments can be estimated. A reasonably good agreement of these estimations with the experimental results was achieved for all fuels investigated. That verifies the correct definition of the release-processes responsible for major mass loss contributions which are:

- below 400°C: H_2O-release
- 400 - 850°C: decomposition of $CaCO_3$ (very pronounced for Ca-rich wood ashes)
- 850 - 1,150°C: degradation of K_2CO_3 to CO_2 and K_2O as well as evaporation of KCl. A significant release of KCl can be observed for the Cl-rich miscanthus and straw ashes (4.42% and 4.22% respectively), which is in good agreement with estimations based on chemical analyses of the input material.
- 1,150 - 1,300°C: most likely decomposition of sulfates and release of K2O

In Table 3, a comparison of the ash melting peaks identified during the TGA/DSC tests with results regarding the deformation temperature gained from ash melting tests according to DIN 51730 are presented. Generally an acceptable agreement can be observed whereas for ashed fuel samples with low melting temperatures, very good agreement is achieved. Especially for these ashes the TGA/DSC method bears the additional advantage that different melting stages can be determined separately, which is not possible with the standard ash melting test.

		Wood pellets	Wood chips (spruce)	Wood chips (beech)	Bark (spruce)	Waste wood (Q1-Q4)
Deformation temperature	°C	n.o.	1,320	1,380	1,310	1,230

DSC melting peaks	°C	> 1,300	> 1,300	> 1,300	> 1,300	~ 850 – 1,250

		Miscanthus	SRC (poplar)	Sewage sludge	Straw
Deformation temperature	°C	820	1,390	1,080	850
DSC melting peaks	°C	~ 850	> 1,300	~ 1,130	~ 900 – 1,200

Table 6-3: Comparison of the ash melting peaks determined by TGA/DSC with the deformation temperature according to the standard ash melting test (DIN 51730). Explanations: n.o. … did not occur.

The data gained from the tests performed as well as a comprehensive description of the methodology have also been implemented in the SciToBiCom advanced fuel database (Task 5.6).

In order to gain deeper insights into the different phases formed during the melting processes, the ashes treated in the STA have been subjected to XRD analyses. Especially for the ash poor fuels (e.g. wood chips and wood pellets) only very low amounts of ashes could be made available (due to the low sample intake of about 20 mg for the STA/DSC tests). Also the formation of amorphous phases complicated the evaluation of the results especially for straw ashes. Therefore, the results gained from the XRD analyses have to be interpreted as solely qualitative results.

Regarding wood and bark ashes it was found that Ca_2SiO_4 plays an important role in the ash composition. Moreover, $Ca_3MgSi_2O_8$ (merwinite), K_2MgSiO_4 (diopside) and MgO (periclase) were found in higher quantities. The poplar sample showed higher amounts of $CaCO_3$ (calcite), $K_2Ca(CO_3)_2$ (buetschlite), $CaSO_4$ (anhydrite), $Ca(OH)_2$ (portlandite) and MgO (periclase) as well as of $Ca_3MgSi_2O_8$ (merwinite).

The composition of the sewage sludge ash sample on the other side was dominated by $Ca_3(PO_4)_2$ (wittlockite), Fe_2O_3 (hematite) and SiO_2 (cristobalite).

Even if these XRD data have, due to the low samples masses, to be treated with care and only in a qualitative way, they provided a good basis for the evaluation of the melting curves calculated with the TEC-based model within Task 2.2. A comparison with the main constituents of the different phases calculated by TEC showed acceptable agreement with the XRD results.

6.4 Task 5.4: Lab-scale combustion tests (BE2020+)

As a further advanced fuel characterisation method lab-scale reactor tests have been performed by BE2020/TUG. The lab-scale reactor applied was especially developed in order to investigate the combustion and volatiles release behaviour of different fuels and fuel mixtures in fixed-bed systems. It further provides comprehensive information regarding the release of NO_x precursor species, the release of ash forming elements as well as first indications concerning ash melting.

The core of the reactor is a cylindrical retort which is heated electrically and controlled by two separated PID-controllers. The fuel is put in a cylindrical sample holder of 100 mm height and 95 mm inner diameter which is equipped with 5 thermocouples (NiCr-Ni) in order to monitor the fuel bed temperatures during the test runs. The material of the reactor wall and the sample holder is silicon carbide, which is inert under reducing and oxidising conditions, and therefore does not react with the fuel, ash and flue gas. The mounting and vessel for the fuel bed are placed on the plate of a scale. The scale is mechanically separated from the retort by a liquid sealing and is used to determine the weight loss of the sample over the test run period. The sample holder with the biomass is introduced into the pre-heated reactor and therefore a rapid heating, which is well comparable with the one in real-scale thermal conversion processes, can be achieved.

Flue gas samples are extracted from the gas volume above the fuel bed, partly treated respectively conditioned (dilution, temperature stabilization) and introduced into different gas analyzers. Moreover, the flow and temperatures of the reaction medium (e.g.: air, N_2 or different mixtures of O_2 and N_2) as well as several flue gas and reactor temperatures are recorded with NiCr-Ni thermocouples. By analyzing the fuel as well as the residual ashes, also information about inorganic element release can be gained via mass and element balances over the test run. More detailed information about the lab-scale reactor setup, the measurement equipment applied as well as the test run protocol can be taken from [Brunner et al., 2012].

Test runs with all SciToBiCom fuels have been performed. As an example in Figure the trends regarding the mass loss, the fuel bed and flue gas temperatures as well as the concentrations of the main gas species and of the NO_x precursors over a test run with beech wood chips are displayed. As it can be seen, the test run duration was about 1,020 seconds. At the beginning, mainly drying takes place

indicated by a moderate mass loss, low fuel bed temperatures and the release of H_2O. After about 140 seconds, fuel decomposition starts indicated by decreasing O_2 concentrations and increasing CO_2 concentrations in the flue gas.

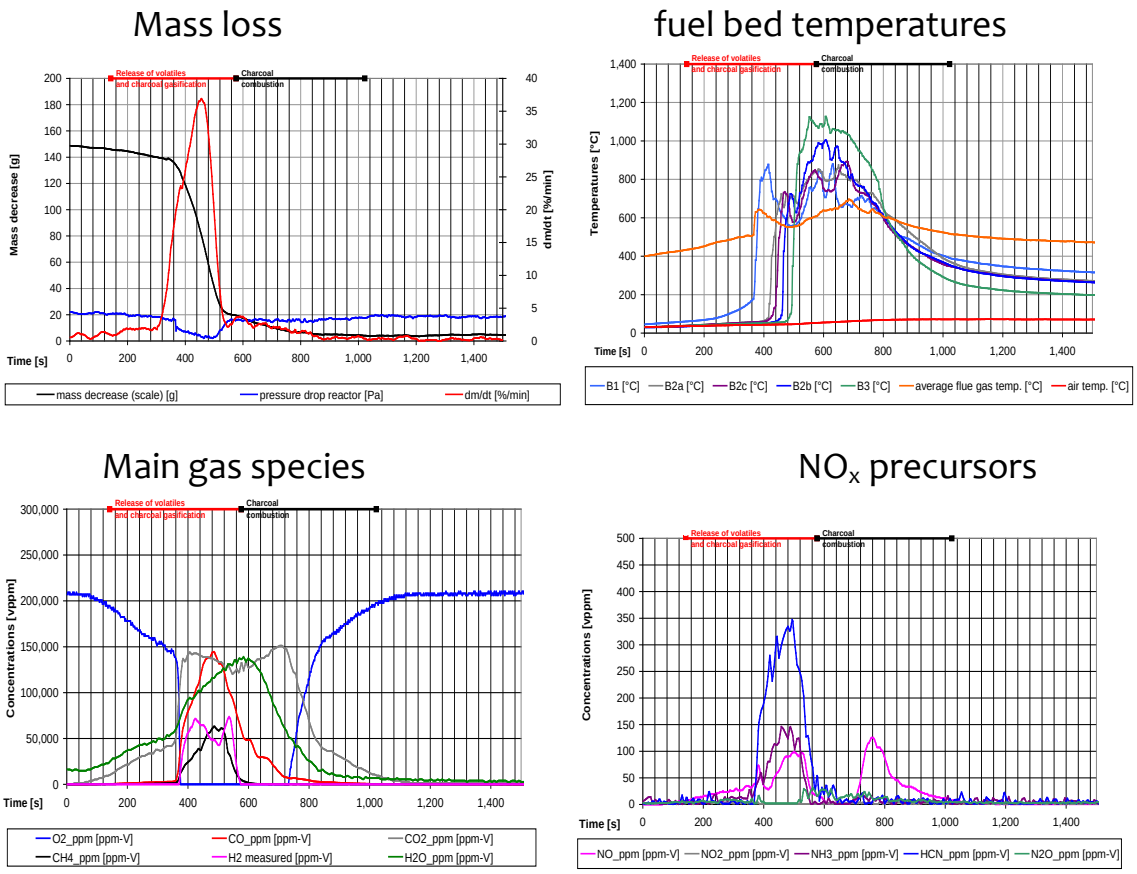

Figure 6-16: Measured trends regarding the mass loss, the fuel bed and flue gas temperatures, main gas species as well as of the NO_x precursor concentrations for a test run with beech woodchips. Explanations: fuel bed temperature measurements: B1: top, B2: middle and B3: bottom of the sample holder.

The main decomposition phase starts with a rapid decrease of the O_2 concentration to zero level after 360 seconds. Release of volatiles and parallel charcoal gasification take place until around 600 seconds of the test run duration. A rapid mass loss, an increase of the bed temperatures to 400°C - 550°C as well as combustion air ratios below 1 are typical indicators for this phase. Mainly CO_2, CO, H_2O, CH_4 and H_2 as well as minor amounts of other hydrocarbons are released to the gas phase. After 560 seconds H_2 and CH_4 drop to zero which is taken as an indicator for the end of the release of volatiles and the start of the charcoal combustion phase. This phase is characterised by smaller amounts of CO and increasing CO_2 concentrations in the flue gas as well as slowly increasing O_2

concentrations (increasing excess air ratio). During this phase typically the highest fuel bed temperatures, in this case 1,127°C, are measured.

In general, the maximum fuel bed temperatures during volatilisation and charcoal gasification varied between 791°C (sewage sludge) and 1,290°C (softwood pellets). During charcoal combustion they reached values between 1,033 (SRC poplar) and 1,301 (softwood pellets). These temperature levels are comparable with those achieved during real-scale combustion processes, which is important for the applicability of the lab-scale reactor data. In the following the most relevant results regarding NO_x precursor release and inorganic element release are presented. More detailed information can be taken from [Brunner et al., 2012]

Regarding the conversion of the fuel N into N bound in NO_x precursors, a decreasing ratio with increasing fuel N-content is observed. While for the N-poor fuels such as softwood pellets, spruce woodchips and torrefied wood almost 100% of the fuel N are converted, this number decreases to 33.7 wt% for the N-rich fuel sewage sludge. In Figure the share of different NO_x precursors on TFN is summarized. An interesting information that can be gained from this diagram is that for chemically untreated wood fuels HCN is the most relevant NO_x precursor while for waste wood, sewage sludge, miscanthus and straw NH_3 strongly dominates and HCN only plays a minor role.

In Figure 6-18, the data concerning the release of aerosol forming elements from the fuel is summarized and Figure 6-19 shows the maximum potential for aerosol emissions that can be calculated from these data. For all fuels high Cl (>91 wt%) and S (>71 wt%) release rates occur. Also Pb shows for all fuels with the exception of straw and sewage sludge release rates of more than 93 wt%. The Zn release is with the exception of sewage sludge, poplar and straw always higher than 70 wt% reaching values of more than 94 wt% for softwood pellets, torrefied softwood and waste wood. Regarding K and Na, significant differences regarding the release are observed when comparing the different fuels. The rates vary from 1 wt% for sewage sludge to around 51 wt% for torrefied softwood.

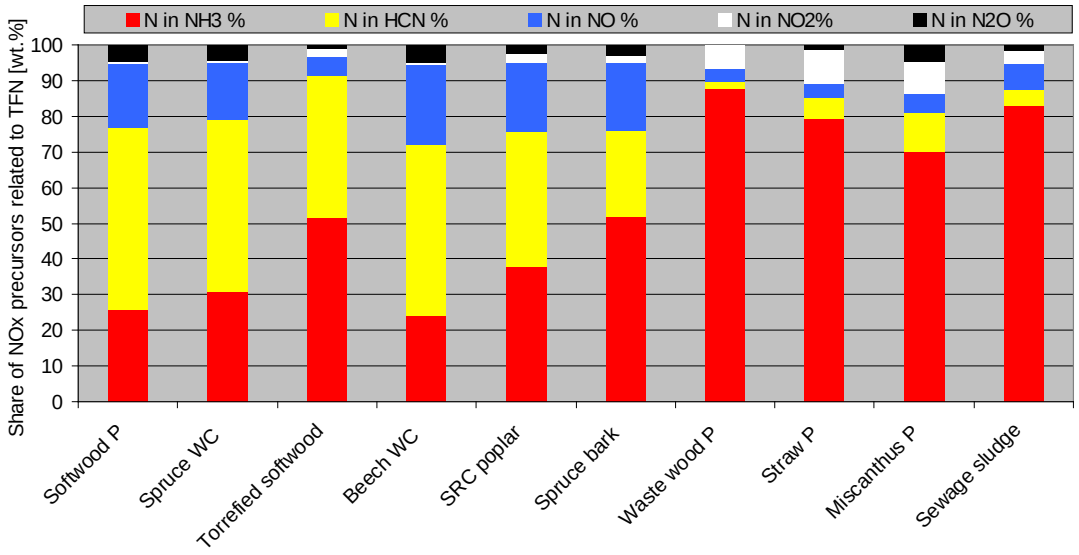

Figure 6-17: Share of NOx precursors related to TFN. Explanations: TFN … total fixed nitrogen (sum of N in NO, NH_3, HCN, NO_2 and N_2O); P … pellets; WC … woodchips.

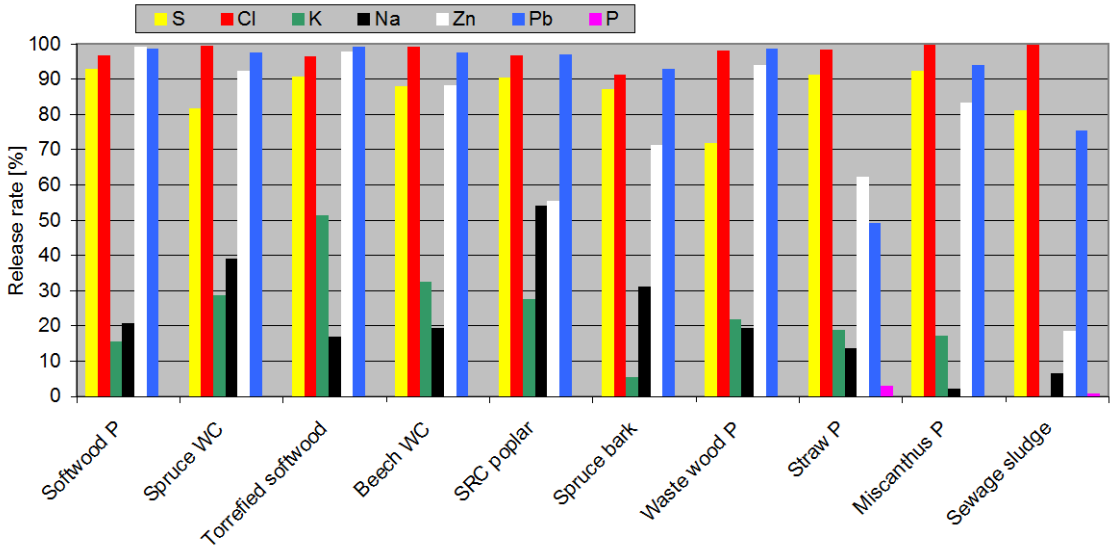

Figure 6-18: Release of inorganic elements from the fuel to the gas phase. Explanations: Release rate … (1 – element mass in the ash/element mass in the fuel) *100; P … pellets; WC … woodchips

The release (in mg/kg dry fuel) of ash forming vapours is dominated by K-species except for sewage sludge (dominated by P). Overall, softwood pellets and spruce show the lowest aerosol emission potential. The potential increases over bark,

torrefied softwood, beech, waste wood, miscanthus, SRC, and sewage sludge to straw.

All relevant results gained from the lab-scale reactor test runs as well as detailed descriptions of the reactor and the testing protocol have been implemented into the SciToBiCom advanced fuel database (Task 5.6).

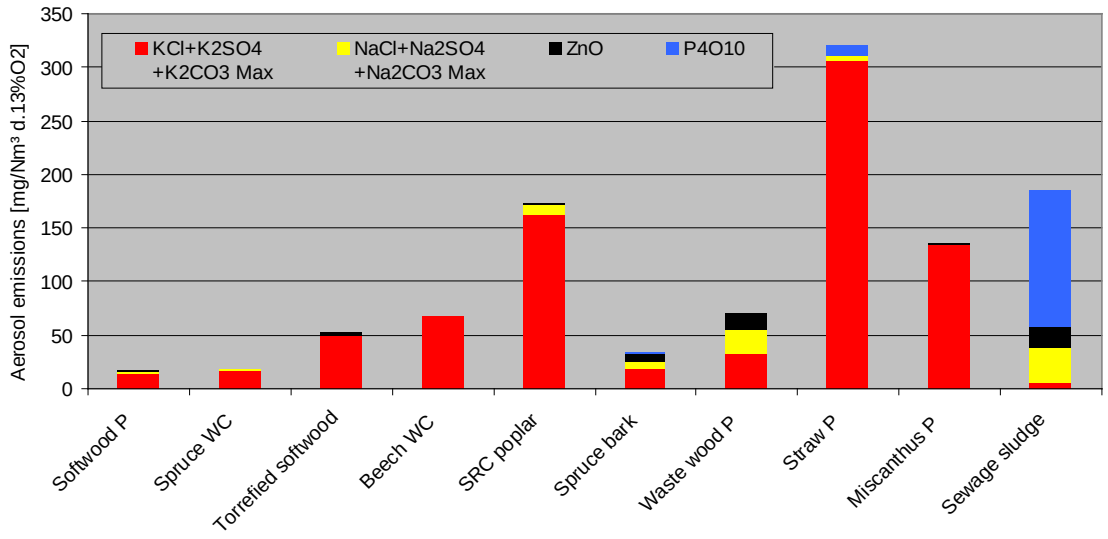

Figure 6-19: Estimated aerosol emissions as well as compositions of the aerosol emissions. Explanations: P … pellets; WC … woodchips.

6.5 Task 5.5: Determination of Release Curves for Alkali Metals and Heavy Metals

The alkali metals and heavy metals, as well as S and Cl are most important ash forming elements cause operational problems during biomass combustion. Alkali metals and heavy metals are partly released from the fuel to the gas phase, which either undergo complex chemical reactions or instantly form aerosols. The release of alkali metals and heavy metals are relevant for the formation of particular matters, deposits formation on heat transfer surfaces and deposits induced corrosion in biomass fired boilers. Quantitative data are needed regarding release of alkali metals and heavy metals from the biomass fuels during combustion, in order to estimate concentration and composition of aerosols and inorganic gases in the flue gas.

The objective of Task 5.5 was to obtain quantitative data on the release of alkali metals and heavy metals during biomass combustion. To facility the interpretation of the results, scanning electrical microscopy combined with Energy-dispersive X-ray analysis (SEM-EDX) were conducted for microstructure and chemistry examination of solid residues from combustion experiments.

To study the release of alkali metals and heavy metals, combustion experiments of biomass pellets were performed in Åbo Akademi Single Particle Reactor (SPR). The core part of the SPR is a quartz tube heated in an electrically heated ceramic furnace. Mixtures of air and nitrogen are fed directly to the tube reactor and flows of gases are controlled by mass flow controllers. The oxygen concentration 3 vol% was used for combustion experiments. The reactor was first heated up to the desired temperature. The combustion experiments were performed for four fuels at three different temperatures: 800 °C, 900 °C and 1050 °C. These temperatures have been proved to be critical for both alkali metals and heavy metals release during thermal conversion of biomass fuels. The milled fuels were first pelletized under 10 bar pressure into pellets with size of 8 x 6 (d x h) mm and mass around 200 mg. The sample pellet was inserted into the hot reactor by using a movable probe in a fraction of seconds. The sample holder is a quartz plate on which one fuel pellet was placed on. The evolved gas from the fuel pellet combustion were monitored by three commercial gas analyzer for the measurement of O2, CO, CO_2, NO and SO_2.

Since the combustion experiments were conducted at high temperatures, it is difficult to determine the drying time for each fuel pellet. In this study, the combustion of one fuel pellets was divided into four stages: devolatilization, 50% char burnout, char burnout and char burnout with extra 5 minutes time. The times for first and third stage were determined from the recorded product gas signals. The last stage represents ash cooking process after complete combustion a fuel pellet. Figure 1 shows an example of length of four stages and weight loss information during the straw pellet burn at 800 °C. It should be noted that the both length of four conversion stages and weight loss are different for each sample at different conversion temperatures. For each combustion experiment, the initial weight of fuel pellet and weight of solid residues were measured. The solid residues were collected and digested for further ICP analysis.

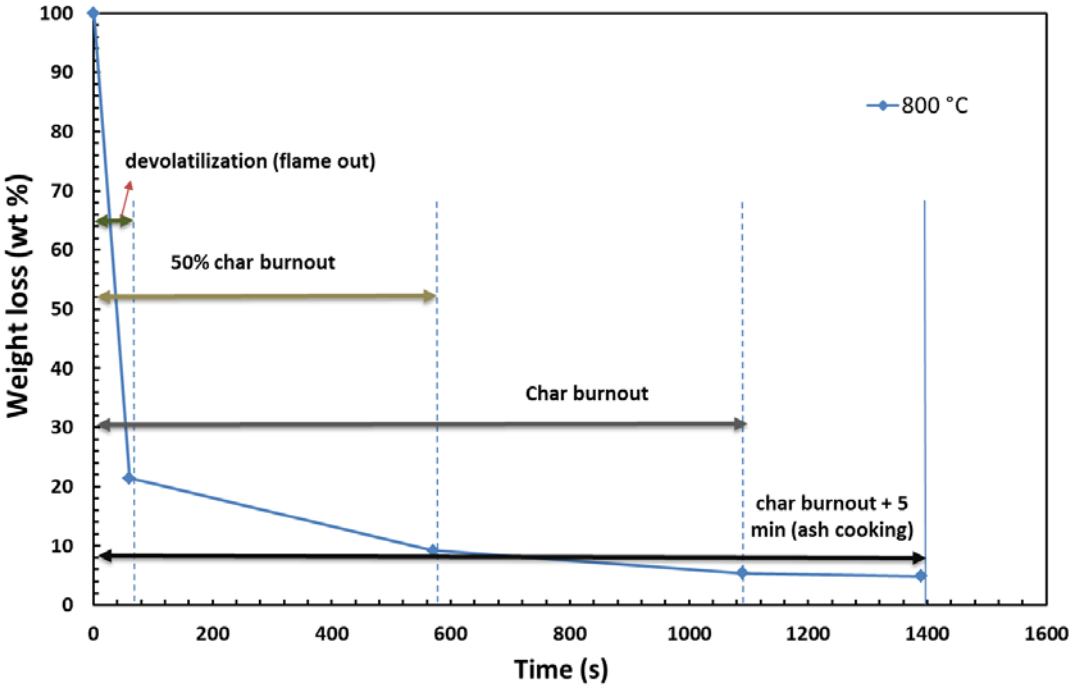

Figure 6-20: Weight loss of the straw pellet after four conversion stages at 800 °C. The length of each stage is indicated.

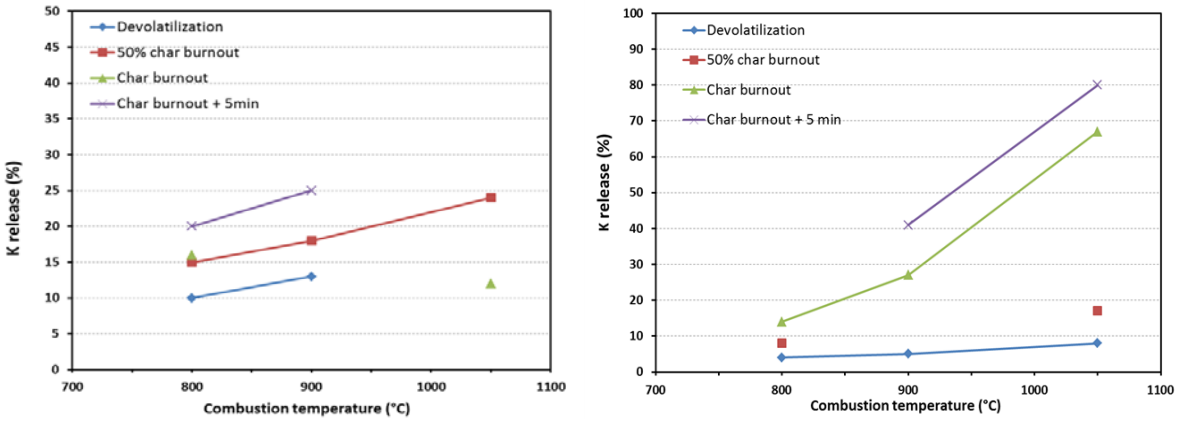

(a) miscanthus (b) torrefied softwood

Figure 6-21: Release of K to gas phase as function of the combustion temperature for (a) miscanthus and (b) torrefied softwood.

In Figure 5.2, the release data of alkali metal K are presented. Although there are several values for fraction of K released not shown in this figure due to significantly scattering of data, it can be seen that the trend are more or less

similar to those observed K for two fuels. The release of K started already at 800 °C, which increase of gradually as a function of temperature. In addition, longer residence time is favored for K release at certain temperature level. The similar K release trends were also observed for straw and bark in this study. For the torrefied wood, the K release sharply to over 60 % at 1050 °C after long enough combustion time.

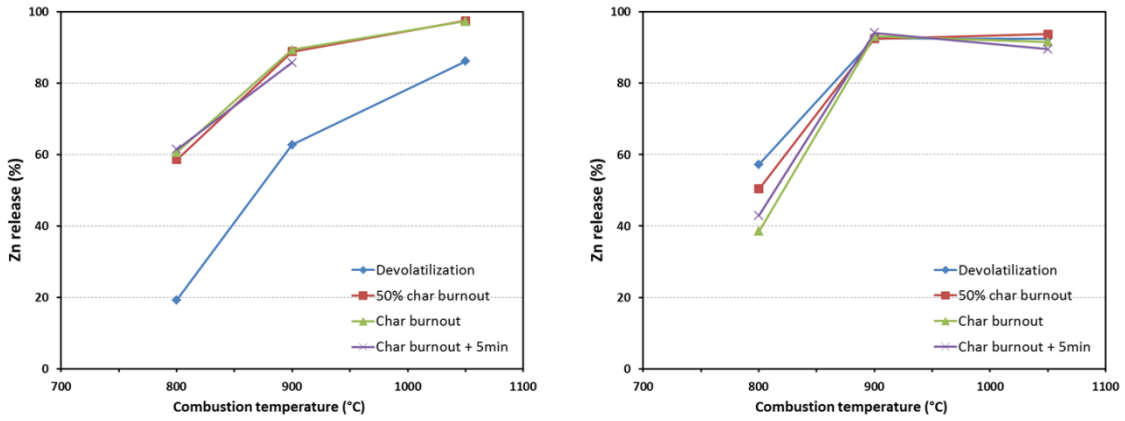

(a) spruce bark (b) torrefied softwood

Figure 6-22: Release of Zn to gas phase as function of the combustion temperature for (a) spruce bark and (b) torrefied softwood

The release data of Zn from spruce bark and torrefied softwood are shown in Figure 6-22. For the two fuels, a relative low release of Zn (20% for spruce bark and 40% for torrefied softwood) was observed up to 800 °C. At 900 °C, the release of Zn increase significantly. For the torrefied softwood, the combustion time showed rather weak effects on Zn release as the temperature higher than 800 °C.

The chemical composition of ash residues from bark combustions are dominated by calcium. No clear ash melting can be observed from SEM images took from bark ashes. Considering low Si and high Ca contents in the bark ash, alkali metals (i.e. K) readily release during combustion process. Ashes from straw and miscanthus are rich in K, Si and Ca. As the fuel pellets combusted at 900 °C, the ashes from straw and miscanthus start to melt. After burned at 1050 °C, ashes from straw and miscanthus largely fused with homogeneous and continuous structure. The fused structures contain mainly K, Si and C. It indicates that melting of straw and miscanthus are mainly related to formation of low temperature melting potassium-calcium silicates. Formation of potassium silicates may limit K

release to gas phase, which is retained in the silicates structure in the ash residues instead.

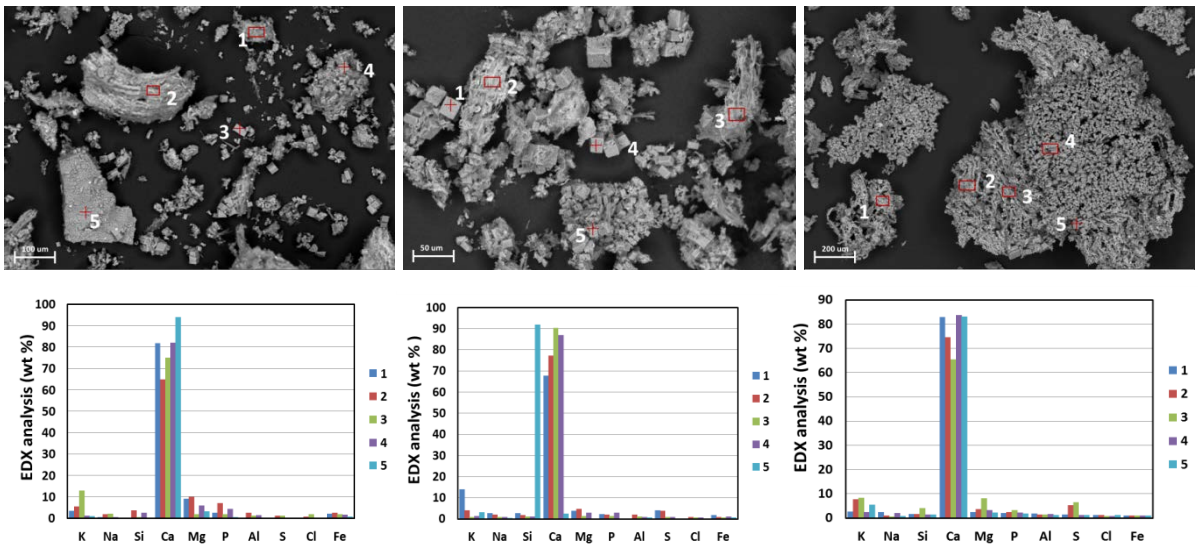

(a) 800 °C (b) 900 °C (c) 1050 °C

Figure 6-23: SEM-EDX analysis of ash residue obtained from bark combustion at 800 °C, 900 °C and 1050 °C

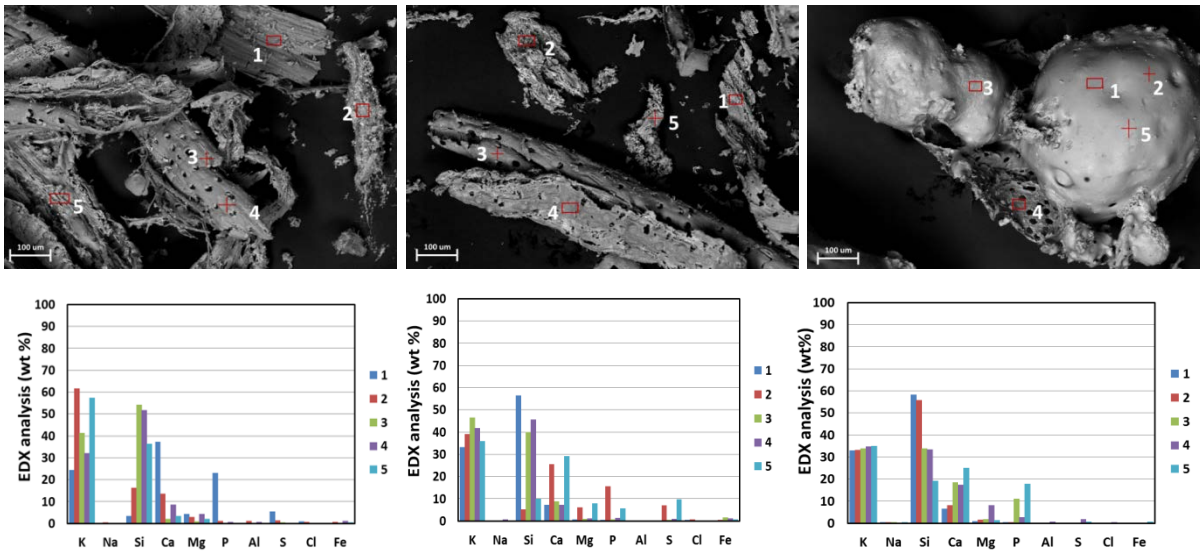

(a) 800 °C (b) 900 °C (c) 1050 °C

Figure 6-24: SEM-EDX analysis of ash residue obtained from bark combustion at 800 °C, 900 °C and 1050 °C.

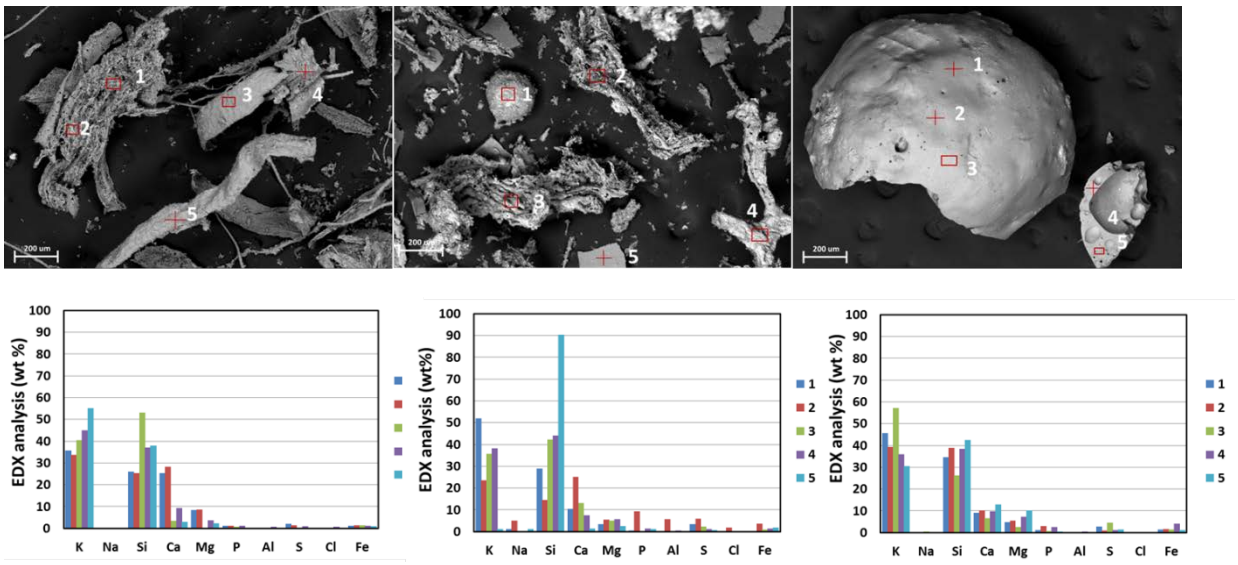

(a) 800 °C (b) 900 °C (c) 1050 °C

Figure 6-25: SEM-EDX analysis of ash residue obtained from bark combustion at 800 °C, 900 °C and 1050 °C.

To sum up, for all studied fuels, the combustion temperature and time, as well as ash composition greatly affect the quantity of K released to the gas phase under the investigated conditions. The release of heavy metals starts from 800 °C and increases sharply at 900 °C, which therefore heavily depends on the combustion temperature.

6.6 Task 5.6: Establishment of an Advanced Fuel Database

Finally, all data gained from the different biomass fuel characterisation methods investigated within WP5 were summarized in the SciToBiCom advanced fuel database. This database contains the following datasets for the fuels investigated:

- Fuel analyses data
  - moisture content, ash content, C, H, N, S, Cl, Si ,Ca, Mg, Al, Fe, Mn, P, K, Na, Cu, Zn, Pb and Cd
- Fuel indexes
  - K+Na+Zn+Pb, Si/K, 2S/Cl, (K+Na)/[x*(2S+Cl)], Si/(Ca+Mg), (Si+P+K)/(Ca+Mg)

- Chemical fractionation (stepwise leaching) regarding Si, Al, Fe, Ti, Mn, Ca, Mg, P, Na, K, S, Cl
  - untreated fuel analyses from chemical fractionation
  - amount in the water leached fraction related to the whole fuel input
  - amount in the acetate leached fraction related to the whole fuel input
  - amount in the HCl leached fraction related to the whole fuel input
  - amount in the rest fraction related to the whole fuel input
- Ash melting behaviour
  - results from standard ash melting tests (shrinkage starting temperature, deformation temperature, hemisphere temperature, flow temperature)
  - results from lab-scale reactor tests (max. bed temperature, status of ash after test run including pictures)
  - results from TGA/DSC tests with ashed fuel samples (first melting peaks detected)
  - SEM images, EDX spot and mapping analyses of ashed fuel samples
- Release of NO_x pre-cursors and NO_x formation
  - N release to the gas phase from a packed fuel bed (share of NO_x pre-cursors related to TFN, conversion rate of NO_x (gas) from fuel N)
  - NO formation during char combustion of a single particle
    - kinetic parameters for NO reduction inside biomass char particles
    - kinetic parameters with CO as the reaction product
  - N release according to results of NTNU lab-scale tests
  - NO formation during combustion/pyrolysis of single particles
- Release of ash forming species
  - Release of ash forming elements to the gas phase from a packed fuel bed (K, Na, P, Zn, Pb, S and Cl)
  - Release of K and Cl in dependence of the temperature (700, 800, 900 and 1,000°C)
- Pyrolysis and charcoal characteristics
  - Decomposition times of a single particle, fuel density, char density, devolatilisation time at 800 °C and 1050 °C, char oxidation time at 800 °C and 1050 °C
  - Thermal decomposition behaviour of fuels according to TGA (volatile components, hemicelluloses, cellulose, lignin, other component, fixed carbon, characteristic reaction temperatures)

Besides these data also comprehensive information about the different methods applied is given which is directly linked with the respective data.

The database has been programmed in MS Excel® which enables an easy extraction of selected datasets and a quick comparison of different fuels as well as results of characterisation methods for one selected fuel.

As a final result of the work performed within Task 5.6, a comprehensive advanced fuel database could be programmed. With the SciToBiCom fuels a broad range of different relevant fuel characteristics could be covered and therefore, also the data contained in the database reflect the wide range of test results possible. The database can in future be utilized to compare new fuels with the characteristics of the fuels already contained in the database and thereby derive relevant indications regarding possible combustion related problems which may occur when utilizing these fuels. Moreover, it can be applied for the validation of newly developed fuel characterisation tools.

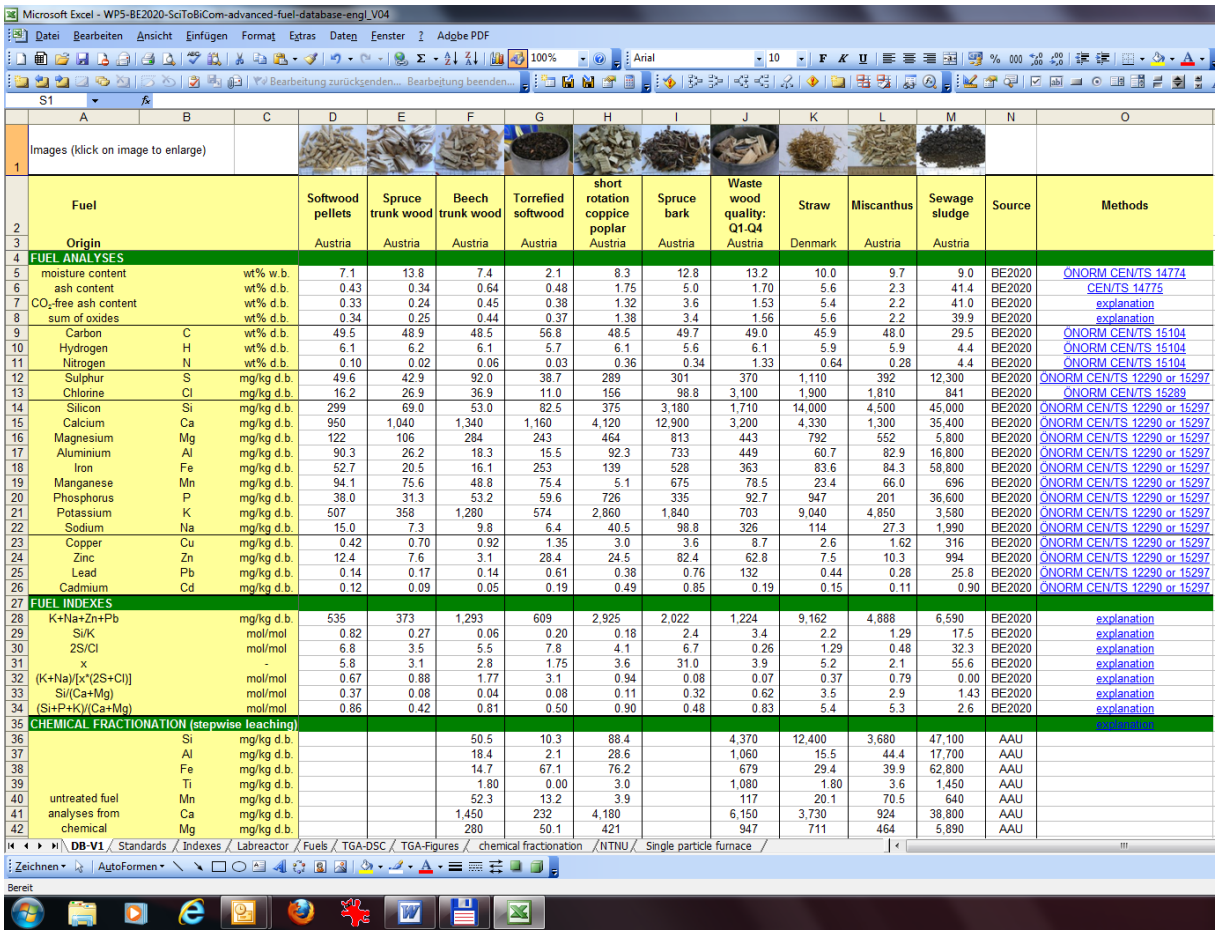

Fuel			Softwood pellets	Spruce trunk wood	Beech trunk wood	Torrefied softwood	short rotation coppice poplar	Spruce bark	Waste wood quality: Q1-Q4	Straw	Miscanthus	Sewage sludge	Source	Methods
Origin			Austria	Austria	Austria	Austria	Austria	Austria	Austria	Denmark	Austria	Austria		
FUEL ANALYSES														
moisture content		wt% w.b.	7.1	13.8	7.4	2.1	8.3	12.8	13.2	10.0	9.7	9.0	BE2020	ÖNORM CEN/TS 14774
ash content		wt% d.b.	0.43	0.34	0.64	0.48	1.75	5.0	1.70	5.6	2.3	41.4	BE2020	CEN/TS 14775
CO_2-free ash content		wt% d.b.	0.33	0.24	0.45	0.38	1.32	3.6	1.53	5.4	2.2	41.0	BE2020	explanation
sum of oxides		wt% d.b.	0.34	0.25	0.44	0.37	1.38	3.4	1.56	5.6	2.2	39.9	BE2020	explanation
Carbon	C	wt% d.b.	49.5	48.9	48.5	56.8	48.5	49.7	49.0	45.9	48.0	29.5	BE2020	ÖNORM CEN/TS 15104
Hydrogen	H	wt% d.b.	6.1	6.2	6.1	5.7	6.1	5.6	6.1	5.9	5.9	4.4	BE2020	ÖNORM CEN/TS 15104
Nitrogen	N	wt% d.b.	0.10	0.02	0.06	0.03	0.36	0.34	1.33	0.64	0.28	4.4	BE2020	ÖNORM CEN/TS 15104
Sulphur	S	mg/kg d.b.	49.6	42.9	92.0	38.7	289	301	370	1,110	392	12,300	BE2020	ÖNORM CEN/TS 12290 or 15297
Chlorine	Cl	mg/kg d.b.	16.2	26.9	36.9	11.0	156	98.8	3,100	1,900	1,810	841	BE2020	ÖNORM CEN/TS 15289
Silicon	Si	mg/kg d.b.	299	69.0	53.0	82.5	375	3,180	1,710	14,000	4,500	45,000	BE2020	ÖNORM CEN/TS 12290 or 15297
Calcium	Ca	mg/kg d.b.	950	1,040	1,340	1,160	4,120	12,900	3,200	4,330	1,300	35,400	BE2020	ÖNORM CEN/TS 12290 or 15297
Magnesium	Mg	mg/kg d.b.	122	106	284	243	464	813	443	792	552	5,800	BE2020	ÖNORM CEN/TS 12290 or 15297
Aluminium	Al	mg/kg d.b.	90.3	26.2	18.3	15.5	92.3	733	449	60.7	82.9	16,800	BE2020	ÖNORM CEN/TS 12290 or 15297
Iron	Fe	mg/kg d.b.	52.7	20.5	16.1	253	139	528	363	83.6	84.3	58,800	BE2020	ÖNORM CEN/TS 12290 or 15297
Manganese	Mn	mg/kg d.b.	94.1	75.6	48.8	75.4	5.1	675	78.5	23.4	66.0	696	BE2020	ÖNORM CEN/TS 12290 or 15297
Phosphorus	P	mg/kg d.b.	38.0	31.3	53.2	59.6	726	335	92.7	947	201	36,600	BE2020	ÖNORM CEN/TS 12290 or 15297
Potassium	K	mg/kg d.b.	507	358	1,280	574	2,860	1,840	703	9,040	4,850	3,580	BE2020	ÖNORM CEN/TS 12290 or 15297
Sodium	Na	mg/kg d.b.	15.0	7.3	9.8	6.4	40.5	98.8	326	114	27.3	1,990	BE2020	ÖNORM CEN/TS 12290 or 15297
Copper	Cu	mg/kg d.b.	0.42	0.70	0.92	1.35	3.0	3.6	8.7	2.6	1.62	316	BE2020	ÖNORM CEN/TS 12290 or 15297
Zinc	Zn	mg/kg d.b.	12.4	7.6	3.1	28.4	24.5	82.4	62.8	7.5	10.3	994	BE2020	ÖNORM CEN/TS 12290 or 15297
Lead	Pb	mg/kg d.b.	0.14	0.17	0.14	0.61	0.38	0.76	132	0.44	0.28	25.8	BE2020	ÖNORM CEN/TS 12290 or 15297
Cadmium	Cd	mg/kg d.b.	0.12	0.09	0.05	0.19	0.49	0.85	0.19	0.15	0.11	0.90	BE2020	ÖNORM CEN/TS 12290 or 15297
FUEL INDEXES														
K+Na+Zn+Pb		mg/kg d.b.	535	373	1,293	609	2,925	2,022	1,224	9,162	4,888	6,590	BE2020	explanation
Si/K		mol/mol	0.82	0.27	0.06	0.20	0.18	2.4	3.4	2.2	1.29	17.5	BE2020	explanation
2S/Cl		mol/mol	6.8	3.5	5.5	7.8	4.1	6.7	0.26	1.29	0.48	32.3	BE2020	explanation
x		-	5.8	3.1	2.8	1.75	3.6	31.0	3.9	5.2	2.1	55.6	BE2020	explanation
(K+Na)/[x*(2S+Cl)]		mol/mol	0.67	0.88	1.77	3.1	0.94	0.08	0.07	0.37	0.79	0.00	BE2020	explanation
Si/(Ca+Mg)		mol/mol	0.37	0.08	0.04	0.08	0.11	0.32	0.62	3.5	2.9	1.43	BE2020	explanation
(Si+P+K)/(Ca+Mg)		mol/mol	0.86	0.42	0.81	0.50	0.90	0.48	0.83	5.4	5.3	2.6	BE2020	explanation
CHEMICAL FRACTIONATION (stepwise leaching)														explanation
	Si	mg/kg d.b.			50.5	10.3	88.4		4,370	12,400	3,680	47,100	AAU	
	Al	mg/kg d.b.			18.4	2.1	28.6		1,060	15.5	44.4	17,700	AAU	
	Fe	mg/kg d.b.			14.7	67.1	76.2		679	29.4	39.9	62,800	AAU	
	Ti	mg/kg d.b.			1.80	0.00	3.0		1,080	1.80	3.6	1,450	AAU	
untreated fuel	Mn	mg/kg d.b.			52.3	13.2	3.9		117	20.1	70.5	640	AAU	
analyses from	Ca	mg/kg d.b.			1,450	232	4,180		6,150	3,730	924	38,800	AAU	
chemical	Mg	mg/kg d.b.			280	50.1	421		947	711	464	5,890	AAU	

Figure 6-26: SciToBiCom advanced fuel database – screenshot.

Moreover, it provides the possibility that users also may add their own data for other fuels or data regarding comparable fuels gained from other characterisation methods to the database. Therefore, it forms not only a comprehensive tool for advanced fuel characterisation but also can be extended by the user and thereby further improved.

References:

1. Benson S.A., Holm P.L., Comparison of inorganic constituents in three low rank coals, Ind. Chem. Eng. Prod. Res. Dev., 24, (1985), pp 145-149.)
2. Baxter L.L., A Task 2 . Pollutant emission and deposit formation during combustion of biomass fuels, Livermore, (CA), (1994)
3. Zevenhoven M., Ash-forming matter in biomass fuels, Academic dissertation, Åbo Akademi University, Turku, Finland (2001), ISBN 952-12-0813-9.
4. Zevenhoven, M., Skrifvars B-J., Yrjas P., Hupa M., Nuutinen L., Laitinen R., Searching for improved characterisation of ash forming matter in biomass, the proceedings of the 16th International Conference on Fluidized Bed Combustion, Reno, NV, USA, (2001).
5. Werkelin J., Ash-forming elements and their chemical forms in woody biomass fuels, Report 08-06, Academic dissertatiom, Uniprint ISBN 978-952-12-2125-5.
6. Characterization of Ash-Forming Matter in Various Solid Fuels by Selective Leaching and Its Implications for Fluidized-Bed Combustion, By Maria Zevenhoven, Patrik Yrjas, Bengt-Johan Skrifvars, and Mikko Hupa, Energy Fuels, 2012, 26 (10), pp 6366–6386.

7. WP6: Advanced Fuel Characterization – Fuel Pretreatment

Coordinated by Dr. Peter Arendt Jensen, DTU

Heat and power production from biomass has in most cases been based on grate-fired or fluid bed boilers. Suspension-fired units have a higher electrical efficiency compared to traditional grate-fired units. However, a number of problems associated with the handling (low energy content), storage (moisture uptake and biological activity), use (corrosion and super heater fouling) and grinding (high energy demand) of raw biomass in suspension-fired units must be overcome. Suspension firing requires sub-millimeter size feedstock particles and it is difficult and expensive to reduce the biomass to this size due to the fibrous structure and tenacity of biomass. A possible solution to some of these issues could be a torrefaction pre-treatment (low temperature pyrolysis) of the biomass, yielding a dry, partly hydrophobic and brittle product with a higher energy density. Torrefaction is a process of thermal degradation of biomass at relatively low temperatures and low heating rate of less than 50 °C min^{-1} under anoxic conditions. The torrified biomass product is brittle and can be pulverized down to a small particle size without undue energy consumption. The heating of the biomass course a net reduction of the heating value and the drawback of using the torrefaction process is a reduction in the amount of energy provided to a boiler compared to the original biomass. A possible use of the torrefaction process is by integration of the process with a power plant, and thereby a high total energy efficiency can be obtained. Possibly the gas released during the torrefaction process can be combusted in the boiler and used for steam superheating, and low temperature steam or flue gas from the boiler may be used to supply energy for the torrefaction process. A possible reactor used for such a torrefaction process could be a ball mill where the biomass is simultaneous heated and milled. In the present study there are conducted investigations that can support the development of such a torrefaction ball mill reactor. The main objectives of the project are listed below:

- To provide the fundamental data needed for the design of a torrefaction ball mill reactor
- To provide a better understanding of the torrefaction properties of different biomasses and provide recommendations for a torrefaction characterization method
- To provide data on the release of S and Cl during the torrefaction process

- To investigate a possible design for a torrefaction ball mill reactor

The project work includes the following activities:

- Design and construction of a novel laboratory scale experimental setup (rotating cylinder) for simultaneous torrefaction and grinding, and development of adequate experimental procedures
- An experimental campaign using straw and spruce to determined the influence of reactor operation conditions on conversion and milling
- A broader range of biomasses have been tested to investigate how biomass properties such as ash content, ash composition and carbohydrate composition influence torrefaction
- The gas phase release of Cl and S have been investigated by batch experiments
- Work on a torrefaction reactor design have been initiated

A simultaneous laboratory torrefaction and grinding reactor has been constructed. The set up contains a reactor chamber in which a biomass sample is placed together with some metal balls. The reactor chamber can be simultaneously heated and rotated and thereby torrefaction and pulverization takes place. In addition the set up consists of a water cooling section, an electric oven, a gas cooling section, and five thermocouples as shown in Figure 1 and 2. A motor is used to rotate the reactor chamber. In most of the conducted experiments, a biomass sample and 12 metal balls (10 mm in diameter) were introduced into the reactor chamber and placed in the water cooled part of the set up. The reactor was then purged with nitrogen and the flow is controlled with a mass flow controller to keep the system inert and remove volatile products from the reactor. After five minutes of purging, the pyrolysis reactor was quickly pushed into the hot zone and the rotation was started. The biomass samples were simultaneously torrified and grinded at different temperatures (range from 200 °C – 400 °C) and residence times (30 and 90 minutes). After the torrefaction process the solid product was cooled down in the cooling section. Then, the char was collected and the weight was measured in order to determine the mass loss of the samples. The heating value of char is determined by using a bomb calorimeter. In order to study the grindability, the treated samples are sieved to determine the particle size distributions.

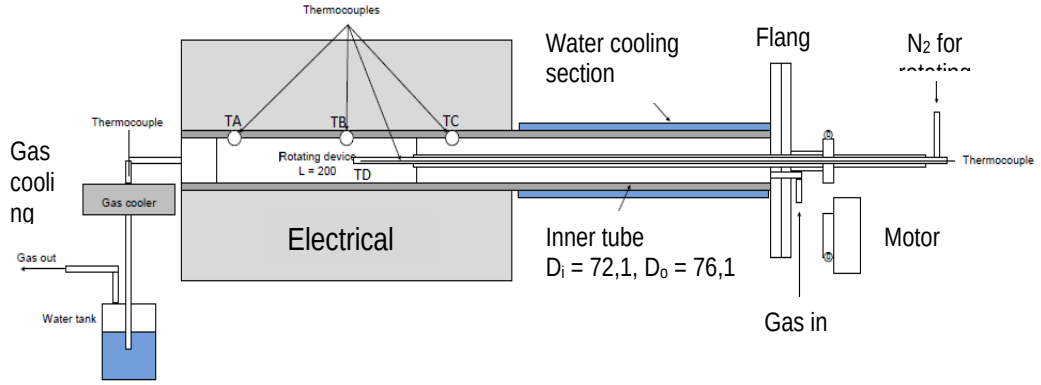

Figure 7-1: Bench scale experimental set up for simultaneous torrefaction and grinding process. All dimensions are in mm.

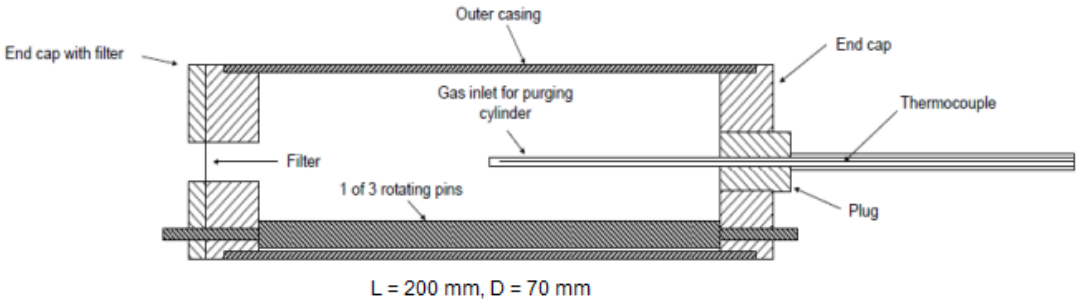

Figure 7-2: Pyrolysis reactor for biomass sample and metal balls, equipped with rotating pins and thermocouple

Samples of straw and wood chips (spruce) with a particle size less than 4 mm were used to investigate the influence of torrefaction temperature, residence time, and biomass type on characteristics of solid product, such as solid yield, heating value and particle size distribution. Initially, a series of experiments were conducted to develop an adequate experimental procedure. This was done by investigating the influence of amount of sample in the reactor chamber, and the size and type of balls.

In this study, the torrefaction temperature is defined as the final reactor temperature inside the reactor chamber that contains the fuel. The residence time is defined as the time from the reactor chamber that contains the biomass sample and metal balls is pushed into the hot zone and the grinding is started, until the grinding and torrefaction process is stopped. This residence time includes the heating of particles from room temperature to the reactor temperature (it takes approximately 15 minutes to heat the samples to 200 °C).

Influence of sample size and grinding balls

Torrefaction of straw

The objective of this investigation is to study the influence of sample size on the temperature profile inside the reactor and the particle size distribution of the torrified product. Experiments were conducted by setting the oven temperature to 420 °C which leads to a final temperature inside the pyrolysis reactor of approximately 350 °C (T_D). The residence time was 30 minutes and 12 tungsten carbide balls with 10 mm in diameter were used. The amounts of samples sizes used were: 7 g, 14 g, 20 g, 30 g, and 40 g. The bed heights inside the reactor chamber with the different amount of samples are illustrated in Figure 3. The obtained temperature profiles and particle size distributions of torrified straw are presented in Figure 4.

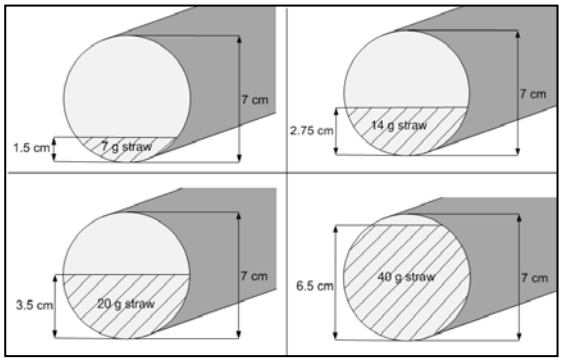

Figure 7-3: Different bed height for different sample size of straw inside the reactor chamber

Using a large sample size of 30 g or 40 g cause a less pulverized sample to be produced. This may be caused by a lower final temperature obtained, which are 340 °C and 337 °C for 30 g and 40 g, respectively, compared to 350 °C for the 20 g sample. However, it may also the case that with a large amount of biomass the balls cannot move freely around in the reactor and the grinding process is thereby reduced. It was decided to use 20 g of a standard sample load in the further straw experiments. Repeated experiments with 20 g straw showed a very nice reproduction of temperature reactor profiles and particle size distributions.

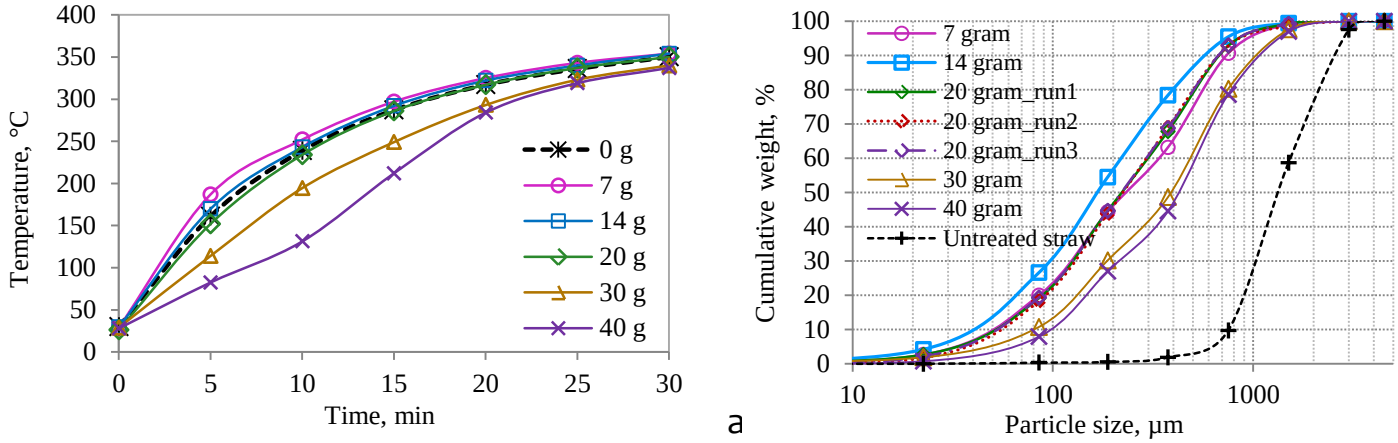

Figure 7-4: Reactor temperature profile (a) and particle size distribution of torrified straw obtained from torrefaction of different amounts of straw (Operating conditions: T_{oven} = 420 °C, residence time = 30 minutes, balls = 12WC10, rotational speed = 120 rpm)

Torrefaction of wood chips (spruce)

A set of experiments were performed with different amount of wood chips in order to study the influence of sample size towards temperature profile inside the reactor and particle size distribution of the torrified product. Experiments were conducted by setting the oven temperature to 450 °C which leads to a final temperature inside the pyrolysis reactor of approximately 375 °C (T_D). The residence time was 30 minutes and 12 tungsten carbide balls with 10 mm in diameter were used. The amounts of samples sizes used were: 20 g, 40 g, 60 g, 80 g, and 100 g. The bed heights inside the reactor chamber with different amount of samples are illustrated in Figure 5 and the results obtained are presented in Figure 6-6.

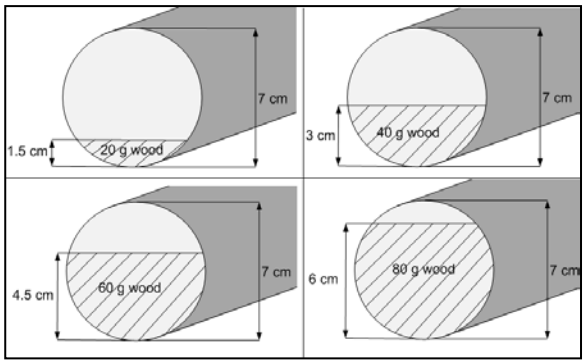

Figure 7-5: Different bed height for different sample size of wood chips inside the reactor chamber

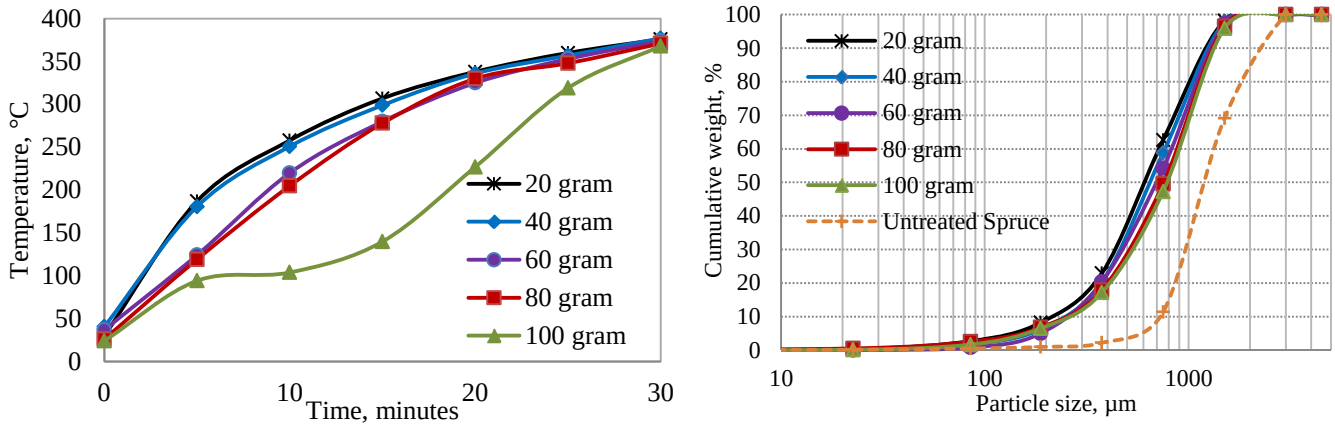

a) b)

Figure 7-6: Reactor temperature profile (a) and particle size distribution of torrified wood chips obtained from torrefaction of different amounts of wood chips (Operating conditions: T_{oven} = 450 °C, residence time = 30 minutes, balls = 12WC10, rotational speed = 120 rpm)

After 30 minutes of torrefaction of 20 - 60 gram wood samples, a final temperature about 375 °C is obtained. It can be observed in Figure 6 that by using 20 and 40 gram of wood, almost similar temperature profile is obtained, while increasing the amount of wood resulted in decreasing of the temperature profile. When 100 gram of wood is used, the temperature profile is obviously lower than the other sample amounts, and this leads to a larger particle size produced after torrefaction process.

Comparison of sample size between straw and wood chips

A comparison between torrefaction of straw and wood chips using different amounts of feedstock are shown in Figure 7. Torrefaction experiments were conducted at 450 °C for 30 minutes. The temperature profiles for 20 g and 40 g of wood are almost similar with the profile for 20 g of straw, while a significant decrease of the temperature profile is observed for 60 g of wood. The particle size distribution for 20 g and 40 g of wood did not show any substantial difference, implies that a higher amount of samples can be used and the similar result will be obtained. From these results, 40 gram of wood is used as a standard condition for further torrefaction experiments.

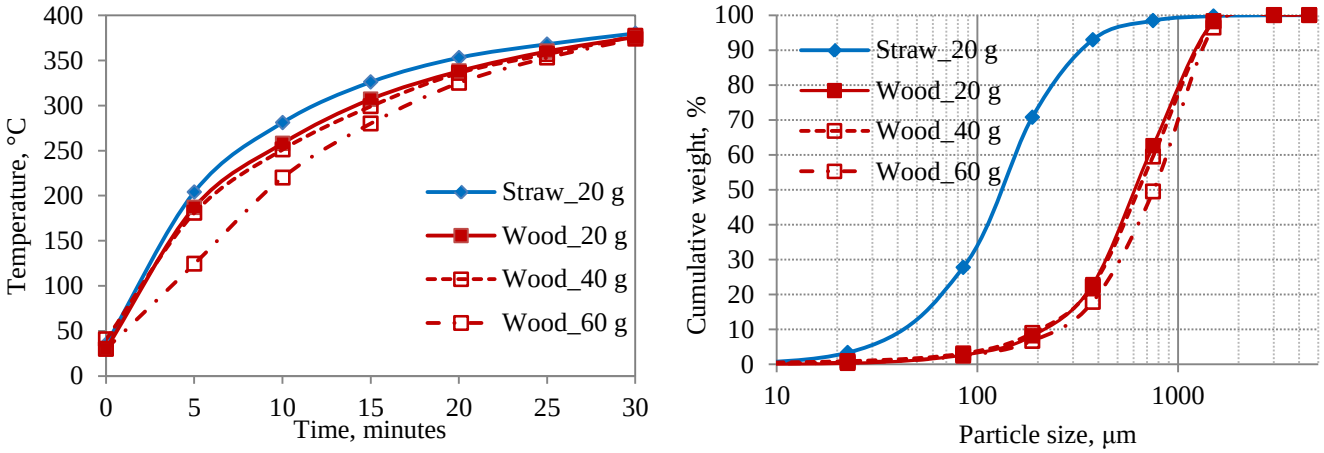

a) b)

Figure 7-7: Reactor temperature profile (a) and particle size distributions of torrified straw and wood chips obtained from torrefaction of different amount of wood and straw

Influence of different size and type of balls

Two types of balls were available for this study, which are stainless steel (SS) and tungsten carbide (wolfram carbide, WC). Three different sizes of stainless steel balls, 10 mm, 15 mm and 20 mm, were used, while 10 mm of tungsten carbide balls were available. In the experiments, 20 gram of straw was torrified for 30 minutes at an oven setting temperature to 380 °C, and different types and sizes of balls were used. In all experiments, 12 balls were used. The results obtained are summarized in Table 1. The notations used in the Table 1 are: WC10 (tungsten balls with a diameter of 10 mm), SS10 (stainless steel balls with a diameter of 10 mm), SS15 (stainless steel balls with a diameter of 15 mm) and SS20 (stainless steel balls with a diameter of 20 mm).

Table 7-1: Summary from the investigation of different type and size of balls used during torrefaction process

Balls (type/size)	Toven, °C	Final reactor temperature (TD), °C	Residence time, minutes	D_{50} values, µm
WC10	380	312	30	520
SS10	380	307	30	540
SS15	380	308	30	550
SS20	380	284	30	940

There is no large influence between using SS10, SS15 and WC10 on the obtained particle size distribution curves. But a slight increase in the temperature profile

and also a small reduction of the particle size distribution when tungsten carbide balls were used is observed. The tungsten carbide balls have a higher density and better thermal conductivity compared to the stainless steel balls. A large difference is observed when 20 mm stainless steel balls were used. The temperature profile is low compared to the other conditions, resulting in a product with larger particle sizes. The change is probably caused by the heat capacity of the 20 mm balls.

The initial oven tests have lead to the following conclusions:

- A torrefaction treatment in the laboratory rotation reactor leads to a reduced particle size
- By using 20 g of straw or 40 g of wood in the torrefaction reactor the fuels obtain a reasonable heating rate and the balls moves adequately in the reaction chamber to mill the samples. 12 balls of tungsten carbide (WC10) are used for further experiments, since these balls provide a good particle size reduction and do not reduce heat uptake by the biomass
- Repeated experiments with 20 g straw have shown that temperature profiles and particle size distributions can be accurately reproduced
- Tests on the solid recovery in the reactor (not documented in this resume report) have shown that the solid material is contained in the reactor during experiments and that all solid products can be recovered.

The torrefaction process

Torrefaction of wheat straw and wood chips (spruce) have been conducted in order to investigate the influence of operation conditions especially the influence of temperature and residence time on solid yield and grindability. To further study the influence of biomass type on the torrefaction process, 4 other biomasses were included in the investigation. These biomasses as well as information about them were supplied by Bioenergy 2020 + GmbH, Graz, Austria. The chemical compositions of the biomasses are presented in tables 2 and 3.

The applied feedstock biomasses include both herbaceous and wood type biomasses. The feedstock's ash contents vary from 0.3 to 6 wt% and the potassium contents from 0.04 to 0.9 wt%. Also large variations in carbohydrate compositions are seen with hemicelluloses contents from 13 to 25 wt%.

Table 7-2: Composition of the biomass (data provided by BioEnergy 2020+ GmbH), dry basis wt%.

Compon	Wheat	Miscanth	Bark	Spruce	Beech	Pine
Ash	5,57	2,26	4,98	0,34	0,64	0,5
C	45,93	47,97	49,66	48,88	48,50	53,2
H	5,86	5,92	5,63	6,23	6,05	6,2
N	0,64	0,28	0,34	<0,1	<0,1	0,1
S	0,111	0,039	0,03	0,004	0,009	0,05
Cl	0,19	0,181	0,01	0,003	0,004	0,005
K	0,904	0,485	0,184	0,036	0,128	0,056
Si	1,4	0,45	0,318	0,007	0,005	0,05
Al	0,006	0,008	0,073	0,003	0,002	0,01
P	0,095	0,02	0,034	0,003	0,005	0,007
Fe	0,008	0,008	0,053	0,002	0,002	0,003
Mg	0,079	0,055	0,081	0,011	0,028	0,029
Ca	0,433	0,13	1,29	0,104	0,134	0,1
Na	0,011	0,003	0,01	<0,001	0,001	0,005

Table 7-3: Carbohydrate analysis (data provided by DTU Risø-Campus), dry basis wt%.

Components	Straw	Miscanthus	Spruce	Beech	Pine	Spruce
Xylan-based hemicelluloses	23,1	18,1	5,6	16,2	5,1	3,9
Mannan-based hemicelluloses	0	0	11,0	2,3	10,0	4,0
Other hemicelluloses	2,3	2,0	1,8	2,7	5,4	5,0
Total hemicelluloses	25,4	20,1	18,4	21,2	20,5	12,9
Cellulose	42,7	48,5	45	40,8	38,6	24,1
Lignin	17,3	22,4	27,6	23,8	29,2	36,8
Ash	4,2	1,0	0,3	0,5	0,4	5,4
Extractives	3,2	4,3	1,0	1,0	4,7	5,7
Residuals	7,3	3,7	7,8	12,8	6,7	15,0

The influence of torrefaction operation conditions on yield and particle size

Straw and spruce wood chips were used to investigate the influence of changed operation conditions on yields and obtained particle size distributions. In figure 8 the mass loss and energy loss at different torrefaction temperature and residence time for straw and wood chips are shown. The grindability of torrified biomass is evaluated using the d_{50} value, obtained from the sieving particle size distribution curve. The relative d_{50} reduction of torrified biomass is calculated with respect to the d_{50} value of raw biomass, and the results are shown in Figure 9.

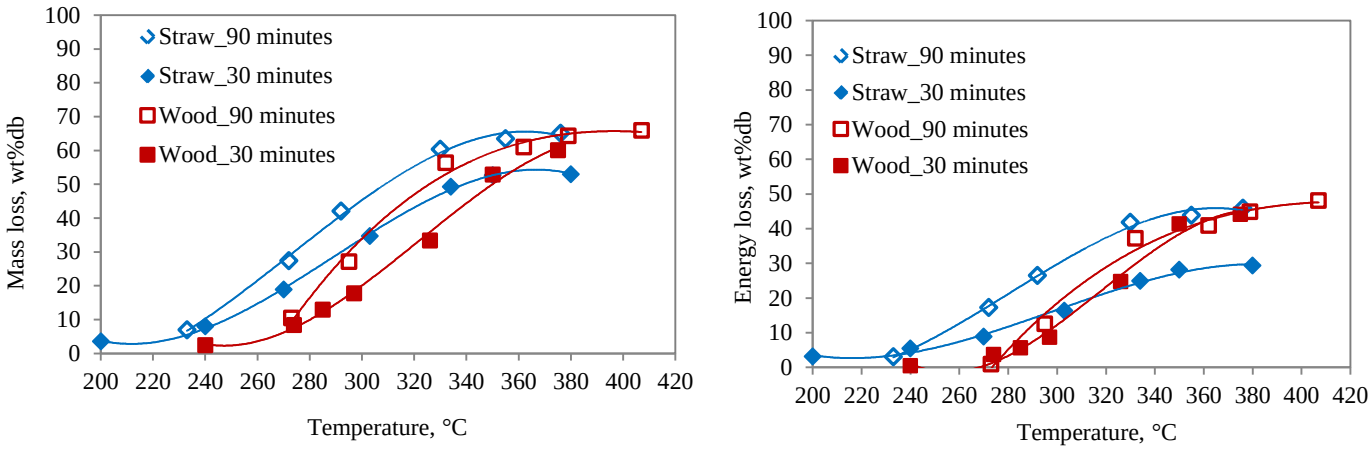

Figure 7-8: Influence of temperature and residence time on mass loss and energy loss of torrified straw and wood chips (spruce)

The initial d_{50} values were 1.3 mm for straw and 1.2 mm for the wood chips. There are observed different behavior of the straw and the wood sample. A higher conversion (larger mass loss) is observed for the straw compared to the wood at similar temperatures; and there is also observed a larger particle size reduction of the straw sample. To obtain a reduction of d_{50} of 50% (at 90 min residence time) the straw has to be heated to 260°Cwhereby an energy loss of 15% is observed, while to obtain a d_{50} reduction of 50% the wood the sample has to be heated to 320°C and an energy loss of 28% is observed.

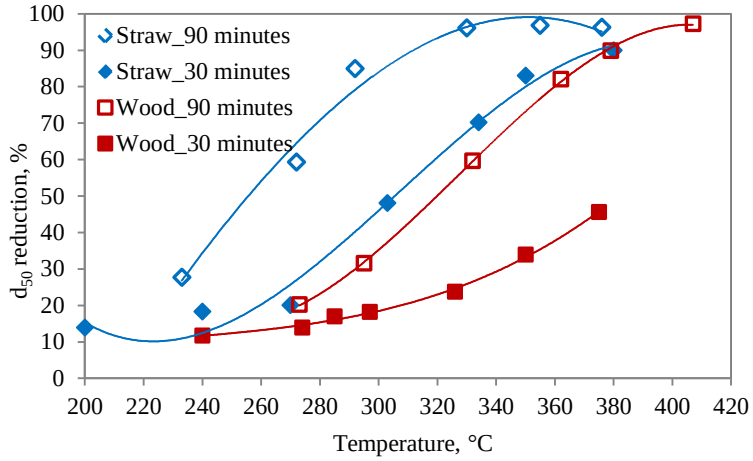

Figure 7-9: Influence of temperature and residence time on d_{50} reduction of torrified straw and wood chips (spruce)

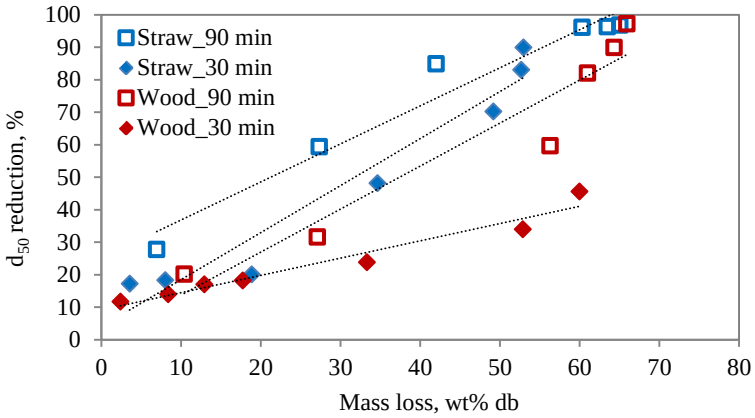

Figure 7-10: A comparison of relationship between d_{50} reduction and mass loss for straw and wood

In order to look further into the grindability of torrified biomass, the d_{50} reduction as a function of mass loss was printed and the graphs are shown in Figure 10. A reasonable linear relationship is observed for straw at both residence times with a nice correlation coefficient of r^2 >0,9. It is observed that at similar mass loses yields a higher d_{50} reduction is observed for the 90 minutes experiments compared to the 30 minutes experiments. It is also seen that straw always obtain a higher d_{50} reduction than the wood at similar mass loss levels.

The differences between the torrefaction characteristics of the straw and wood chips may be caused by several different phenomena:

a) Influence of different distribution of hemicelluloses type and lignocelluloses compositions
b) Alkali catalytic influence on pyrolysis

c) Influence of particle size, geometry and mass

To investigate the pyrolysis process of wood and straw without the heat transfer limitations that appear in the torrefaction reactor thermal gravimetric analysis (TGA) by using heating rate of 5K/min were performed. The TGA curves in Figure 11 shows also a higher mass loss for straw than for wood at low temperatures (below 350°C).The TGA results indicates that the observed differences in solid yield can be related to the chemical differences between wood and straw since the heat transfer conditions in the STA is similar for the two samples. The observed different mass loss profiles may be related to differences in carbohydrate composition or to catalytic properties of the ash. Straw has a higher xylan-based hemicelluloses content compared to the spruce (see Table 3), and xylan-based hemicellulose is more reactive compared to the mannan-based hemicelluloses in spruce [4]. Xylan is the most thermally unstable polymer of all, thus biomasses with higher amounts of xylan tend to breakdown more rapidly [5]. Furthermore, straw has higher content of hemicelluloses than wood, and this may contribute to the higher mass loss of straw at temperature lower than 350 °C. They have almost similar amount of cellulose, however spruce has higher lignin content than straw. Besides the carbohydrate composition the high alkali content may also influence the pyrolysis process and this will be further discussed in section 3.2.

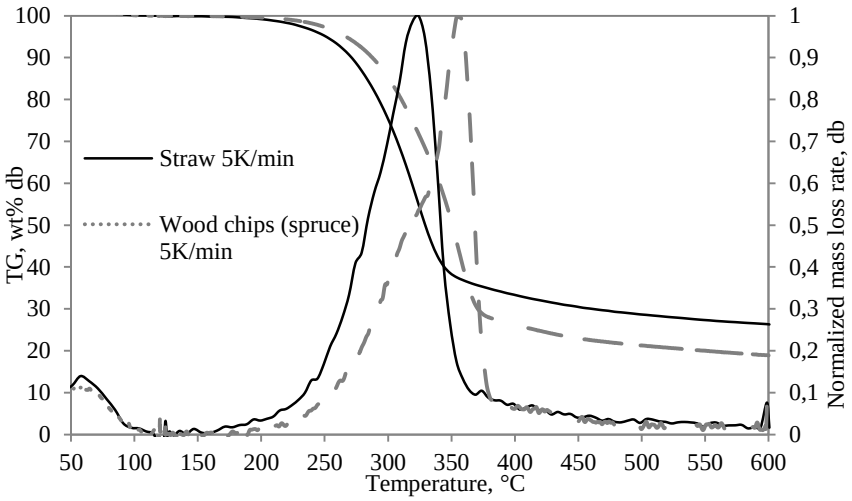

Figure 7-11: Comparison of TG-DTG curves for pyrolysis of straw and wood in nitrogen at 5K/min.

When evaluating the mass loss of torrified biomass (as the data shown in Figure 8), other factors than the chemical properties of feedstocks may influence the results. The size, morphology and weight of single particles may influence both

heat transfer and particle breakup. The particle size distribution of the wood and straw, and the corresponding particle weight of the different particle classes are shown in Figure 12. The straw and wood biomass particles have almost similar weight for the particle size less than 0,8 mm, while the weight of wood particle is a small amount larger than straw for the particle size larger than 0,8 mm. While the weight of the single particles only shows a small difference, also the form of the particles may influence the results and this will later be investigated.

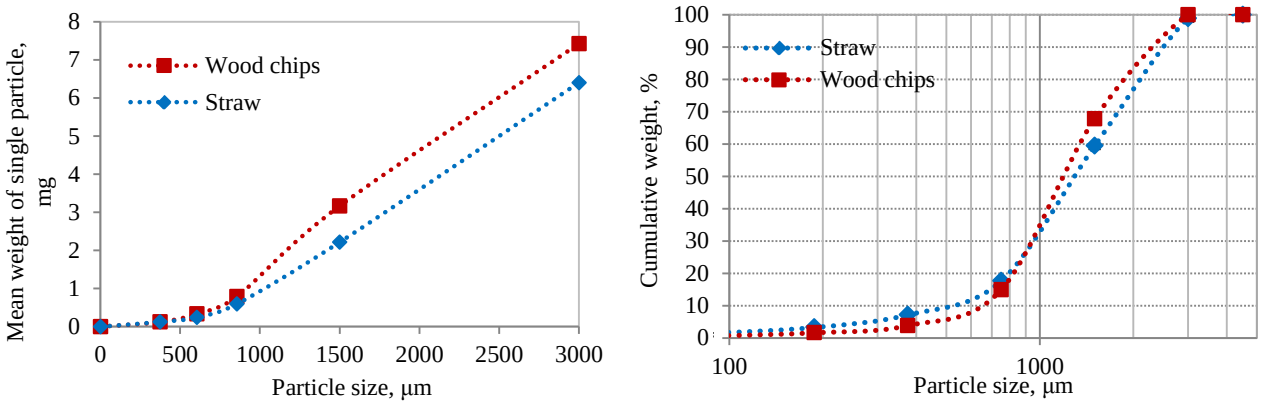

Figure 7-12: Mean weight of single particle and particle size distribution for straw and spruce chips

The obtained results for the study on the influence of operation conditions on yield and particle size are summarized below:

- The influence of reactor temperature and residence time on mass loss, energy loss and particle size reduction have been established for wood and straw. Straw obtain a higher conversion than wood at similar temperatures. The reason for this difference shall be further investigated.
- By doing experiments with both simultaneous and separate heating and grinding of wood and straw the relative influence of the heating and grinding processes have been investigated (This study is not documented in detail in this summery report). The investigation showed that heat transfer is the rate limiting step. When the biomass is heated without grinding the following grinding process takes maximal five minutes to obtain a similar particle size as to the combined process.

Some further studies shall be done to obtain a full understanding of the process:

- The influence of feedstock particle size will later be investigated.
- A characterization of the morphology of the applied particles will be done to investigate the influence of particle shape.

- The influence of carbohydrate composition and ash elements on the torrefaction behavior is further investigated, and this work is described in section 3.2.

The influence of feedstock properties on torrefaction behavior

As it is seen in section 3.1 the torrefaction behavior of wood and straw differs significantly. In many cases the torrefaction process will be used where a minimum mass loss is wanted (a minimum loss of heating value) and at the same time a large particle size reduction shall be obtained. It is therefore wanted to have some capability to predict the torrefaction behavior of different biomass types. Several STA based studies have investigated the influence of biomass alkali content on biomass pyrolysis behavior [6, 7, 8]. Alkali metals have been found to catalyze the pyrolysis process and have a strong influence on the products distribution. It has been observed that a high alkali content cause a relatively high yield of char at temperatures above 500 °C, and the initial pyrolysis starts at lower temperatures for alkali rich biomasses. Also the biomass carbohydrate composition influences the biomass pyrolysis properties [8]. The low temperature pyrolysis is dominated by hemicelluloses decomposition, while the pyrolysis conversion taking place above 380°C is dominated by lignin decomposition. In this study six different biomasses were pyrolyzed in a TGA and torrified in the CHEC torrification reactor; and the obtained results were compared with the biomass ash and carbohydrate compositions (shown in Table 2 and 3). To further investigate the influence of alkali metals on torrefaction characteristics also some washed biomass samples (to remove alkali) and some impregnated samples (with KCl and K_2CO_3) were included in the study. All samples were pyrolyzed in a STA in a N_2 atmosphere with a heating rate of 5 K/min up to 600 °C.

The results of the STA measurements are shown in Figures 13 and 14. In Figure 13 the char yields (residual solid mass) at 270°C and 300°C as a function of sample alkali content is shown and in Figure 13 the temperature at maximum pyrolysis conversion as a function of sample alkali content is shown. In Figure 12 it is seen that at both 270°C and 300°C the solid mass yield decreases significantly when the biomass alkali content is increased from 0 to 0.2 wt%. Increasing the alkali content from 0.2 up to 1.0 wt% has a less pronounced influence. The same tendencies are observed for most of the washed and impregnated samples (washed spruce, washed straw, spruce + KCl, washed straw + K_2CO_3). However, in some cases (

spruce + K_2CO_3 and washed straw + KCl at 270°C; and spruce + K_2CO_3, washed straw + KCl and washed straw + K_2CO_3 at 300°C) the impregnated samples shows lower solid mass yields than the raw biomasses. In Figure 14 the temperature of maximum pyrolysis conversion rate as a function of biomass alkali content is shown. It is observed that a high potassium content decrease the temperature of maximum conversion, confirming that alkali catalyze the pyrolysis process. All data shows similar trends except the K_2CO_3 impregnated samples that obtains the lowest maximum conversion temperatures.

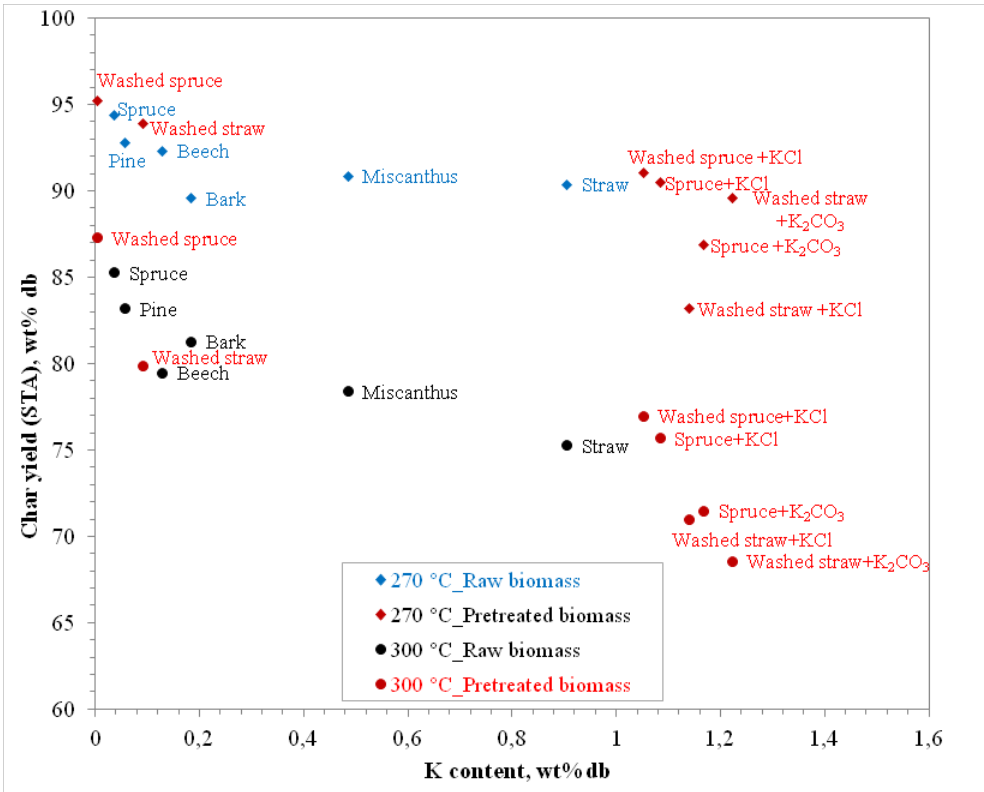

Figure 7-13: Influence of K content on char yield at 270 °C and 300 °C of biomass samples pyrolyzed on STA with a heating rate of 5 °C/min. By pretreatment is ment that the biomass was washed (to remove alkali) or was impregnated with KCl or K_2CO_3.

In Figure 6-15 the obtained solid yields in the laboratory torrefaction reactor is shown for experiments conducted at 270 and 300°C. There is observed the same general tendency as seen in the TGA data with decreased solid yields with increased alkali content, and the most strong influence of increasing potassium content at a potassium content of less than 0.2 wt%.

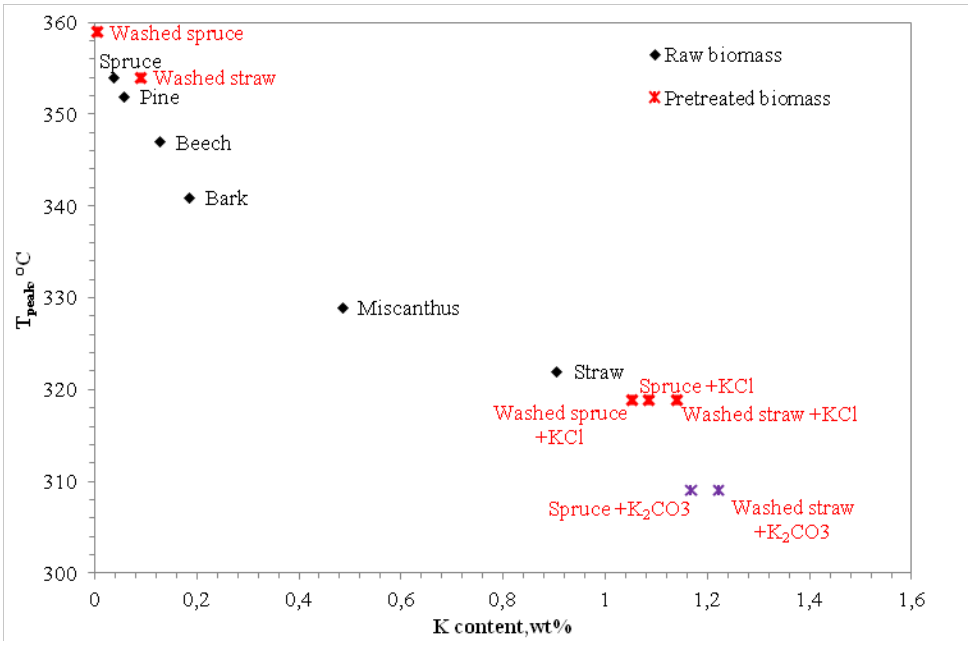

Figure 7-14: Influence of K content on peak conversion temperature (maximum mass loss rate) for raw biomasses and pretreated biomasses pyrolyzed on STA with a heating rate of 5 °C/min

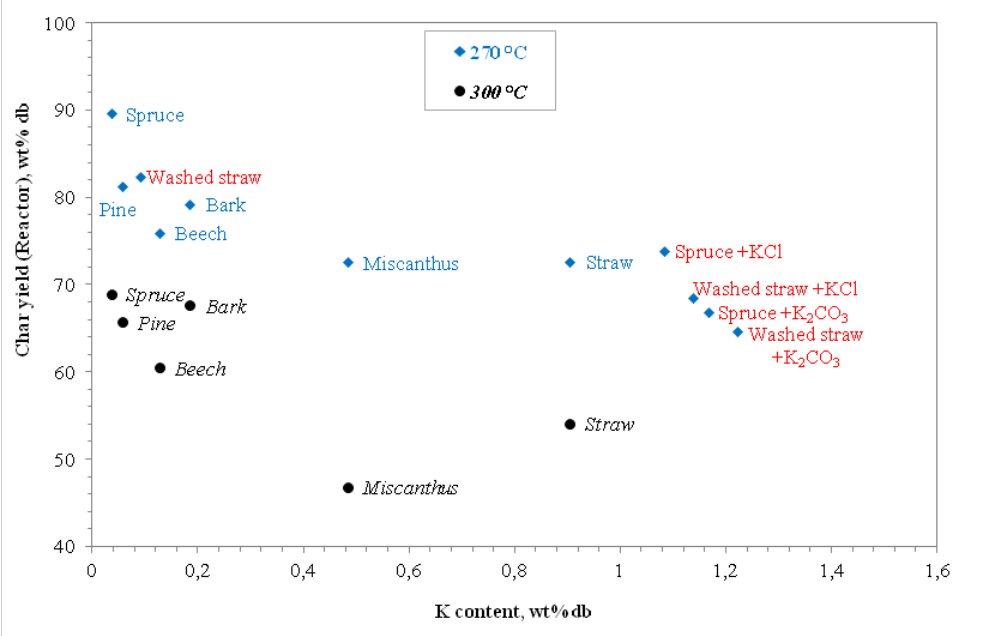

Figure 7-15: The solid yields obtained on the torrefaction reactor as a function of the biomass K contents. There was used reactor temperatures of 270 °C and 300 °C and residence times of 90 minutes.

In Figure 16 is shown a comparison of the carbohydrate compositions, the potassium contents and the solid yields obtained in the torrefaction reactor and on the TGA of the raw biomass samples. The biomasses have reasonably similar carbohydrate compositions. The exception is the bark sample that has a lower

hemicelluloses content of 12 wt% db (with the other biomasses having approximately 20 wt% db of hemicelluloses) a lower celluloses content of 22 wt% db (with the other biomasses having from 34 wt% db to 44 wt% db of celluloses) and a higher lignin content of 35 wt% db (with the other biomasses having from 17 wt% db to 29 wt% db of lignin). Generally it is seen that the solid mass yield decreases with an increase in the alkali content. However, the only exception is the bark sample that has relatively low hemicelluloses and celluloses contents, and therefore shows a higher solid yield. It can be concluded, that the solid yield is mainly determined by the biomass potassium content but is also influenced by the carbohydrate composition.

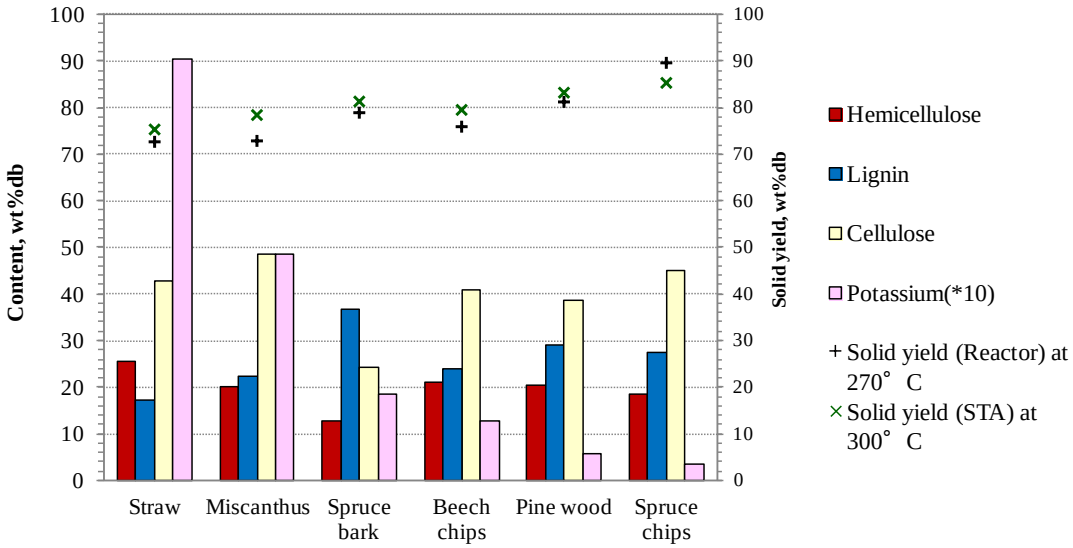

Figure 7-16: Comparison of biomass key composition data and the solid yields obtained on TGA and the torrefaction reactor. There are shown the lignocelluloses composition and the potassium contents of the biomass samples (Note that the potassium content value is multiplyed by 10). The cross markers represents the solid yields obtained from the torrefaction reactor at 270 °C (and 90 minutes residence time) and 300 °C STA data (heating rate of 5 °C/min)

In Figure 17 the relative particle size d_{50} reduction obtained on the torrefaction reactor at 270 and 300°C as a function of biomass alkali content is shown. With an increased alkali content up to 0.2 wt% db the relative d50 increases a lot, while higher potassium contents do not seems to influence the particle size reduction. Increasing the reactor temperature from 270 to 300°C does in all cases increases the particle size reduction. The samples with added KCl or K_2CO_3 show a

somewhat unpredictable behavior. Samples impregnated with KCl shows a higher particle size reduction than samples impregnated with K_2CO_3.

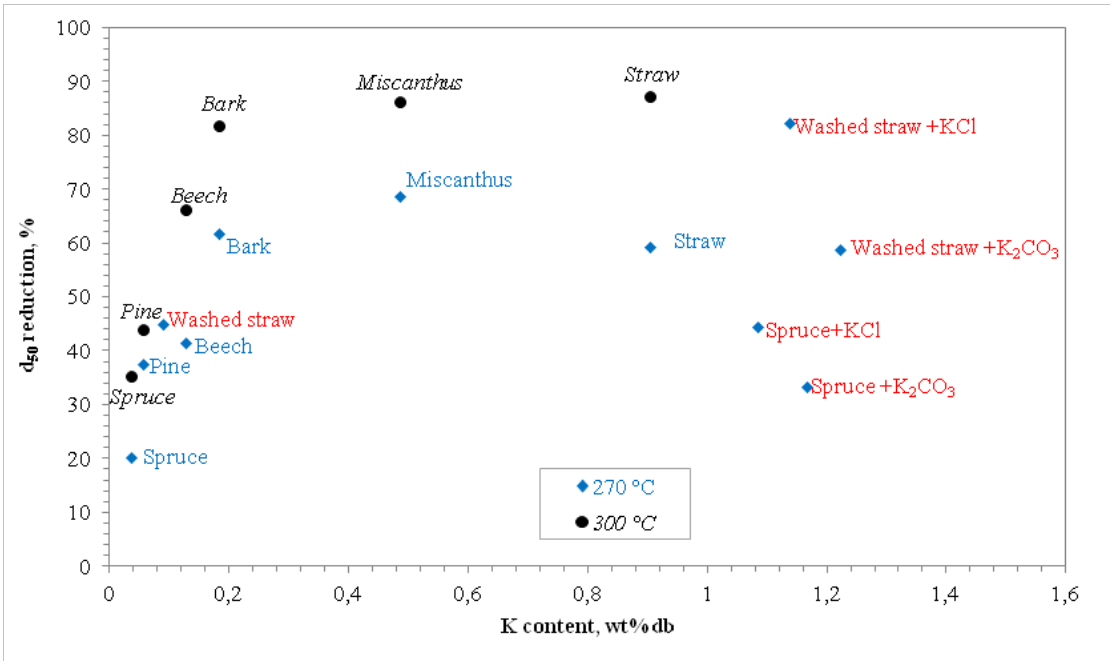

Figure 7-17: Relative reduction of particle size (d_{50} reduction) as a function biomass potassium content. Experiments conducted on the torrefaction reactor at temperatures of 270 °C and 300 °C and residence times of 90 minutes.

On figure 18 is shown the relation between mass loss (1- solid yield) and the obtained particle size reduction in the torrefaction reactor at 270 and 300°C. At a specific reactor temperature there is observed a reasonable linear relation between mass loss and particle size reduction. The exception is bark torrified at 300°C that experiences a high d_{50} reduction of 80% with a mass loss of 34 wt%. The reason is probably that the relatively low content of hemicelluloses in the bark to a high degree has been converted to gas and char. The destruction of hemicelluloses makes the biomass brittle. In Figure 19 the pretreated biomasses are shown together with the Torrification data of the raw biomasses. It is observed that the biomasses impregnated with KCl shows trends similar to the raw biomasses, while the K_2CO_3 impregnated biomasses cause a relatively high mass loss without a corresponding high particle size reduction.

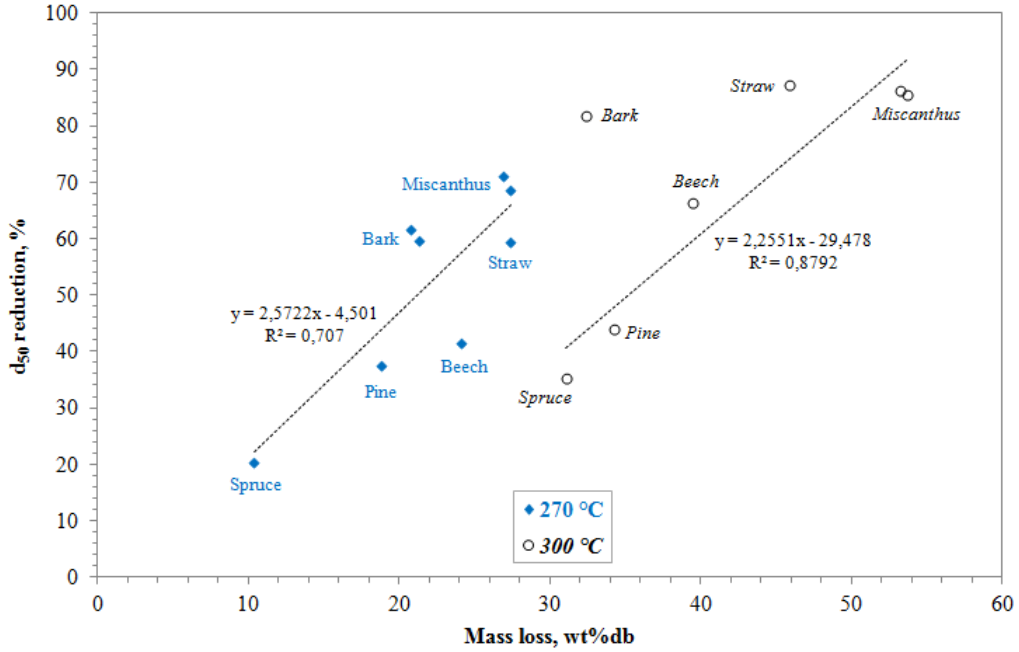

Figure 7-18: Relative reduction of particle size (d_{50} reduction) as a function the mass loss obtained on the torrefaction reactor. There were used reactor temperatures of 270 °C and 300 °C and residence times of 90 minutes. The fitted line of the 300 °C data is excluding the bark.

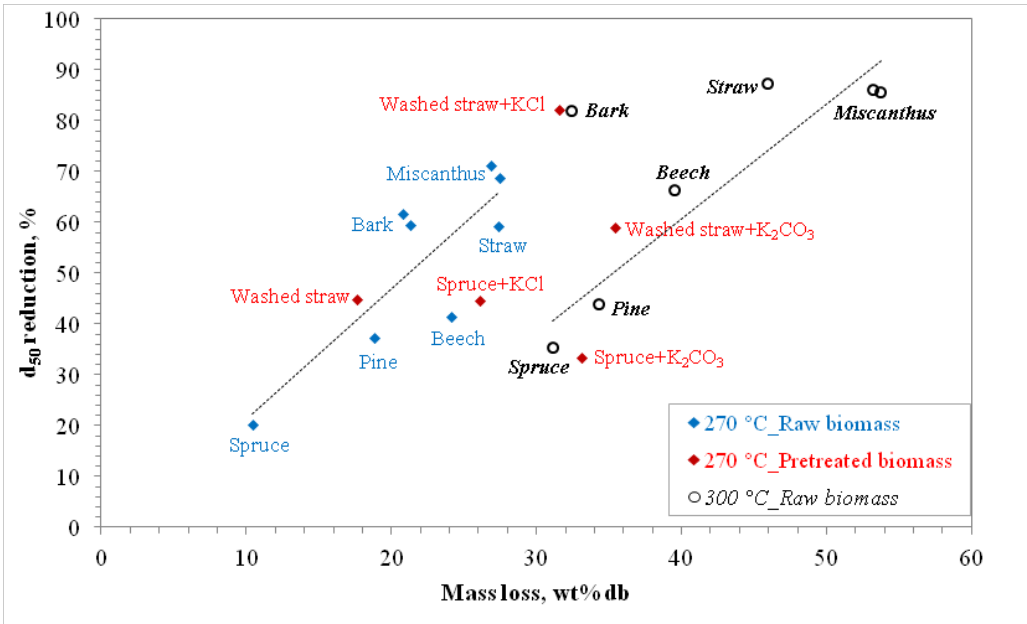

Figure 7-19: Relative reduction of particle size (d_{50} reduction) as a function the mass loss obtained on the torrefaction reactor. There were used reactor temperatures of 270 °C and 300 °C and residence times of 90 minutes.

The main conclusions of the study on the biomass composition influence on the torrefaction process can be summarized in the following points:

- The solid yield at typical torrefaction temperatures of 270 to 300°C is strongly influenced by the biomass potassium content. High biomass potassium content leads to a relatively low solid yield. Also the carbohydrate composition influences the solid yield, such that low hemicelluloses content leads to a relatively high solid yield.
- Biomasses that experiences a high mass loss during the torrefication process do also experiences a relatively high particle size reduction

Release of chlorine and sulfur

During the torrefaction process some Cl and S may be released to gas phase. If the gas is used in a combustion unit the S and Cl species may cause some corrosion of heat transfer surfaces. It is therefore wanted to have some knowledge on the amount of Cl and S released during torrefaction. The aim of this study is to determine the release of Cl and S from different biomasses pyrolyzed in the temperature range of 150-500 °C in a nitrogen atmosphere. Several biomasses were investigated using the torrefaction reactor and a fixed bed reactor. However, the analysis of the Cl and S content of many of the biomasses had a very high uncertainty because of the low concentration levels. In this section is therefore only presented data on Cl and S release from straw.

The relative and absolute release of Cl and S were calculated by use of mass balance and analysis of the straw before and after torrefaction. The results are presented in figures 20 and 21. The data indicate that only a small amount of Cl is released up to a temperature of 250°C. When the temperature is increased from 250°C to 350°C 50 to 65 wt% of the straw Cl is released to the gas phase. In Figure 21, the release of Cl as a function of sample size is shown. With 5 gram in the loader a release of 79 % was observed, with 20 gram in the loader a release of 65 % was observed and with 40 gram in the loader a release of 55 % was observed. A possible reason for this could be that some of the initially released Cl is re-captured in the solid sample. By collecting the gas from four of the experiments and conducting GC analysis on the gas samples, it was found that a major part of the released Cl appeared as methyl chlorine (CH_3Cl).

The release of sulfur happens gradually between 150 and 500°C, and approximately 50 wt% of the straw sulfur content is released to the gas phase at 500°C. In experiments with different sample sizes (Figure 21) there was not observed any connection between sample size and release of S.

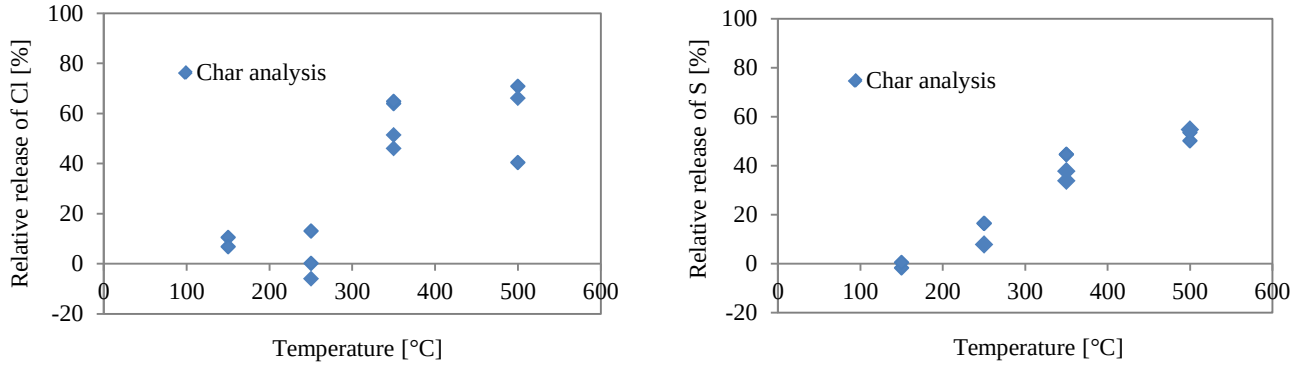

Figure 7-20: Influence of temperature on relative release of Cl and S to gas phase. Data from torrefaction reactor experiments with 20 g biomass samples.

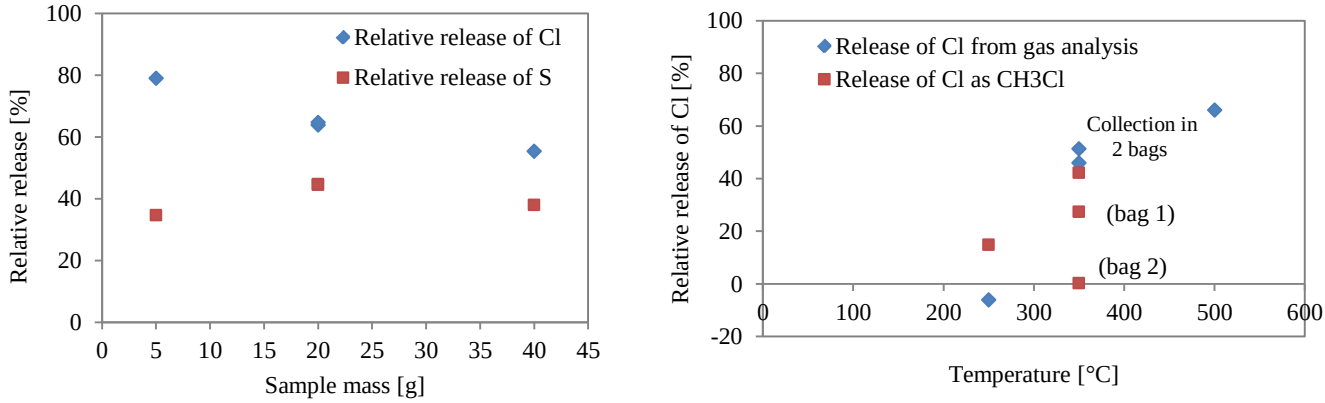

Figure 7-21: Influence of sample mass on relative release of Cl and S (left side) and relative release of Cl from the gas analysis

By this study on Cl and S gas phase release at torrefaction conditions it was observed that a large release of both Cl (up to 65%) and S (up to 50%) can take place. The chlorine is mainly release as methyl chlorine (CH_3Cl).

Design calculations on rotary kiln torrefaction reactor

This section describes the initial design considerations regarding the dimensions of a rotary kiln torrefaction plant supplying torrified biomass and gas to a 100 MW_{th} suspension-fired power plant unit. A possible concept is shown in Figure 22

where the energy supply for the torrification process is delivered by a partial combustion of the evolved gasses. Biomass and a hot gas stream will be supplyed to the combined ball mill and torrefaction reactor. The fine particles leaving the reactor with the gas stream will be separated and sent to the boiler, while part of the gas stream will be combusted and the remaining gas stream recycled to the reactor, after heat exchange with the hot gas stream from the combustion. The size of a ball mill torrefaction reactor for simultaneous torrefaction and grinding will be evaluated based on heat transfer considerations. Initial evaluations will be based on assumptions of a well mixed reactor and a uniform biomass particle size.

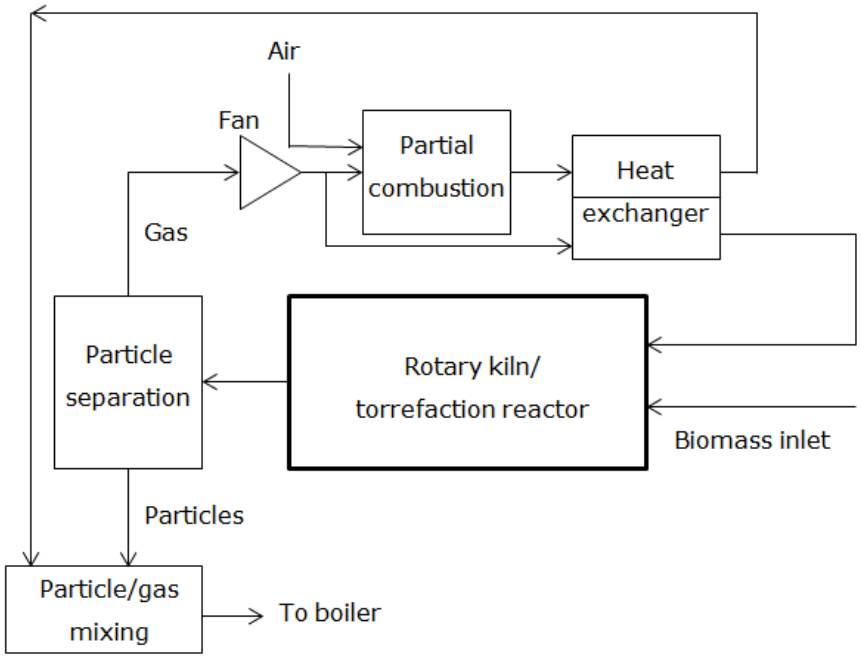

Figure 7-22: Outline of torrefaction plant

Heat transfer and reactor dimensions

Figure 6-23 illustrates the basic outline of a torrefaction reactor with integrated grinding. The raw biomass is feed into the rotating kiln, where drying, heating and low temperature pyrolysis takes place. The heated biomass is more brittle and the presence of metal balls causes grinding of the biomass. In the following it will be assumed that the particles will be grinded when they reach a temperature of 270 °C, the fine particles formed will then be entrained by the gas flow and exit the reactor. Heating of the bed material may be performed though the walls or by a hot gas stream. With the assumption of instantaneous grinding of the

pyrolyzed particles the reactor dimensions will be determined by either the heat transfer to the bed, mixing within the bed or heat conduction within particles for a given feed rate and particle size. The steady rotation of a kiln ensures a good particle mixing and temperature distribution within the bed – this heat transfer resistance is therefore being assumed negligible [Li, et. al., 2005]. The influence of heat transfer to the bed (external heat transfer) and heat conduction within particles (internal heat transfer) will be covered in greater detail in the next sections.

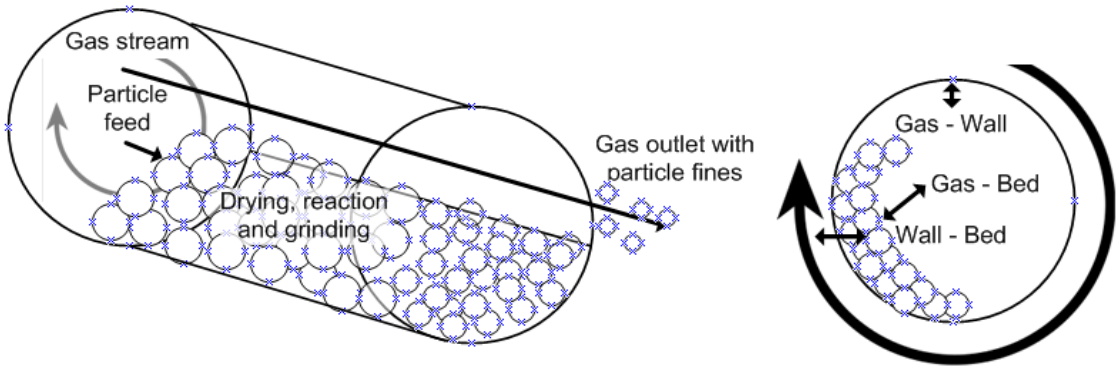

Figure 7-23: Torrefaction reactor outline (left) and modes of heat transfer (right)

The amount of straw/woody biomass needed to supply a 100 MW_{th} plant can be calculated by equation 1, assuming that the energy released during processing is fully utilised by a nearby power plant/boiler (~ 0 % energy loss).

$$\dot{m} = \frac{100MWh \cdot 3600MJ/MWh}{15MJ/kg} = 24000\frac{kg}{h} \qquad [1]$$

This corresponds to approximately 46 big bales of straw or 80 m^3 wood chips per hour.

The energy input required for heating the dry biomass to 270 °C becomes 2.98 MW (equation 2), the presence of 5 wt % moisture increases the required heat input with 0.87 MW. In addition to these numbers additional energy/electricity inputs, such as for the rotation of the cylinder, may be required.

$$Q_{dry\_feed} = \dot{m}_{wood,dry} \cdot C_{p,wood} \cdot \Delta T + \frac{0.01 \cdot \%_{H_2O}}{1 - 0.01 \cdot \%_{H_2O}} \cdot \dot{m}_{wood,dry} \cdot \left(H_{vap} + C_{p,H_2O} \frac{kJ}{kg \cdot C} \cdot T_{boil} - T_{start} \right) \qquad [2]$$

$$Q_{dry\_feed} = 6.7\frac{kg}{s} \cdot 1780\frac{J}{kg \cdot {}^{o}C} \cdot (270 - 20)^{o}C = 2.97MW$$

$$Q_{5wt\%\_H_2O} = 2,98 + 0.05 \cdot \dot{m}_{wood} \cdot \left(2257 \frac{kJ}{kg} + 4.18 \frac{kJ}{kg \cdot C} \cdot 80^o C \right) = 3,85 MW$$

Figure 6-24 shows the transient development in internal temperature distribution for 1, 10 and 25 mm particles. Initially considerable internal temperatures gradients are observed for 10 and 25 mm particles. As the final temperature is approached the gradients becomes much less pronounced and an assumption of a uniform particle temperature can be reasonable for this latter part of the heating process.

Internal particle heat transfer limitations

The influence of internal particle heat transfer will be evaluated based on the one-dimensional heat conduction within single spherical particles. Equation 3a describes the transient and internal development of particle temperature due to heat conduction in spherical coordinates. This equation can be expressed as a dimensionless temperature increase (equation 3b) based on Fourier's number (Fo = α · t/ R^2), Biot's number (Bi = h R /k_b), the thermal diffusivity of wood (α), the thermal conduction coefficient of wood (k_b), the gas to bed heat transfer coefficient (h), the particle radius (R) and time (t) [Green, 2008; Cengel, 2008].

$$\frac{\partial T}{\partial t} = \frac{\alpha}{r^2} \cdot \frac{\partial}{\partial r}\left(r^2 \cdot \frac{\partial T}{\partial r} \right) \qquad T(r,0) = T_i \quad \frac{\partial T(0,t)}{\partial r} = 0 \quad -k \cdot \frac{\partial T(R,t)}{\partial r} = h\left(T - T_\infty\right) \qquad [3a]$$

$$\rightarrow \frac{T(r,t) - T_i}{T_\infty - T_i} = \sum_{n=1}^{\infty} \frac{4\left(\sin\lambda_n - \lambda_n \cos\lambda_n\right)}{2\lambda_n - \sin\left(2\lambda_n\right)} \cdot e^{-\lambda_n^2 \cdot Fo} \cdot \frac{\sin\left(\lambda_n \cdot r / R\right)}{\lambda_n \cdot r / R} \qquad [3b]$$

with λ_n being the roots of $1 - \lambda_n \cdot \cot\lambda_n = Bi$

Equation 3b can also be used calculate the time required to heat the centre of the particle within for example 5 % of the final temperature (i.e. the centre temperature has increased 95 % of T_∞-T_i). The times required to heat the centre of a range of particle sizes is presented in Table 1 alongside the reactor volume (equation 4) required to treat 24000 kg/h dry biomass particles at 20 % volumetric reactor loading in the case of internal heat transfer control (i.e. swift heat transfer from wall/gas to the bed, negligible reaction time and instantaneous grinding).

$$V(d_p = 10mm) = \frac{\dot{m} \cdot t}{\rho} \cdot \frac{1}{0.2} = \frac{6.67 kg/s \cdot t}{650 kg/m^3} \cdot \frac{1}{0.2} \qquad [4]$$

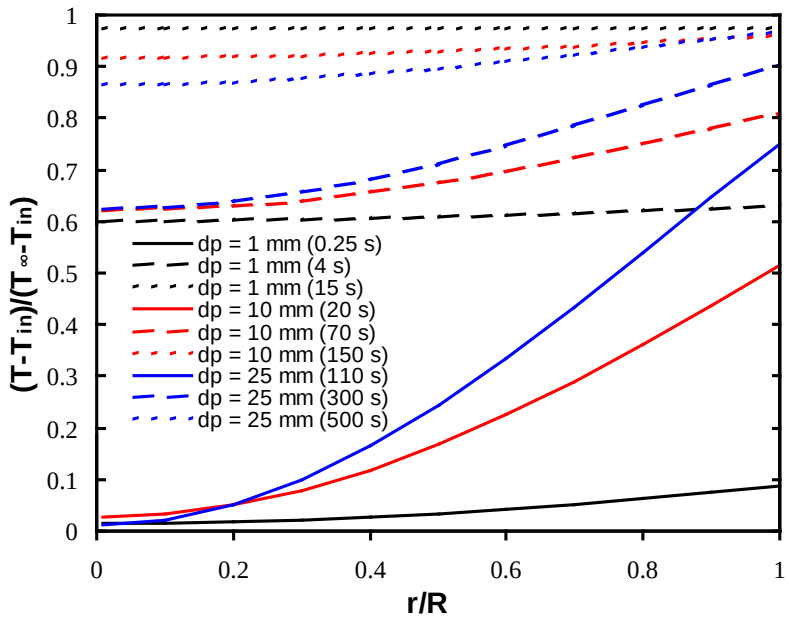

Figure 7-24: Transient development in internal temperature distribution for 1, 10 and 25 mm particles. Thermal conduction coefficient of wood (k_b)= 0,228 W/m K (at 600 K), gas to bed heat transfer coefficient (h_{eb}) = 73 W/m^2 K and thermal diffusivity of wood (α) = 1.3 10^{-7} m^2/s

Table 7-4: Time required to heat particle centre within 5 % of final temperature

Particle diameter [mm]	1	10	25	50
Heating time [s]	13	178	698	2267
Reactor volume [m^3]	1	9	36	116

Table 7-4 summarises the heating/residence times and the needed reactor volumes to process 24000 kg/h dry biomass particles with initial diameters ranging from 1 to 50 mm. Limited residence times and reactor volumes are required below a particle diameter of 25 mm.

Gas to bed heat transfer limitations

The influence of heat transfer from the gas phase to the bed material will be evaluated in this section based on heat transfer coefficients for rotary kilns obtained from the literature. As illustrated by figure 2 heat transfer may take place form gas to bed, wall to bed and between wall and gas. This section will focus on the gas to bed heat transfer (though the beds exposed surface) because

of the high heat transfer coefficients that can be obtained by this relative simple mechanisms (heating by a gas phase as opposed to heating the wall of the rotating reactor). Based on the low torrefaction reaction temperature (~270 °C) heat transfer by radiation is assumed negligible, and only heat transfer by convection will therefore be covered. The convective gas to bed heat transfer coefficient in a rotating kiln can be estimated by equation 5 based on gas density at 450 °C and an assumed gas velocity (0.9 m/s – corresponding to a gas flow of 46 t/h for a D = 6 m reactor) [Boateng, 2008].

$$\dot{h}_{eb} = 0.4 \cdot \left(v_g \cdot \rho_g \cdot 3600 s/h \right)^{0.62} = 0.4 \cdot \left(0.9 m/s \cdot 0.5 kg/m^3 \cdot 3600 s/h \right)^{0.62} \quad [5]$$

$$\rightarrow \dot{h}_{eb} = 39 \frac{W}{m^2 \cdot K}$$

Based on the needed energy input (to process 24 tons straw per hour), the gas velocity, the reactor diameter (assumed to be 6 m), the gas inlet temperature (assumed to be 600 °C) and an assumed uniform bed temperature of 270 °C and co current flow, the change in gas temperature from inlet to exit (equation 6 – a simple energy balance) and the effective temperature difference from gas to bed surface (equation 7) can be determined.

$$T_{g(i)} - T_{g(o)} = \frac{Q_{dry\_feed}}{(1 - fill\%) \cdot \pi \cdot R^2 \cdot v \cdot \rho_g \cdot C_{p,g}} = \frac{2.97 MW}{0.8 \cdot \pi \cdot (3m)^2 \cdot 0.9 m/s \cdot 0.5 kg/m^3 \cdot 0.001 MW/kg \cdot C} \quad [6]$$

$$\Rightarrow T_{g(i)} - T_{g(o)} = 292\ ^o C$$

$$\Delta T_m = \frac{\Delta T_i - \Delta T_u}{\ln \frac{\Delta T_i}{\Delta T_u}} = \frac{(500 - 270) - ((600 - 292) - 270)}{\ln \frac{(500 - 270)}{((600 - 292) - 270)}} = 135^o C \quad [7]$$

The surface area required for heat transfer can then be calculated from equation 8, based on the energy requirement for heating dry biomass (equation 2), the heat transfer coefficient (equation 5) and the effective temperature difference from gas to bed surface (equation 7). The heat transfer area will be the surface area of the bed material layer spread out by the rotation – at a 20 % loading the surface area of a stationary bed corresponds to approximately 25 % of the wall area, which may increase towards 33 % of the wall area due to the rotation [Tscheng & Watkinson, 1979].

$$A = \frac{Q_{dry\_feed}}{h \cdot \Delta T} = \frac{2.97MW}{39\frac{W}{m^2 \cdot K} \cdot 135^o C} \quad [8]$$

$$\rightarrow A_{bed\_surface} = 563m^2$$

$$\rightarrow A_{wall} = 2228m^2$$

The required surface area (2228 m^2) corresponds to a 118 m long cylindrical (D = 6 m, V = 3342 m^3) rotating kiln, which is considerable larger than the volume required for particle heat-up (Table 1). Initiatives to improve the gas/particle contact, such as passing the gas trough the bed material, using baffles etc. may significantly increase the contact area and thereby decrease the required dimension of the reactor. If a 10 fold increase in contact area can be obtained by these measures the reactor dimensions becomes much more manageable (L = 12 m and V = 334 m^3). The external heat transfer to the bed is still the limiting step in the reactor design in this case – this will only be further enhanced in the case of higher biomass moisture contents, because of the increased thermal conductivity and the additional energy requirement for drying and water evaporation.

To summarize this short design study it can be stated, that compared to the relatively fast particle heat up by internal heat conduction, the external heat transfer to the fuel bed is the limiting step in the reactor design even when initiatives for increased gas/bed contact is used (passing the gas trough the bed material, using baffles etc). Using a modified rotary kiln having a 10 fold increase in gas to bed contact area (contact area increase compared to rotary kiln without baffles) and assuming treatment of 24 tons straw per hour the reactor dimensions becomes D = 6m, L = 12 m (V = 334 m^3) and in the case of heating of the bed material by a 600 ^oC (inlet temperature) flue gas.

The findings in this work should be supplemented by evaluations of the wall to gas and wall to bed heat transfer. The potential for improved heat transfer through changes in reactor design and operating conditions should also be addressed

In summary, a possible use of a torrefaction process is by integration with a power plant, and thereby a high total energy efficiency can be obtained. Possibly the gas released during the torrefaction process can be used for supplying energy for the torrification process or be supplied to the boiler. A possible reactor used for such a torrefaction process could be a ball mill where the biomass is simultaneous heated and milled. In the present study there are conducted

investigations that can support the development of such a torrefaction ball mill reactor:

- Design and construction of a novel laboratory scale experimental setup (rotating cylinder) for simultaneous torrefaction and grinding was performed, and the reactor was used to torrification experiments with straw and spruce to determine the influence of reactor operation conditions on feedstock conversion and milling
- A broader range of biomasses have been tested to investigate how biomass properties such as ash content, ash composition and carbohydrate composition influence torrefaction
- The gas phase release of Cl and S have been investigated by batch experiments
- Work on a torrefaction reactor design have been initiated

The influence of operation conditions such as reactor temperature and residence time on mass loss, energy loss and particle size reduction have been established for wood and straw. Straw obtain a higher conversion than wood at similar temperatures. By doing experiments with both simultaneous and separate heating and grinding of wood and straw the relative influence of the heating and grinding processes have been investigated (This study is not documented in detail in this summery report). The investigation showed that heat transfer and not the grinding process is the rate limiting step. When the biomass is heated without grinding the following grinding process takes maximal five minutes to obtain a similar particle size as to the combined process.

The biomass composition influence on the torrefaction process was investigated by treating six different biomasses and some biomasses impregnated with KCl or K_2CO_3 on a TGA and in the laboratory torrification reactor. It was observed that the solid yield at typical torrefaction temperatures of 270 to 300°C is strongly influenced by the biomass potassium content. High biomass potassium content leads to a relatively lower solid yield. Also the carbohydrate composition influences the solid yield, such that low hemicelluloses content leads to a relatively high solid yield. It was also seen that biomasses that experiences a high mass loss during the torrification process do also experiences a relatively high particle size reduction.

The gas phase release of Cl and S from wheat straw at torrification conditions was investigated by fixed bed experiments. There was observed a large release of

both Cl (up to 65%) and S (up to 50%) at 350°C. The chlorine is mainly released as methyl chlorine (CH_3Cl).

The torrification reactor design study showed, that compared to the relatively fast particle heat up limited by internal heat conduction, the external heat transfer to the fuel bed is the limiting step in the reactor design even when initiatives for increased gas/bed contact is used (passing the gas trough the bed material, using baffles etc). Using a modified rotary kiln having a 10 fold increase in gas to bed contact area (contact area increase compared to rotary kiln without baffles) and assuming treatment of 24 tons straw per hour the reactor dimensions becomes D = 6m, L = 12 m (V = 334 m^3) in the case of heating of the bed material by a 600 °C (inlet temperature) flue gas.

References

1. Deng, J., Wang, G.J., Kuang, J.H., Zhang, Y.L., Luo, Y.L., Pretreatment of agricultural residues for co-gasification via torrefaction, *Journal of Analytical and Applied Pyrolysis* 86 (2009) 169-175.
2. Bridgeman, T.G., Jones, J.M., Williams, P.T., and Waldron, D.J., An investigation of the grindability of two torrefied energy crops, *Fuel* 89 (2010) 3911 – 3918.
3. Pimchuai, A., Dutta, A., Basu, P., Torrefaction of Agriculture Residue To Enhance Combustible Properties, *Energy & Fuels* 24 (2010) 4638 – 4645.
4. Verhoef, F., Pels, J.R., Boersma, A. R.; Zwart, R. W. R.; Kiel, J. H. A., ECN Torrefaction Technology heading for demonstration, 19th European Biomass Conference and Exhibition (EU BC&E), ICC Berlin, Germany, 2011.
5. Ciolkosz, D. E., and Wallace, R., Torrefaction of Biomass as a Bioenergy Feedstock. *Biofuels, Bioproducts and Biorefining* 5(2011) 317–329.
6. Saddawi, A., Jones, J.M., Williams, A., Influence of alkali metals on the kinetics of the thermal decomposition of biomass, Fuel Process. Technol. (2012) DOI:10.1016/j.fuproc.2012.05.014
7. Fahmi, R., Bridgwater, A.V., Donnison, I., Yates, N., Jones, J.M., The effect of lignin and inorganic species in biomass on pyrolysis oil yields, quality and stability, *Fuel* 87 (2008) 1230 – 1240.
8. Jensen, A., Dam-Johansen, K., Wo´jtowicz, M.A., Serio, A., TG-FTIR Study of the Influence of Potassium Chloride on Wheat Straw Pyrolysis, *Energy & Fuels* 12 (1998) 929 – 938.

9. Olsson, J.G., Ja¨ glid, U., Pettersson, J.B.C., Alkali metal emission during pyrolysis of biomass, *Energy & Fuels* 11 (1997) 779 – 784.
10. Boateng, A.A. *Rotary kilns – Transport Phenomena and Transport Processes*, Butterworth Heinemann, **2008**.
11. Cengel, Y.A. *Heat and mass ytansfer – a practical approach 3rd edition*, McGraw-Hill, **2007**.
12. Haynes, W.M., ed. *CRC handbook of Chemistry and Physics 92nd edition* (Internet version 2012), CRC Press/Taylor and Francis, Boca Raton, FL, **2012**.
13. Green, D.W., ed. *Perry's chemical engineers' handbook 8nd edition*, McGraw-Hill, **2008**
14. Li, S.Q.; Ma, L.B.; Wan, W and Yao, Q. A Matematical Model of Heat Transfer in a Rotary Kiln Thermo-Reactor. *Chemical Engineering and Technology;* 28(12); pp. 1480-1489, **2005**.
15. Tscheng, S.H.; Watkinson A.P.. Convective Heat Transfer in a Rotary Kiln. *The Canadian Journal of Chemical Engineering;* 57, pp. 433-444, **1979**,

8. Summary and Conclusions

This chapter contain a brief summary af what have been achieved within the overall project on a work package by work package base.

In WP1, a detailed model for the gas-phase nitrogen chemistry was developed and validated. The model emphasizes mainly the oxidation chemistry of amines (NH_3, $C_2H_5NH_2$, CH_3NHCH_3). Based on the detailed chemical kinetic model, a simplified scheme for oxidation of N-volatiles from biomass has been completed. For high-temperature applications, only 26 species are required to yield a good prediction of NO_x. Biomass char-N oxidation has been characterized in laboratory experiments. Results were obtained for straw and bark, with reference experiments for a bituminous coal. A simplified model for char-N oxidation, involving only two steps (char-N+O_2 → NO, char+NO → O_2) has been developed and parameterized based on the experimental results.

As part of WP2, thermodynamic calculations showed that the fate of the heavy metals is dependent on the other chemistry in the system. Chlorine and sulfur in the gas phase interact strongly with heavy metals and alkali metals. Variation in these three elements influences the partitioning of the heavy metals studied. Understanding this complex chemistry is vital for being able to interpret modeling results of more complex systems.

Further, a 2-step model based on thermodynamic equilibrium calculations (TEC) considering the different constraints in a fuel bed regarding bed composition (unburned fuel, charcoal), atmosphere and temperature was developed in order to predict the release of ash forming elements during fixed-bed combustion. The data gained from the TEC were compared with the results of the lab-scale reactor test runs performed within WP5. Summing up the 2-step model resulted, compared with a 1-step approach, in an improvement of the K and Na-release prediction accuracy in most cases. The applied model seems to be suitable for the description of the release behaviour of Cl and Pb. The calculated S release is also acceptable in most cases (beech, softwood, sewage sludge), but for poplar the prediction accuracy was still unsatisfying (underestimated) and also for the Zn-

release the prediction preciseness varied between the different fuels investigated.

Therefore, it can be concluded that the 2-step model has provided some improvements, but still cannot be claimed as an universal solution for the description of the release behavior of aerosol forming species from the fuel bed. One relevant responsible factor are supposed to be secondary reactions of the inorganic vapors released with other ash forming compounds in the fuel bed which cannot be considered in a global equilibrium approach. Consequently, further work on this topic will be needed in future.

Concerning the prediction of the ash melting process a reliable model could be developed. By means of the empirically estimated limits for molar ratios of (Si+K+P)/(Ca+Mg), K/(Si+P) and Al/Si the model was optimized to be used for a wide range of different biomass ash compositions. The modeling results were validated against the data regarding the deformation temperature and the flow temperature, determined according to standard ash melting test (DIN 51730) and against experimental data received from STA. The results achieved qualify TEC as a suitable technique for the prediction of the ash melting processes and the characteristic melting temperatures for biomass ashes, if the optimized thermodynamic model is applied. The advantages of TEC for the evaluation of the ash melting behavior are that they provide a more detailed insight in the melting processes as well as in the distribution of molten phases involved. Moreover, the application of TEC is possible for the total fuel ash but also for dedicated ash fractions occurring within a plant which makes it attractive for practical applications. A general restriction of the TEC-model is at present, that it is not recommended for P-rich biomass ashes, as the quality of the thermodynamic data concerning P compounds is still insufficient. Here an urgent demand for further experimental and theoretical work exists.

Finally, in WP2, in order to assist the work packages related to deposition and corrosion in grate-fired and pulverized fuel fired systems and in gasification, S/Cl/K transformations in thermal processes has been characterized. The release of the elements S, Cl, and K from biomass combustion has been quantified as a function of fuel composition and temperature. A detailed chemical kinetic model for the gas-phase transformations of S, Cl, and K, emphasizing sulphation of KCl, has been validated against measurements from flames. A simplified aerosol formation model has been developed, based on aerosol theory, and sulfation of particulate KCl has been quantified and modelled.

In WP3, the work on modeling of fixed combustion plants had the following major objectives:

- Implementation of a release model for ash forming elements into a CFD model for fixed bed combustion model
- Selection of a turbulence model applicable for low-Re flows
- Development of gas phase combustion model suitable for low-Re and high-Re flows
- Streak formation modeling

A 2-step approach for the release of the ash forming elements in the pyrolysis zone and the char burnout zone was evaluated in Task 2.2 based on thermodynamic equilibrium calculations. The results showed that the approach is not able to predict the release of ash forming volatiles appropriately. Therefore, an in-house developed 3D packed bed combustion model of BE2020+/TUG was used to calculate profiles of particle temperatures as well O_2 concentrations along the grate. The location of the release during pyrolysis and char burnout is determined by the packed bed model whereas the corresponding release rates have to be taken from the experimental data gained within WP5.

Especially for small-scale combustion applications and in the region above the fuel bed, gas phase mixing is highly influenced by laminar and low turbulence zones. Here, the gas phase combustion models are not valid anymore, since they are originally developed for highly turbulent flows. Therefore, a CFD gas phase reaction model which is applicable in the whole Reynolds range from laminar to turbulent flows was developed. It is a hybrid Eddy Dissipation Concept / finite rate kinetics model which calculates the effective reaction rate from laminar finite rate kinetics and the turbulent reaction rate and weights them depending on the turbulent Reynolds number. The model development was supported by experimental data from literature for different jet flames. Moreover, since the prediction of flow and turbulence properties is an important basis for gas phase combustion simulation, the SST k-ω turbulence model suitable for low-Re flows as well was selected by a comparison with cold flow experiments with a flame reactor of BE2020+/TUG.

State-of-the-art packed bed models supply continuous concentration profiles as boundary conditions for subsequent CFD-simulations of gas phase, leading to premixed combustion conditions. However, in reality the "porous" nature of the packed bed leads to streak formation. In order to account for the influence of the streaks on gas phase combustion, a gas streak model based on a correlation

between the local gas residence time and a mixing time where the streaks are fully mixed has been developed by BE2020+/TUG. The cold-flow reactor experiments as well as a numerical case study with an ideally packed bed were used to calibrate the model constants.

Finally, the gas streak formation model and the newly developed gas phase reaction model were successfully tested with an in-house developed packed bed combustion model of BE2020+/TUG. Simulations of a 20 kW pellet underfeed stoker furnace were performed for model evaluation. These first tests showed a more realistic prediction of gas phase combustion in the primary combustion zone than the simulations with the Eddy Dissipation Model with global reaction kinetics and without consideration of streak formation and a relevant improvement of gas phase combustion simulation for packed beds could be achieved.

Further, in Task 3.3, a computationally efficient particle model has been improved and extended in this project. The model allows for resolving intra-particle gradients. Especially the processes during the char conversion stage have been in focus in this project. For this stage new models for char gasification have been investigated. Also a new model for the release of NO during the char oxidation stage has been developed. This semi-empirical model is based on the assumption that the heterogeneous NO conversion takes place close to the external surface of the char particle. Especially the models for the char conversion stage can easily be utilized also with less complex particle models. Using the models a better description of the fuel conversion is obtained, thus leading to more reliable results.

The models developed for CFD-modeling of bubbling fluidized bed combustors in this project mainly focus on the fuel particle behavior in the bed. For the fuel conversion in the free board the developed single particle model is directly applicable. The aim of this project has been to develop a predictive description of the fuel behavior in the bed and in the splash zone. The chosen model uses a stochastic approach to model the dispersion the fuel in the bed. The dispersion rate can be estimated using basic expression from the bubbling bed theory. Using the same theory, whit the additional assumption that the bed particles are the main transport vehicle for energy, an effective thermal conductivity can be calculated in order to get a realistic description of the bed temperature. Using this kind of model, presumed release location of volatiles from the bed can be avoided. Consequently, the model facilitates the investigation of fuel feed modifications, particle size changes and bed material changes on the behavior of the bubbling bed combustor.

A numerical prediction of ash release would only be possible by the link with reaction kinetics. However, since the kinetics should comprise heterogeneous reactions in the packed bed, which are not available, there is a need for further comprehensive R&D work to develop such kinetics and to implement them in packed bed combustion models.

A new hybrid Eddy Dissipation Concept (EDC) / finite rate kinetics model, which calculates the effective reaction rate from laminar finite rate kinetics and the turbulent combustion rate with the EDC depending on the turbulent Reynolds number, was developed. This model is able to cover the whole rage from laminar to turbulent flows. Hence, it contributes to an improved prediction of gas phase combustion in biomass combustion plants since in small-scale plants and in the region above the packed bed low-Re flow conditions occur. However, this model needs further development concerning the reduction of calculation time and comprehensive validation simulations for low-Re jet flames and real-scale applications.

Moreover, a gas streak model based on a correlation between the local gas residence time and a streak mixing time was developed by BE2020+/TUG in order to account for the influence of the streaks on gas phase combustion. This new approach constitutes an important step towards an improved gas phase combustion modeling in the region above the packed bed since state-of-the-art CFD models are not able to consider the influence of gas streaks arising from the fuel bed on the reaction progress which leads e.g. to an over-prediction of flue gas temperatures and CO burnout. Also in this case, further model development work on the streak formation model, e.g. the correlation between the mixing time and the mixing function as well as comprehensive validation work for biomass grate furnaces is necessary in order to supply a reliable CFD model which can be applied as engineering tool.

The Lagrangian particle model approach has to be combined with an ending criterion to avoid impractical calculation times: large biomass particles may need minutes before complete conversion.

The available mixtures proved to be very similar with respect to CFD modeling. The sludge wetted the other fuel fractions and could not be identified/model as a separate fuel: it only changed the moisture content and the ash content compared. The bark and the refuse derived fuels had very similar heating value on dry ash free bases and very similar particle size distribution. Consequently, these two fuels behaved in a similar way as well. As a result, although in-furnace and flue gas measurements were available, these were not useful for validating the

model for various mixtures. In the biomass particle model, the only significantly changing parameters were the moisture content and the ash content.

The predicted temperatures in the bed region showed some discrepancies compared to observation using an IR-camera. The possible reason for this is uncertainties in the mass dispersion rate of the fuel.

A computationally efficient particle model has been improved and extended in this project. The model allows for resolving intra-particle gradients. Especially the processes during the char conversion stage have been in focus in this project. For this stage new models for char gasification have been investigated. Also a new model for the release of NO during the char oxidation stage has been developed. This semi-empirical model is based on the assumption that all fuel nitrogen is initially converted to NO. This conversion takes place close to the external surface of the particle, and assuming that the char oxidation is mass transfer limited, the NO partial pressure at the surface can be assumed to be proportional to the bulk concentration of O_2. The NO reduction on the char particle can then be modeled using a simple expression applicable to CFD modeling. Especially the models for the char conversion stage can easily be utilized also with less complex particle models. Using the models a better description of the fuel conversion is obtained, thus leading to more reliable results. Nevertheless, the models require fuel specific parameters for which laboratory fuel characterization tests are necessary.

As part of WP4, NTNU investigated various operating parameters and their effect on NOx emission levels. Different experimental studies were carried out on biomass fuels in order to study the effect of fuel properties and combustion parameters on pollutant emissions. Advanced experimental equipment was used in these studies. The experiments showed the effects of staged air combustion, compared to non-staged combustion, on the emission levels clearly. A NOx reduction of up to 85% was reached with staged air combustion using demolition wood as fuel. An optimum primary excess air ratio of 0.8–0.95 was found as a minimizing parameter for the NOx emissions for staged air combustion. Air staging had, however, a negative effect on N2O emissions. Less effect was found by temperature variations and by fuels staging. These findings are all important for further design of biomass combustion furnaces.

Within WP5, BE2020 investigated different fuel indexes taken from literature regarding their applicability for biomass and developed some new fuel indexes to estimate relevant combustion related properties of biomass fuels. Comparisons

with real-scale test run data show that fuel indexes can be a useful tool for the assessment of biomass fuels with respect to slagging tendencies, aerosol and deposit formation as well as corrosion related problems. With some restrictions also first indication regarding gaseous HCl and SO_x emissions can be gained.

However, there is still a considerable potential to improve the prediction preciseness of fuel indexes. For the prediction of HCl and SO_x emissions for instance, a more detailed investigation of the K-release to the gas phase and also of possible Ca interactions are necessary. To gain more knowledge about the K-release from biomass fuels, interactions of Si and P with K as well as of the combustion temperature and the mode of occurrence of K in biomass fuels need to be investigated more detailed.

The most important ash forming element from the fireside problems point of view is potassium. Potassium is the root cause to bed sintering, fouling and corrosion when using biomass based fuels. K is present in the fuel in different forms, and it is of vital interest to identify these forms. Here, the selective leaching analysis of the ash forming matter is very useful. The insoluble part of the potassium is most often in the form of silicate contaminations of the fuel (clay etc). This part of potassium is in a very inert form and does not take part in the lively chemistry of the more reactive forms of potassium. In biomass based fuels K is mostly in soluble form. It can be present either in ionic form in salts in the aqueous fluids of the plant, or as directly organically bound K ions These potassium compounds will be effectively released in combustion and thus be easily available to any further reactions in the flue gases.

Calcium is the element present in the highest concentration in woody biomasses. It is partially organically bonded and thus exchangeable in the ammonium acetate leaching. It is also present as crystalline salt particles, mostly calcium oxalate – especially in biomasses having a high content of Ca, such as bark . This fraction of Ca is found mainly in the acid soluble fraction of the leaching test. The organic calcium compounds will be converted to calcium oxide. Calcium oxide has a low vapor pressure and a high melting point. Consequently, organic calcium in biomass is released in combustion as small solid particles, CaO(s). Calcium oxalate (several crystalline forms containing crystal water) in the biomass will also form finely divided small oxide particles under hot furnace conditions

Chlorine is present in biomass fuels as chloride salts. These salts may vaporize at combustion as alkali chlorides (KCl(g), NaCl(g)) or decompose and release the Cl which rapidly converts to HCl(g). Most (all) chloride salts in fuels are soluble and show up in the soluble fraction of the leaching test Some part of Cl may also be

present as organic chlorine compounds. The most important of these are waste derived fuels containing rests of polyvinyl chloride (PVC) polymers. The Cl in PVC is insoluble in the leaching test and will stay in the rest fraction.

Sulfur is present in biomasses as both inorganic sulfate anions and as organic sulfur. According to recent studies roughly ¾ of the sulfur in woody biomasses is organically bound and ¼ as soluble alkali sulfates. The organic sulfur will be fully released in combustion – primarily as H_2S and other reduced gaseous species which then oxidize to SO_2. The fate of the sulfur in alkali sulfate is not clear. It may stay connected to the alkali sulfate, but it also may be released due to some decomposition reaction of the alkali sulfate.

Phosphorus may be present in biomass fuels as either soluble phosphate salts, or in organic molecules containing phosphorus. In woody biomass around 3/4 of the phosphorus is inorganic and some 1/4 organic. However, in other biomasses this ratio may be different. In some annual plants the phosphorus content may be very high. The release and fate of the various phosphorus compounds in combustion furnaces and flue gases is not well studied. However, it is clear that both alkali and calcium phosphates may form.

TGA/DSC as a method for assessing the fusion of ashes provides an appropriate tool for the continuous description of ash melting, which is detected as endothermic reaction. Unfortunately the method cannot be recommended for the quantification of molten fractions.

In all cases where the fuels show increased molar Si/K and/or Si/(Ca+Mg) ratios as well as elevated Cl-contents (waste wood, miscanthus, straw), as expected, initial melting peaks were already detected in the temperature range of 850 to 900°C.

Comparing ash melting properties derived from DSC with results obtained by the standard ash melting test (DIN 51730), an acceptable agreement could be observed. In addition, the DSC method is able to provide a more detailed determination of separate melting stages in the form of characteristic endothermic peaks.

The results of test with the lab-scale reactor provide relevant information about the thermal decomposition behavior of a fuel in a fixed-bed as well as concerning the main flue gas species released from the fuel during volatilization and charcoal combustion. These data can further be used for the development, validation and

calibration of models for fixed-bed combustion, which can then form the basis for more detailed CFD simulation models. Moreover, the information gained about the release of NO_x precursors from the fuel can be used as input data for NO_x formation simulations in the gas phase. Also the data gained regarding ash related problems, such as the release data for easily volatile elements like S and Cl, semi-volatile elements such as K and Na as well as easily volatile heavy metals like Zn and Pb, are important for the characterization of a fuel with respect to aerosol emissions and deposit formation tendencies. They can also be used as input data for CFD-based aerosol and deposit formation modeling.

In conclusion, the test runs performed with the lab-scale reactor proved to be a valuable instrument to gain advanced fuel characterization data.

As a final result of the work performed within Task 5.6, a comprehensive advanced fuel database could be programmed. With the SciToBiCom fuels a broad range of different relevant fuel characteristics could be covered and therefore, also the data contained in the database reflect the wide range of test results possible. The database can in future be utilized to compare new fuels with the characteristics of the fuels already contained in the database and thereby derive relevant indications regarding possible combustion related problems which may occur when utilizing these fuels. Moreover, it can be applied for the validation of newly developed fuel characterization tools.

In WP6, a possible use of a torrefaction process by integration with a power plant, was investigated. By this, a high total energy efficiency can be obtained. Possibly the gas released during the torrefaction process can be used for supplying energy for the torrification process or be supplied to the boiler. A possible reactor used for such a torrefaction process could be a ball mill where the biomass is simultaneous heated and milled. In the present study there are conducted investigations that can support the development of such a torrefaction ball mill reactor:

- Design and construction of a novel laboratory scale experimental setup (rotating cylinder) for simultaneous torrefaction and grinding was performed, and the reactor was used to torrification experiments with straw and spruce to determined the influence of reactor operation conditions on feedstock conversion and milling

- A broader range of biomasses have been tested to investigate how biomass properties such as ash content, ash composition and carbohydrate composition influence torrefaction
- The gas phase release of Cl and S have been investigated by batch experiments
- Work on a torrefaction reactor design have been initiated

The influence of operation conditions such as reactor temperature and residence time on mass loss, energy loss and particle size reduction have been established for wood and straw. Straw obtain a higher conversion than wood at similar temperatures. By doing experiments with both simultaneous and separate heating and grinding of wood and straw the relative influence of the heating and grinding processes have been investigated (This study is not documented in detail in this summery report). The investigation showed that heat transfer and not the grinding process is the rate limiting step. When the biomass is heated without grinding the following grinding process takes maximal five minutes to obtain a similar particle size as to the combined process.

The biomass composition influence on the torrefaction process was investigated by treating six different biomasses and some biomasses impregnated with KCl or K_2CO_3 on a TGA and in the laboratory torrification reactor. It was observed that the solid yield at typical torrefaction temperatures of 270 to 300°C is strongly influenced by the biomass potassium content. High biomass potassium content leads to a relatively lower solid yield. Also the carbohydrate composition influences the solid yield, such that low hemicelluloses content leads to a relatively high solid yield. It was also seen that biomasses that experiences a high mass loss during the torrification process do also experiences a relatively high particle size reduction.

The gas phase release of Cl and S from wheat straw at torrification conditions was investigated by fixed bed experiments. There was observed a large release of both Cl (up to 65%) and S (up to 50%) at 350°C. The chlorine is mainly released as methyl chlorine (CH_3Cl).

The torrification reactor design study showed, that compared to the relatively fast particle heat up limited by internal heat conduction, the external heat transfer to the fuel bed is the limiting step in the reactor design even when initiatives for increased gas/bed contact is used (passing the gas trough the bed material, using baffles etc). Using a modified rotary kiln having a 10 fold increase

in gas to bed contact area (contact area increase compared to rotary kiln without baffles) and assuming treatment of 24 tons straw per hour the reactor dimensions becomes D = 6m, L = 12 m (V = 334 m^3) in the case of heating of the bed material by a 600 ^oC (inlet temperature) flue gas.